

University of Louisville

ThinkIR: The University of Louisville's Institutional Repository

Electronic Theses and Dissertations

5-2022

Characterization of fundamental parameters that modulate acoustofluidic-mediated molecular delivery to cells.

Connor Sterling Centner
University of Louisville

Follow this and additional works at: <https://ir.library.louisville.edu/etd>



Part of the [Molecular, Cellular, and Tissue Engineering Commons](#)

Recommended Citation

Centner, Connor Sterling, "Characterization of fundamental parameters that modulate acoustofluidic-mediated molecular delivery to cells." (2022). *Electronic Theses and Dissertations*. Paper 3863.
<https://doi.org/10.18297/etd/3863>

This Doctoral Dissertation is brought to you for free and open access by ThinkIR: The University of Louisville's Institutional Repository. It has been accepted for inclusion in Electronic Theses and Dissertations by an authorized administrator of ThinkIR: The University of Louisville's Institutional Repository. This title appears here courtesy of the author, who has retained all other copyrights. For more information, please contact thinkir@louisville.edu.

CHARACTERIZATION OF FUNDAMENTAL PARAMETERS THAT MODULATE
ACOUSTOFLUIDIC-MEDIATED MOLECULAR DELIVERY TO CELLS

By

Connor Sterling Centner
B.S., University of Louisville, 2017
M.Eng., University of Louisville, 2018

A Dissertation Submitted to the
Graduate School, University of Louisville,
In Partial Fulfillment of the Requirements
For the Degree of

Doctor of Philosophy in Interdisciplinary Studies with Specialization in
Translational Bioengineering

Interdisciplinary Studies
University of Louisville
Louisville, Kentucky

May 2022

© 2022 Connor Sterling Centner

CHARACTERIZATION OF FUNDAMENTAL PARAMETERS THAT MODULATE
ACOUSTOFLUIDIC-MEDIATED MOLECULAR DELIVERY TO CELLS

By

Connor Sterling Centner
B.S., University of Louisville, 2017
MEng., University of Louisville, 2018

A Dissertation Approved on

02/18/2022

By the following Dissertation Committee:

Jonathan A. Kopechek, Ph.D. (Chair)

Thomas J. Roussel, Ph.D.

Joseph Chen, Ph.D.

Paula J. Bates, Ph.D.

Kavitha Yaddanapudi, Ph.D.

DEDICATION

This dissertation is dedicated to my parents

Mr. Robert Martin Centner

and

Mrs. Robin Catherine Centner

who have given invaluable educational opportunities.

ACKNOWLEDGMENTS

This dissertation would not have been possible without support of family, friends, and colleagues. I would like to start by thanking my advisor, Dr. Jonathan A. Kopechek, for mentoring me during my capstone project, master's thesis, and Ph.D. studies. Dr. Kopechek has spent a tremendous amount of time and energy to help me develop my research knowledge and skills. I'm amazed by how much I have learned during my studies. He has abundant enthusiasm for teaching students and is incredibly kind. I will always be grateful for all that Dr. Kopechek has provided for me.

I also want to thank my dissertation committee: Dr. Thomas J. Roussel, Dr. Joseph Chen, Dr. Paula J. Bates, and Dr. Kavitha Yaddanapudi. They were immensely helpful throughout my graduate studies. As a student in an interdisciplinary field, it was incredibly beneficial to have committee members with expertise in many different areas. Your willingness to serve on my committee is greatly appreciated.

I would like to thank Drs. Kopechek and Bates for supporting my National Science Foundation (NSF) INTERN application where I received multiple awards to intern at Sexton Biotechnologies, a BioLife Solutions company. It was a tremendous experience and provided me with great insight for my dissertation.

Next, I would like to thank Dr. Patricia S. Soucy and Dr. Gina E. Bertocci (co-directors of my program) for assisting me with setting up my clinical practicum at University of Louisville School of Medicine. Having hands on-experience with cancer patients proved to be an invaluable experience. Understanding issues from a clinical perspective and knowing current limitations of medicine has enabled me to have a greater breadth of knowledge and allowed me to think of creative ways to address current limitations observed in medicine.

I would like to thank all my colleagues who I worked with at the University of Louisville. Specially, I want to thank everyone past or current lab members of the Theranostic Ultrasound Laboratory who spent many long hours in the lab patiently helping me with my experiments and engaging in thoughtful discussion with me. It was so much fun, and I really appreciate their invaluable help.

I would like to thank my incredibly supportive family. My parents (Rob & Robin) unending support helped me reach this point and wouldn't have been able to achieve it alone. They helped me so much, I can never say thank you enough. I want to thank my parents for always pushing me to always pursue my passion.

Finally, I want to thank my fiancée, Nicole. Nicole is truly my best friend and bring so much joy to my life, even when I'm writing manuscripts late-at-night or conducting research on the weekends. She is an incredible person to share life with.

ABSTRACT

CHARACTERIZATION OF FUNDAMENTAL PARAMETERS THAT MODULATE ACOUSTOFLUIDIC-MEDIATED MOLECULAR DELIVERY TO CELLS

Connor S. Centner

February 18th, 2022

Cell-based therapies represent the latest biotechnological revolution in medicine, but significant limitations exist in non-viral intracellular delivery techniques during manufacturing of cell therapies. To address these limitations, a novel acoustofluidic device was developed to deliver ultrasound waves into a flow chamber for rapid molecular delivery to human cells. Our acoustofluidic device delivers biomolecules by inducing expansion and collapse of exogenous gas-filled microbubbles (“cavitation”), which enhances molecular delivery to nearby cells.

Experimental studies were conducted to characterize key parameters that influence acoustofluidic-mediated molecular delivery to human cells. A clinical ultrasound transducer was generally utilized with varying cationic microbubble concentrations. Intracellular delivery of a fluorescent dye was assessed using flow cytometry. Preliminary studies with erythrocytes and primary T cells used a polydimethylsiloxane-based acoustofluidic device, while subsequent studies with Jurkat T cells used a 3D-printed acoustofluidic device to increase compatibility for cell manufacturing applications.

For erythrocytes, ultrasound pressure and microbubble concentration were important parameters that influenced fluorescein delivery. Initial Jurkat T cell studies indicated that microbubble concentration, surface charge, and ultrasound pressure influenced molecular delivery. Subsequent experiments directly compared refined parameters of the acoustofluidic device and a static ultrasound configuration. The acoustofluidic device and the static ultrasound configuration had similar levels of intracellular delivery with small (calcein) and large (150 kDa-FITC Dextran) molecules, although less ultrasound exposure and lower microbubble concentrations were required in the acoustofluidic device.

Bioeffects from acoustofluidic treatment were assessed in subsequent experiments. Cell plating density and media formulation influenced acoustofluidic-mediated molecular delivery. Confocal microscopy indicated that actin patches form in response to acoustofluidic treatment and plug perforations in the plasma membrane. In addition, disruption of organelle structures, such as the nucleus, were observed after acoustofluidic treatment. Cell cycle phases also influenced molecular delivery, and cell proliferation was briefly reduced after acoustofluidic treatment.

The results of this dissertation indicate that acoustofluidic parameters and biological characteristics have important effects on molecular delivery to human cells. Our acoustofluidic device achieved similar molecular delivery levels to Jurkat T cells as a static ultrasound configuration, which indicate that acoustofluidic

devices offer potential advantages for cell processing applications and may improve manufacturing of cell therapies.

TABLE OF CONTENTS

CHAPTER I – INTRODUCTION	1
I.1. Background and Significance	2
I.2. Background in Ultrasound-induced Molecular Delivery	6
I.3. Acoustofluidics review	8
I.3.1. Acoustofluidic-induced Molecular Delivery Applications.....	9
I.4. Research Hypotheses and Specific Aims	10
CHAPTER II – ASSEMBLY AND OPERATION OF AN ACOSUTOFLUIDIC DEVICE FOR ENHANCED DELIVERY OF MOELCULAR COMPOUNDS TO CELLS	12
II.1. Introduction.....	13
II.2. Protocol	16
II.3. Representative Results	25
II.4. Discussion.....	28
CHAPTER III – ULTRASOUND-INDUCED MOLECULAR DELIVERY TO ERYTHROCYTES USING A MICROFLUIDIC SYSTEM	33
III.1. Introduction.....	34
III.2. Methods	39
III.2.1. Acoustofluidic device design and fabrication	39
III.2.2. Microbubble synthesis	41
III.2.3. Fluorescein delivery to erythrocytes	41
III.2.4. Ultrasound image analysis of microbubble destruction	42
III.2.5. Recovery and viability of erythrocytes after freeze-drying and rehydration.....	43
III.2.6. Statistical analysis	44
III.3. Results	44
III.3.1. Effect of ultrasound and flow parameters on erythrocyte viability	44
III.3.2. Effect of ultrasound and flow parameters on fluorescein delivery into erythrocytes ..	45
III.3.3. Ultrasound Image Analysis of Microbubble Destruction	49
III.3.4. Recovery and viability of erythrocytes after freeze-drying and rehydration.....	51
III.4. Discussion	51
III.5. Conclusions	58

CHAPTER IV – ACOUSTOFLUIDIC-MEDIATED MOLECULAR DELIVERY TO HUMAN T CELLS WITH A THREE-DIMENSIONAL-PRINTED FLOW CHAMBER	59
IV.1. Introduction	60
IV.2. Methods.....	65
IV.2.1. Acoustofluidic device design and assembly	65
IV.2.2. Microbubble synthesis	67
IV.2.3. Microbubble attenuation measurements	68
IV.2.4. Molecular delivery to human T cells.....	69
IV.2.5. Computational modeling of fluid dynamics	71
IV.2.6. Protein generation and purification	72
IV.2.7. Statistical Analysis	73
IV.3. Results.....	74
IV.3.1. Effect of microbubble surface charge on molecular delivery.....	74
IV.3.2. Effect of molecular exposure time point on intracellular delivery.....	76
IV.3.3. Effect of acoustofluidic channel geometries on molecular delivery	77
IV.3.4. Effect of ultrasound pressure on molecular delivery.....	80
IV.3.5. Effect of microbubble dose on molecular delivery	82
.....	83
IV.3.6. sfGFP loading in acoustofluidic device.....	83
.....	84
IV.4. Discussion	84
IV.5. Conclusion.....	93
CHAPTER V – COMPARISON OF ACOUSTOFLUIDIC AND STATIC SYSTEMS FOR ULTRASOUND-MEDIATED MOLECULAR DELIVERY TO T LYMPHOCYTES.....	94
V.1. Introduction	95
V.2. Methods.....	100
V.2.1. Molecular Delivery to Human T Lymphocytes	100
V.2.2. Static Ultrasound Treatment.....	104
V.2.3. Acoustofluidic Treatment	104
V.2.4. Microbubble Synthesis	106
V.2.5. Microbubble Attenuation Measurement.....	107
V.2.6. Statistical Analysis	109
V.3. Results.....	109
V.3.1. Effect of Microbubble Concentration on Intracellular Calcein Delivery in Static Ultrasound System.....	109
V.3.2. Effect of Microbubble Concentration on Intracellular Calcein Delivery in Acoustofluidic Device	111
V.3.3. Effect of Ultrasound Output Pressure on Molecular Delivery in Static Ultrasound System.....	113
V.3.4. Effect of Ultrasound Output Pressure on Molecular Delivery in Acoustofluidic System	115

V.3.5. Effect of Ultrasound Treatment Time on Molecular Delivery in Static System	117
V.3.6. Effect of Ultrasound Duration on Molecular Delivery in Acoustofluidic System.....	119
V.3.7. Comparison of Refined Static and Acoustofluidic Conditions on Intracellular Molecular Delivery	121
V.4. Discussion	123
V.5. Conclusion.....	130
CHAPTER VI– BIOMODULATORY EFFECTS OF MOLECULAR DELIVERY IN HUMAN T CELLS USING A 3D-PRINTED ACOUSTOFLUIDIC DEVICES.....	131
VI.1. Introduction	132
VI.2. Methods.....	137
VI.2.1. Molecular Delivery to Human T Lymphocytes.....	137
VI.2.2. Microbubble Synthesis.....	140
VI.2.3. Confocal Microscope Imaging.....	141
VI.2.4. Statistical Analysis	141
VI.3. Results.....	142
VI.3.1. Effect of Cell Plating Density on Molecular Delivery.....	142
VI.3.2. Effect of Serum Concentration on Molecular Delivery.....	145
VI.3.3. Effect of Calcium Chelator on Molecular Delivery.....	146
VI.3.4. Effect of Cell Cycle Phases on Molecular Delivery.....	147
VI.3.5. Effect of Acoustofluidic Treatment on Cell Cycle Phase and	149
VI.3.6. Effect of Acoustofluidic Treatment on Cellular Structures	152
VI.3.7. Effect of Microbubble Concentration on Acoustofluidic Molecular Delivery in Different Cell Lines	155
VI.4. Discussion	158
CHAPTER VII – CONCLUSIONS AND FUTURE WORK.....	170
VII.1. Summary	171
VII.2. Results & Future Directions.....	172
REFERENCES.....	177
CURRICULUM VITAE.....	197

LIST OF FIGURES

Figure 1: Flow scheme representing a typical cell manufacturing process for T cell therapies. This process is critically dependent on effective transfection/transduction efficiency to generate the therapeutic product. The total manufacturing time is typically ~3 weeks, but some products may take longer than 6 weeks to generate (Vormittag et al., 2018).....	3
Figure 2: Photo of acoustofluidic system. The acoustofluidic flow system contains a PDMS-based flow chamber with an integrated PZT transducer driven by a microcontroller. A 3D-printed case with an LED indicator and on/off push button are optional additional features.	27
Figure 3: Acoustofluidic treatment enhances fluorescein delivery to human T cells. (A) Fluorescence intensity in primary T cells increased after acoustofluidic treatment with fluorescein compared to the untreated control group (no acoustofluidics and no and no microbubbles) ($p < 0.05$, $n = 3/\text{group}$). (B) Cell viability decreased slightly after acoustofluidic treatment but remained above 80% as measured by flow cytometry ($p < 0.05$, $n = 3/\text{group}$). (C) Representative flow cytometry histogram indicating higher fluorescence in the acoustofluidic treatment group.....	27
Figure 4: Acoustofluidic treatment enhances trehalose delivery to human lung cancer cells. Trehalose uptake increased in A549 lung carcinoma cells compared to flow only (no ultrasound and no microbubbles) and the untreated control group (ANOVA $p < 0.05$, $n = 3/\text{group}$). (B) Cell viability remained above 90% after acoustofluidic treatment as measured by trypan blue assay ($n = 3-7/\text{group}$).	28
Figure 5: Illustration of ultrasound-induced microbubble (MB) rupture leading to transient perforation of cell membranes — enabling enhanced intracellular delivery of soluble compounds such as trehalose (not to scale).	35
Figure 6: (A) Top: Microfluidic device design with 200 μm channel width. Bottom: a photo of one of the microfluidic devices. (B) Schematic of experimental setup (Not to scale). (C) Top: Ultrasound waveform transmitted by the ultrasound probe (ATL P4-1). Bottom: Transverse profile of the ultrasound beam (-3 dB beamwidth = ~5 mm).	40
Figure 7: (A) Representative flow cytometry scatter plot with the gate used to detect viable erythrocytes based on forward and side scatter profiles. High viability of erythrocytes was observed at (B) different microbubble concentrations, (C) different acoustic pressures, (D) different pulse intervals, and (E) different microfluidic flow rates. Statistically significant decreases in viability were detected at a microbubble dose of 9% (ANOVA $p < 0.05$) and with ultrasound treatment at a microfluidic flow rate of 20 mL/h ($p < 0.05$) compared to the no ultrasound control groups.....	45

Figure 8: (A) Effect of microbubble concentrations on ultrasound-mediated fluorescein uptake. There was a trend toward statistical significance (ANOVA $p=0.12$, $n=4$ /group). (B) Effect of peak negative acoustic pressure on ultrasound-mediated fluorescein uptake. There were statistically significant differences with ultrasound pressures at 0.5 and 0.9 MPa compared to the 0 MPa (no ultrasound) control group (ANOVA $p = 0.01$, $n=4-7$ /group). (C) Effect of pulse interval on ultrasound-mediated fluorescein uptake. There were no statistically significant differences between the different pulse intervals ($n=4-5$ /group). (D) Effect of microfluidic flow rate on ultrasound-mediated fluorescein uptake. Ultrasound treatment and flow rate effect fluorescein uptake, respectively ($p < 0.05$, $n=5$ /group).48

Figure 9: (A) Representative fluorescence intensity histograms after ultrasound treatment at peak negative pressures of 0.25 MPa, 0.5 MPa, 0.9 MPa, or no ultrasound (negative control). Fluorescence intensity increased up to peak negative acoustic pressures of 0.9 MPa indicating enhance molecular delivery to erythrocytes. (B) Representative fluorescence microscopy image of an erythrocyte after ultrasound treatment at a peak negative acoustic pressure of 0.9 MPa demonstrating fluorescein delivery (scale bar = 5 μm). (C) Fluorescence intensity of erythrocytes over time after fluorescein treatment as measured by flow cytometry, indicating no significant difference over time ($n=3$ /group)......49

Figure 10: Ultrasound image mean grayscale intensity as a function of time at peak negative acoustic pressures of 0.5 MPa, 0.9 MPa, and 1.3 MPa. At higher pressures (1.3 MPa), the mean grayscale value decreases more rapidly indicating higher rates of microbubble destruction compared to lower pressures (0.5 MPa and 0.9 MPa).50

Figure 11: Number of intact viable erythrocytes following freeze-drying and rehydration. Microfluidic ultrasound treatment with trehalose caused a statistically significant increase in recovery of intact viable cells compared to the control groups ($p<0.05$, $n=4-8$ /group).51

Figure 12: Rectilinear acoustofluidic device design with 1 mm channel width. Right: Rectilinear acoustofluidic device design with 2 mm channel width. (B) Experimental configuration of ultrasound transducer (P4-1) placed on top of acoustofluidic device with ultrasound gel for acoustic coupling with the acoustofluidic device. (C) Ultrasound waveform generated by P4-1 transducer as measured by needle hydrophone.65

Figure 13: (A) Schematic of acoustic attenuation chamber with a recessed 1.3 cm x 1.3 cm cuvette holder to ensure consistent cuvette sample placement. (B) Photo of acoustic attenuation chamber with polystyrene cuvette placed at the center of the ultrasound beam. The acoustic attenuation chamber contains two co-axially aligned single-element transducers, with one transducer acting as the source and the other transducer acting as the receiver. (C) Representative time-domain waveforms acquired using the acoustic attenuation chamber with microbubbles (2.5% v/v) and without microbubbles (reference). Acquired time-domain waveforms were transformed to the frequency domain to calculate acoustic attenuation coefficients using Equation 168

Figure 14: Effect of microbubble surface charge on molecular delivery in the 1 mm rectilinear channel acoustofluidic device. (A) Microbubbles with cationic surface

charge enhanced calcein delivery to Jurkat T cells in the acoustofluidic device compared to microbubbles with neutral surface charge (ANOVA $p < 0.001$, $n = 5-6$ /group). (B) Cell viability was moderately reduced after acoustofluidic treatment with cationic microbubbles compared to neutral microbubbles (ANOVA $p < 0.001$, $n = 3$ /group). (C) There was no statistically significant difference in acoustic attenuation between cationic microbubbles and neutral microbubbles ($p > 0.05$, $n = 15$ /group).75

Figure 15: Effect of molecular exposure time point on calcein uptake in Jurkat T cells. Calcein was added to cell solutions at various timepoints before and after passing through the 1 mm rectilinear acoustofluidic device with ultrasound treatment (3.8 MPa peak negative pressure) and cationic microbubbles. Calcein delivery was enhanced when delivered prior to treatment compared to all post-treatment exposure time points (ANOVA $p < 0.001$, $n = 5-6$ /group).76

Figure 16: Effect of acoustofluidic channel geometry on molecular delivery. (A) Ultrasound treatment (3.8 MPa peak negative pressure) enhanced calcein delivery to Jurkat T cells in each channel geometry compared to control groups passed through the channels without ultrasound treatment (ANOVA $p < 0.001$, $n = 6$ /group). With ultrasound treatment the 1 mm concentric spiral geometry significantly enhanced calcein delivery to Jurkat T cells compared to the 1 mm and 2 mm rectilinear channel geometry (ANOVA $p < 0.001$) and 2 mm rectilinear channel geometry (ANOVA $p < 0.001$). (B) Ultrasound treatment reduced cell viability in acoustofluidic devices (ANOVA $p < 0.001$, $n = 3-6$ /group), but viability remained above 75% in all groups. (C) Ultrasound treatment reduced acoustic attenuation of microbubble solutions after treatment in each acoustofluidic channel geometry compared to the no flow control condition (ANOVA $p < 0.001$, $n = 6$ /group), indicating that ultrasound treatment induced microbubble destruction in the channels. There was no statistically significant difference in acoustic attenuation between each channel geometry.77

Figure 17: Computational modeling of wall shear stress in each acoustofluidic channel geometry for a flow rate of 1.5 mL/min. (A) Representative images of wall shear stress patterns from computational modeling of each acoustofluidic channel geometry. (B) Average wall shear stress was higher in the concentric spiral geometry compared to rectilinear geometries.79

Figure 18: Effect of ultrasound pressure on molecular delivery to Jurkat T cells in acoustofluidic device. (A) The highest ultrasound pressure evaluated (5.1 MPa peak negative ultrasound output pressure) resulted in the highest amount of intracellular calcein delivery compared to all other treatment groups (ANOVA $p < 0.001$, $n = 6$ /group). (B) Cell viability remained above 75% at all ultrasound pressure conditions ($n = 3$ /group). (C) Acoustic attenuation was significantly reduced in samples treated at peak negative ultrasound pressures 3.8 MPa and higher, indicating ultrasound-mediated microbubble destruction at higher acoustic pressures (ANOVA $p < 0.05$, $n = 5-7$ /group).80

Figure 19: Intracellular delivery of 10 kDa FITC-dextran at various cationic microbubble concentrations, using a concentric spiral acoustofluidic device at 5.1 MPa peak negative ultrasound output pressure. (A) Acoustofluidic treatment with 10 $\mu\text{g/mL}$ (1 mM) of 10 kDa FITC-Dextran increased intracellular delivery to Jurkat

T cells at a microbubble concentration of 5% (v/v) compared to lower microbubble concentrations (0-1% v/v, ANOVA $p < 0.001$, $n = 6-9$ /group) and higher microbubble concentrations (10% v/v, $p < 0.01$). (B) Acoustofluidic treatment with a cationic microbubble concentration of 5% (v/v) had reduced cell viability compared to the 0% (v/v) microbubble concentration control group (ANOVA $p < 0.001$, $n = 6-9$ /group), 1-2.5% (v/v) microbubble concentrations ($p < 0.05$), and 10% (v/v) microbubble concentration ($p < 0.05$).83

Figure 20: Intracellular delivery of green fluorescent protein (GFP) using the concentric spiral acoustofluidic device at 5.1 MPa peak negative ultrasound output pressure and a cationic microbubble concentration of 5% (v/v). (A) Molecular delivery with 2 μ M of 26 kDa sfGFP was increased after acoustofluidic treatment compared to flow only without ultrasound (negative control; Student's T-test $p < 0.05$, $n = 6$ /group). (B) Cell viability was reduced after acoustofluidic treatment compared to flow only without ultrasound (Student's T-test $p < 0.001$, $n = 6$ /group), but viability remained above 90% in each group.84

Figure 21: (A) Static configuration with an ultrasound imaging probe transmitting pulsed ultrasound signal to induce microbubble cavitation in cell solution for enhanced molecular delivery to Jurkat T lymphocytes (not to scale). (B) Acoustofluidic device with an ultrasound imaging probe transmitting pulsed ultrasound signal into fluidic channel so that microbubble cavitation occurs in cell solution for enhanced molecular delivery to Jurkat T lymphocytes (not to scale). (C) Concentric spiral acoustofluidic device design with 1 mm x 1 mm channel geometry (not to scale).100

Figure 22: Representative flow cytometry scatter plot of Jurkat T lymphocytes population based on FITC Fluorescence Intensity and Propidium Iodide Fluorescence Intensity. Values in the left-half plane indicate viable cells (PI-) and values in the right-half plane represent non-viable cells (PI+), respectively. (A) Representative flow cytometry scatter plot for a flow only control sample without ultrasound treatment. (B) Representative flow cytometry scatter plot for a sample with acoustofluidic treatment, indicating that FITC fluorescence is significantly increased for both viable (PI-) and non-viable (PI+) cells. Low resolution103

Figure 23: Representative brightfield microscopy image of cationic microbubbles, which can oscillate in response to ultrasound waves and enhance molecular delivery to nearby cells. Scale bar represents 50 μ m.107

Figure 24: (A) Delivery efficacy of calcein (100 μ g/mL) with varying microbubble concentrations using static ultrasound treatment (3.8 MPa, 30s). 94 μ g/mL microbubble concentration enhanced biomolecular delivery of calcein compared to 0-9 μ g/mL microbubble concentrations (ANOVA $p < 0.001$, $n = 7-8$ /group) and 24 μ g/mL microbubble concentration ($p < 0.01$). (B) 94 μ g/mL microbubble concentration had reduced viability compared to 0-24 μ g/mL microbubble concentrations ($p < 0.001$) and 47 μ g/mL microbubble concentration ($p < 0.05$), respectively. Cell viability remained above 80% for all treatment groups. (C) Acoustic attenuation was significantly reduced for 47 and 94 μ g/mL microbubble concentrations when treated with ultrasound compared to no ultrasound treatment controls, indicating significant microbubble destruction occurred at these concentrations (ANOVA $p < 0.001$, $n = 6$ /group).....109

Figure 25: (A) Delivery efficacy of calcein (100 $\mu\text{g}/\text{mL}$) with varying microbubble concentrations using acoustofluidic treatment (3.8 MPa). 24 $\mu\text{g}/\text{mL}$ microbubble concentration enhanced molecular delivery of calcein compared to all other microbubble concentrations (ANOVA $p < 0.001$, $n = 5-6/\text{group}$). (B) 24 $\mu\text{g}/\text{mL}$ microbubble concentration had decreased viability compared to lower microbubble concentrations (0-9 $\mu\text{g}/\text{mL}$). However, cell viability remained above 85% for all treatment groups. (C) Acoustic attenuation was significantly reduced for 47 $\mu\text{g}/\text{mL}$ (ANOVA $p < 0.05$, $n = 6/\text{group}$) and 94 $\mu\text{g}/\text{mL}$ ($p < 0.001$) microbubble concentrations when treated with ultrasound compared to no ultrasound treatment controls, indicating significant microbubble destruction occurred at these concentrations.

.....111

Figure 26: (A) Static ultrasound treatment (30s) with 94 $\mu\text{g}/\text{mL}$ microbubble concentration and varying peak negative output pressure. 5.1 MPa peak negative pressure enhanced calcein (100 $\mu\text{g}/\text{mL}$) delivery compared to all other 0 MPa and 2.5 MPa, respectively (ANOVA $p < 0.001$, $n = 9-10/\text{group}$). (B) Cell viability remained above 65% in all samples. Cationic microbubble present with and without ultrasound treatment at different treatment pressure. (C) Acoustic attenuation was significantly reduced in samples treated with ultrasound pressures above 2.5 MPa (ANOVA $p < 0.001$, $n = 6/\text{group}$), indicating microbubble destruction at higher acoustic pressures.....114

Figure 27: (A) Acoustofluidic device delivery efficacy of calcein (100 $\mu\text{g}/\text{mL}$) with 24 $\mu\text{g}/\text{mL}$ microbubble concentration and varying peak negative output pressures. 3.8 and 5.1 MPa conditions enhanced calcein delivery in Jurkat T lymphocytes compared to 0 MPa (no ultrasound treatment) and 2.5 MPa, respectively (ANOVA $p < 0.001$, $n = 6-7/\text{group}$). (B) Cell viability was reduced in 3.8 MPa and 5.1 MPa treatment conditions compared to 0 MPa and 2.5 MPa treatment conditions, respectively ($p < 0.001$). Cell viability remained above 75% in all samples. (C) Acoustic attenuation was significantly reduced in samples treated with ultrasound pressures above 2.5 MPa compared to flow conditions without ultrasound treatment (ANOVA $p < 0.001$, $n = 4-6/\text{group}$). Additionally, 3.8 MPa ($p < 0.05$) and 5.1 MPa ($p < 0.01$) had decreased acoustic attenuation compared to 2.5 MPa, indicating microbubble destruction at higher acoustic pressures.116

Figure 28: (A) Delivery efficacy of calcein (100 $\mu\text{g}/\text{mL}$) with varying treatment time for static ultrasound treatment (5.1 MPa, 94 $\mu\text{g}/\text{mL}$ microbubble concentration). 45 and 60 seconds of static ultrasound treatment time enhanced biomolecular delivery of calcein compared to no ultrasound treatment (0 seconds) and 15 seconds of static ultrasound treatment time (ANOVA $p < 0.001$, $n = 7-9/\text{group}$). Additionally, 45 second static ultrasound treatment time enhanced calcein delivery compared to 30 seconds of static ultrasound treatment time ($p < 0.01$). Similar results were observed between 45 seconds and 30 seconds of ultrasound treatment time ($p < 0.05$). (B) Cell viability was reduced with 60 seconds of treatment time compared to 0 second treatment time (no ultrasound; $p < 0.01$). Cell viability remained above 70% for all treatment groups. (C) Acoustic attenuation was significantly reduced in samples with 30 seconds or above of ultrasound treatment time compared to 0 seconds (ANOVA $p < 0.01$, $n = 6-12/\text{group}$).119

Figure 29: (A) Delivery efficacy of calcein (100 µg/mL) with varying treatment time for acoustofluidic treatment (3.8 MPa, 24 µg/mL microbubble concentration). 1x acoustofluidic treatment and 2x acoustofluidic treatment enhanced biomolecular delivery of calcein compared to their no ultrasound treatment control, respectively (ANOVA $p < 0.001$, $n = 6/\text{group}$). (B) Cell viability remained above 85% for all treatment groups with no statistical significance detected between groups. (C) Acoustic attenuation was significantly reduced in samples with multiple acoustofluidic treatments compared to multiple flow only control where microbubbles were added prior to each treatment (ANOVA $p < 0.001$, $n = 6/\text{group}$).

.....117

Figure 30: (A) Delivery efficacy using 0.6 µg/mL (1 mM) of calcein (0.6 kDa) and 150 µg/mL (1 mM) of 150 kDa FITC-Dextran were assessed with refined static treatment (5.1 MPa, 45 s, and 94 µg/mL microbubble concentration) and acoustofluidic treatment (5.1 MPa, 24 µg/mL microbubble concentration) parameters. Static treatment and acoustofluidic treatment enhanced biomolecular delivery of calcein (ANOVA $p < 0.01$, $n = 5-6/\text{group}$) and 150 kDa FITC-Dextran ($p < 0.001$) compared to negative control (no ultrasound treatment), respectively. (B) Static and acoustofluidic treatment had decreased cell viability compared to negative control ($p < 0.001$). No statistically significant differences in cell viability were detected between static and acoustofluidic treatment for calcein and 150 kDa FITC-Dextran treatment groups, respectively ($p > 0.05$).

.....121

Figure 31: Cell viability and proliferation after acoustofluidic treatment, as measured with trypan blue assay. Immediately after treatment (day 0), the number of viable cells was not statistically different between acoustofluidic treatment and the flow only control group (ANOVA $p > 0.05$, $n = 5/\text{group}$). At two days after treatment, the number of viable cells was higher in the flow only control group compared to the acoustofluidic treatment group ($p < 0.001$), but cell proliferation was evident by higher numbers of viable cells in both groups compared to day 0 ($p < 0.001$).

.....122

Figure 32: Schematic of acoustofluidic setup for intracellular molecular delivery to human cells. The acoustofluidic system utilizes an ultrasound transducer coupled with a 3D-printed flow chamber. A peristaltic pump is used to push solutions through the acoustofluidic channels and enhance intracellular molecular delivery (schematic is not to scale).

.....137

Figure 33: Representative schematic of gating for Jurkat T cell population based on cell cycle determined by violet fluorescence intensity. Values on the left portion (red), middle portion (blue), and right portion (black) of the x-axis represent G0/G1 Phase, S Phase, and G2/M Phase, respectively. On the y-axis is number of cells counted based on violet fluorescence.

.....139

Figure 34: Effect of cell plating density on molecular delivery in Jurkat T cells. (A) Delivery efficiency of calcein (100 µg/mL) in Jurkat T cells after acoustofluidic treatment with 2.5% v/v microbubbles dose and a peak rarefaction ultrasound pressure output of 5.1 MPa. Cells were resuspended at 100,000 cells/mL prior to acoustofluidic treatment after 2 days of culture with varying plating densities. Delivery efficiency was significantly enhanced after acoustofluidic treatment compared to corresponding flow only control groups (ANOVA $p < 0.001$, $n = 7-$

8/group). Molecular delivery was higher after acoustofluidic treatment in cells harvested from flasks with a plating density of 100,000 cells/mL compared to cells harvested from flasks with plating densities of 200,000 cells/mL ($p < 0.01$) and 300,000 cells/mL ($p < 0.001$). (B) Cell viability was reduced after acoustofluidic treatment compared to flow only conditions (ANOVA $p < 0.001$, $n = 7-8$ /group) but viability remained above 70% in all conditions. Viability was slightly lower after acoustofluidic treatment in cells harvested from flasks with plating densities of 200,000 cells/mL compared to plating densities of 100,000 cells/mL ($p < 0.01$) and 300,000 cells/mL ($p < 0.001$).....142

Figure 35: Confocal microscopy imaging of F-actin staining revealed differences in the cytoskeleton network between Jurkat T cells treated with flow only (control, left panels) and acoustofluidic treatment (right panels) for cells harvested from flasks seeded at different plating densities 2 days prior to treatment. Qualitative assessment indicates that polymeric F-actin increased in cells after acoustofluidic treatment compared to respective control samples. Additionally, confocal imaging indicates that increased polymerization occurred in cells harvested from flasks at low plating density (100,000 cells/mL) compared to medium plating density (200,000 cells/mL) and high plating density (300,000 cells/mL). Scale bar indicates 10 μm144

Figure 36: Effect of fetal bovine serum (FBS) concentrations on acoustofluidic-mediated molecular delivery in Jurkat T cells. (A) Delivery efficiency of calcein (100 $\mu\text{g/mL}$) with varying concentrations of fetal bovine serum (0% and 10%) and acoustofluidic treatment using a cationic microbubble concentration of 2.5% and a peak rarefaction ultrasound pressure output of 5.1 MPa. Acoustofluidic treatment without FBS (0%) and with 10% FBS in loading media increased molecular delivery compared to the respective flow only control groups (ANOVA $p < 0.001$, $n = 10-12$ /group). Additionally, molecular delivery was significantly increased after acoustofluidic treatment with 0% FBS compared to 10% FBS ($p < 0.001$). (B) Cell viability was reduced after acoustofluidic treatment with 0% FBS and 10% FBS compared to respective flow only control groups (ANOVA $p < 0.001$, $n = 10-12$ /group). Additionally, viability was further reduced after acoustofluidic treatment in cells without FBS compared to cells in 10% FBS ($p < 0.001$).....145

Figure 37: Effect of extracellular calcium on molecular delivery in Jurkat T cells. (A) Delivery efficiency of calcein (100 $\mu\text{g/mL}$) was measured with varying loading media (RPMI and 1x PBS) with and without calcium chelator (1 mM EGTA) and acoustofluidic treatment using a cationic microbubble concentration of 2.5% and a peak rarefaction ultrasound pressure output of 5.1 MPa. Acoustofluidic treatment with RPMI media significantly enhanced molecular delivery compared to flow only control groups or compared to acoustofluidic treatment in other media (ANOVA $p < 0.001$, $n = 6$ /group). Acoustofluidic-mediated molecular delivery was significantly reduced for cells in RPMI + EGTA, indicating that addition of a calcium chelator influenced acoustofluidic delivery efficiency in Jurkat cells. (B) Cell viability was reduced after acoustofluidic treatment for all loading media compared to flow only control groups. Viability was further reduced for cells in PBS compared to cells in RPMI media for each treatment condition (ANOVA $p < 0.01$, $n = 6$ /group).....146

Figure 38: Effect of cell cycle phases on molecular delivery in Jurkat T cells. (A) Delivery efficiency of 150 kDa FITC-Dextran (1.5 mg/mL) was analyzed for cells in various cell cycle phases (G0/G1, G2/M, S) with acoustofluidic treatment using a cationic microbubble concentration of 2.5% and a peak rarefaction ultrasound pressure output of 5.1 MPa. Molecular delivery was significantly higher after acoustofluidic treatment for cells in all cell cycle phases compared to their respective flow only control groups (ANOVA $p < 0.001$, $n = 9/\text{group}$). Molecular delivery was further enhanced for cells in the S phase compared to cells in the G0/G1 phase ($p < 0.01$) or G2/M phase ($p < 0.001$). (B) Cell viability was reduced after acoustofluidic treatment for cells in the G0/G1 phase ($p < 0.001$) and S phase ($p < 0.05$) compared to their respective flow only control groups. Viability was lower for cells in the G0/G1 phase after acoustofluidic treatment compared to cells in the G2/M phase or S phase after acoustofluidic treatment ($p < 0.001$).....148

Figure 39: Effect of acoustofluidic treatment on cell cycle phases and proliferation rates. (A-C) The relative percentage of cells in each cell cycle phase was measured at 0 days and 2 days after acoustofluidic treatment compared to flow only control or no treatment groups. The percentage of cells in the G0/G1 phase and the S phase was significantly higher at 2 days after acoustofluidic treatment compared to their respective no treatment groups (ANOVA $p < 0.05$, $n = 6/\text{group}$), whereas the percentage of cells in the G2/M phase was significantly lower at 2 days after acoustofluidic treatment compared to the respective no treatment group. (D) The number of viable cells was significantly lower at 2 days after acoustofluidic treatment compared to no treatment and flow only control groups, as measured by trypan blue assay (ANOVA $p \leq 0.001$, $n = 4/\text{group}$). (E) High viability was observed for cells at 2 days after acoustofluidic treatment as measured by trypan blue assay, even though the overall number of cells was lower in the acoustofluidic treatment group compared to the control groups. (F) Cells were resuspended at a concentration of 100,000 cells/mL at 2 days after acoustofluidic treatment and cultured for an additional 2 days. After 4 days of culture post-treatment there was no statistically significant difference in the number of viable cells for the acoustofluidic treatment group compared to no treatment and flow only control groups, as measured by trypan blue assay (ANOVA $p > 0.05$, $n = 4/\text{group}$).....149

Figure 40: CellMask Orange was used to stain F-actin (indicated in red). Higher localized fluorescence indicated the presence of increased F-actin levels. A significant increase in F-actin levels was observed in Jurkat T cells after acoustofluidic treatment at day 0, compared to cells in the flow only control group. However, minimal differences in F-actin levels were observed at day 2 and day 4 after acoustofluidic treatment. Scale bar represents 10 μm151

Figure 41: Effect of acoustofluidic treatment on cellular structures. Panel A represents cells in the flow only control group, whereas panels B-D represent cells after acoustofluidic treatment. Cells were stained with an ER (red), Golgi (green), and nuclear (dark blue) stain using the CytoPainter kit, while LysoView 405 was used to stain lysosomes (light blue). Panel A shows that minimal disruption to cellular structures occurred in the flow only control group. Panel B is an example of a cell that underwent acoustofluidic treatment but had minimal disruption to cell structures. Panels C and D represent a cell at different planes of view to illustrate

structural changes that occurred after acoustofluidic treatment, including permeabilization of the nucleus. These images demonstrate that acoustofluidic treatment can cause significant disruption of cellular structures, including the nucleus, ER, Golgi, and lysosomes. Scale bar represents 10 μm152

Figure 42: Effect of acoustofluidic treatment on cellular and nuclear structures. Panel A represents cells in the flow only control group, while panels B-D represent cells after acoustofluidic treatment. Cells were stained with an ER (red), Golgi (green), and nuclear (dark blue) stain using the CytoPainter kit, while MitoView Blue was used to stain mitochondria (light blue). Purple coloration is due to the very tight overlap of ER and mitochondria (red and light blue overlap). Panel B demonstrates cells with relatively minor disruption of the nucleus but major disruption of the ER, Golgi, and mitochondria. Panels C and D provide two examples of cells where the sonoporation entry wound (white arrow) and exit wound (red arrow) are visible after acoustofluidic treatment. In panels B-D, blue fluorescence in the cytoplasm and as a node(s) in the nucleus may be due to off-staining of the cationic mitochondrial dye, as it competes for anionic interaction partners with the cationic lipids and cationic ions that enter the cells during acoustofluidic treatment. Scale bar represents 10 μm153

Figure 43: Comparison of acoustofluidic-mediated molecular delivery in different cell lines. (A) Delivery efficiency of 150 kDa FITC-Dextran (1 mM) to Jurkat T cells with varying microbubble concentration using acoustofluidic treatment (5.1 MPa). A microbubble concentration of 5% v/v significantly enhanced intracellular delivery of 150 kDa FITC-Dextran compared to microbubble concentrations of 0-1% v/v (ANOVA $p < 0.01$, $n = 6/\text{group}$) and compared to a microbubble concentration of 10% v/v ($p < 0.05$), respectively. (B) Cell viability was reduced after acoustofluidic treatment for all microbubble concentrations compared to the negative control condition without microbubbles (0% v/v; $p < 0.001$). Additionally, cell viability was reduced after acoustofluidic treatment at microbubble concentrations of 2.5%-7.5% v/v compared to microbubble concentrations of 1% v/v and 10% v/v ($p < 0.001$). (C) Delivery efficiency of 150 kDa FITC-Dextran (1 mM) to MDA-MB-231 human breast carcinoma cells with varying microbubble concentration using acoustofluidic treatment (5.1 MPa). A microbubble concentration of 5% v/v significantly enhanced intracellular delivery of 150 kDa FITC-Dextran compared to microbubble concentrations of 0-2.5% v/v or 7.5-10% v/v (ANOVA $p < 0.001$, $n = 6/\text{group}$). (D) Cell viability was reduced after acoustofluidic treatment at microbubble concentrations of 2.5%-7.5% v/v compared to the negative control condition without microbubbles (0% v/v, $p < 0.001$). (E) Delivery efficiency of 150 kDa FITC-Dextran (1 mM) to A549 human lung carcinoma cells with varying microbubble concentration using acoustofluidic treatment (5.1 MPa). A microbubble concentration of 5% v/v significantly enhanced intracellular delivery of 150 kDa FITC-Dextran compared to the negative control conditions without microbubbles (0% v/v, ANOVA $p < 0.001$, $n = 9/\text{group}$). (F) Cell viability was reduced after acoustofluidic treatment with a microbubble concentration of 5% v/v compared to microbubble concentrations of 0-2.5% v/v or 7.5%-10% v/v ($p < 0.001$), respectively. (G) Delivery efficiency of 150 kDa FITC-Dextran (1 mM) to HEK293 cells with varying microbubble concentration using acoustofluidic treatment (5.1

MPa). A microbubble concentration of 1-10% v/v significantly enhanced intracellular delivery of 150 kDa FITC-Dextran compared to the negative control condition without microbubbles (0% v/v, ANOVA $p < 0.01$, $n = 3-6/\text{group}$). Additionally, acoustofluidic treatment with a microbubble concentration of 5% v/v increased molecular delivery compared to 7.5% v/v ($p < 0.01$) (H) Cell viability was reduced after acoustofluidic treatment with a microbubble concentration of 5-10% v/v (0% v/v, ANOVA $p < 0.001$, $n = 3-6/\text{group}$) and 2.5% v/v ($p < 0.05$) compared to the negative control condition without microbubbles. Cell viability remained above 80% for all treatment conditions.158

CHAPTER I – INTRODUCTION

I.1. Background and Significance

Cell-based therapies represent the latest biotechnological revolution in medicine. Potential therapeutic applications include treating cancers, treating autoimmune disease, treating infectious diseases, and repairing damaged tissue (Buzhor *et al.*, 2014). Most cell-based therapies are currently undergoing preliminary evaluation in a laboratory and/or clinical setting, but some cell-based therapies have reached FDA-approval, such as modified Cytotoxic T Lymphocytes (CTLs) for treatment of blood related disorders. Recent results in modified immune cells for cancer applications, specifically CTLs, enhance cytotoxic activity while reducing off-target effects and has distinct advantages over traditional treatment regimens (*e.g.*, chemotherapy). Although cell-based therapies have a diverse range of applications and cell material, there are common translational challenges that need to be addressed to bring these therapies to the clinical market.

Cell-based therapies may be classified by therapeutic application, donor source, and/or cell type (Mount *et al.*, 2015). A broad spectrum of cell classes may be used in a clinical setting depending on the application required. Rather than assessing the field on cell classes and therapeutic application alone, it may be beneficial to assess cell-based therapies from a technological perspective, which has important implications on development of new cell therapies and manufacturing processes. Cell manufacturing processes comprise numerous steps, which typically follow a similar process regardless of cell type or application (Fig. 1). This review focuses on molecular delivery of biomolecules to immune cells. From a technological perspective of delivering biomolecules, delivery

vehicles for cell-based therapies will be broadly classified as viral and non-viral delivery methods.

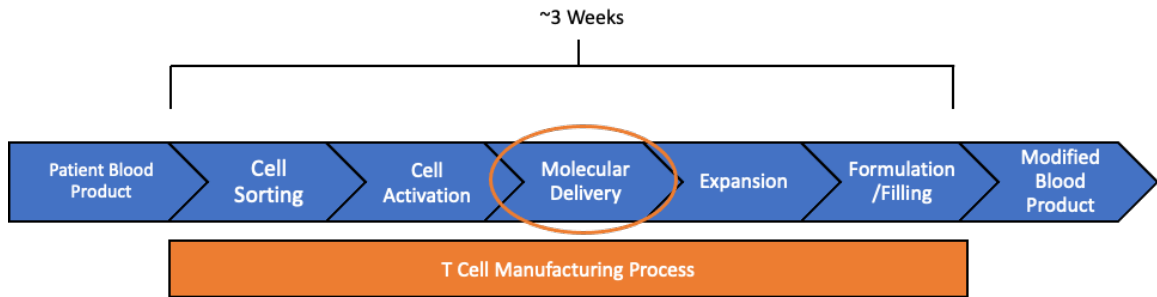


Figure 1: Flow scheme representing a typical cell manufacturing process for T cell therapies. This process is critically dependent on effective transfection/transduction efficiency to generate the therapeutic product. The total manufacturing time is typically ~3 weeks, but some products may take longer than 6 weeks to generate (Vormittag *et al.*, 2018).

Currently viral vector technology is being utilized for *ex vivo* modification of CTLs (Zhang *et al.*, 2017a). Viral vectors are infectious entities that are adapted to deliver nucleic acid to the cytoplasm or nucleus (Nayerossadat *et al.*, 2012b). Transduction for T cell therapies is a common modality for gene delivery, but has limitations that include low/inconsistent transduction efficiency, potential insertional mutagenesis, limited transgenic capacity, and limited non-nucleic acid delivery (Hacein-Bey-Abina *et al.*, 2010; Brentjens *et al.*, 2011; Dai *et al.*, 2015; Porter *et al.*, 2015). Low/inconsistent transduction efficiency provides a critical issue as some groups have reported efficiencies between 4-70% in their respective studies (Brentjens *et al.*, 2011; Dai *et al.*, 2015; Porter *et al.*, 2015). Additionally,

low/inconsistent transduction efficiency has been observed with other immune cells, such as dendritic cells (Rossi *et al.*, 2019). These factors may limit novel cell-based therapies from reaching the market, which can impact patient outcomes. For example, tisagenlecleucel (chimeric antigen receptor (CAR)-T therapy) may require up to 10^9 cells/kg bodyweight for the therapeutic applications (Awasthi *et al.*, 2020). Thus, alternative molecular delivery approaches should be considered to increase molecular delivery levels along with consistency to expedite the cell manufacturing process.

Non-viral molecular delivery techniques are in development and are commercially available for a broad range of biomedical and research applications. To enhance molecular delivery of biomolecules to cells, common techniques may include mechanical, electrical, hydrodynamic, or use of laser-based energy (Nayerossadat *et al.*, 2012b). These techniques commonly focus on modifying the permeability of the plasma membrane to enhance intracellular molecular delivery via mechanisms such as transient perforation (Sugar and Neumann, 1984a; Gehl, 2003b; Chen *et al.*, 2006a; Nayerossadat *et al.*, 2012b; Hashimoto and Takemoto, 2015a).

A commercially available technique that is frequently utilized is electroporation. Large biotechnology companies, such as ThermoFisher, generally have their own commercially available electroporation devices. Electroporation induces transient perforation of the plasma membrane, but this involves a stochastic process and electroporation-mediated molecular delivery to cells is generally dependent on passive diffusion through transient pores (Sugar and

Neumann, 1984a). Coupling of electroporation and microfluidic devices have been demonstrated to address scalability issues (Wang and Lu, 2006; Geng and Lu, 2013). This technology is currently being brought to market by companies such as Kytopen. Although this technology is being brought to market, limitations such as passive diffusion have not been fully addressed.

Another non-viral process that has been explored involves microfluidic squeezing where the distance between capillary walls is smaller than the diameter of cells. The microfluidic channel constricts cells and transiently increased permeability of the plasma membrane, enabling uptake of molecular compounds in the media via diffusion (Sharei *et al.*, 2013). To overcome processing limitations, microfluidic squeezing devices utilize channel parallelization to increase throughput rate up to approximately 10^6 cells/sec (Sharei *et al.*, 2015; Szeto *et al.*, 2015). However, channel blockage and limited loading efficiency may inhibit successful translation for many immune cell manufacturing applications (Dressaire and Sauret, 2016). This technology was brought to market by SQZBiotech and is under preclinical and clinical evaluation using erythrocytes and professional antigen presenting cells to treat a variety of diseases by carrying antigens of interest to spleen or lymph nodes to prime the immune system. This approach can enable treatment to occur within a week of blood collection since lower amounts of antigen carrying cells are required than typical cell manufacturing applications. However, it still requires priming of the adaptive immune system, which can take multiple weeks to reach significant levels for primary exposure to an antigen. In fact, high transfection efficiency is not required to generate a cytotoxic T cell

response. An antigen-specific response can be generated with <1% transfection efficiency (Grunebach *et al.*, 2003). Thus, successful translational of antigen presenting cells may not necessarily translate into successful *ex vivo* modification of non-antigen presenting cells, such as natural killer (NK) cells or T cells. Furthermore, microfluidic squeezing intends to deliver cargo into the cytosol and may be ineffective at nuclear delivery.

Viral and non-viral delivery technologies have key limitations that have important implications on the potential success of cell-based therapies. Thus, other technologies should be considered that may have the capacity to induce rapid, consistent molecular delivery not only to the cytosol but potentially to the nucleus. Ultrasound-induced molecular delivery may be a viable option to address these challenges, but further exploration is required.

1.2. Background in Ultrasound-induced Molecular Delivery

B-mode ultrasonography is a common modality that uses ultrasound echoes originally generated by the ultrasound transducer in the form of pulsed ultrasound pressure waves, which reflect back to the transducer based on the material properties such as differences in speed of sound and material density. Common applications include neonatal imaging and cardiac imaging. Ultrasound contrast agents (UCAs) are currently utilized to enhance echogenicity of blood and delineate surrounding structures (Cosgrove, 2006). UCAs are FDA approved for echocardiograms and generally consist of a perfluorocarbon core and a surfactant, such as lipid or protein, to stabilize the microbubble for persistence in the circulatory system.

For ultrasound-based molecular delivery techniques, mechanical bioeffects are desired in order to enhance molecular delivery to cells (Izadifar *et al.*, 2017). To reduce the ultrasound pressure required for generating mechanical bioeffects, exogenous microbubbles are added to the buffer which enhance molecular delivery when located near cell membranes. Microbubble cavitation involves rapid expansion and contraction of microbubbles in response to ultrasound waves. This process triggers reversible plasma membrane perforation when microbubbles are near cells, a phenomenon known as “sonoporation”. Additionally, biological effects induced by cavitation, such as enhanced endocytosis, have been observed (Hauser *et al.*, 2009).

With advancements of gene and molecular engineering, more scientists have been exploring *ex vivo* modifications to cells (Brentjens *et al.*, 2007; Barrangou and Doudna, 2016; Annesley *et al.*, 2018a). Many studies have utilized static ultrasound treatment for enhanced delivery of biomolecules to cells, by utilizing a static solution that contains cells and exogenous microbubbles in a sample chamber placed in the ultrasound focus. In fact, numerous studies utilizing immune cells have investigated ultrasound-induced molecular delivery in static ultrasound configurations, but these studies have mainly utilized dendritic cells (Deng *et al.*, 2010; De Temmerman *et al.*, 2011). A critical factor for ultrasound-induced transfection was found to be related to cavitation dynamics, with inertial cavitation identified as having increased plasma membrane disruption and molecular delivery compared to stable cavitation activity (Fan *et al.*, 2013). However, static ultrasound configurations currently have some major limitations

such as its lack of a standardized process, a more heterogenous solution resulting in inconsistent ultrasound pressures, and low throughput/slow processing times. These limitations pose a major hurdle for translation of ultrasound-based technology into cell manufacturing applications. Thus, utilizing an ultrasound-based flow chamber is necessary to overcome these limitations. Acoustofluidic devices in development may address these challenges by combining ultrasound waves in fluidic channels containing cells and microbubbles.

I.3. Acoustofluidics review

Acoustofluidics technologies have increasingly been utilized to address challenges in manufacturing and clinical applications, especially in diagnostics and therapeutics (Li *et al.*, 2015; Chen *et al.*, 2016; Wu *et al.*, 2017). Furthermore, acoustofluidic-based devices have the potential to enable point-of-care (POC) for patient bedside and outpatient applications due to their operator simplicity and rapid processing capabilities. In fact, acoustofluidic-based devices have been developed for a variety of applications including acoustophoresis (Pettersson *et al.*, 2007; Lenshof *et al.*, 2012), fluid mixing (Shilton *et al.*, 2008; Friend and Yeo, 2011; Yeo *et al.*, 2011), and biomarker analysis (Wang *et al.*, 2020; Zhou *et al.*, 2021). One of the first acoustofluidic products to reach the market was the Ekko Acoustic Cell Processing System by FloDesign Sonics for cell concentration, media exchange, and cell expansion or differentiation applications to address limitations in other aspects of the cell manufacturing process. However, few research studies have been conducted investigating acoustofluidics for molecular delivery applications to immune cells, which is the focus of this dissertation.

I.3.1. Acoustofluidic-induced Molecular Delivery Applications

Recent advancements in genome editing have led to significant research involving *ex vivo* cell manipulation for therapeutic applications such as treatment of cancer and HIV (Deeks *et al.*, 2002; Brentjens *et al.*, 2007; Kochenderfer *et al.*, 2010; Jinek *et al.*, 2012; Mali *et al.*, 2013; Barrangou and Doudna, 2016; Ying *et al.*, 2019). Recently, acoustofluidic-induced molecular delivery platforms have been assessed to overcome limitations of viral transduction and other non-viral delivery methods (Belling *et al.*, 2020a; Centner *et al.*, 2020; Centner *et al.*, 2021b). Acoustofluidics for molecular delivery applications is a platform technology that can allow delivery of a vast array of biomolecules. Multiple parameters/mechanisms can play a fundamental role in enhancing molecular delivery to cells.

Prior research studies have investigated acoustofluidics for molecular delivery without exogenous microbubbles. Some acoustofluidic platforms induced molecular delivery without microbubbles by taking advantage of Gor'kov potential where acoustic pressure is lowest at the capillary wall opposite of the transducer (Guo *et al.*, 2016; Belling *et al.*, 2020a). This ultimately induces an acoustic radiation force on the cell and moves the cell to the capillary wall opposite of the transducer. Research groups have tethered molecular compounds to the capillary wall opposite of the transducer to improve molecular delivery to cells as acoustic radiation force and shear stress are likely involved in increasing permeabilization of the plasma membrane (Belling *et al.*, 2020a).

Acoustofluidic-induced molecular delivery with exogenous microbubbles is a novel concept and requires more research to understand its effects on cells. A variety of physical parameters may affect biomolecular delivery, such as ultrasound pressure, ultrasound frequency, exposure time, pulse duration, acoustofluidic channel dimensions, and microbubble size and composition (Forbes *et al.*, 2011; Helfield *et al.*, 2016c; Centner *et al.*, 2020). Biological effects may also affect biomolecular delivery to cells in a static ultrasound configuration or acoustofluidic device (De Cock *et al.*, 2015). Physical and biological parameters, however, have only been thoroughly investigated in static ultrasound configurations. Thus, characterization of physical and biological parameters that influence molecular delivery in an acoustofluidic device represents a significant gap in knowledge. Molecular delivery to lymphocytes, specifically T lymphocytes, and erythrocytes will be the focus, but acoustofluidic systems are platform technologies that can be used for other cell lines.

I.4. Research Hypotheses and Specific Aims

The motivation of this dissertation is the need for rapid, sequential molecular delivery to cells for a variety of applications. The overall objective of this dissertation is to elucidate the role of acoustofluidic parameters and mechanisms in molecular delivery for modification of cells. The central hypothesis is that an ***acoustofluidic platform with exogenous microbubbles in solution enhances molecular delivery efficiency to human cells.*** Key parameters in the acoustofluidic platform with microbubble-enhanced delivery have not been

assessed in previous acoustofluidic studies. The experiments described in this dissertation were designed to test the central hypothesis and answer underlying research questions:

1. What are fundamental parameters that modulate molecular delivery efficiency?
2. Does microbubble destruction in acoustofluidic channels correlate with molecular delivery to cells?
3. Does acoustofluidic treatment achieve similar levels of molecular delivery compared to a static ultrasound system?
4. What bioeffects do acoustofluidic treatment and cell culture media formulations induce on molecular delivery and cell dynamics?

The underlying research questions in conjugation with the central hypothesis were used to guide the **specific aims**:

Specific Aim 1 (Chapter 3): Assess key parameter effects on molecular delivery efficiency

Specific Aim 2 (Chapter 4): Assess effects of ultrasound and microbubbles in acoustofluidic system on molecular delivery to human T cells

Specific Aim 3 (Chapter 5): Assess levels of molecular delivery to human T cells with acoustofluidic treatment compared to treatment with a static ultrasound chamber

Specific Aim 4 (Chapter 6): Assess key biological and cell culture media factors on molecular delivery and characterize the effect of acoustofluidic treatment on subcellular organelle structures

CHAPTER II – ASSEMBLY AND OPERATION OF AN ACOSUTOFLUIDIC DEVICE FOR ENHANCED DELIVERY OF MOELCULAR COMPOUNDS TO CELLS

¹ Sections of text and figures in this chapter are reproduced from the following reference:

Connor S. Centner, Emily M. Murphy, Bryce F. Stamp, Mariah C. Priddy, John T. Moore, Paula J. Bates, Michael A. Menze, Kavitha Yaddanapudi, Jonathan A. Kopechek, “Assembly and Operation of an Acoustofluidic Device for Enhanced Delivery of Molecular Compounds to Cells,” *Journal of Visualized Experiments: JoVE*, 167 (2021). Reprinted with permission of JoVE.

II.1. Introduction

Viral and non-viral platforms have been utilized to enhance molecular delivery to cells. Viral delivery (transduction) is a common technique utilized in cell-based therapies requiring genomic modification. Limitations with viral delivery include potential insertional mutagenesis, limited transgenic capacity, and undesired multiplicity of infection (Wahlers *et al.*, 2001b; Gardlik *et al.*, 2005). Therefore, non-viral molecular delivery techniques are in development for a broad range of biomedical and research applications. Common techniques include mechanical, electrical, hydrodynamic, or the use of laser-based energy to enhance uptake of biomolecules into cells (Nayerossadat *et al.*, 2012a). Electroporation is a commonly used non-viral molecular delivery platform which has the ability to induce transient perforation in the plasma membrane for intracellular delivery of molecular compounds (Sugar and Neumann, 1984b; Weaver, 1993; Gehl, 2003a; Lin *et al.*, 2004; Chen *et al.*, 2006b; Hashimoto and Takemoto, 2015b). However, the transient perforation of the plasma membrane is a stochastic process and molecular uptake via electroporation is generally dependent on passive diffusion across the transient membrane pores (Sugar and Neumann, 1984b; Weaver, 1993; Chen *et al.*, 2006b).

An alternative method is the utilization of ultrasound for enhanced intracellular molecular delivery via cavitation of ultrasound contrast agents (*i.e.*, gas-filled microbubbles). Microbubble cavitation induces microstreaming effects in the surrounding media which can cause transient perforation of nearby plasma membranes (“sonoporation”) allowing rapid intracellular uptake of biomolecules via

passive or active transport mechanisms (Klibanov, 2006; Klibanov *et al.*, 2010; Fan *et al.*, 2014a). Sonoporation is an effective technique for rapid molecular delivery to cells, but this approach often requires expensive equipment and static ultrasound treatment methods which are limited by lower throughput and higher variability in ultrasound exposure conditions (Secomski *et al.*, 2017). To address these limitations, acoustofluidic devices are currently in development which enable consistent sonoporation of cells in suspension.

Acoustofluidics is an expanding field that integrates ultrasound and microfluidic technologies for a wide variety of applications. This approach has previously been used for particle separation by applying continuous ultrasound energy to induce standing acoustic waves within the fluidic channels (Shi *et al.*, 2009a; Shi *et al.*, 2009b; Gedge and Hill, 2012a; Shields *et al.*, 2016). Particles are sorted toward different parts of the device based on a variety of properties such as particle size, density, and compressibility relative to the medium (Shi *et al.*, 2009b). Acoustofluidic technologies are also in development to enable rapid molecular delivery to a variety of cell types for research applications and manufacturing of cell therapies (Belling *et al.*, 2020b). Recently, we demonstrated enhanced molecular delivery to erythrocytes using a PDMS-based acoustofluidic device (Centner *et al.*, 2020). In the acoustofluidic platform, cell and microbubble dynamics can be manipulated to induce physical interactions that enable enhanced delivery of biomolecules. The efficiency and consistency of intracellular molecular delivery can potentially be increased by optimizing the distance between cells and microbubbles.

One important application for acoustofluidic-mediated sonoporation involves transport of biomolecules into primary human T cells. Immunotherapies based on adoptive T cell transfer, such as Chimeric Antigen Receptor T cell (CAR T) therapy, are rapidly emerging for treatment of various diseases, including cancer and viruses such as HIV (Qi *et al.*, 2020). CAR T therapy has been particularly effective in pediatric acute lymphoblastic leukemia (ALL) patients, with complete remission rates of 70-90% (Annesley *et al.*, 2018b). However, T cell manufacturing for these therapies generally depends on viral transduction which is limited by potential insertional mutagenesis, long processing times, and challenges of delivering non-genetic biomolecules such as proteins or small molecules (Gardlik *et al.*, 2005). Acoustofluidic-mediated molecular delivery methods can potentially overcome these limitations and improve manufacturing of T cell therapies.

Another important application for acoustofluidic-mediated sonoporation involves intracellular delivery of preservative compounds, such as trehalose, which protect cells during freezing and desiccation. Trehalose is produced by some organisms in nature and helps them tolerate freezing and desiccation by protecting their cellular membranes (Hand and Menze, 2015; Zhang *et al.*, 2017b). However, trehalose is not produced by mammalian cells and is impermeable to mammalian cell membranes. Therefore, effective molecular delivery techniques, such as sonoporation, are necessary in order to achieve sufficient intracellular trehalose levels required to protect internal cellular membranes. This approach is currently in development for dry preservation of various cell types.

This protocol provides a detailed description of the assembly and operation of a relatively low-cost acoustofluidic system driven by a microcontroller. Ultrasound contrast agents are utilized to induce sonoporation within the fluidic channels and enable rapid molecular delivery to various cell types, including T cells and cancer cells. This acoustofluidic system can be used for a variety of research applications and may also be useful as a prototype system to evaluate sonoporation methods for improved cell therapy manufacturing processes.

II.2. Protocol

Ethics Statement: Whole blood donations were collected from healthy donors following protocols approved by the institutional review board at the University of Louisville.

1. *Fabrication of Acoustofluidic Device*

1.1 Obtain a photomask with a concentric spiral design containing channels with a diameter of 500 μm . A CAD file is provided in the supplemental files as an example. A custom photomask can be ordered from a commercial vendor or patterned using a mask writer.

1.2 Prepare a mold of the concentric spiral design on a photoresist-coated silicon wafer using standard photolithography techniques:

1.2.1. Add approximately 2 Tbsp (~30 mL) of SU-8 2100 to a 100 mm silicon wafer.

1.2.2. Spin-coat the wafer on a spinner at a speed of 150 rpm for 30 s to spread

out the photoresist, then increase speed to 1200 rpm for 60 s to yield a thickness of 200 μm .

1.2.3. Cure the photoresist-coated wafer in a polyimide vacuum oven with a 30 min ramp up and 30 min dwell at 115 $^{\circ}\text{C}$, then ramp down for 30 min.

1.2.4. Expose the photoresist-coated wafer for 130 s using a mask aligner with the photomask from step #1.

1.2.5. Bake the wafer after exposure following the same process described in step 1.2.3.

1.2.6. Develop the photoresist in SU-8 developer solution for approximately 8 min
CAUTION: only use developer solution in a well-ventilated chemical fume hood.

1.3 Silanize the mold to make the surface more hydrophobic. Place the photoresist-coated wafer into a desiccator and add a 20 μL drop of trichlorosilane ($\text{C}_8\text{H}_4\text{Cl}_3\text{F}_{13}\text{Si}$, Gelest, Morrisville, PA, USA). Apply vacuum to the chamber for 30 s, then seal the chamber and leave overnight.

CAUTION: Trichlorosilane is very hazardous and flammable. Exposure causes severe burns and eye damage.

1.4 Combine 54 g of polydimethylsiloxane (PDMS) base and 6 g of curing agent in a cup and mix vigorously and thoroughly with a spatula for at least 1 min.

1.5 Place the cup containing the PDMS solution into a desiccator for approximately 30 minutes or until remnant air bubbles are removed from the solution.

1.6 Place photoresist-coated wafer with the patterns facing upward in a 150-mm petri dish.

- 1.7 Pour the PDMS solution over the mold inside the 150-mm petri dish.
- 1.8 If needed, place the 150-mm petri dish inside a desiccator and apply vacuum until remnant air bubbles disappear.
- 1.9 Transfer the 150-mm petri dish into a lab oven and bake for 2 hr at 60 °C to cure the PDMS.
- 1.10 After curing, carefully remove the PDMS from the petri dish by cutting around the edges of the wafer using a razor blade.
- 1.11 Cut out each individual device using a knife or razor blade.
- 1.12 Punch holes through the inlet and outlet ports of each device using a 2.5-mm biopsy punch (Harris Uni-Core, Electron Microscopy Sciences, Hatfield, PA, USA).
- 1.13 Place each PDMS device in a plasma asher with channels exposed (facing upward). Apply oxygen plasma treatment (100 W for 45 s, 500 mbar O₂) then immediately place each PDMS device onto a clean soda lime glass microscope slide (75 mm x 25 mm x 1 mm) with channels facing the glass surface.
- 1.14 Let devices bond overnight at room temperature.
- 1.15 Gently apply silicone to the surface of the 1-cm diameter piezo transducer at a thickness of ~1-2mm, then carefully align the transducer with the concentric spiral and gently press it onto the bottom of the glass microscope slide (opposite side from the PDMS device).

2. Assembly and Operation of Acoustofluidic System

- 2.1 Connect a microcontroller to a computer using a USB A to B cable. A green

power LED indicator (labelled PWR) should illuminate.

2.2 Use the associated program on the computer to upload a program which generates an 8 MHz signal. An example program is provided in the Supplemental files. After uploading the program, it will be stored into microprocessor memory and will not need to be uploaded again.

2.3 Solder a 1" 22G wire to the end of each wire on the PZT transducer.

2.4 Connect the negative (black) terminal wire of PZT transducer to a GND pin via the soldered wire.

2.5 Connect the positive (red) terminal wire of PZT transducer to the output pin (#9 in the provided example program) via the soldered wire.

2.6 Optionally, mount the acoustofluidic device and the microcontroller in a 3D-printed case. CAD files are provided in the Supplemental files as examples. Additional wires can be connected to other microcontroller pins to control an external LED indicator and on/off push button if desired.

2.7 Cut 3-6" sections of tygon PVC soft plastic tubing (1/16" ID, 1/8" OD) and push the tubing into the inlet and outlet ports. It may be necessary to rotate the tubing while applying pressure until it fits in the opening. Optionally, after inserting the tubing into each port, glue can be applied at the junction to bond the PDMS and tubing together.

2.8 Assemble microfluidic reservoir according to manufacturer's instructions.

2.9 Cut a 3-6" section of tygon PVC soft plastic tubing (1/16" ID, 1/8" OD) and push the tubing over the 1/32" ID tubing from the microfluidic reservoir output tubing. Optionally, wrap the junction with parafilm to prevent leakage.

2.10 Fill a 60-mL syringe with ambient air (optionally, filter the air with a 0.2- μ m filter and connect it to tygon PVC tubing (1/16" ID, 1/8" OD) on the side of the microfluidic reservoir.

2.11 Set the syringe pump to a rate of 200 mL/hr to push the cell/ultrasound contrast agent solutions through the acoustofluidic device at a volumetric flow rate of 50 mL/hr and collect the samples from the output of the acoustofluidic device into a 50-mL centrifuge tube. Optionally, rinse channel prior to acoustofluidic treatment with 15 mL of 70% ethanol solution to increase sterility of fluidic channels. Additionally, channels can be rinsed with 15 mL of deionized water to remove residual ethanol in the device prior to pumping cells through the system.

3. *Preparation of ultrasound contrast agents*

NOTE: Ultrasound contrast agents significantly enhance acoustofluidic delivery of molecular compounds by transiently increasing permeabilization of nearby cellular membranes (Centner *et al.*, 2020). Molecular delivery is very limited without ultrasound contrast agents in this system.

3.1. Prepare a phospholipid solution in a 20-mL scintillation vial containing the following mixture:

3.1.1. Add 25 mg of 1,2-distearoyl-sn-glycero-3-phosphocholine (DSPC).

3.1.2. Add 11.6 mg of 1,2-distearoyl-sn-glycero-3-ethylphosphocholine (DSEPC).

3.1.3. Add 0.26 mg of 1,2-distearoyl-sn-glycero-3-phosphoglycerol (DSPG).

3.1.4. Add 0.88 mg of polyoxyethylene 40 stearate.

3.2. Add chloroform until all phospholipids are dissolved (e.g., 3 mL of

chloroform).

3.3. Evaporate chloroform in a desiccator for 48 hr to form a dry lipid film (evaporation under argon or with a rotary evaporator can be used to accelerate the drying process).

3.4. Rehydrate the lipid film with 10 mL of sterile phosphate-buffered saline (PBS).

3.5. Sonicate the lipid solution for 3 min at 40% amplitude to form a cationic micellar solution.

3.6. After sonication store the phospholipid solution at 2-6 °C for up to 1 month.

3.7. To prepare ultrasound contrast agents, add 200 μ L of cationic micellar solution and 600 μ L of sterile PBS to a 2 mL glass septum vial.

3.8. Seal the vial by crimping the cap.

3.9. Use a 1.5" 20G needle to fill the vial head space with decafluorobutane gas for 30 s.

3.10. Amalgamate the vial for 45 s at 4350 cpm to form perfluorobutane gas-filled ultrasound contrast agents.

3.11. Add 25 μ L of ultrasound contrast agent solution per 1 mL of cell solution immediately before pumping the combined contrast agent/cell mixture through the acoustofluidic device. The cell solution can be modified as desired by the user, but in our studies the cell solution consisted of primary T cells in step 4.21, and A549 lung cancer cells in step 5.7, respectively.

4. Preparation of primary T cells

- 4.1 Isolate peripheral blood mononuclear cells (PBMCs) from whole blood solutions and store at -150 °C. Density gradient separation containing a substrate is commonly utilized to separate PBMCs from whole blood.(Ulmer *et al.*, 1984; Jaatinen and Laine, 2007; Grievink *et al.*, 2016)
- 4.2 Thaw frozen vial in 37 °C water bath.
- 4.3 Dilute thawed PBMCs 1:10 with PBS in a 15-mL centrifuge tube. Each 1-mL vial contains approximately 10 million PMBCs.
- 4.4 Centrifuge diluted PMBCs at 580g for 11 min at 4 °C.
- 4.5 Aspirate supernatant and add 13 mL of MACs running buffer then resuspend the cells.
- 4.6 Count the PMBCs with an automated cell counter or hemocytometer.
- 4.7 Centrifuge the PMBCs again at 580g for 11 min at 4 °C and aspirate the supernatant.
- 4.8 Add 40 µL of chilled running buffer per 10 million PMBCs.
- 4.9 To isolate T cells, add 10 µL of Pan T-Cell Biotin Antibody Cocktail per 10 million PMBCs.
- 4.10 Gently agitate the PMBCs and store the solution at 4 °C for 5 min per 10 million cells.
- 4.11 Add 30 µL of running buffer and 20 µL of Pan T-Cell MicroBead Cocktail per 10 million PMBCs.
- 4.12 Mix the PMBCs and beads thoroughly and incubate for an additional 15 min at 4 °C.

- 4.13 Add running buffer to reach a total volume of 500 μ L.
- 4.14 Separate primary T cells with a commercially available benchtop magnetic sorting instrument using the “depletes separation” setting following manufacturer’s protocol. This step should yield between 5-10 million T cells after cell sorting.
- 4.15 Count T cells using an automated cell counter or hemocytometer.
- 4.16 Dilute T cells in 10 mL of sterile PBS and centrifuge at 580 x g for 10 min at 4 °C to pellet the cells.
- 4.17 Aspirate the supernatant and resuspend T cells in 1 mL of PBS.
- 4.18 Count T cells using an automated cell counter or hemocytometer and aliquot 1 million/mL for experiments.
- 4.19 Prepare a 1 mg/mL fluorescein solution in PBS.
- 4.20 Add 100 μ L of 1 mg/mL fluorescein solution per 1 mL of T cell solution (final fluorescein concentration = 100 μ g/mL) immediately prior to processing.
- 4.21 Add 25 μ L of ultrasound contrast agent solution as previously described in step 3.11.
- 4.22 Process 1-mL aliquots of cells using the acoustofluidic system (see steps 2.10-2.11). This step enhances delivery of fluorescein into primary T cells.
- 4.23 Immediately after treatment, wash cells three times via centrifugation at 580 x g for 10 min with 500 μ L of PBS to remove extracellular fluorescein. Cells should be washed within 10 min after adding fluorescein solution.
- 4.24 After final washing step, resuspend cells in 250 μ L of PBS and measure fluorescence on flow cytometer.

5. *Preparation of A549 lung cancer cells*

5.1 Culture A549 (adenocarcinomic human alveolar basal epithelial) cells in complete DMEM media (10% fetal bovine serum, 1% penicillin/streptomycin) at 37 °C and 5% CO₂ in a flat-bottom tissue culture flask.

5.2 Harvest A549 cells when they reach 70-90% confluency. Aspirate media from the flask and wash the cells once with PBS to remove serum proteins.

5.3 Add trypsin (0.25%) EDTA to the flask and incubate for 5 min at 37 °C. Trypsin is a digestive enzyme which causes the cells to detach from the bottom surface of the tissue culture flask.

5.4 Transfer trypsin solution to a 15-mL centrifuge tube and neutralize it by adding complete DMEM media at a 1:3 ratio.

5.5 Pellet the cells via centrifugation at 1500 x g for 5 min at 4 °C.

5.6 Aspirate the supernatant and resuspend the pellet at a concentration of 100,000/mL in PBS solution containing 200 mM trehalose in 15-mL conical vial.

5.7 Add 25 µL of ultrasound contrast agent solution as previously described in step 3.11.

5.8 Process 1-mL aliquots of cells using the acoustofluidic system (see steps 2.10-2.11). This step enhances delivery of trehalose into A549 lung cancer cells.

5.9 Immediately after treatment, wash cells three times via centrifugation with 500 µL of PBS to remove extracellular trehalose. Cells should be washed within 10 min after adding trehalose solution.

5.10 After final washing step, resuspend cells in 100 µL of PBS.

5.11 Add 11 µL of 1% Triton X-100 solution to lyse cells and release intracellular

trehalose.

5.12 Vortex for 15 s, then incubate for 30 min at room temperature.

5.13 Vortex again for 15 s, then measure trehalose concentration using commercially available trehalose assay following manufacturer's recommendation.

II.3. Representative Results

An image of the acoustofluidic system assembled inside a 3D-printed case is shown in Figure 2. This protocol produces an acoustofluidic system that can be used to enhance intracellular molecular delivery in multiple cell lines using ultrasound contrast agents.

Figure 3 demonstrates enhanced intracellular delivery of a fluorescent compound, fluorescein, to primary human T cells with acoustofluidic treatment compared to an untreated control group ($p < 0.05$, $n = 3/\text{group}$). T cells were suspended at a concentration of 1 million/mL in PBS with 100 $\mu\text{g}/\text{mL}$ fluorescein solution and 25 $\mu\text{L}/\text{mL}$ ultrasound contrast agent solution, and the mixture was passed through the acoustofluidic device for ultrasound treatment. Intracellular fluorescein delivery and cell viability were measured with flow cytometry after washing cells via centrifugation to remove extracellular fluorescein. T cells in the untreated control group were also suspended at 1 million/mL in PBS with 100 $\mu\text{g}/\text{mL}$ fluorescein solution, but ultrasound contrast agent solution was not added, and cells were not passed through the acoustofluidic device. The fluorescence intensity of T cells increased by 5-fold after acoustofluidic treatment relative to the fluorescence intensity of T cells in the untreated control group, indicating enhanced

delivery of fluorescein. Cell viability decreased slightly after acoustofluidic treatment but remained above 80% ($p < 0.05$, $n = 3/\text{group}$).

Figure 4 demonstrates enhanced intracellular delivery of a preservative compound, trehalose, to human A549 lung carcinoma cells with acoustofluidic treatment compared to flow alone (no ultrasound contrast agents or ultrasound exposure) and compared to cells in the untreated control group (ANOVA $p < 0.05$, $n = 3/\text{group}$). A549 cells were suspended at a concentration of 100,000/mL in PBS with 200 mM trehalose solution and 25 $\mu\text{L}/\text{mL}$ ultrasound contrast agent solution, and the mixture was passed through the acoustofluidic device for ultrasound treatment. A549 cells in the control groups (“Flow Only” and “No Treatment”) were also suspended at 100,000/mL in PBS with 200 mM trehalose, but ultrasound contrast agent solution was not added, and cells were not exposed to ultrasound treatment. Intracellular trehalose was quantified using a trehalose assay kit and normalized to the untreated control group. Cell viability was measured with trypan blue assay. There was no statistical difference in cell viability between groups ($n = 3-7/\text{group}$).

Figures and Table Legend

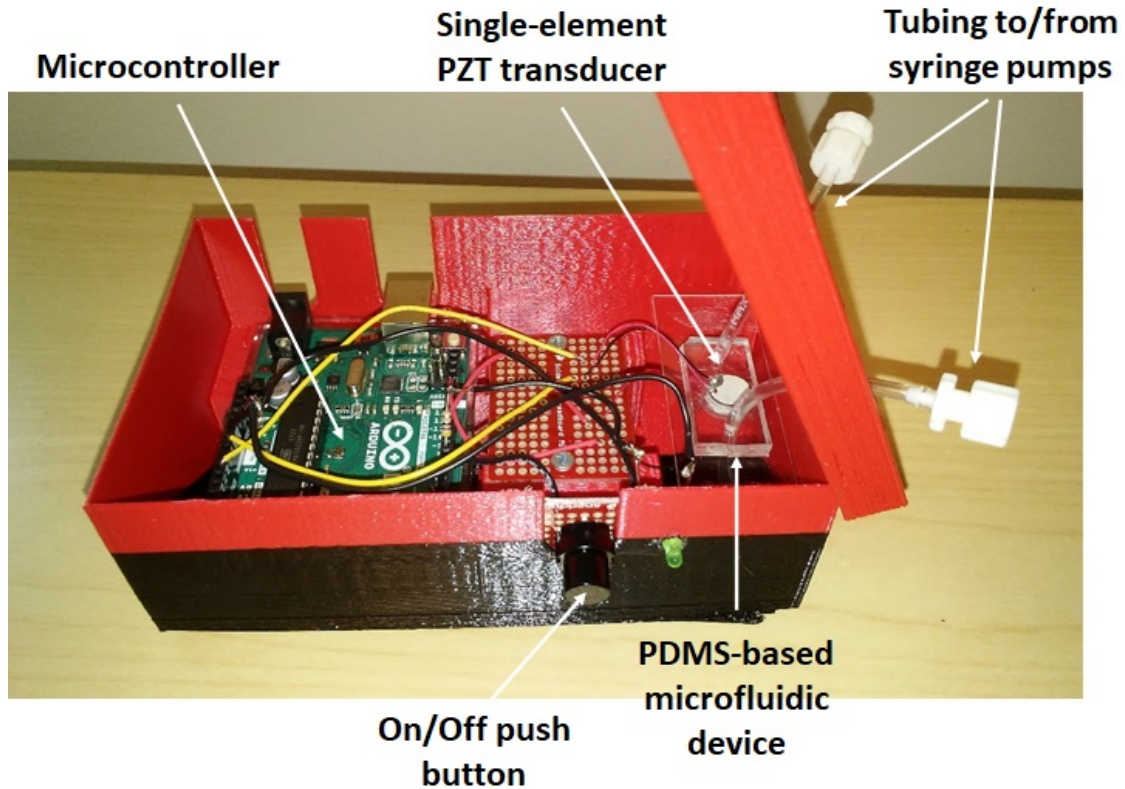


Figure 2: Photo of acoustofluidic system. The acoustofluidic flow system contains a PDMS-based flow chamber with an integrated PZT transducer driven by a microcontroller. A 3D-printed case with an LED indicator and on/off push button are optional additional features.

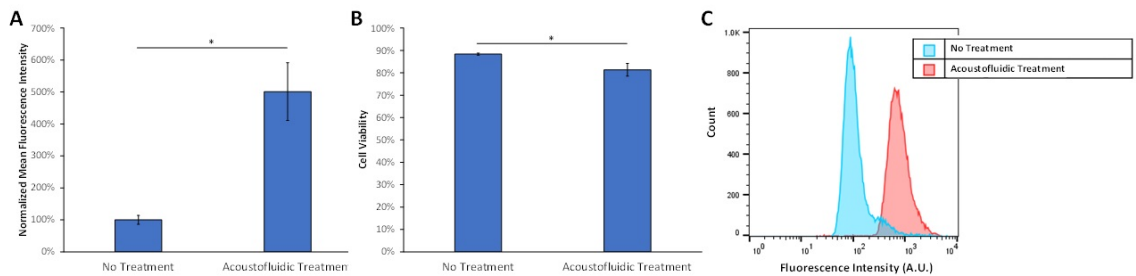


Figure 3: Acoustofluidic treatment enhances fluorescein delivery to human T cells. (A) Fluorescence intensity in primary T cells increased after acoustofluidic treatment with fluorescein compared to the untreated control group (no acoustofluidics and no and no microbubbles) ($p < 0.05$, $n = 3/\text{group}$). (B) Cell viability decreased slightly after acoustofluidic treatment but remained above 80% as measured by flow cytometry ($p < 0.05$, $n = 3/\text{group}$). (C) Representative flow

cytometry histogram indicating higher fluorescence in the acoustofluidic treatment group.

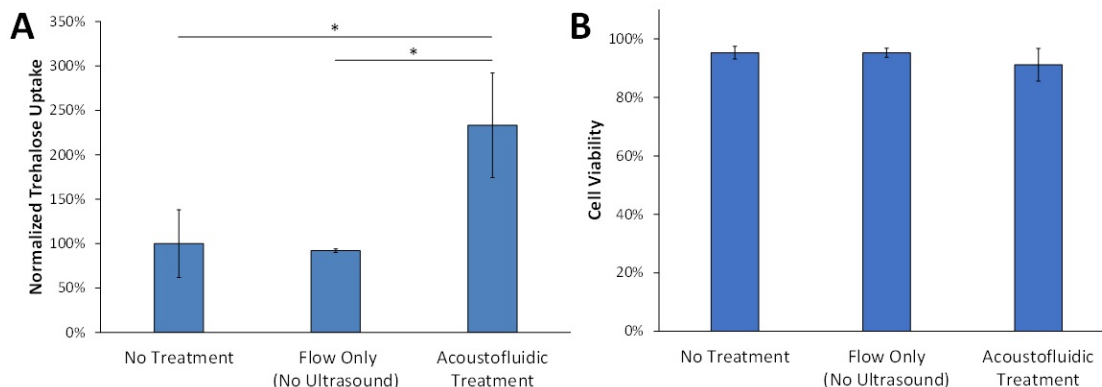


Figure 4: Acoustofluidic treatment enhances trehalose delivery to human lung cancer cells. Trehalose uptake increased in A549 lung carcinoma cells compared to flow only (no ultrasound and no microbubbles) and the untreated control group (ANOVA $p < 0.05$, $n = 3/\text{group}$). (B) Cell viability remained above 90% after acoustofluidic treatment as measured by trypan blue assay ($n = 3-7/\text{group}$).

II.4. Discussion

This protocol describes the assembly and operation of a low-cost acoustofluidic system which enhances intracellular delivery of biomolecules for research applications. There are several important factors to consider when assembling and operating this system. The acoustofluidic device is fabricated in PDMS, which is a biocompatible material that can easily be molded with consistent channel dimensions (Halldorsson *et al.*, 2015). The device channels can be rinsed with 15 mL of 70% ethanol solution prior to acoustofluidic processing in order to increase sterility when working with cultured cells. Following ethanol cleaning, 15 mL of deionized water can be used to rinse the device to remove residual ethanol from the channels prior to adding cell solutions. A limitation of this system is that the small acoustofluidic channels can easily become blocked by debris or cell

aggregates. Thoroughly rinsing channels between samples will help prevent problems with channel blockage. In addition, PDMS devices can be fabricated in batches and quickly replaced if needed. For ultrasound-based applications, it is important to produce PDMS devices with a consistent thickness, as differences in PDMS thickness can affect the ultrasound pressures within the fluidic channels. Ultrasound waves propagate continuously through the device and transmitted waves interact with reflected waves to form standing acoustic wave patterns that are very sensitive to differences in PDMS thickness.(Shields *et al.*, 2016) The PDMS thickness is primarily determined by the amount of PDMS added to the mold (step 1.7) and this protocol yields a PDMS thickness of 3.5 mm.

The maximum output frequency of the microcontroller (8 MHz) was selected to produce the smallest acoustic wavelength within the fluidic channel. The microcontroller output is typically a square wave, but oscilloscope measurements revealed that the output at 8 MHz becomes more similar to a sinusoid waveform due to slew rate limitations. A limitation of this system is that the maximum voltage output of the microcontroller is 5V and an external RF amplifier is required if higher voltage outputs are desired. The free-field pressure output of the transducer in this system was 18 kPa at 1 cm as measured with a needle hydrophone (Precision Acoustics, Dorchester, United Kingdom). Although this pressure is relatively low, standing waves within the channels can increase the acoustic pressures which samples are exposed to as they pass through the ultrasound beam. Operating outside of resonance frequency (Versluis *et al.*, 2020) and having a low ultrasound

pressure output, an ultrasound contrast agent is ultimately required for molecular delivery.

Ultrasound contrast agents are used to nucleate acoustic cavitation within the acoustofluidic channels which enhances delivery of biomolecules across cell membranes (Hu *et al.*, 2013a; Helfield *et al.*, 2016b). This protocol describes synthesis of perfluorocarbon gas-filled microbubbles encapsulated by a cationic phospholipid membrane. As previously described, this formulation consists of microbubbles primarily between 1-3 μm in diameter (Kopechek *et al.*, 2015). The positively charged surface of the microbubbles attracts them toward negatively-charged cell membranes, which increases sonoporation-mediated molecular delivery when the microbubbles and cells are in close proximity. The concentration of microbubbles in the cell solution is a critical factor that can influence the efficiency of molecular delivery and cell viability after acoustofluidic treatment, and the optimal microbubble concentration may be specific to each cell type (Centner *et al.*, 2020). The concentration of gas-filled microbubbles with a lipid shell can decrease over time after synthesis so ultrasound contrast agents should be used within a few hours after synthesis.

We demonstrated delivery of a fluorescent compound (fluorescein) to primary non-activated human T cells using the acoustofluidic system in this protocol. It is important to note that the activation status of primary human T cells may affect the efficiency of intracellular molecular delivery. The fluorescence properties of fluorescein enable sensitive intracellular detection with flow cytometry, but other soluble compounds can also be delivered into cells using this

acoustofluidic system. For example, we demonstrated acoustofluidic delivery of trehalose into human lung cancer cells. Acoustofluidic delivery of trehalose into cells may enable increased recovery after frozen and dry storage, which could have significant impacts on a range of biomedical and research applications (Centner *et al.*, 2020).

Acoustofluidic delivery of other biomolecules, such as proteins or DNA plasmids, is also possible, although a limitation of this system is that the efficiency of molecular delivery may be lower for larger compounds (Bhutto *et al.*, 2018; Belling *et al.*, 2020b). Furthermore, a change in ultrasound frequency should be considered to match the resonance frequency of microbubbles as this may also influence molecular delivery efficiency. Optimization of ultrasound pressure, acoustofluidic flow rate, concentrations of ultrasound contrast agents, cell concentrations, and media may be needed for delivery of other biomolecules. In addition, optimal parameters may vary between different cell types due to factors such as cell diameter, morphology, membrane properties, and other phenotypic properties.

The acoustofluidic system described in this protocol can be easily assembled and operated at relatively low cost. Additionally, this system can be customized for other applications by connecting other signal sources or ultrasound transducers to generate specific output pressures and frequencies (Miller *et al.*, 1999; Forbes *et al.*, 2011; Helfield *et al.*, 2016c). In addition, the syringe pump system described in this protocol can be replaced with peristaltic pumps if desired. At a flow rate of 50 mL/hr the residence time for cells within the ultrasound beam

as they pass through the acoustofluidic channel is approximately 1 s, but this residence time can be modified as needed for specific applications by adjusting the fluid flow rate.

Unlike other common transfection techniques, biomolecules can be delivered into cells within minutes instead of hours and this system does not require specialized and expensive equipment. In addition, this system is compatible with a wide range of commonly used cell culture media or other buffers. In summary, this acoustofluidic system enables rapid delivery of biomolecules to cells, which may be useful for a wide range of research applications.

CHAPTER III – ULTRASOUND-INDUCED MOLECULAR DELIVERY TO ERYTHROCYTES USING A MICROFLUIDIC SYSTEM

² *Sections of text and figures in this chapter are reproduced from the following reference:*

Connor S. Centner*, Emily M. Murphy*, Mariah C. Priddy, John T. Moore, Brett R. Janis, Michael A. Menze, Andrew P. DeFilippis, Jonathan A. Kopechek, "Ultrasound-induced molecular delivery to erythrocytes using a microfluidic system," *Biomicrofluidics* 14(2):024114 (2020). Reprinted with permission of American Institute of Physics.

* indicates co-1st author

III.1. Introduction

Blood transfusions are one of the most common medical procedures performed in U.S. hospitals (Pfundner *et al.*, 2006). Current FDA-approved storage methods for erythrocytes require refrigeration at 1-6 °C for up to 42 days before blood units expire due to detrimental storage effects on morphological and biochemical properties (“storage lesions”) (Bunn *et al.*, 1969; Haradin *et al.*, 1969; Greenwalt *et al.*, 1990; Izzo *et al.*, 1999). The limited shelf-life of refrigerated erythrocytes can lead to shortages in supply (Nightingale *et al.*, 2003; Shi *et al.*, 2014), especially when donations decrease due to natural disasters or other factors. Less common techniques for long-term storage include freezing at -80 °C, allowing erythrocytes to be stored for up to 10 years. However, freezing erythrocytes requires a complex and sensitive glycerol-loading process that is time-consuming and poses challenges in cases where blood transfusions are required quickly. Significant research efforts have attempted to develop artificial blood substitutes but these products have failed clinical trials (Chen *et al.*, 2009) and no artificial blood substitutes are currently approved for routine clinical use (Silverman and Weiskopf, 2009). As an alternative approach to hemoglobin-based artificial blood substitutes, recent efforts have focused on generating stem cell-derived erythrocytes (Shah *et al.*, 2014). These products are entering clinical trials and potentially offer a new source of erythrocytes for clinical application. However, stem cell-derived erythrocytes face similar challenges as described above — limited shelf-life and thermal stability. Alternatively, an approach to store erythrocytes in a dried state at ambient temperatures would reduce cell membrane

oxidation and storage lesion, thereby increasing the shelf-life. In addition, dry preservation of erythrocytes would enable blood transfusions in locations where it is not currently feasible or extremely challenging, including remote medical centers, far forward military operations, and long-duration space missions. Therefore, there is a significant need for an effective and inexpensive method to store erythrocytes at ambient temperatures for extended periods of time without refrigeration or freezing.

A wide variety of organisms in nature, including tardigrades (“water bears”) and brine shrimp (“sea monkeys”), can survive freezing (“cryobiosis”) and desiccation (“anhydrobiosis”) for decades or longer before returning to normal physiological function after thawing or rehydration (Hengherr *et al.*, 2009; Crowe *et al.*, 2011; Tsujimoto *et al.*, 2016). Given that entire organisms can survive desiccation, it seems plausible that erythrocytes could also be preserved in

this manner. The fact that erythrocytes lack nuclei and other organelles, such as mitochondria, would suggest that dry-preservation may be even more feasible than for more complex nucleated cells. Organisms that have developed the ability to

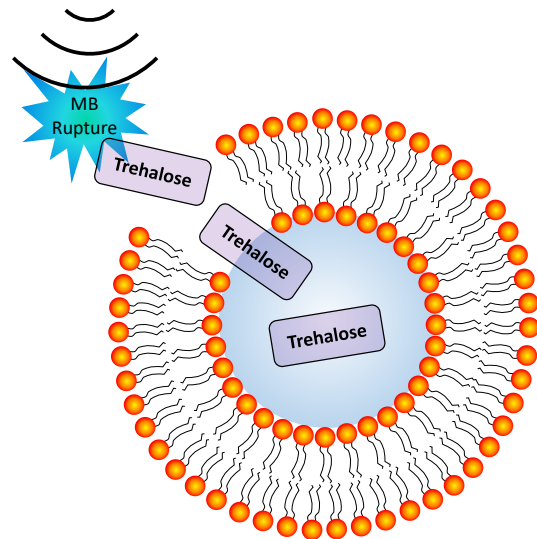


Figure 5: Illustration of ultrasound-induced microbubble (MB) rupture leading to transient perforation of cell membranes — enabling enhanced intracellular delivery of soluble compounds such as trehalose (not to scale).

survive desiccation generally produce various protective compounds, such as late embryogenesis abundant proteins and the non-reducing sugar trehalose, to stabilize cellular structures during the freezing and drying process. Trehalose is biocompatible and already used in vaccines and food products (Patist and Zoerb, 2005). However, high levels of trehalose (~100 mM) are required intracellularly and mammalian cells lack transporters for this sugar. Therefore, an effective method is required to load mammalian cells with preservative compounds for desiccation (Crowe *et al.*, 2005). Prior approaches have focused on passive loading of erythrocytes, platelets, or other mammalian cells via endocytosis, genetically engineered pores, or electroporation (Eroglu *et al.*, 2000; Shirakashi *et al.*, 2002; Satpathy *et al.*, 2004; Zhou *et al.*, 2010; Arav and Natan, 2012; Fitzpatrick *et al.*, 2013). These studies demonstrated that intracellular trehalose could protect some mammalian cells during drying and rehydration, but intracellular loading either required a long process (7+ hours) at 37 °C which increases susceptibility to oxidative damage and reduces cell viability (Kanias and Acker, 2009), or the throughput was low and inefficient. An alternative loading approach by ectopically expressing trehalose transporters in mammalian cells to facilitate uptake showed promise but scale-up of this approach to large numbers of cells is very challenging (Kikawada *et al.*, 2007; Chakraborty *et al.*, 2012; Uchida *et al.*, 2017).

To address these limitations, our group is developing a novel approach to preserve erythrocytes with protective compounds, such as trehalose, by utilizing ultrasound and microbubbles to induce transient pore formation in cellular

membranes, or “sonoporation” (Figure 5). Sonoporation can occur due to inertial cavitation when ultrasound waves at sufficient pressure amplitudes induce rapid collapse of microbubbles proximal to the cell membranes and transiently perforate the cell membrane enabling rapid uptake of molecular compounds (Fan *et al.*, 2014b). The pores in the cell membrane typically seal quickly in an active repair process influenced by factors such as pore size and Ca^{2+} concentration (Feril *et al.*, 2006; Kudo *et al.*, 2009; Kumon *et al.*, 2009; Hassan *et al.*, 2010; Crowe *et al.*, 2011). Thus, this approach can potentially enable rapid loading of compounds into cells with higher efficiency and viability compared to other methods that are solely dependent on endocytosis and/or passive diffusion (Feril *et al.*, 2006). Furthermore, microbubbles are approved for clinical use as intravenous ultrasound contrast agents to image cardiac blood flow (Villanueva, 2010). Ultrasound and microbubbles are also in development for targeted gene and drug delivery applications, including delivery of trehalose into platelets (Hernot and Klivanov, 2008; Zhang *et al.*, 2009; Kopechek *et al.*, 2015; Kopechek *et al.*, 2019).

Consistent intracellular delivery of trehalose is fundamental to preservation of cells in a desiccated state and variability in trehalose delivery may cause reduced recovery of viable erythrocytes after drying and rehydration. To address this need for homogeneous compound delivery we have developed a microfluidic system for cell processing and molecular loading which utilizes submillimeter channels that enable consistent flow with a homogeneous mixture of erythrocytes, molecular compounds dispersed in solution, and microbubbles during ultrasound exposure. The utilization of biomicrofluidics technologies for cell processing and

analysis is rapidly expanding due to the microscale manipulation capabilities. It is being studied extensively for its applications towards single-cell analysis and measurement, microscale biophysics and biochemistry manipulation, and tissue engineering. Previous studies have explored molecular delivery to cells through small microfluidic channels without ultrasound treatment (Wang *et al.*, 2008). The use of ultrasound-integrated biomicrofluidics (“acoustofluidics”) for intracellular molecular delivery is a rapidly growing topic of interest to address current challenges in cell transfection efficiency (Carugo *et al.*, 2011; Bose *et al.*, 2015). In this study we have characterized an acoustofluidic system designed to enable more consistent ultrasound and microbubble exposure of each erythrocyte compared to bulk treatment approaches, thereby leading to increased consistency of ultrasound-mediated molecular delivery.

The objective of this study was to assess the role of various ultrasound and flow parameters on the efficiency of molecular delivery into erythrocytes using an ultrasound-integrated polydimethylsiloxane (PDMS)-based microfluidic device. Although sonoporation and ultrasound-mediated molecular delivery to cells is a well-established phenomenon, this study utilizes a novel acoustofluidic setup to demonstrate the efficacy of loading erythrocytes with molecular compounds via sonoporation for dry preservation. In addition, this study yields new insights into the effects of various parameters on the efficiency of intracellular loading in an acoustofluidic system. We assessed the delivery efficiency of a fluorescent compound (fluorescein), which can be readily detected intracellularly with flow cytometry. Various ultrasound pressures, ultrasound pulse intervals, microbubbles

doses, and microfluidic flow rates were tested in order to determine the effect of each parameter. In addition, we also assessed the recovery of erythrocytes after freeze-drying and rehydration following trehalose loading with the ultrasound-integrated microfluidic system. These results aim to provide new knowledge toward optimization of ultrasound-mediated molecular delivery to cells in a microfluidic system for preservation of erythrocytes or other applications.

III.2. Methods

III.2.1. Acoustofluidic device design and fabrication

Acoustofluidic devices were designed using a concentric spiral in order to maximize the time that erythrocytes were exposed to ultrasound pulses. A channel width of 200 μm and height of 180 μm were designed to reduce shear stress on erythrocytes while increasing time spent within the ultrasound beam. Microfluidic devices were fabricated using standard photolithography techniques at the University of Louisville Micro/Nano Technology Center. A photomask was printed with a UV laser patterning system (DWL 66FS, Heidelberg Instruments, Heidelberg, Germany). SU-8 photoresist (MicroChem, Westborough, MA, USA) was spin-coated at a thickness of 200 μm on a 4" silicon wafer and cross-linked using a mask aligner (MA6/BA6, Suss, Garching, Germany) to form the master, followed by silane treatment. PDMS was obtained from Ellsworth Adhesives (Sylgard 184 Silicone Elastomer Kit, Germantown, WI, USA). A 10:1 mixture of base to curing agent was combined until a net weight of 66 grams was reached. Air bubbles were removed by vacuum for 30 min and the PDMS was pored over

the SU-8 master in a 150 mm petri dish. The PDMS was cured for 2 h at 60 °C. Input and output ports were cut in the PDMS using a 2.5 mm biopsy puncher (Harris Uni-Core) and the PDMS devices were immediately bonded onto glass microscope slides after oxygen plasma treatment (100V for 60s, 500 mbar O₂, Axic HF-8 plasma asher, Gardnerville, NV, USA). To set up the microfluidic device for experiments, the device was held with clamps and ring stands at the surface of a water-filled 20-gallon aquarium tank. A segment of Tygon PVC clear tubing (1/16" ID, 1/8" OD, McMaster-Carr, Aurora, OH, USA) was inserted into the inlet and outlet ports of the device. The inlet tubing was connected to a 3-way valve. One valve was connected to a syringe filled with the erythrocyte solution on a syringe pump (NE-300, Farmingdale, NY, USA). The other valve was connected to a phosphate buffered saline (PBS) solution on a separate syringe pump to push any remaining erythrocyte sample through the tubing. The outlet tubing was connected to another 3-way valve to allow sample collection and waste collection into 15-mL centrifuge tubes (Figure 6).

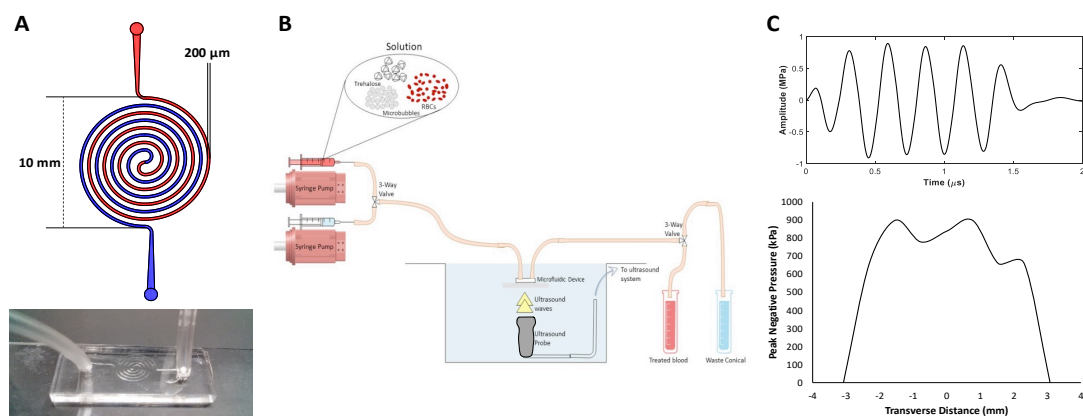


Figure 6: (A) Top: Microfluidic device design with 200 μm channel width. Bottom: a photo of one of the microfluidic devices. (B) Schematic of experimental setup (Not to scale). (C) Top: Ultrasound waveform transmitted by the ultrasound probe (ATL P4-1). Bottom: Transverse profile of the ultrasound beam (-3 dB beamwidth = ~5 mm).

III.2.2. Microbubble synthesis

Ultrasound-responsive gas-filled microbubbles were synthesized to enhance intracellular delivery of molecular compounds to erythrocytes. Microbubbles were composed of a perfluorocarbon gas core encapsulated by a phospholipid shell as previously described (Bhutto *et al.*, 2018). Chloroform solutions of 1,2-distearoyl-sn-glycero-3-phosphocholine (DSPC, Avanti Lipids, Alabaster, AL, USA); 1,2-distearoyl-sn-glycero-3-ethylphosphocholine (DSEPC, Avanti Lipids); 1,2-distearoyl-sn-glycero-3-phosphoglycerol (DSPG, Avanti Lipids); and polyethylene glycol-40 stearate (Sigma-Aldrich, St. Louis, MO, USA) at the molar ratio of 100:43:1:4.5 were dried with argon gas. An aqueous micellar lipid solution was prepared by adding PBS and sonicating (Qsonica, Newtown, CT, USA) to disperse the lipids. The resulting 10 mg/mL lipid solution was diluted 1:4 in PBS and sealed in a glass vial. The vial head space was filled with decafluorobutane gas (FlouroMed, Round Rock, TX, USA), followed by amalgamation for 30 s at 4350 cpm (DB-338, COXO, Foshan City, China) to form perfluorobutane gas-filled microbubbles (MBs). This process yields microbubbles with a mean diameter of $2 \pm 1 \mu\text{m}$ as previously described (Kopechek *et al.*, 2015; Kopechek *et al.*, 2016).

III.2.3. Fluorescein delivery to erythrocytes

Human erythrocytes were obtained from de-identified clinical blood samples following protocols approved by the Institutional Review Board and stored in citrate-phosphate-dextrose (CPD) solution with additive solution 1 (AS-1) at 4 °C

for up to 35 days after collection (Simon *et al.*, 2016). A P4-1 ultrasound transducer with 96 elements (ATL, Bothell, WA, USA) on an ultrasound imaging system (Vantage 64LE, Verasonics, Kirkland, WA, USA) was placed inside the water tank below the microfluidic device and the ultrasound focus was aligned to the center of the microfluidic device at a distance of 40 mm. Ultrasound pulses were transmitted in flash mode by triggering all 96 elements of the ultrasound transducer array at the same time.

The stock erythrocyte solution was diluted with PBS to 5 million cells/mL in presence of 100 µg/mL fluorescein. Microbubbles were added shortly before running each sample through the acoustofluidic device. After treatment, each sample was washed 3X via centrifugation with 1 mL of PBS to remove extracellular fluorescein prior to flow cytometry. Samples were stored on ice prior to analysis.

Flow cytometry was performed using a MACSQuant Analyzer 10 (Miltenyi Biotec, Auburn, CA, USA) with 10,000 events recorded per sample. Data were analyzed using FlowJo (Ashland, OR, USA). The mean fluorescence in the FITC channel was calculated after gating the populations on forward and side scatter plots. In addition, fluorescence microscopy images of erythrocytes were acquired with a 40X objective on an EVOS cell imaging system (American Microscopy Group, Mill Creek, Washington, USA).

III.2.4. Ultrasound image analysis of microbubble destruction

Ultrasound imaging was used to assess the rate of microbubble destruction at different ultrasound pressures. Microbubbles were imaged using B-mode

ultrasound with a Verasonics Vantage system (ATL P4-1 probe, 2.5 MHz center frequency). A region of interest (ROI) was selected and the mean grayscale intensity was computed using MATLAB to determine the change in contrast over time due to loss of echogenicity/microbubble destruction at different ultrasound pressures (0.5 – 1.3 MPa).

III.2.5. Recovery and viability of erythrocytes after freeze-drying and rehydration

The stock cell solution was diluted 40X in PBS with trehalose dissolved at a concentration of 200 mM. Microbubbles (2 %v/v) were added shortly before running the sample through the microfluidic device. After trehalose loading in the device, the samples were transferred to cryovials and frozen to -80 °C at a rate of -1 °C/min using a CoolCell container (Biocision, San Rafael, CA, USA). After storage for a minimum of 24 h at -80 °C, samples were quickly transferred to a lyophilizer (BenchTop 4K, VirTis, Los Angeles, CA, USA) and placed under vacuum below 300 mTorr for at least 48 h. After freeze-drying, samples were stored at room temperature for 24 h and rehydrated with 0.5 mL of deionized water. Recovery of erythrocytes after rehydration was determined by counting cells on a hemocytometer. Esterase activity was used as a proximate for erythrocyte viability and determined via flow cytometry using a calcein-AM (Sigma-Aldrich) viability assay.

III.2.6. Statistical analysis

Statistical analysis was conducted using Minitab 19 (State College, PA, USA). Statistical comparisons between groups were determined using ANOVA with statistical significance defined as $p < 0.05$ (two-tailed). Post-hoc analysis was performed using Tukey's test for one-way ANOVA. Bars represent mean \pm standard deviations.

III.3. Results

III.3.1. Effect of ultrasound and flow parameters on erythrocyte viability

Viability of erythrocytes was assessed using flow cytometry after treatment with various ultrasound and flow parameters (Figure 7). A representative flow cytometry scatter plot is shown in Figure 7A indicating the gating used to determine erythrocyte viability. There was high viability in all groups ($>80\%$) with no statistically significant differences between different ultrasound pressures or different pulse intervals. A statistically significant decrease in viability was observed at the highest microbubble dose tested (9% v/v, ANOVA $p < 0.05$) and also at a microfluidic flow rate of 20 mL/h ($p < 0.05$), but viability remained above 80% in those groups.

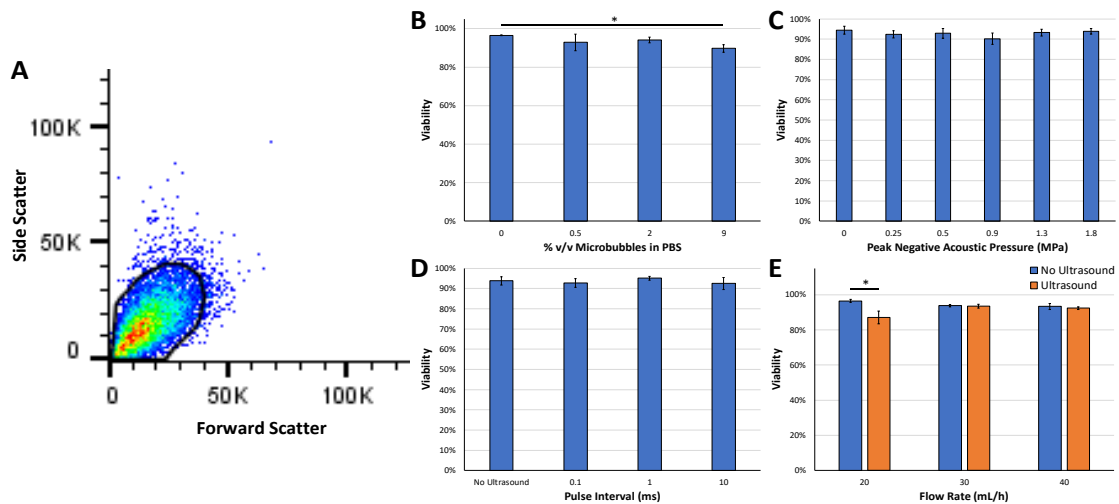


Figure 7: (A) Representative flow cytometry scatter plot with the gate used to detect viable erythrocytes based on forward and side scatter profiles. High viability of erythrocytes was observed at (B) different microbubble concentrations, (C) different acoustic pressures, (D) different pulse intervals, and (E) different microfluidic flow rates. Statistically significant decreases in viability were detected at a microbubble dose of 9% (ANOVA $p < 0.05$) and with ultrasound treatment at a microfluidic flow rate of 20 mL/h ($p < 0.05$) compared to the no ultrasound control groups.

III.3.2. Effect of ultrasound and flow parameters on fluorescein delivery into erythrocytes

Ultrasound-mediated intracellular delivery of fluorescein to erythrocytes was evaluated at various microbubble concentrations in PBS (%v/v) as measured by flow cytometry post-treatment. There was a trend toward a statistically significant difference in fluorescein uptake at a microbubble dose of 2% compared to the control group which passed through the microfluidic device without ultrasound or microbubbles (Figure 8A, $n=4$, ANOVA $p=0.12$).

Intracellular delivery of fluorescein to erythrocytes at varying ultrasound pressures was assessed by flow cytometry. Since a microbubble dose of 2 %v/v

yielded the highest amount of fluorescein delivery as shown in Figure 8, the effect of peak negative pressure on loading efficiency was examined at this concentration. Ultrasound treatment enhanced intracellular delivery by up to $73 \pm 37\%$ compared to no ultrasound (ANOVA $p < 0.05$). Tukey's test indicated statistically significant differences in intracellular delivery between the control group (0 MPa) and ultrasound pressures of 0.5 MPa or 0.9 MPa (Figure 8B).

The impact of pulse intervals on compound delivery was investigated and ultrasound-mediated intracellular delivery of fluorescein was assessed at pulse intervals ranging from 0.1-10 ms. No statistical differences in fluorescein delivery, as measured by flow cytometry, were detected between different pulse intervals (Figure 8C, $p > 0.05$, $n = 3-4/\text{group}$).

Another factor that can impact the efficiency of ultrasound-mediated molecular delivery is the time that cells are exposed to ultrasound waves, which directly correlates with the flow rate through the microfluidic device. Therefore, ultrasound-mediated intracellular delivery of fluorescein was examined at varying mean flow rates with or without ultrasound treatment. No statistically significant differences in fluorescein delivery were observed at different flow rates without ultrasound. On the other hand, ultrasound treatment enhanced intracellular delivery of fluorescein by up to $44 \pm 33\%$ to erythrocytes at mean flow rates of 20 mL/hr and 30 mL/hr compared to no ultrasound groups, but not at a higher mean flow rate of 40 mL/hr (Figure 8D, $p < 0.05$, $n = 5/\text{group}$). In addition, ultrasound treatment at a microfluidic flow rate of 20 mL/hr enhanced fluorescein delivery by $40 \pm 32\%$ compared to ultrasound treatment at a flow rate of 30 mL/hr.

Representative flow cytometry histograms are shown in Figure 9A which demonstrate the increase in fluorescence intensity of erythrocytes after fluorescein delivery at ultrasound pressures up to 0.9 MPa. In addition, a representative fluorescence microscopy image demonstrates enhanced fluorescence of the erythrocyte after ultrasound-mediated loading with fluorescein (Figure 9B). The fluorescence intensity of erythrocytes increased slightly 30 minutes and remained relatively constant up to 60 minutes after treatment, suggesting that leakage was minimal in that time frame (Figure 9C).

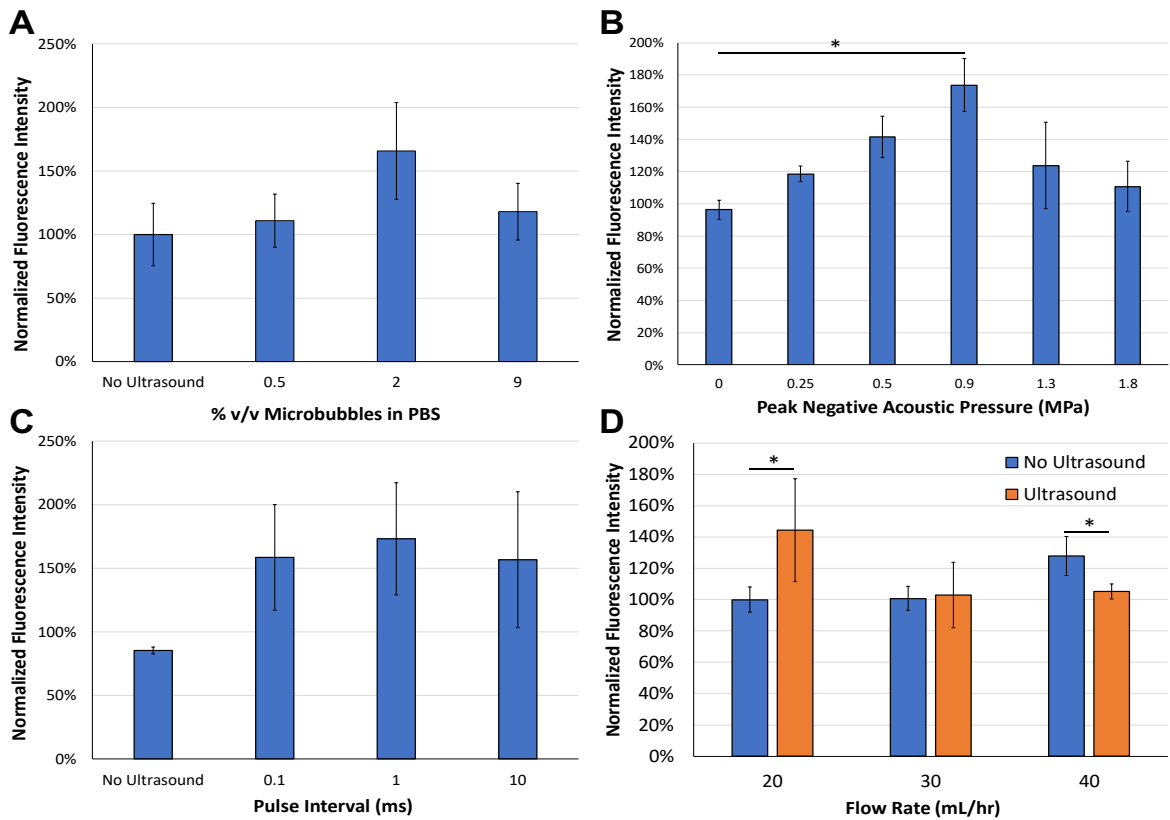


Figure 8: (A) Effect of microbubble concentrations on ultrasound-mediated fluorescein uptake. There was a trend toward statistical significance (ANOVA $p=0.12$, $n=4/\text{group}$). (B) Effect of peak negative acoustic pressure on ultrasound-mediated fluorescein uptake. There were statistically significant differences with ultrasound pressures at 0.5 and 0.9 MPa compared to the 0 MPa (no ultrasound) control group (ANOVA $p = 0.01$, $n=4-7/\text{group}$). (C) Effect of pulse interval on ultrasound-mediated fluorescein uptake. There were no statistically significant differences between the different pulse intervals ($n=4-5/\text{group}$). (D) Effect of microfluidic flow rate on ultrasound-mediated fluorescein uptake. Ultrasound treatment and flow rate effect fluorescein uptake, respectively ($p < 0.05$, $n=5/\text{group}$).

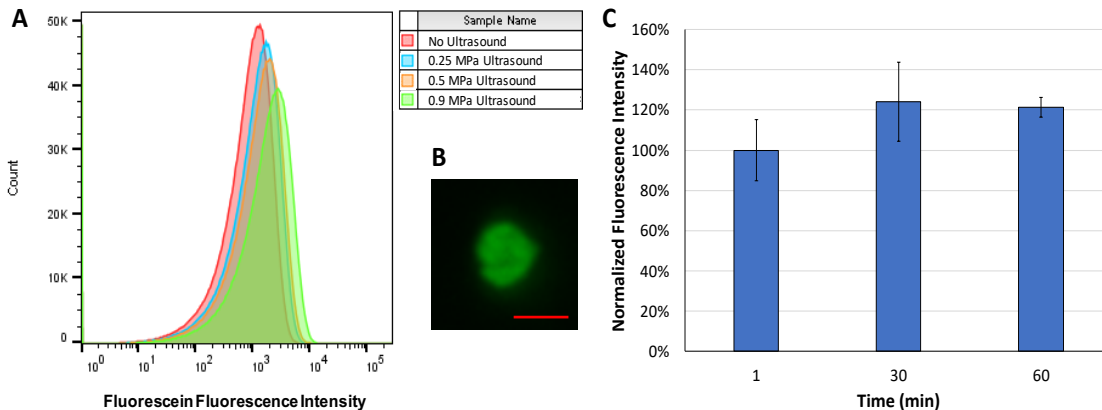


Figure 9: (A) Representative fluorescence intensity histograms after ultrasound treatment at peak negative pressures of 0.25 MPa, 0.5 MPa, 0.9 MPa, or no ultrasound (negative control). Fluorescence intensity increased up to peak negative acoustic pressures of 0.9 MPa indicating enhance molecular delivery to erythrocytes. (B) Representative fluorescence microscopy image of an erythrocyte after ultrasound treatment at a peak negative acoustic pressure of 0.9 MPa demonstrating fluorescein delivery (scale bar = 5 μ m). (C) Fluorescence intensity of erythrocytes over time after fluorescein treatment as measured by flow cytometry, indicating no significant difference over time (n=3/group).

III.3.3. Ultrasound Image Analysis of Microbubble Destruction

Ultrasound contrast images were acquired and analyzed to assess the effect of ultrasound pressure on microbubble destruction (Figure 10). At lower acoustic pressures (0.5 MPa and 0.9 MPa) there was only a small decrease in contrast (less than 10%) after 30 seconds of ultrasound exposure, indicating minimal microbubble destruction. However, at a higher ultrasound pressure (1.3 MPa) ultrasound image contrast decreased rapidly by over 25% within 30 seconds of ultrasound exposure, indicating a higher rate of microbubble destruction. These results suggest that there is a pressure threshold between 0.9 MPa and 1.3 MPa at which there is a notable increase in the rate of microbubble destruction and this

could potentially have effects on the efficiency of molecular delivery at different acoustic pressures.

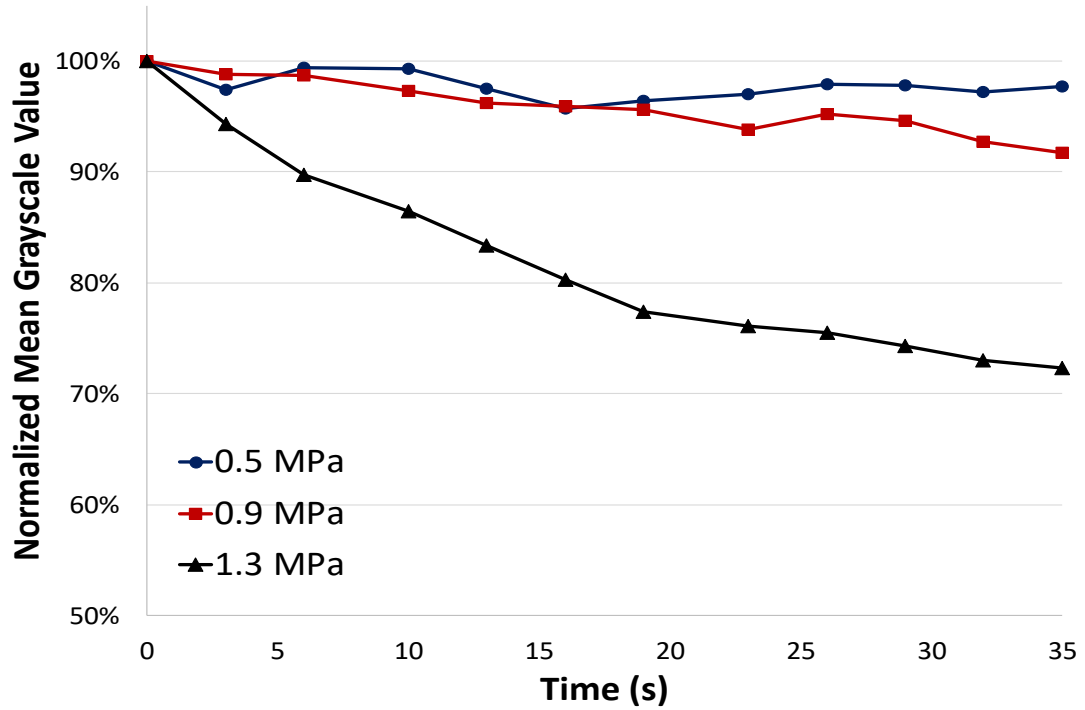


Figure 10: Ultrasound image mean grayscale intensity as a function of time at peak negative acoustic pressures of 0.5 MPa, 0.9 MPa, and 1.3 MPa. At higher pressures (1.3 MPa), the mean grayscale value decreases more rapidly indicating higher rates of microbubble destruction compared to lower pressures (0.5 MPa and 0.9 MPa).

III.3.4. Recovery and viability of erythrocytes after freeze-drying and rehydration

Recovery of intact viable erythrocytes was assessed across multiple conditions after freeze-drying and rehydration. Recovery of viable erythrocytes increased by up to 128 ± 32% when trehalose and microbubbles were loaded in PBS solution and ultrasound was applied to induce

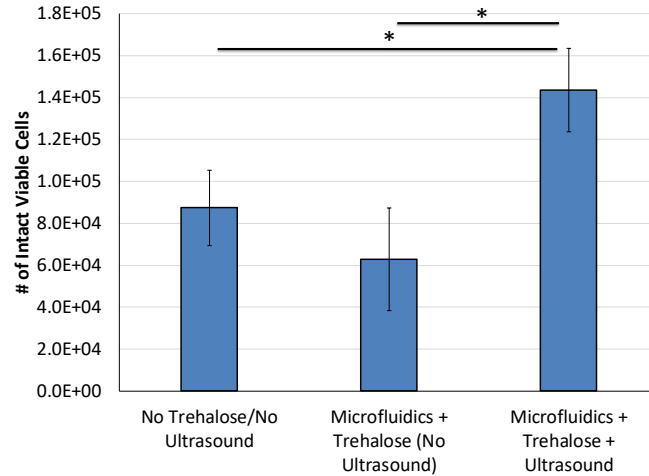


Figure 11: Number of intact viable erythrocytes following freeze-drying and rehydration. Microfluidic ultrasound treatment with trehalose caused a statistically significant increase in recovery of intact viable cells compared to the control groups ($p < 0.05$, $n = 4-8$ /group).

sonoporation prior to freeze-drying and rehydration, compared samples with no trehalose and/or no ultrasound treatment (Figure 11, $p < 0.05$, $n = 4-8$ /group).

III.4. Discussion

The development of acoustofluidics technologies is rapidly growing for a wide variety of applications (Antfolk *et al.*, 2015; Bose *et al.*, 2015; Lajoinie *et al.*, 2016; Pereno *et al.*, 2018; Li and Huang, 2019). In this study, acoustofluidic devices were designed to enhance ultrasound-mediated molecular delivery to human erythrocytes. An ultrasound transducer array was used with the PDMS-based microfluidic device placed at the focal distance in order to expose cells to a relatively uniform ultrasound beam and induce transient sonoporation for rapid

molecular delivery. In addition, a concentric spiral design was used for the microfluidic channels in order to maximize the time that erythrocytes were exposed to ultrasound waves as the cells passed through the channels. Using this acoustofluidic system, ultrasound-mediated intracellular delivery can be achieved in small samples within minutes. Larger volumes can also be processed rapidly by parallelizing the acoustofluidic systems.

The results of this study demonstrate for the first time that ultrasound and microbubbles enhance molecular delivery to erythrocytes in a microfluidic device when the ultrasound pressure and microfluidic flow rate are optimized. These findings represent an early step toward development of optimized methods to produce dried blood for long-term storage at ambient temperatures. The experimental findings in this study demonstrate that several key parameters in the ultrasonic flow system have significant effects on the efficiency of intracellular molecular delivery using an acoustofluidic approach, including acoustic pressure and microfluidic flow rate. At the same time, viability remained high (>80%) for all parameters tested in this study. We conducted initial studies with fluorescein, which has a similar molecular weight as trehalose (332 Da for fluorescein and 342 Da for trehalose). Fluorescein was tested due to its fluorescent properties that enable precise intracellular detection via flow cytometry.

In this study, there was a trend toward a statistically significant difference between microbubble doses (Figure 8A), with the highest fluorescein uptake detected at a microbubble dose of 2% v/v. Lower microbubbles doses will cause lower levels of sonoporation resulting in reduced intracellular delivery, while higher

microbubble doses can cause “shadowing” effects due to scattering and attenuation of ultrasound waves, resulting in reduced ultrasound pressures within part of the sample which also limits intracellular delivery. Thus, there is an optimal “therapeutic window” for the range of microbubble doses which enhance intracellular molecular delivery to cells.

The effects of ultrasound pressure and pulse interval on intracellular delivery of molecular compounds have been described in previous studies using a bulk treatment approach, but acoustofluidic-mediated molecular delivery to erythrocytes has not been previously investigated (Sennoga *et al.*, 2017; Bhutto *et al.*, 2018). In this study, a statistically significant increase in fluorescence was observed at peak negative pressures of 0.5 MPa and 0.9 MPa compared to the no ultrasound control group (Figure 8B and Figure 9). These results indicate that 0.5 MPa and 0.9 MPa induced significant sonoporation and enhanced intracellular delivery of fluorescein as erythrocytes passed through the acoustofluidic channels. Interestingly, higher acoustic pressures (1.3 MPa and 1.8 MPa) were less effective at enhancing molecular delivery. Although this result was not initially expected, it is consistent with other previous studies which found that sustained microbubble cavitation was more effective at inducing therapeutic effects compared to rapid microbubble destruction caused by inertial cavitation (Datta *et al.*, 2006; Gourevich *et al.*, 2015; Sun *et al.*, 2017a). It’s important to consider that biological properties may have important implications on molecular delivery. Thus, these results may not directly translate to nucleated cells, such as T cells. Furthermore, analysis of ultrasound image contrast from microbubbles exposed to different ultrasound

pressures suggests a possible inverse correlation between the rate of microbubble destruction and fluorescein delivery, where decreased rates of microbubble destruction at lower acoustic pressures (0.5 MPa and 0.9 MPa) were associated with higher levels of fluorescein delivery compared to higher acoustic pressures.

Additionally, the effect of ultrasound pulse interval was investigated but no statistically significant difference in fluorescence was observed between each pulse interval that was tested (Figure 8C). This suggests that differences in ultrasound pulse intervals in the range of 0.1 – 10 ms are not a significant factor in molecular delivery. However, very short pulse intervals or higher duty cycles were not tested in this study and may have a more significant impact on molecular delivery. Other studies which used a static bulk treatment approach have reported that ultrasound duty cycle can influence the efficiency of molecular delivery to cultured cells, and it is likely that a wider range of pulse intervals and duty cycles in acoustofluidic devices would cause differences in intracellular delivery as well (Marin *et al.*, 2001; Rahim *et al.*, 2006).

The results of this study also indicate that the microfluidic flow rate is an important parameter that affects the efficiency of ultrasound-mediated molecular delivery to erythrocytes. Interestingly, the fluorescence intensity at 40 mL/hr was actually higher without ultrasound compared to the ultrasound treated group ($p < 0.05$). This finding was unexpected and the mechanism is not fully understood, although it is likely due to a combination of multiple separate factors. Shear forces on the cells are higher at increased flow rates, so as the flow rate increases and shear forces become more significant the permeability of the cells increases and

passive fluorescein uptake is greater, even without ultrasound. When ultrasound is present the microbubbles surround the cell membrane and may potentially have a shielding effect on shear forces in the surrounding fluid. On the other hand, the high flow rates reduce the amount of time that erythrocyte are exposed to ultrasound as they flow through the channels, which also limits fluorescein uptake. Cell-microbubble interaction likely requires further investigation to understand the effect that microbubble surface charge has on molecular delivery. Residence time in the acoustofluidic device is likely a fundamental parameter, especially with pulsed ultrasound. These effects could potentially explain the results observed at a higher flow rate of 40 mL/hr. Relatively low flow rates were used in the concentric spiral acoustofluidic system for two reasons: (1) to increase the number of ultrasound pulses that each cell experiences as it passes through the microfluidic channels, and (2) to reduce shear stress on cells in the microfluidic channels. If the flow rate is too high some cells could pass through the entire microfluidic chamber between each ultrasound pulse. Additionally, high flow rates can increase fluid pressures within the channels and cause failure of the PDMS-bonded devices.

Freeze-drying is a low temperature dehydration process that involves the removal of ice through sublimation to allow product storage in a desiccated state. Intracellular delivery of trehalose is critical for cell preservation in a desiccated state and freeze-drying erythrocytes without trehalose or with only extracellular trehalose (without ultrasound-induced sonoporation to load trehalose intracellularly) yielded low recovery of intact, viable erythrocytes compared to acoustofluidic treatment (Figure 11). This indicates that flowing erythrocytes

through the microfluidic channels alone without ultrasound exposure does not induce sufficient uptake of trehalose to confer protection during freeze-drying. However, ultrasound exposure of erythrocytes with trehalose in the microfluidic system significantly increased recovery of intact and viable erythrocytes after freeze-drying and rehydration (Figure 11). This finding suggests that optimized acoustofluidic parameters can enhance intracellular trehalose delivery which is required for successful recovery of viable erythrocytes after freeze-drying.

This study explored ultrasound-enhanced delivery of small molecules (*i.e.*, fluorescein and trehalose). Larger molecules can also be delivered intracellularly using sonoporation but the uptake efficiency is decreased as we have previously described (Bhutto *et al.*, 2018). There are two important limitations to results of this study. The recovery of erythrocytes after freeze-drying and rehydration was less than 5% even after acoustofluidic-mediated trehalose loading. Further optimization of the freezing and drying process is needed and additional improvements in acoustofluidic techniques are also possible. In addition, other trehalose concentrations can be tested to determine if a higher trehalose concentration would increase trehalose delivery and erythrocyte recovery after freeze-drying and rehydration. The optimal trehalose concentration will be within a specific “therapeutic window.” If the extracellular trehalose concentration is too low the amount of delivery will not be sufficient to protect cells during drying and rehydration, but if the extracellular trehalose concentration is too high there would be significant osmotic stress and damage to the cells. Our study used a trehalose concentration of 200 mM based on previous studies in brine shrimp that survive

drying and rehydration with trehalose at these levels (Crowe *et al.*, 2005; Hand and Menze, 2015), but further optimization of the trehalose concentration may be needed for ultrasound-mediated loading. Another limitation of this study is the low erythrocyte concentration (5 million/mL), which was significantly lower than the typical concentration in whole blood (~5 billion/mL). Further studies will need to assess the feasibility of acoustofluidic molecular delivery at high concentrations. An alternative approach could involve concentrating erythrocytes via centrifugation after trehalose loading if required. Despite these limitations, the results of this study still represent important steps toward addressing the challenges of effective intracellular trehalose delivery into erythrocytes.

These results demonstrate that an acoustofluidic approach can significantly enhance intracellular molecular delivery and increase recovery of viable, intact erythrocytes after freeze-drying and rehydration. Dry storage of erythrocytes could have a fundamental impact in transfusion medicine, particularly in austere environments, air ambulance operations, remote medical centers, and long-duration space missions. Further studies will need to assess optimal microfluidic designs and other parameters (*e.g.*, ultrasound frequency, cell concentration, trehalose concentration, etc.) in order to further enhance intracellular trehalose delivery to erythrocytes for dry preservation. This acoustofluidic system is a platform technology which may also have utility for molecular delivery to other cell types such as platelets, immune cells, and stem cells. The optimal acoustofluidic parameters may be different for each cell type but it is expected that general trends

will be similar and ultrasound pressure and microfluidic flow rates will be critical factors for enhanced intracellular molecular delivery.

III.5. Conclusions

The results of this study demonstrate the feasibility of an acoustofluidic approach to rapidly load human erythrocytes with molecular compounds. Key parameters that affect the efficiency of intracellular delivery include the ultrasound pressure level and the microfluidic flow rate. Acoustofluidic delivery of trehalose into erythrocytes increased the recovery of intact, viable cells after freeze-drying and rehydration. Further optimization to increase erythrocyte recovery after rehydration could eventually lead to long-term storage of blood at ambient temperatures, which would have a major impact on the feasibility of blood transfusions in austere environments such as remote medical centers, air ambulance services, far-forward military operations, and long-duration space missions.

CHAPTER IV – ACOUSTOFLUIDIC-MEDIATED MOLECULAR DELIVERY TO HUMAN T CELLS WITH A THREE-DIMENSIONAL-PRINTED FLOW CHAMBER

³ *Sections of text and figures in this chapter are reproduced from the following reference:*

Connor S. Centner, John T. Moore, Mary E. Baxter, Zachary T. Long, Jacob M. Miller, Ekaterina S. Kovatsenko, Benjamin Xie, Michael A. Menze, R. Eric Berson, Paula J. Bates, Kavitha Yaddanapudi, and Jonathan A. Kopechek “Acoustofluidic-mediated molecular delivery to human T cells with a three-dimensional-printed flow chamber,”

Journal of the Acoustical Society of America 150(6), 4534. (2021). Reprinted with permission of Acoustical Society of America.

IV.1. Introduction

Acoustofluidics (*i.e.*, coupling of ultrasound and fluidic channels) has increasingly been investigated to address challenges in manufacturing and clinical applications, especially in diagnostics and therapeutics. Acoustofluidics technologies have the potential to offer point-of-care (POC) devices for patient bedside use due to improved simplicity and potential for rapid processing. Acoustofluidic research has investigated many potential applications including acoustophoresis (Petersson *et al.*, 2007; Shi *et al.*, 2009c; Wu *et al.*, 2018), biomarker analysis (Wang *et al.*, 2020; Zhou *et al.*, 2021), cell concentrator applications (Li *et al.*, 2007; Chen *et al.*, 2014; Kurashina *et al.*, 2017), fluid mixing applications (Shilton *et al.*, 2008; Friend and Yeo, 2011; Yeo *et al.*, 2011), and recently, biomolecular delivery (Belling *et al.*, 2020a; Centner *et al.*, 2020). However, the key acoustofluidic parameters that affect biomolecular delivery to cells have not been thoroughly investigated. In addition, the effect of ultrasound-driven microbubble oscillation on molecular delivery to cells within acoustofluidic channels has not been fully characterized. Optimization of acoustofluidic parameters for biomolecular delivery to cells could potentially enable utilization of this technology for non-viral manufacturing of cell therapies and other applications.

Cell-based therapies represent the latest biotechnological revolution in medicine. Potential therapeutic applications include treating cancers, treating autoimmune diseases, treating infectious diseases, and repairing damaged tissue (Buzhor *et al.*, 2014). Recent breakthroughs in adoptive cell therapies, specifically chimeric antigen receptor (CAR)-T cells, have had a significant impact on the

treatment of B-cell malignancies, such as leukemia or lymphoma (Buzhor *et al.*, 2014; Kochenderfer *et al.*, 2017; Turtle *et al.*, 2017; Maude *et al.*, 2018), with over 80% of patients achieving complete remission in some trials. CAR-T may also have the potential to treat other forms of cancer and other diseases, such as HIV (Deeks *et al.*, 2002). CAR-T has indicated the ability to enhance targeted cytotoxic activity while reducing off-target effects due to its specificity, which is a distinct advantage over traditional treatment regimens (*e.g.*, chemotherapy, radiation) for cancer (Moghimi *et al.*, 2021). However, the current manufacturing techniques for CAR-T, which are heavily dependent on viral vectors, have several limitations that limit more widespread adoption of this biotechnology.

Viral vectors, which are infectious entities that are adapted to deliver nucleic acids to the cytoplasm or nucleus, are currently the primary technique utilized for *ex vivo* modification of T cells (Wang and Riviere, 2015). Viral vectors have been shown to have high efficacy in modifying T cells for clinical trials of new immunotherapies (Ghani *et al.*, 2009; Kochenderfer *et al.*, 2015; Schuster *et al.*, 2017). However, there are several limitations with this technique, including potential insertional mutagenesis and undesired multiplicity of infection (Piscopo *et al.*, 2018). In addition, viral vectors generally cannot deliver non-nucleic acid biomolecules to cells.

To address these limitations, non-viral techniques are being developed which can enhance intracellular molecular delivery. Techniques include nanocarriers and nanoparticles where therapeutic agents may be loading internally or liganded to the surface to improve molecular delivery to specific cells *in vivo* or

in vitro (Majumder *et al.*, 2019). These techniques, however, rely heavily on endocytosis pathways, which may limit molecular delivery efficiency or loading rate by biomodulatory signaling molecules such as mTOR, proton pumps, and cathepsins (Sahay *et al.*, 2013). Additionally, molecular delivery can be reduced via exocytosis of these particles and associated therapeutic agents (Sahay *et al.*, 2013; Oh and Park, 2014). These could have important implications on treatment efficacy as low delivery efficiency or slow loading rates could delay essential cell-based therapies for patients. Another treatment technique includes nanostraw membrane stamping where the plasma membrane is mechanically penetrated. This technique has shown over 85% delivery efficiency of small molecules in adherent cell lines (Zhang *et al.*, 2019). For anchorage independent cells, this technique may be insufficient and has yet to demonstrate feasibility.

Transient permeabilization of the plasma membrane has generated interest since it may allow molecules to enter the cytosol rapidly. Electroporation is a technique that induces transient permeabilization of the plasma membrane and has generated significant interest as a potential method to overcome limitations of viral vectors. However, bulk electroporation may not have the capacity to achieve sufficient levels of molecular delivery that are required for functional applications, such as CAR-T (Annesley *et al.*, 2018a). In an attempt to improve delivery efficiency, stimuli-responsive nanoparticles, conjugated nanoparticles, and nanocarriers have been studied in conjugation with electroporation (Kim and Lee, 2017). Another fundamental limitation of electroporation is the risk of epigenetic modifications that can induce a significant increase in cytokine release, which can

cause severe immunomodulatory effects after treatment (Falk *et al.*, 2017; He *et al.*, 2019). For example, unintended amplification of critical pro-inflammatory interleukins, such as interleukin-2, may induce cytokine release syndrome where the immune system inadvertently attacks native tissues and organ, which can be fatal in severe cases. An alternative approach that has been explored for non-viral molecular delivery involves microfluidic squeezing, where cells are passed through microfluidic channels with small constrictions that transiently increase membrane permeability for intracellular delivery of biomolecules (Sharei *et al.*, 2013). However, channel blockage and limited throughput are challenges that can occur with constricted channels.

Acoustofluidics potentially offers an alternative method of biomolecular delivery to T cells, which could address limitations of viral transduction and other approaches. Recent advancements of targeted endonucleases that modify the genome, such as clustered regulatory interspaced palindromic repeats (CRISPR)-Cas9, offers efficient targeting of gene(s) for gene disruption, gene correction, or gene insertion (Morgan *et al.*, 2017). These target genome-editing techniques require alternative intracellular delivery methods as viral vectors have size limitations, which has hindered the encapsulation of targeted endonucleases into a singular viral delivery vehicle (Hirsch *et al.*, 2016; Yang *et al.*, 2016). Acoustofluidic approaches can rapidly deliver biomolecules into cells by transiently increasing membrane permeability (Belling *et al.*, 2020a; Centner *et al.*, 2020). Several previous studies have evaluated acoustofluidic-enhanced molecular delivery without ultrasound contrast agents by utilizing acoustic radiation force and

shear stress to induce transient perforation in the plasma membrane (Carugo *et al.*, 2011; Belling *et al.*, 2020a). In this study, we have characterized acoustofluidic-enhanced molecular delivery with microbubbles in order to understand the key parameters that affect the efficiency of molecular delivery to human T cells.

Although the acoustofluidic device has the potential to address limitations in viral transduction, current acoustofluidic devices utilized for molecular delivery are likely untranslatable for cell manufacturing applications. These studies utilized polydimethylsiloxane (PDMS)-based devices (Centner *et al.*, 2020; Centner *et al.*, 2021b), which have several limitations such as batch-to-batch variability, limitations with sterilization, frequent channel blockage, and high risk of device failure after frequent use. Utilizing a 3D-printed acoustofluidic device further enables the potential of an acoustofluidic utilization in a cell manufacturing setting as it can be fabricated with low batch-to-batch variability and is a durable, scalable design that can be easily sterilized for clinical applications.

The objective of this study was to assess the role of important acoustofluidic parameters on molecular delivery and cell viability. The concepts of sonoporation and ultrasound-mediated molecular delivery to cells are well-established in static ultrasound systems and have demonstrated significant molecular delivery with consistent treatment parameters (Miller *et al.*, 1999). Recently, a PDMS-based acoustofluidic device was utilized to assess physical effects of microbubbles on enhancing molecular delivery to *in situ* tissue (Pereno *et al.*, 2018); however, this approach has not been thoroughly characterized in an acoustofluidic system as a method to enhance molecular delivery in *in vitro* applications with lipid-coated

microbubbles. This study aims to provide new insights into the effect of microbubble phospholipid surface charge, acoustofluidic channel geometry, molecular exposure time point, acoustic pressure, and microbubble concentration on molecular delivery efficiency in a 3D-printed acoustofluidic device. These parameters may have a key role in the development of effective acoustofluidic approaches for manufacturing of cell-based therapies or other molecular delivery applications.

IV.2. Methods

IV.2.1. Acoustofluidic device design and assembly

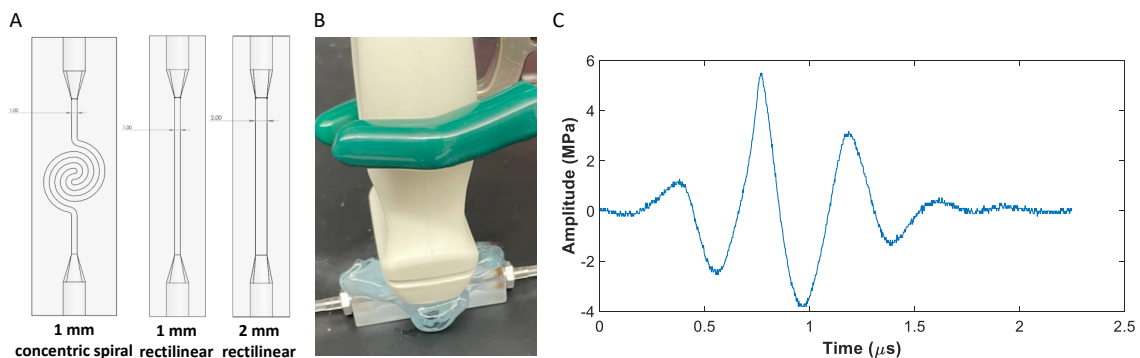


Figure 12: Rectilinear acoustofluidic device design with 1 mm channel width. Right: Rectilinear acoustofluidic device design with 2 mm channel width. (B) Experimental configuration of ultrasound transducer (P4-1) placed on top of acoustofluidic device with ultrasound gel for acoustic coupling with the acoustofluidic device. (C) Ultrasound waveform generated by P4-1 transducer as measured by needle hydrophone.

Acoustofluidic devices were fabricated in Accura 60 plastic using stereolithography 3D printing (Xometry, Gaithersburg, MD, USA). Stainless steel barbed tube fittings (McMaster-Carr, Elmhurst, IL, USA) were inserted into pre-threaded inlet and outlet ports for connection with PVC tubing (1/16" ID, 10-32 threads). Three different acoustofluidic channel geometries were designed in

SolidWorks (Waltham, MA, USA) and fabricated for comparison of molecular delivery efficiencies (Figure 12A). Two acoustofluidic designs had rectilinear channels, with square cross-sectional diameters of 1 mm x 1 mm or 2 mm x 2 mm. Additionally, a concentric spiral channel design was also fabricated with a square cross-sectional diameter of 1 mm x 1 mm to increase residence time within the ultrasound beam compared to the rectilinear channel geometry. 1 mm and 2 mm will allow approximately 1.67 wavelengths and 3.33 wavelengths of ultrasound signal in the acoustofluidic channel with a 2.5 MHz center frequency, respectively. Additionally, the selected center frequency (2.5 MHz) is near the microbubble resonance frequency and should provide sufficient oscillation power with lipid-encapsulated microbubbles (Versluis *et al.*, 2020).

All experiments were performed with the acoustofluidic devices connected to a peristaltic pump at a flow rate of 1.5 mL/min. The ultrasound transducer was placed directly on top of the acoustofluidic device with ultrasound gel for acoustic coupling (Figure 12B). A P4-1 ultrasound transducer (96 elements, 2.5 MHz center frequency, ATL, Bothell, WA, USA) was used to transmit B-mode pulses generated by an ultrasound imaging system (Vantage 64LE, Verasonics, Kirkland, WA, USA). The free-field ultrasound pressure output was measured using a calibrated 0.2-mm needle hydrophone (Precision Acoustics, Dorset, UK) 40 mm away from P4-1 ultrasound transducer in a water tank with water as the medium. The -3 dB beamwidth was 8 mm, and the peak negative ultrasound pressure output was 3.8 MPa for all experiments unless otherwise specified (waveform shown in Figure 12C).

IV.2.2. Microbubble synthesis

Phospholipid-coated gas-filled microbubbles were custom synthesized to enhance biomolecular delivery to T cells in the acoustofluidic devices. Microbubbles with a cationic surface charge were synthesized using chloroform solutions of 1,2-distearoyl-sn-glycero-3-phosphocholine (DSPC, Avanti Lipids, Alabaster, AL, USA); 1,2-distearoyl-sn-glycero-3-ethylphosphocholine (DSEPC, Avanti Lipids); 1,2-distearoyl-sn-glycero-3-phosphoglycerol (DSPG, Avanti Lipids); and polyethylene glycol-40 stearate (Sigma-Aldrich, St. Louis, MO, USA) at a molar ratio of 100:43:1:4.5. The cationic lipid DSEPC conferred a net positive surface charge on the microbubbles as previously described (Kopechek *et al.*, 2015; Kopechek *et al.*, 2016; Kopechek *et al.*, 2019). Microbubbles with neutral surface charge were synthesized with chloroform solutions of DSPC and 1,2-distearoyl-sn-glycero-3-phosphoethanolamine-N-[amino(polyethylene glycol)-2000] (DSPE-PEG2000, Avanti Lipids) at a molar ratio of 96:4 (Myrset *et al.*, 2011). Chloroform was evaporated under vacuum and an aqueous micellar lipid solution was prepared by adding 1x phosphate buffered solution (PBS) and sonicating (125W, Qsonica, Newtown, CT, USA) to disperse the lipids. The resulting 10 mg/mL lipid solution was diluted 1:4 in PBS and sealed in a glass vial. The vial head space was filled with decafluorobutane gas (FlouroMed, Round Rock, TX, USA), followed by amalgamation for 45 s at 4350 cpm (DB-338, COXO, Foshan City, China) to form perfluorobutane gas-filled microbubbles (MBs). This process yields microbubbles with a mean diameter of 2 μm as previously described (Kopechek *et al.*, 2015).

IV.2.3. Microbubble attenuation measurements

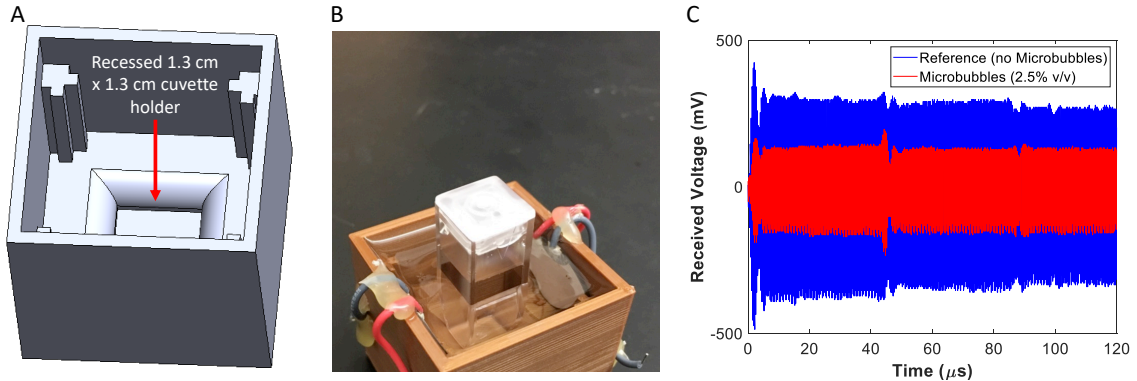


Figure 13: (A) Schematic of acoustic attenuation chamber with a recessed 1.3 cm x 1.3 cm cuvette holder to ensure consistent cuvette sample placement. (B) Photo of acoustic attenuation chamber with polystyrene cuvette placed at the center of the ultrasound beam. The acoustic attenuation chamber contains two co-axially aligned single-element transducers, with one transducer acting as the source and the other transducer acting as the receiver. (C) Representative time-domain waveforms acquired using the acoustic attenuation chamber with microbubbles (2.5% v/v) and without microbubbles (reference). Acquired time-domain waveforms were transformed to the frequency domain to calculate acoustic attenuation coefficients using Equation 1.

Acoustic attenuation measurements of microbubble solutions were conducted to assess effects of microbubble properties, acoustofluidic channel geometries, and ultrasound parameters on microbubble destruction. A custom 3D-printed acoustic chamber was designed in SolidWorks (Figure 13A) and fabricated using fused filament deposition with 1.75-mm polylactic acid filament (PLA, McMaster-Carr) with an Ender-3 3D printer (Creality, Shenzhen, China). Two lead zirconate titanate (PZT) transducers (3.3 MHz center frequency, 25 mm diameter, StemInc, Davenport, FL, USA) were aligned opposite each other 31 mm apart and used as a source and receiver to measure acoustic attenuation. Microbubble solutions (2.5% v/v in 3 mL PBS) were added to 4.5-mL disposable polystyrene cuvettes (VWR, Radnor, PA, USA) which were placed in the acoustic chamber at

the center of the ultrasound beam (Figure 13B). A waveform generator (DG822, Rigol, Suzhou, China) was used to generate a 3.3-MHz pulse with 500 cycles at a pulse interval of 10 ms. Received ultrasound signals (300 traces per sample) were acquired with a digital oscilloscope (DS1202Z-E, Rigol) at a sampling rate of 10 MHz and transferred to a desktop computer for processing with MATLAB (Mathworks, Natick, MA, USA). Representative waveforms are shown in Figure 13C. The attenuation coefficient was calculated as previously described (Kopechek *et al.*, 2011). Power spectra were computed for each waveform and averaged to obtain the average power spectrum for each sample. The peak magnitude was determined at 3.30 MHz for each sample, $|S_s|$, and for each corresponding reference measurement without microbubble solution, $|S_r|$. The acoustic path length through the sample (inside the cuvette) was 1 cm. Therefore, the acoustic attenuation coefficient in decibels per unit length (dB/cm) can be computed as follows:

$$\alpha_{dB} = 10 \log_{10} \left(\frac{S_r}{S_s} \right). \quad (1)$$

IV.2.4. Molecular delivery to human T cells

Jurkat T cells were cultured with complete RPMI-1640 (10% fetal bovine serum, 1% penicillin/streptomycin) at 37 °C and 5% CO₂ in a flat-bottom tissue culture flask. Jurkat T cells were harvested when 70-90% confluent and were resuspended in complete RPMI-1640 at a concentration of 100,000 cells/mL after centrifugation at 1500g for 5 min at 4 °C. Microbubbles were added to cell solutions at a 2.5% (v/v) concentration for calcein loading experiments, unless otherwise

indicated. For delivery efficiency assessment with different microbubble concentrations (0-10% v/v), 10 µg/mL (1 mM) of 10 kDa FITC-Dextran was utilized. Additionally, 5% (v/v) concentration was used for intracellular delivery of 26 kDa sfGFP. Microbubbles with a cationic surface charge were used for all acoustofluidic experiments unless otherwise indicated. In separate experimental studies, calcein, 10 kDa FITC-Dextran, and 26 kDa sfGFP were added to Jurkat T cell/microbubble solutions at a final concentration of 100 µg/mL, 10 µg/mL (1 mM), and 52 µg/mL (2 µM), respectively. Unless otherwise noted, the molecular compound was added to each sample 1 min prior to acoustofluidic treatment. After treatment, each sample was washed three times via centrifugation with 3 mL of PBS to remove extracellular calcein prior to flow cytometry analysis. After washing each sample, propidium iodide (PI) was added 1-hour post-acoustofluidic treatment to a final concentration of 20 µg/mL to detect non-viable cells via flow cytometry.

Flow cytometry was performed using a MACSQuant Analyzer 10 (Miltenyi Biotec, Auburn, CA, USA) with 10,000 events recorded per sample. Data were analyzed using FlowJo software (Ashland, OR, USA). Forward and side-scatter plots were gated to the main cell population (based on untreated control samples) and the mean fluorescence intensity in the FITC channel was calculated to assess intracellular calcein delivery. Cell viability was assessed by gating PI fluorescence intensity in the untreated control samples and determining the percentage of cells in the treatment groups that exceeded the gated PI fluorescence threshold using the PE/Texas Red channel.

IV.2.5. Computational modeling of fluid dynamics

Fluid dynamics in the acoustofluidic devices were modeled using ANSYS (Canonsburg, PA, USA). Acoustofluidic channel geometries were imported from SolidWorks and transferred to the meshing component. Mesh sensitivity analysis was performed for element sizes between 0.2 mm and 3 mm to determine the optimal mesh sizes for each simulation. An element size of 0.5 mm (18,169 elements) was used for the 1-mm diameter rectilinear channel, an element size of 0.4 mm (49,495 elements) was used for the 2-mm diameter rectilinear channel, and an element size of 0.4 mm (30,690 elements) was used for the 1-mm diameter concentric spiral channel. Each mesh was transferred to ANSYS Fluent and a discrete phase model was used to compute the wall shear stress throughout each acoustofluidic channel, assuming laminar flow. To model perfluorobutane microbubbles within the acoustofluidic channels, particles were generated with a mean diameter of 2 μm , modeled as a Rosin-Rammler distribution, with a particle density of 24.6 kg/m^3 and a specific heat of 809 $\text{J}/(\text{kg}\cdot\text{K})$ in the discrete phase model. Given the very small microbubble diameter (2 μm) and the relatively short duration within the device ($\sim 2\text{-}3$ s), buoyancy is not expected to be a significant factor and was therefore ignored in the computational model. The expected terminal rise velocity of microbubbles in the acoustofluidic channel, U_b , was calculated assuming low Reynolds number as previously described (Stokes, 1851; Parmar and Majumder, 2015):

$$U_b = \frac{D_b^2 g (\rho_l - \rho_g)}{18 \mu_l}, \quad (2)$$

where D_b represents microbubble diameter, g represents acceleration due to gravity, ρ_l represents density of the liquid, ρ_g represents density of the gas, and μ_l represents viscosity of the liquid. Assuming a microbubble diameter of 2 μm , a liquid density of 1000 kg/m^3 for water, a gas density of 11.2 kg/m^3 for perfluorobutane, and a liquid viscosity of 1 $\text{mPa}\cdot\text{s}$ for water, the terminal rise velocity would be 2.1 $\mu\text{m}/\text{s}$. At this rate, the microbubble would be expected to rise no more than 6.3 μm , or 0.63% of the 1-mm channel diameter, while passing through the acoustofluidic device within 3 seconds. The fluid material was modeled as water at 25 °C (density of 1000 kg/m^3 and viscosity of 0.91 cP). The channel inlet velocity was set to 0.002 m/s (1.5 mL/min) and the channel inlet pressure and outlet pressure boundary conditions were set to 1 atm for each simulation. The volume average wall shear stress was computed for each acoustofluidic channel geometry.

IV.2.6. Protein generation and purification

sfGFP (plasmid #51562, Addgene, Watertown, MA) was expressed in frame with a chitin-binding protein (CBP) and self-splicing intein protein spacer for purification purposes. The plasmid was transformed into the *Escherichia coli* strain BL21 Star (Thermo Fisher Scientific, Waltham, MA) and cells were grown on Luria-Bertani (LB) medium-based agarose plates containing 100 $\mu\text{g}/\text{mL}$ ampicillin. Antibiotic resistant colonies were grown to an optical density of 0.6 using $\lambda = 595$ nm in liquid culture on an orbital shaker at 225 rpm and 37°C in LB containing 100 $\mu\text{g}/\text{mL}$ ampicillin. Protein expression was induced for 2h after adding isopropyl- β -

1-thiogalactopyranoside (IPTG) to a final concentration of 0.6 mM and the bacteria were harvested via centrifugation at 5000g for 30 min at 4°C. Cell pellets were resuspended in a small volume of buffer A (1M NaCl, 50 mM Tris-HCl, pH 8.5) containing 1 mM phenylmethylsulfonyl fluoride (PMSF) to inhibit serine protease activity. The resuspended pellets were stored at -80 °C for up to 4 months before purification. For sfGFP purification, cells were lysed by sonication (Q500, Qsonica, Newtown, CT) and bacterial debris was removed by centrifugation for 30 min at 5000g at 4°C. The supernatant was loaded via gravity flow onto a 15 mL chitin resin (NEB Biolabs, Ipswich, MA) containing column. The column was then washed with 20 column volumes of buffer A. The sfGFP protein was eluted after incubation with 50 mM DTT dissolved in buffer A at 4 °C for 48 h. The eluted protein was then dialyzed into 50 mM phosphate buffer at a pH of 7.0 and concentrated using centrifugal filter units (Amicon Ultra 10 kDa, Millipore Sigma, St. Louis, MO). The purity of the protein was confirmed by SDS-PAGE and averaged at least 95%. Purified protein aliquots were snap frozen in liquid nitrogen and stored at -80°C until used in experiments.

IV.2.7. Statistical Analysis

Statistical analysis was conducted using SPSS 26 (Armonk, NY, USA). Statistical comparisons between groups for were determined using ANOVA, unless stated otherwise, with statistical significance defined as $p < 0.05$ (two-tailed). Post-hoc analysis was conducted using Tukey's test for ANOVA. Bars represent mean \pm standard deviations.

IV.3. Results

IV.3.1. Effect of microbubble surface charge on molecular delivery

Ultrasound-mediated intracellular delivery of calcein to Jurkat T cells was evaluated with various microbubble phospholipid formulations at 2.5% (v/v) in PBS as measured by flow cytometry post-treatment. Control groups without ultrasound treatment were tested for each microbubble formulation to determine if microbubbles alone enhanced calcein delivery when samples passed through the fluidic channels without ultrasound exposure. In the absence of ultrasound exposure there was no statistically significant difference in calcein delivery to T cells between samples containing microbubbles with neutral surface charge and samples containing microbubbles with a cationic surface charge. However, significant uptake of calcein was observed in Jurkat T cell samples containing microbubbles that were exposed to 3.8 MPa peak negative ultrasound pressure as they passed through the 1 mm rectilinear channel acoustofluidic device, compared to control groups without ultrasound treatment (Figure 14A, ANOVA $p < 0.001$, $n = 5-6$ /group). Post-hoc analysis indicated that calcein delivery was significantly enhanced in Jurkat T cell samples with cationic microbubbles that were treated with ultrasound compared to ultrasound-treated samples with neutral microbubbles or ultrasound-treated samples with no microbubbles (ANOVA $p < 0.001$).

PI was added to samples post-treatment to assess cell viability as measured by flow cytometry. No statistically significant differences in cell viability were observed in ultrasound-treated samples with neutral microbubbles or no exogenous microbubbles compared to control groups without ultrasound treatment for each condition, respectively. However, post-hoc analysis indicated that cell viability was significantly reduced in ultrasound-treated samples with cationic microbubbles after acoustofluidic treatment, compared to samples with cationic microbubbles which were not exposed to ultrasound as they passed through the acoustofluidic device (Figure 14B, ANOVA $p=0.001$, $n=3/\text{group}$). These results indicate that microbubble surface charge has a significant impact on acoustofluidic-mediated effects in Jurkat T cells and cationic surface charge significantly enhances molecular delivery compared to neutral surface charge, but moderately reduced cell viability compared to respective control groups.

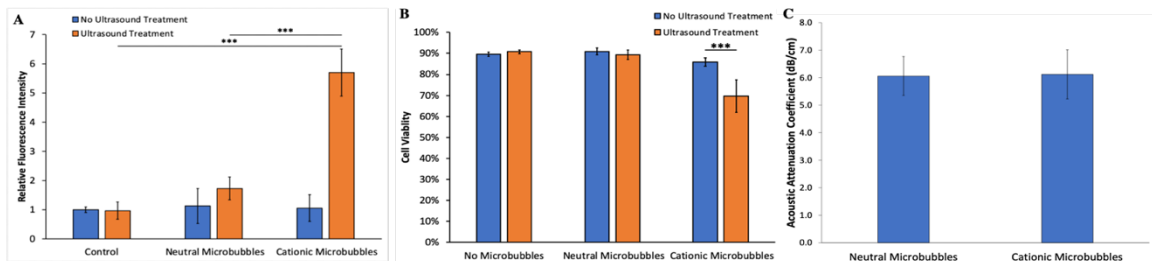


Figure 14: Effect of microbubble surface charge on molecular delivery in the 1 mm rectilinear channel acoustofluidic device. (A) Microbubbles with cationic surface charge enhanced calcein delivery to Jurkat T cells in the acoustofluidic device compared to microbubbles with neutral surface charge (ANOVA $p<0.001$, $n=5-6/\text{group}$). (B) Cell viability was moderately reduced after acoustofluidic treatment with cationic microbubbles compared to neutral microbubbles (ANOVA $p<0.001$, $n=3/\text{group}$). (C) There was no statistically significant difference in acoustic attenuation between cationic microbubbles and neutral microbubbles ($p>0.05$, $n=15/\text{group}$).

IV.3.2. Effect of molecular exposure time point on intracellular delivery

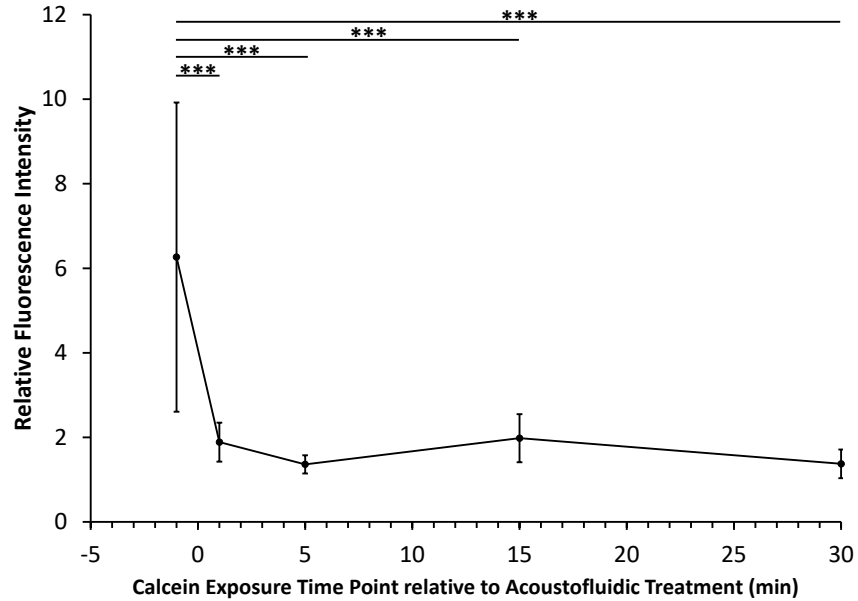


Figure 15: Effect of molecular exposure time point on calcein uptake in Jurkat T cells. Calcein was added to cell solutions at various timepoints before and after passing through the 1 mm rectilinear acoustofluidic device with ultrasound treatment (3.8 MPa peak negative pressure) and cationic microbubbles. Calcein delivery was enhanced when delivered prior to treatment compared to all post-treatment exposure time points (ANOVA $p < 0.001$, $n = 5-6/\text{group}$).

The impact of molecular exposure time points on intracellular delivery was investigated using the 1 mm rectilinear acoustofluidic device with ultrasound treatment at 3.8 MPa peak negative pressure output in Jurkat T cell samples with cationic microbubbles. The highest level of molecular delivery occurred when calcein was added 1 min prior to acoustofluidic treatment, with intracellular fluorescence enhanced by 6.26 ± 3.66 -fold compared to baseline. Post-hoc analysis with Tukey's test indicated that molecular delivery was significantly enhanced when samples were exposed to calcein at 1 min prior to acoustofluidic treatment compared to adding calcein at 1 min, 5 min, 15 min, or 30 min post-

acoustofluidic treatment (Figure 15, ANOVA $p < 0.001$, $n = 5-6$). These results indicate that biomolecule presence in solution during acoustofluidic treatment has a greater effect on molecular loading compared to biomolecule addition to solution post-treatment, which suggests that molecular delivery occurs at a faster rate during acoustofluidic treatment compared to other time points.

IV.3.3. Effect of acoustofluidic channel geometries on molecular delivery

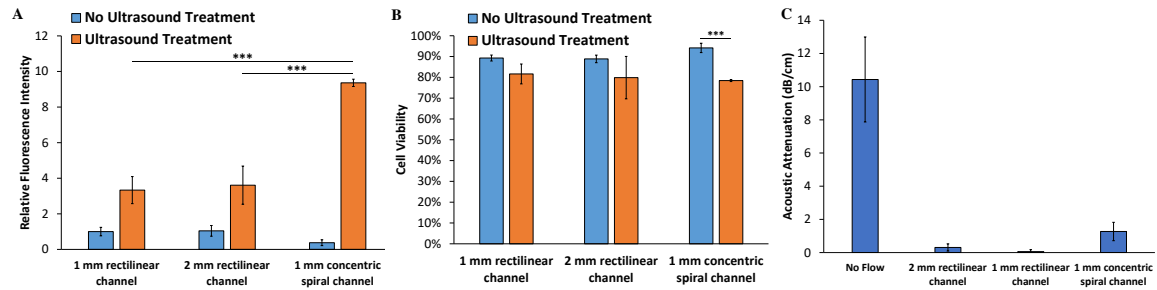


Figure 16: Effect of acoustofluidic channel geometry on molecular delivery. (A) Ultrasound treatment (3.8 MPa peak negative pressure) enhanced calcein delivery to Jurkat T cells in each channel geometry compared to control groups passed through the channels without ultrasound treatment (ANOVA $p < 0.001$, $n = 6/\text{group}$). With ultrasound treatment the 1 mm concentric spiral geometry significantly enhanced calcein delivery to Jurkat T cells compared to the 1 mm and 2 mm rectilinear channel geometry (ANOVA $p < 0.001$) and 2 mm rectilinear channel geometry (ANOVA $p < 0.001$). (B) Ultrasound treatment reduced cell viability in acoustofluidic devices (ANOVA $p < 0.001$, $n = 3-6/\text{group}$), but viability remained above 75% in all groups. (C) Ultrasound treatment reduced acoustic attenuation of microbubble solutions after treatment in each acoustofluidic channel geometry compared to the no flow control condition (ANOVA $p < 0.001$, $n = 6/\text{group}$), indicating that ultrasound treatment induced microbubble destruction in the channels. There was no statistically significant difference in acoustic attenuation between each channel geometry.

The impact of acoustofluidic channel geometries on molecular delivery was investigated with three geometries (as shown in Figure 12): a 1-mm diameter rectilinear channel, a 2-mm diameter rectilinear channel, and a concentric spiral design with a 1 mm channel diameter, using flow cytometry for analysis after

acoustofluidic treatment. In all three channel geometries, ultrasound treatment significantly enhanced calcein delivery to Jurkat T cells compared to control groups without ultrasound (Figure 16A, ANOVA $p < 0.001$, $n = 6/\text{group}$). Furthermore, post-hoc analysis indicated that calcein delivery to Jurkat T cells was significantly enhanced in samples passed through the 1 mm concentric spiral channel with ultrasound treatment compared to ultrasound-treated samples passed through the 1 mm rectilinear channel (ANOVA $p < 0.001$) and 2 mm rectilinear channel (ANOVA $p = 0.001$), respectively.

PI was added to samples post-treatment to assess cell viability as measured by flow cytometry. Reduced cell viability was observed with ultrasound treatment in acoustofluidic devices compared to control groups without ultrasound (Figure 16B, ANOVA $p < 0.001$, $n = 3-6/\text{group}$). Although reduced viability was observed, viability remained above 75% in all treatment groups. There was no statistically significant difference in viability between each channel geometry.

The effect of acoustofluidic channel geometry on ultrasound-induced microbubble destruction was also assessed using acoustic attenuation measurements. Ultrasound treatment significantly reduced acoustic attenuation in all geometries compared to the control group without ultrasound (Figure 16C, ANOVA $p < 0.001$, $n = 6/\text{group}$). Post-hoc analysis indicated that there was no statistically significant difference between acoustic attenuation after treatment in the 1 mm concentric spiral channel, 1 mm rectilinear channel, and 2 mm rectilinear channel, respectively.

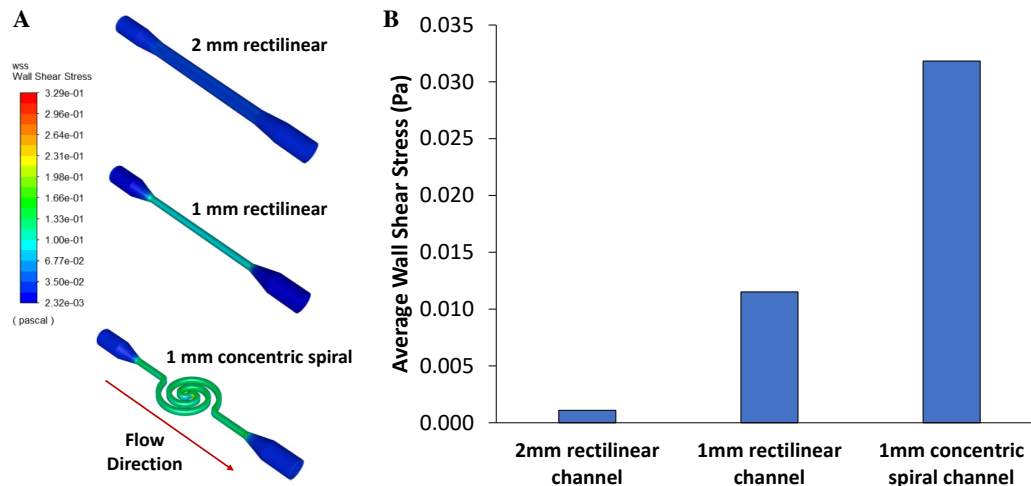


Figure 17: Computational modeling of wall shear stress in each acoustofluidic channel geometry for a flow rate of 1.5 mL/min. (A) Representative images of wall shear stress patterns from computational modeling of each acoustofluidic channel geometry. (B) Average wall shear stress was higher in the concentric spiral geometry compared to rectilinear geometries.

Fluid dynamics within each acoustofluidic channel geometry were analyzed using computational modeling in ANSYS to further assess factors that may influence molecular delivery in each acoustofluidic channel geometry. The simulated Reynolds number in each channel geometry was below 28, indicating laminar flow within the acoustofluidic devices. As shown in Figure 17, the average wall shear stress was ten-fold higher in the 1-mm diameter rectilinear channel compared to the 2-mm diameter rectilinear channel, as would be expected given the relatively higher fluid velocity within the smaller channels. However, the average wall shear stress was even higher in the 1 mm concentric spiral channels (2.8-fold higher compared to the 1 mm rectilinear channel), indicating that the curvature of the concentric spiral channel geometry increases wall shear stress separately from fluid velocity and this may be a key factor that influences

acoustofluidic molecular delivery to cells within the concentric spiral channel geometry.

IV.3.4. Effect of ultrasound pressure on molecular delivery

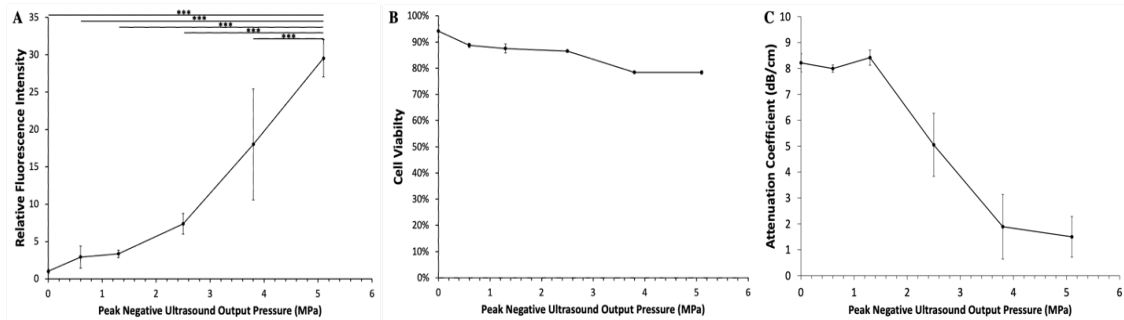


Figure 18: Effect of ultrasound pressure on molecular delivery to Jurkat T cells in acoustofluidic device. (A) The highest ultrasound pressure evaluated (5.1 MPa peak negative ultrasound output pressure) resulted in the highest amount of intracellular calcein delivery compared to all other treatment groups (ANOVA $p < 0.001$, $n = 6/\text{group}$). (B) Cell viability remained above 75% at all ultrasound pressure conditions ($n = 3/\text{group}$). (C) Acoustic attenuation was significantly reduced in samples treated at peak negative ultrasound pressures 3.8 MPa and higher, indicating ultrasound-mediated microbubble destruction at higher acoustic pressures (ANOVA $p < 0.05$, $n = 5-7/\text{group}$).

Acoustofluidic-mediated molecular delivery was evaluated at various ultrasound pressures using the 1-mm diameter concentric spiral design, as measured with flow cytometry. Acoustofluidic treatment was tested at a range of ultrasound pressures between 0-5.1 MPa peak negative ultrasound output pressure. There were no statistically significant differences in calcein delivery to Jurkat T cells at lower ultrasound output pressures (0-1.3 MPa, $p > 0.05$), whereas significant delivery was observed at ultrasound output pressures of 2.5 MPa and higher. Post-hoc analysis indicated that calcein delivery was significantly enhanced at ultrasound output pressures of 2.5 MPa and higher compared to lower ultrasound output pressures (0-1.3 MPa; Figure 18A, ANOVA $p < 0.001$,

n=3/group). Post-hoc analysis also indicated that the highest acoustofluidic ultrasound pressure evaluated (5.1 MPa peak negative ultrasound output pressure) resulted in the highest amount of molecular delivery to Jurkat T cells compared to all other acoustofluidic ultrasound pressures tested in this study (ANOVA $p < 0.001$), with detected intracellular fluorescence intensity increased by a maximum of 22.09 ± 0.13 -fold compared to the 0 MPa control group.

Flow cytometry analysis of PI staining indicated a general trend that as acoustofluidic ultrasound pressures increased there was a corresponding decrease in cell viability, although this difference was relatively small and cell viability remained above 75% at all treatment conditions. These results indicate that acoustofluidic treatment can significantly enhance molecular delivery without significantly impacting cell viability.

Acoustic attenuation of each sample was measured to assess the effect of acoustofluidic ultrasound pressures on microbubble destruction. No evidence of microbubble destruction was observed at peak negative ultrasound output pressures of 0-2.5 MPa, but there was a significant decrease in acoustic attenuation after acoustofluidic treatment with ultrasound output pressures of 3.8 MPa and higher (Figure 18C; ANOVA $p < 0.05$, n=5-7/group), indicating higher levels of microbubble destruction at these conditions. The general trend of acoustic attenuation as a function of ultrasound pressure was roughly inversely related to the trend in molecular delivery, with acoustic attenuation generally lower at ultrasound pressures where fluorescence intensity was higher. This suggests that

microbubble destruction is associated with enhanced intracellular molecular delivery during acoustofluidic treatment.

IV.3.5. Effect of microbubble dose on molecular delivery

Acoustofluidic treatment was tested with a range of cationic microbubble concentrations (0-10% v/v) at 5.1 MPa peak negative ultrasound output pressure to assess molecular delivery with a large molecule (≥ 1 kDa). Molecular delivery was assessed using 10 kDa FITC-Dextran and a poor linear correlation with microbubble concentration was observed ($R^2=0.19$). This indicates that a microbubble concentration within a specific therapeutic window is required for optimal molecular delivery. A microbubble concentration of 5% (v/v) improved molecular delivery compared to lower microbubble concentrations (0-1% v/v, ANOVA $p<0.001$, $n=6-9$ /group) and higher microbubble concentrations (10% v/v, $p<0.01$, $n=6-9$).

Trypan blue assay indicated a weak negative linear correlation with microbubble concentration and cell viability ($R^2=0.17$), which indicated that an increase in microbubble concentration is a poor predictor variable for cell viability. A microbubble concentration of 5% (v/v) reduced viability compared to flow only (0% v/v, ANOVA $p<0.01$, $n=3$ /group) and 1% (v/v), 2.5% (v/v), 10% (v/v, ANOVA $p<0.05$). Of significant interest, no correlation was found between molecular loading and cell viability ($R^2=0.50$), suggesting that increased molecular delivery can be achieved without compromising cell viability.

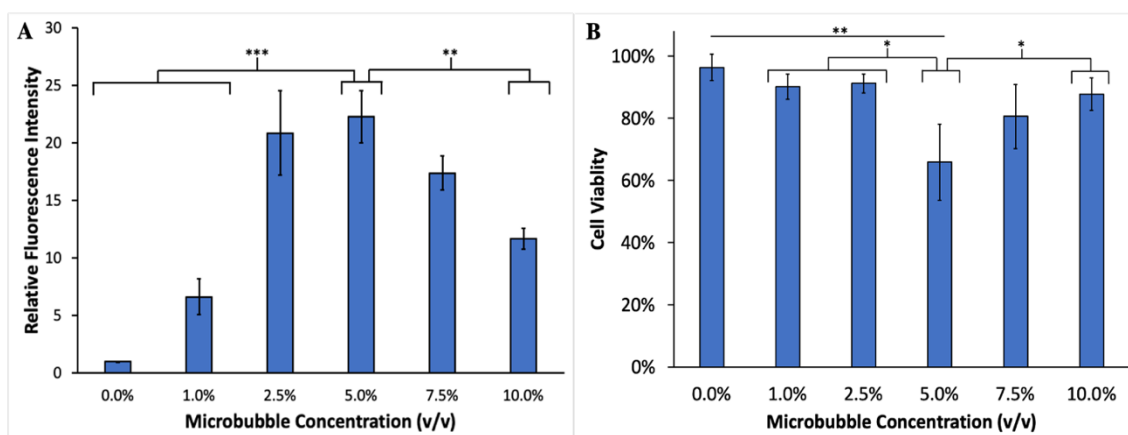


Figure 19: Intracellular delivery of 10 kDa FITC-dextran at various cationic microbubble concentrations, using a concentric spiral acoustofluidic device at 5.1 MPa peak negative ultrasound output pressure. (A) Acoustofluidic treatment with 10 $\mu\text{g/mL}$ (1 mM) of 10 kDa FITC-Dextran increased intracellular delivery to Jurkat T cells at a microbubble concentration of 5% (v/v) compared to lower microbubble concentrations (0-1% v/v, ANOVA $p < 0.001$, $n = 6-9/\text{group}$) and higher microbubble concentrations (10% v/v, $p < 0.01$). (B) Acoustofluidic treatment with a cationic microbubble concentration of 5% (v/v) had reduced cell viability compared to the 0% (v/v) microbubble concentration control group (ANOVA $p < 0.001$, $n = 6-9/\text{group}$), 1-2.5% (v/v) microbubble concentrations ($p < 0.05$), and 10% (v/v) microbubble concentration ($p < 0.05$).

IV.3.6. sfGFP loading in acoustofluidic device

A proteinaceous molecule, sfGFP (26 kDa), was utilized to assess acoustofluidic delivery efficiency at an ultrasound output pressure of 5.1 MPa and a microbubble concentration of 5% (v/v) in the concentric spiral acoustofluidic device. At an extracellular sgGFP concentration of 52 $\mu\text{g/mL}$ (2 μM), a statistically significant increase in intracellular fluorescence was observed compared to the flow only control group without ultrasound treatment (1.86 ± 0.81 -fold, Figure 20A, Student's t-test $p < 0.05$, $n = 6/\text{group}$). Cell viability was reduced after acoustofluidic

treatment compared to the flow only control group without ultrasound treatment (Figure 20B, Student's t-test $p < 0.001$, $n = 6/\text{group}$), but viability remained above 90% in both groups.

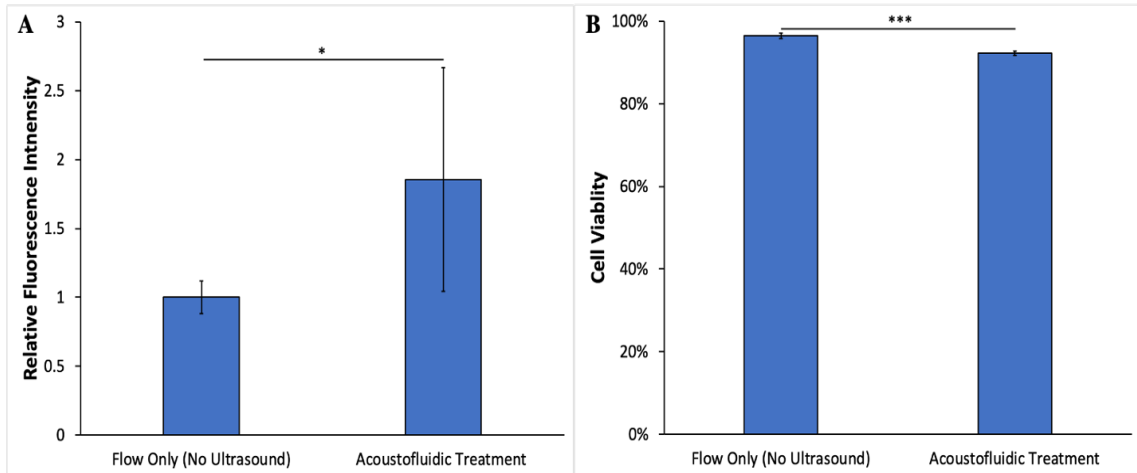


Figure 20: Intracellular delivery of green fluorescent protein (GFP) using the concentric spiral acoustofluidic device at 5.1 MPa peak negative ultrasound output pressure and a cationic microbubble concentration of 5% (v/v). (A) Molecular delivery with 2 μM of 26 kDa sfGFP was increased after acoustofluidic treatment compared to flow only without ultrasound (negative control; Student's T-test $p < 0.05$, $n = 6/\text{group}$). (B) Cell viability was reduced after acoustofluidic treatment compared to flow only without ultrasound (Student's T-test $p < 0.001$, $n = 6/\text{group}$), but viability remained above 90% in each group.

IV.4. Discussion

Acoustofluidics is a rapidly developing field with a wide range of applications (Bruus *et al.*, 2011; Gedge and Hill, 2012b; Lenshof *et al.*, 2012; Carugo *et al.*, 2017; Wu *et al.*, 2017; Belling *et al.*, 2020a). In this study, 3D-printed acoustofluidic devices were designed and evaluated to enhance molecular delivery to human T cells via microbubble-mediated mechanisms. Although single-element transducers with high duty cycle are often used for acoustofluidic applications, in this study we utilized a clinical ultrasound probe to transmit B-mode pulses into the

acoustofluidic channels similar to our previous studies (Centner *et al.*, 2020). The use of gas-filled microbubbles as ultrasound contrast agents reduces the amount of ultrasound energy necessary for molecular delivery compared to approaches without contrast agents. By adding microbubbles to cell solutions that pass through the 3D-printed acoustofluidic device, ultrasound-mediated biomolecular delivery to cells can be achieved rapidly as a single device can process volumes of at least 90 mL/hr.

The results of this study demonstrate for the first time that the microbubble phospholipid surface charge and the molecular exposure time point both have important implications on biomolecular delivery to human T cells in acoustofluidic devices. The experimental findings in this study demonstrate several key parameters in the 3D-printed acoustofluidic devices that have significant effects on intracellular biomolecular delivery. Although this study focused on delivery of a small fluorescent molecule (calcein) for detection via flow cytometry, it is likely that optimization of the important parameters identified in this study will also enable enhanced delivery of many other biomolecules to cells using acoustofluidic devices, including proteins and nucleic acid molecules. Therefore, these findings provide new insights into the development of potential acoustofluidic techniques for manufacturing of cell-based therapies.

In this study, there was a statistically significant difference in molecular delivery based on the surface charge of the microbubble phospholipid coating (Figure 14a), with the highest level of calcein delivery detected when cationic microbubbles were used with ultrasound treatment (3.8 MPa peak negative

pressure output, $p < 0.001$ compared to control group without ultrasound treatment). It was previously determined that microbubble phospholipid surface charge could enhance ultrasound-mediated molecular delivery to HEK 293 cells (Tlaxca *et al.*, 2010). However, there were distinct differences in the previous study by Tlaxca, *et al.*, including utilization of biotinylated-PEG substrate to conjugate the molecules, assessment using anchorage-dependent cells (unlike anchorage-independent Jurkat T cells), and the use of a static ultrasound configuration. These differences may account for the lack of differences in molecular delivery between cationic and neutral lipid-coated microbubbles when treated with ultrasound in other cell lines using the same ultrasound conditions (Tlaxca *et al.*, 2010). It is likely that the positive surface charge on cationic microbubbles increases interactions with negatively-charged components of the T cell surface, such as the glycocalyx, via non-covalent charge-charge interactions (Springer, 1990). These interactions would reduce the distance between the microbubbles and cells, which may play a role in enhancing molecular delivery during ultrasound-driven microbubble activity, possibly through sonoporation mechanisms. However, variance in glycocalyx expression levels can influence microbubble-cell interaction. It is possible that low glycocalyx levels could significantly reduce molecular loading with cationic microbubbles. Microbubbles with a neutral surface charge are also responsive to ultrasound waves as indicated by the acoustic attenuation measurements, however the amount of molecular delivery was significantly reduced when neutral microbubbles were used at equivalent ultrasound conditions compared to cationic microbubbles. This suggests that the neutral microbubbles were cavitating at a

further distance from the cells and therefore had minimal effect on intracellular molecular delivery.

The effects of molecular exposure time point before and after acoustofluidic treatment was a critical factor in calcein delivery, with maximum delivery detected when calcein was added prior to acoustofluidic treatment. Intracellular calcein delivery was also enhanced, albeit to a lesser degree, when calcein was added at various timepoints after acoustofluidic treatment. One potential mechanism to explain this finding is an extended duration of membrane pore opening prior to resealing, but this appears to be unlikely given that pores typically reseal within less than 15 minutes after ultrasound treatment (Zhou *et al.*, 2008; Helfield *et al.*, 2016c). A more likely explanation is the possibility that endocytosis activity may have increased after acoustofluidic treatment due to mechanical stress on cell membranes induced by ultrasound-driven microbubble activity (Juffermans *et al.*, 2009). Although enhanced endocytosis activity may play some role, this does not appear to be the primary mode of intracellular delivery within the 3D-printed acoustofluidic channels given that much higher levels of molecular delivery were detected when calcein was added prior to acoustofluidic treatment.

This study also revealed that channel geometry is another key factor that influences acoustofluidic-enhanced molecular delivery, but this parameter had limited influence on cell viability. Acoustofluidic treatment with a concentric spiral channel geometry caused significantly higher levels of intracellular calcein delivery compared to acoustofluidic treatment with rectilinear channel geometries. The residence time of cells within the ultrasound beam is significantly increased in the

concentric spiral channel geometry compared to rectilinear channel geometries, with a total channel length within the ultrasound beam of 57.7 mm for the concentric spiral geometry compared to 10 mm for each rectilinear geometry tested in this study. Residence time does not appear to have important implications on cell viability with the experimental parameters used in this study when comparing three different acoustofluidic device designs. Although residence time is likely a factor in acoustofluidic-enhanced molecular delivery, but it does not appear to solely explain the differences in results between each channel geometry. Acoustofluidic treatment in rectilinear channels enhanced intracellular fluorescence by approximately three-fold compared to control groups without ultrasound treatment. However, there was no statistically significant difference in acoustofluidic-mediated molecular delivery between the two rectilinear channel geometries that were tested in this study, despite the fact that the average fluid velocity would have been four times faster in the 1-mm channel compared to the 2-mm channel. If residence time was the only factor, one would expect that the 2-mm rectilinear channel would have higher molecular delivery compared to the 1-mm rectilinear channel, due to the four-fold increase in residence time for cells within the ultrasound beam, but this was not observed. Therefore, other differences in fluid dynamics between channel geometries may also be a key factor. Indeed, computational analysis of wall shear stress for each channel geometry revealed that the concentric spiral had significantly higher average wall shear stress compared to the rectilinear channels, even when the channel diameters were identical. The centrifugal force in spiral geometries creates accelerated velocity

near the outer wall, resulting in a sharper velocity gradient and, hence, higher wall shear stress. These results suggest that the curvature of the acoustofluidic channel may also be a key factor in molecular delivery efficiency.

Additionally, the effect of ultrasound pressure amplitude was also found to play a key role on enhancing intracellular molecular delivery. As shown in Figure 18, higher ultrasound pressures (2.4-5.1 MPa peak negative ultrasound pressure output) showed enhanced delivery of calcein compared to lower ultrasound pressures (0-1.4 MPa peak negative ultrasound pressure output). This indicates that molecular delivery is significantly enhanced above a specific ultrasound pressure threshold. Fundamental acoustic parameters that influence molecular delivery in anchorage independent cells have yet to be fully characterized, as multiple modalities could influence molecular delivery, including thermal and mechanical bioeffects. Thermal bioeffects have been observed with ultrasound-based platforms (Haar and Coussios, 2007; Bruning *et al.*, 2019); however, thermal effects were reduced in this acoustofluidic system by utilization of short B-mode pulses (2 μ s) with a low duty cycle (below 1%) and short residence time (~2-3 s in concentric spiral), which is more likely to be conducive to mechanical bioeffects over thermal bioeffects (Haar and Coussios, 2007). Mechanical bioeffects, specifically acoustic radiation force, could influence cell-microbubble interaction by displacing cells and particles to certain regions of the acoustofluidic device (Bruus *et al.*, 2011; Bruus, 2012). Previous studies have shown the capacity for low pressure, pulsed ultrasound to facilitate displacement of ultrasound contrast agents toward vessel walls (Dayton *et al.*, 1999a; Dayton *et al.*, 1999b; Zhao *et*

al., 2004). This could help facilitate molecular delivery to cells via cell-microbubble interactions and migrating towards vessel walls where shear stress is higher. Shear stress has been shown to facilitate molecular delivery in acoustofluidic systems (Belling *et al.*, 2020a). However, the effect of shear stress on molecular delivery with higher acoustic pressures and microbubbles is not fully understood and requires further investigation. Furthermore, our study utilized short ultrasound pulses (duty cycle less than 1%) which may reduce acoustic radiation force effects within the acoustofluidic channel compared to high duty cycles. Prior studies in static chambers have demonstrated that stable or inertial cavitation activity can enhance molecular delivery via sonoporation or other mechanisms (Paula *et al.*, 2011; Fan *et al.*, 2014b; Delalande *et al.*, 2015; Helfield *et al.*, 2016c). Although microbubble cavitation activity was not directly measured in this study, there was a significant decrease in acoustic attenuation after acoustofluidic treatment which indicates microbubbles were destroyed during ultrasound exposure at higher pressures, as would be expected with higher levels of cavitation activity. Additionally, increased ultrasound pressures have been shown to play a critical role in molecular delivery via stable cavitation and inertial cavitation effects (Wu and Nyborg, 2008). For molecular delivery applications to T cells, inertial cavitation may be required for sufficient delivery, which requires higher acoustic pressures. Although the specific mechanisms of action have not been fully elucidated, this study provides evidence that ultrasound-driven microbubble activity has a key role in acoustofluidic-enhanced molecular delivery to cells.

Additionally, microbubble concentration influenced molecular delivery and cell viability. A weak relationship was observed between microbubble concentration and molecular delivery ($R^2=0.19$), even with a significant (5.1 MPa) peak negative ultrasound output pressure. Interestingly, the highest microbubble concentration (10% v/v) was associated with reduced molecular delivery while maintaining higher cell viability. It is typically presumed that an increased microbubble concentration corresponds to increased molecular delivery while potentially inducing more cytotoxic effects. In this circumstance, it is feasible that a high microbubble concentration ($\geq 10\%$ v/v) could induce high levels of ultrasound multiple scattering within the acoustofluidic channels and reduce the acoustic pressure *in situ*. A similar trend has also been reported in a previous acoustofluidic study, albeit with a different cell type (erythrocytes), a different device design (polydimethylsiloxane), and different acoustic parameters with a lower peak negative output pressure (Centner *et al.*, 2020). In this study, the ultrasound frequency was aligned with the microbubble resonance frequency in an attempt to induce sufficient microbubble oscillation for microbubble destruction and intracellular molecular delivery (Doinikov *et al.*, 2009). However, at high microbubble concentrations there may be significant scattering of ultrasound waves which reduces acoustic pressures within most of the acoustofluidic channel and causes less oscillation. This may be particularly critical with short ultrasound pulses in an acoustofluidic device where the microbubbles and cells are typically exposed to ultrasound waves for only ~2-3 seconds.

This study explored ultrasound-enhanced delivery of a small molecule (*i.e.*, calcein) and large molecules (*i.e.*, 10 kDa FITC-Dextran and 26 kDa sfGFP) to human T cells in acoustofluidic channels to assess feasibility for potential cell-based therapy applications, such as CAR-T. The selected molecules are highly fluorescent and do not readily cross cell membranes, thus they are useful for assessing intracellular molecular delivery via flow cytometry. In our study, we demonstrated that the delivery efficiency of larger biomolecules (molecular weight ≥ 10 kDa) could be achieved with an acoustofluidic device, which is necessary for proteinaceous or nucleic acid intracellular delivery. With 1 mM of 10 kDa FITC-Dextran in solution, over a 20-fold increase in intracellular fluorescence was observed at microbubble concentrations between 2.5%-5% (v/v), compared to the flow only control group without ultrasound treatment. Intracellular fluorescence after acoustofluidic treatment with sfGFP was only 1.86 ± 0.81 -fold higher than the flow only control group, but this lower amount of sfGFP delivery compared to FITC-dextran delivery is not surprising given the 500x difference in extracellular molarity between sfGFP (2 μ M) and 10 kDa FITC-Dextran (1 mM) in this study. The extracellular fluorophore concentration could play a significant role in delivery efficiency as we have previously described (Bhutto *et al.*, 2018). Even though significant molecular loading was achieved with 10 kDa FITC-Dextran, it is likely lower compared to small molecules such as calcein (molecular weight of 0.6 kDa), but may still be sufficient to provide the functional effects that are needed for therapeutic efficacy (Bhutto *et al.*, 2018). Further studies are required to determine required cell transfection efficiency for therapeutic applications with an

acoustofluidic device. A multitude of factors likely will influence efficiency of molecular delivery, including cell type, donor source, required cell dose, and cell viability. In addition, multiple doses may also increase molecular delivery to T cells. These factors will likely allow optimization of the acoustofluidic platform to enable manipulation of cells via CRISPR-cas9 gene editing or other techniques that are often used for cell therapy manufacturing applications.

IV.5. Conclusion

The results of this study demonstrate the feasibility of utilizing a 3D-printed acoustofluidic device to rapidly load biomolecular compounds into human Jurkat T cells. Additionally, this study identifies several key acoustic and fluidic parameters that significantly influence the efficiency of intracellular delivery, including microbubble surface charge, microbubble concentration, the time point when the molecular compound is added to solution relative to the acoustofluidic treatment time point, flow channel geometries, and ultrasound pressure. These results provide new insights into techniques to optimize acoustofluidic delivery of biomolecules to human T cells. Further development and validation of acoustofluidic platforms may enable utilization of this technique to improve manufacturing of cell-based therapies, such as CAR-T immunotherapies for treatment of cancer and other diseases.

CHAPTER V – COMPARISON OF
ACOUSTOFLUIDIC AND STATIC SYSTEMS
FOR ULTRASOUND-MEDIATED MOLECULAR
DELIVERY TO T LYMPHOCYTES

V.1. Introduction

Cell-based therapies have the capacity to significantly improve treatment regimens for many diseases, including cancer, autoimmune diseases, infectious diseases, and metabolic diseases (Deeks *et al.*, 2002; Brentjens *et al.*, 2007; Buzhor *et al.*, 2014; Schuster *et al.*, 2017; Annesley *et al.*, 2018a; Ying *et al.*, 2019). Recent developments in adoptive cell therapies, specifically chimeric antigen receptor (CAR) T cells, have significantly improved patient outcomes in B-cell malignancies, such as leukemia or lymphoma (Annesley *et al.*, 2018a). In fact, complete remission rates have been observed in up to 80-90% of B-cell acute lymphoblastic leukemia patients after treatment in clinical trials (Davila *et al.*, 2014; Turtle *et al.*, 2016; Gardner *et al.*, 2017). Although similar efficacy has yet to be observed with CAR T treatment for other diseases, there is significant potential to develop improved CAR T and other cell-based therapies which can enhance targeted cytotoxic activity while reducing off-target effects (Choe *et al.*, 2021). This approach offers a distinct advantage over traditional cancer treatment regimens, such as chemotherapy and radiation, by engineering a patient's own immune cells to directly attack cancer cells. However, limitations with current processing techniques and technologies for CAR T manufacturing have prevented widespread adoption of this biotechnology therapy, such as genotoxicity due to viral vectors (Stoiber *et al.*, 2019).

For *ex vivo* modification of T lymphocytes, viral vector technology is primarily being utilized. Viral vectors have been shown to have high efficacy in delivery of nucleic acids to T lymphocytes; however, these results are not reproducible in all

cell types since intrinsic properties of certain cells make it difficult to consistently deliver nucleic acids intracellularly. For example, innate immune cells, such as dendritic cells and macrophages, have evolved to rapidly recognize microbes (*e.g.*, viruses) through pattern recognition receptors, which are able to recognize common components observed in invading microbes (Kawai and Akira, 2010). This subsequently triggers downstream pathways to destroy the detected microbes. Limitations with viral vector techniques may include potential insertional mutagenesis, undesired multiplicity of infection, and limited non-nucleic acid delivery, such as therapeutic proteins for example. Non-viral transfection approaches have focused on passive loading of human T lymphocytes via physical techniques such as electroporation or shear stress-mediated membrane permeabilization (Sugar and Neumann, 1984a; Hashimoto and Takemoto, 2015a; DiTommaso *et al.*, 2018). Static electroporation techniques have generated significant interest as this method utilizes an applied voltage to induce transient perforation in the plasma membrane and temporally improve intracellular uptake (Sugar and Neumann, 1984a). However, current electroporation methods have several limitations, including challenges with scale-up for manufacturing processes and generally lower delivery efficacy compared to viral vectors (Nayerossadat *et al.*, 2012b). For example, one recent study demonstrated more than 95% transduction in HeLa cells using viral delivery (Prel *et al.*, 2015), while another study reported a transfection efficiency of 66% with electroporation (Chicaybam *et al.*, 2016). Recently, a microfluidic squeezing platform has been developed that induces transient perforations in the plasma membrane by taking advantage of the

compression forces and the shear stress induced as cells pass through a very narrow constricted channel at a high velocity (Sharei *et al.*, 2013; DiTommaso *et al.*, 2018). The formation of transient perforations enables biomolecules to diffuse from the extracellular buffer into the cytosol (Sharei *et al.*, 2013). However, a fundamental limitation of this technology is the potential for cell debris to cause blockage of the narrow microfluidic channels and prevent consistent processing (Dressaire and Sauret, 2016).

To address these limitations, ultrasound technology has demonstrated the ability to rapidly deliver biomolecules intracellularly using ultrasound contrast agents (i.e., microbubbles) to induce a mechanism known as “sonoporation” (Bhutto *et al.*, 2018; Centner *et al.*, 2020). Sonoporation occurs when ultrasound-induced microbubble cavitation occurs near cell membranes. This phenomenon induces transient perforation of the plasma membrane, which allows intracellular transport of macromolecules that may otherwise be impermeant due to macromolecular properties such as size, charge, and polarity. The pores in the cell membrane typically repair quickly via active repair mechanisms influenced by factors such as pore size and Ca^{2+} concentration (Zhou *et al.*, 2008; Hu *et al.*, 2013b). This approach can potentially enable rapid loading of biomolecules into cells with higher efficacy and viability compared to other physical delivery methods. Microbubbles are currently FDA-approved for clinical applications involving cardiac imaging, and they are also in development for gene therapy and biomolecular delivery applications, including antigenic protein delivery or transfection of immune cells such as Dendritic Cells and T lymphocytes (Dewitte *et al.*, 2014; Centner *et*

al., 2021b). The efficiency of intracellular delivery is a fundamental parameter for effective *ex vivo* modifications of cells. The coupling of ultrasound and microbubbles potentially offers a solution to address the intracellular delivery limitations of other physical systems. Static ultrasound delivery systems are often utilized for ultrasound-based molecular delivery systems, which involve single-element transducers or transducer arrays placed in a medium, such as water or cell culture media, with cells suspended or adhered in a static sample chamber, such as a well plate, petri dish, or test tube. However, the volume of these static systems is generally limited due to heterogeneous ultrasound pressures outside of the ultrasound focus, and throughput is a significant limitation for potential large-scale processing of cell-based therapies. Previously, 500- μ L solutions with 1 minute of ultrasound exposure were utilized for molecular delivery applications (Janis *et al.*, 2021), which enables a maximum processing rate of 30 mL/hr.

Acoustofluidic technologies (*i.e.*, coupling of ultrasound and fluidic channels) represent a potential solution to these challenges. Previous studies have demonstrated that acoustofluidics can rapidly enhance intracellular delivery of molecular compounds (Belling *et al.*, 2020a; Centner *et al.*, 2020). Some studies have investigated contrast agent-free acoustofluidic methods for molecular delivery applications (Carugo *et al.*, 2011; Longsine-Parker *et al.*, 2013; Belling *et al.*, 2020a). Initial studies, however, had limited processing rates (0.1 mL/min) or required coupling of electroporation to induce sufficient transient perforation (Carugo *et al.*, 2011; Longsine-Parker *et al.*, 2013). Recently, contrast agent-free acoustofluidic methods have also induced molecular delivery by utilizing acoustic

radiation force to push cells toward the capillary wall coated with a tethered DNA molecule (Belling *et al.*, 2020a). Tethering molecules to the capillary wall may not be feasible for some types of biomolecules and the tethering process may not be compatible with typical aseptic processing methods used for cell therapy manufacturing. We have previously developed acoustofluidic systems that utilize exogenous microbubbles to enhance molecular delivery to multiple cell types, including cancer cells, erythrocytes, and T lymphocytes (Centner *et al.*, 2020; Centner *et al.*, 2021b; Janis *et al.*, 2021). This approach has the capacity to process cell solutions with continuous flow rates above 100 mL/hr, which significantly increases throughput compared to static systems (Centner *et al.*, 2020; Janis *et al.*, 2021). Although acoustofluidics technology has the potential to address limitations of static ultrasound systems for cell processing, the delivery efficiency of each system has not been directly compared.

The objective of this study was to optimize and compare the molecular delivery efficiency using a static ultrasound system and an acoustofluidic system, by modulating microbubble concentration, ultrasound output pressure, and ultrasound exposure duration. Although the concept of sonoporation and ultrasound-mediated molecular delivery are well established, ultrasound-mediated molecular delivery with acoustofluidic systems is not well characterized. In this study, we initially assessed the effect of several key parameters on intracellular delivery efficiency of a fluorescent compound (calcein) in human T lymphocytes. After optimizing key parameters for the static ultrasound system and the acoustofluidic system, we also compared the intracellular delivery efficiency of

molecular compounds with different size (0.6 kDa calcein and 150 kDa fluorescein isothiocyanate (FITC)-dextran) after treatment in each system. The molecular weight of 150 kDa FITC-dextran is similar to or larger than many proteins (Billett, 1990), including clustered regulatory interspaced palindromic repeats (CRISPR) enzymes which can be used for gene editing in CAR T therapy. These results aim to provide new insights into the optimal system and conditions for ultrasound-enhanced molecular delivery of anchorage-independent cells such as T lymphocytes.

V.2. Methods

V.2.1. Molecular Delivery to Human T Lymphocytes

Jurkat T lymphocytes were cultured in RPMI-1640 medium (Cytiva Life Sciences, Marlborough, MA, USA) supplemented with 10% fetal bovine serum (FBS) and 1% penicillin/streptomycin at 37 °C and 5% CO₂ in a flat-bottom tissue culture flask. Jurkat T lymphocytes were harvested when 70-90% confluent and

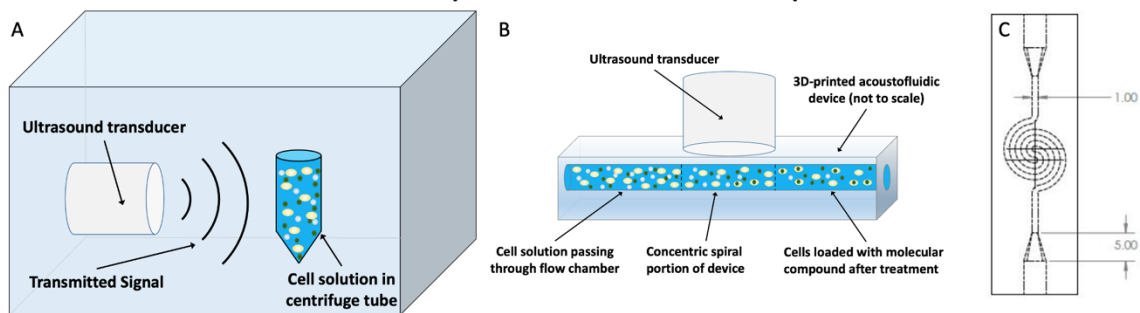


Figure 21: (A) Static configuration with an ultrasound imaging probe transmitting pulsed ultrasound signal to induce microbubble cavitation in cell solution for enhanced molecular delivery to Jurkat T lymphocytes (not to scale). (B) Acoustofluidic device with an ultrasound imaging probe transmitting pulsed ultrasound signal into fluidic channel so that microbubble cavitation occurs in cell solution for enhanced molecular delivery to Jurkat T lymphocytes (not to scale). (C) Concentric spiral acoustofluidic device design with 1 mm x 1 mm channel geometry (not to scale).

were resuspended in complete RPMI-1640 at a concentration of 100,000 cells/mL after centrifugation at 1500g for 5 minutes at 4 °C. Intracellular delivery of calcein (Sigma-Aldrich, St. Louis, MO, USA) was utilized to determine optimal parameters in each system for microbubble concentrations, ultrasound pressure, and ultrasound exposure duration, after ultrasound treatment with an extracellular calcein concentration of 160 μ M. Microbubble concentrations were tested between 0-94 μ g/mL, peak negative ultrasound output pressures were tested between 0-5.1 MPa, and ultrasound exposure durations up to 60 s were tested. 0 μ g/mL, 5 μ g/mL, 9 μ g/mL, 24 μ g/mL, 47 μ g/mL, and 94 μ g/mL microbubble concentration correspond to 0% v/v, 0.5% v/v, 1%, 2.5% v/v, 5% v/v, and 10% v/v microbubble concentration values denoted in other chapters. After optimization of microbubble concentrations, ultrasound pressure, and ultrasound exposure duration for the static system (Figure 21A) and the acoustofluidic system (Figure 21B), a direct comparison of delivery efficiency was assessed by utilizing a small molecule (0.6 kDa calcein) and a large molecule (150 kDa FITC-Dextran; Sigma-Aldrich) at a concentration of 1 μ M.

Following ultrasound treatment, cells were centrifuged and washed three times with phosphate buffer solution (PBS) to remove extracellular fluorescent compounds. Flow cytometry (MACSquant, Miltenyi Biotec, Bergisch Gladbach, Germany) was utilized to measure intracellular molecular delivery by computing the mean fluorescence intensity after gating out non-viable cells as determined by propidium iodide (PI) staining. Based on prior studies, membrane repair typically occurs within less than 5 minutes after sonoporation (Fan *et al.*,

2012; Hu *et al.*, 2013b; Centner *et al.*, 2021a). Therefore, PI was added to samples 30-60 min after ultrasound treatment to ensure sufficient time for membrane repair so that DNA staining was minimized in viable cells. A representative scatter plot is shown in Figure 22 to illustrate the gating procedure after ultrasound treatment. Cells that stained positive for PI were gated out, and the mean fluorescence intensity was computed for all viable cells, which were in the left-hand quadrants (PI-negative). The FITC gate (between upper and lower quadrants) was not used for fluorescence intensity analysis but is shown in the image to illustrate the shift in fluorescence above baseline after ultrasound treatment, indicating intracellular delivery of fluorescent compounds in viable T lymphocytes.

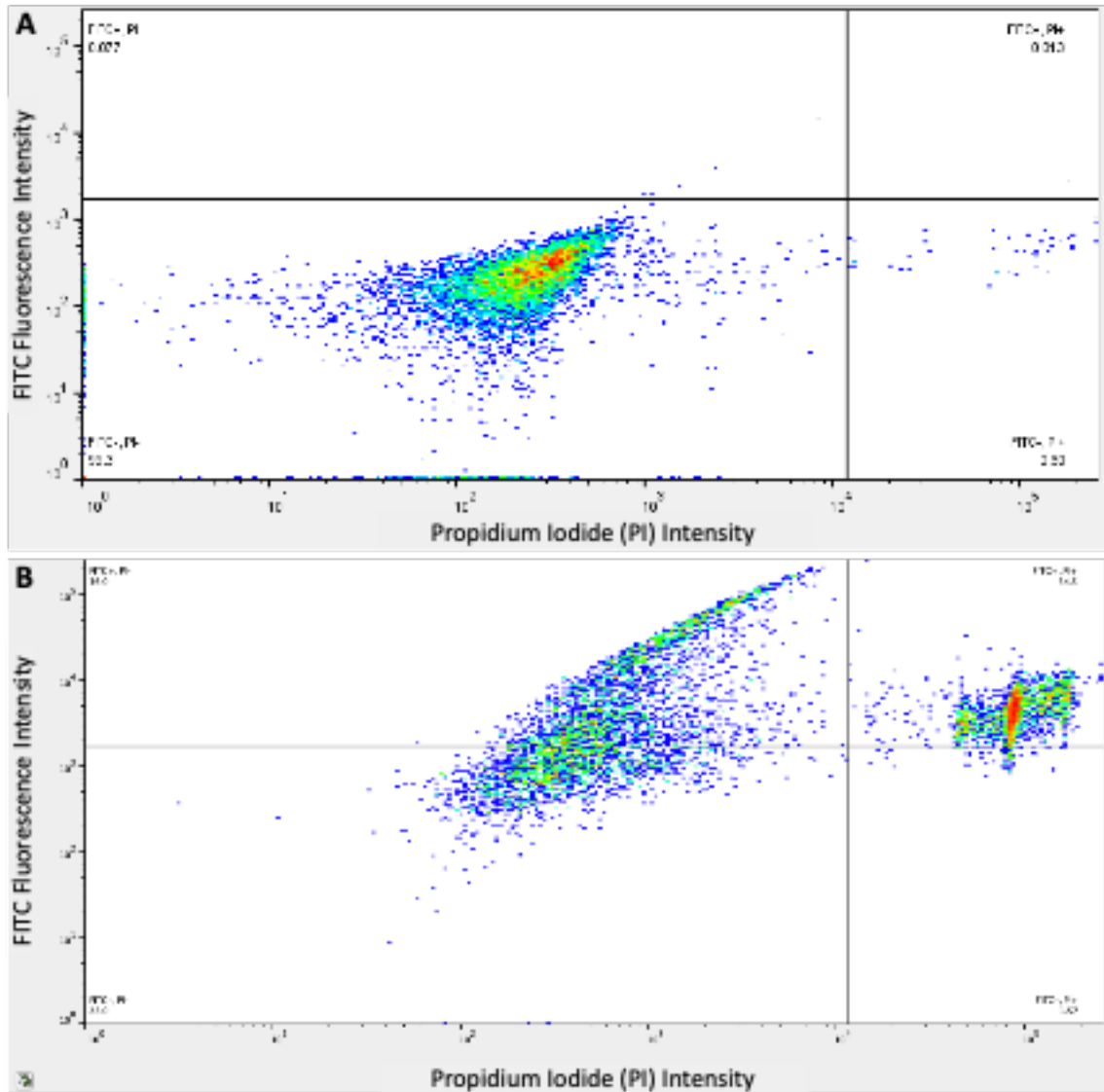


Figure 22: Representative flow cytometry scatter plot of Jurkat T lymphocytes population based on FITC Fluorescence Intensity and Propidium Iodide Fluorescence Intensity. Values in the left-half plane indicate viable cells (PI-) and values in the right-half plane represent non-viable cells (PI+), respectively. (A) Representative flow cytometry scatter plot for a flow only control sample without ultrasound treatment. (B) Representative flow cytometry scatter plot for a sample with acoustofluidic treatment, indicating that FITC fluorescence is significantly increased for both viable (PI-) and non-viable (PI+) cells.

V.2.2. Static Ultrasound Treatment

Static ultrasound treatment was performed in a custom setup as illustrated in Figure 1A, where 'static' refers to the fluid dynamics of the cell solution rather than the dynamic ultrasound wave. This setup was utilized in previous sonoporation studies (Janis *et al.*, 2021) and is based on similar static sonoporation chambers described in the literature (Miller *et al.*, 1999; Kopechek *et al.*, 2015). Jurkat T lymphocytes (100,000 cells in 1 mL of supplemented RPMI medium) were transferred to 15-mL centrifuge tubes with fluorescent compound (calcein or FITC-dextran) and cationic microbubbles one minute prior to ultrasound treatment. The centrifuge tube was placed in a water tank 40 mm away (ultrasound focus) from P4-1 ultrasound transducer (2.5 MHz center frequency, ATL, Bothell, WA, USA) and B-mode pulses were generated by an ultrasound imaging system (Vantage 64LE, Verasonics, Kirkland, WA, USA) with a pulse repetition frequency (PRF) of 3333 Hz and duty cycle below 1%. The free-field ultrasound pressure output was measured using a 0.2-mm needle hydrophone (Precision Acoustics, Dorset, UK) at 40 mm away from P4-1 transducer.

V.2.3. Acoustofluidic Treatment

Acoustofluidic treatment was performed in a flow chamber as illustrated in Figure 1B and Figure 1C. The acoustofluidic flow chamber consisted of a concentric spiral channel geometry designed in SolidWorks (Waltham, MA, USA) and fabricated in Accura 60 plastic using stereolithography 3D printing (Xometry, Gaithersburg, MD, USA) with a cross-sectional channel diameter of 1 mm x 1 mm. The concentric spiral design was used to maximize the exposure duration for cells

within the ultrasound beam. Stainless steel barbed tube fittings (10-32 threads, McMaster-Carr, Elmhurst, IL, USA) were inserted into pre-threaded inlet and outlet ports for connection with PVC tubing (1/16" ID, McMaster-Carr). Cells were pumped through acoustofluidic channels using a peristaltic pump at a flow rate of 1.5 mL/min (Boxer GmbH, Ottobeuren, Germany) leading to approximately 2-3 s of ultrasound exposure. A peristaltic pump was used in this study since these are often utilized for aseptic cell therapy manufacturing processes, but it should be noted that this pump causes pulsatile flow. An ATL P4-1 ultrasound transducer was placed directly on top of the plastic acoustofluidic device with a thin layer of ultrasound gel used for acoustic coupling, and B-mode pulses (2.5 MHz, 12 mm focus, 3333 Hz PRF) were generated by a Verasonics Vantage 64LE ultrasound imaging system. The free-field ultrasound pressure output was measured using a 0.2 mm needle hydrophone (Precision Acoustics) 40 mm away from P4-1 transducer. *In situ* ultrasound pressures within the acoustofluidic channel could not be measured directly. Current approaches to characterize ultrasound fields within acoustofluidic channels typically utilize theoretical simulations of the acoustic field or measurements of motile cells that redistribute spatially based on acoustic pressure patterns within the channels (Barnkob and Bruus, 2009; Kim *et al.*, 2021). In this study, we reported calibrated free-field output pressure measurements as previously described (Centner *et al.*, 2020; Centner *et al.*, 2021a; Janis *et al.*, 2021).

V.2.4. Microbubble Synthesis

Cationic microbubbles were synthesized as previously described to form gas-filled microspheres encapsulated by a phospholipid shell (Kopechek *et al.*, 2019). A microbubble formulation with cationic surface charge was utilized in this study for molecular delivery applications to T lymphocytes, as we previously demonstrated that acoustofluidic treatment with cationic microbubbles significantly enhanced molecular delivery compared to a microbubble formulation with a neutral surface charge (Centner *et al.*, 2021a). Chloroform solutions of 1,2-distearoyl-sn-glycero-3-phosphocholine (DSPC, Avanti Lipids, Alabaster, AL, USA); 1,2-distearoyl-sn-glycero-3-ethylphosphocholine (DSEPC, Avanti Lipids); 1,2-distearoyl-sn-glycero-3-phosphoglycerol (DSPG, Avanti Lipids); and polyethylene glycol-40 stearate (Sigma-Aldrich, St. Louis, MO, USA) at a molar ratio of 100:43:1:4.5 were combined in a 20-mL glass vial and desiccated to remove chloroform. An aqueous micellar lipid solution was prepared by adding PBS and sonicating (Qsonica, Newtown, CT, USA) to resuspend the dry lipid film. The resulting 10 mg/mL phospholipid solution was diluted 1:4 in PBS and sealed in a glass vial. The vial head space was filled with decafluorobutane gas (FlouroMed, Round Rock, TX, USA), followed by amalgamation for 45 s at 4350 cpm (DB-338, COXO, Foshan City, China) to form perfluorobutane gas-filled microbubbles (MBs). This synthesis process yields approximately 2×10^9 microbubbles/mL with a mean diameter of $2 \pm 1 \mu\text{m}$ determined by Coulter counter as previously described (Kopechek *et al.*, 2019). A representative brightfield microscopy image of the microbubble solution is shown in Figure 23.

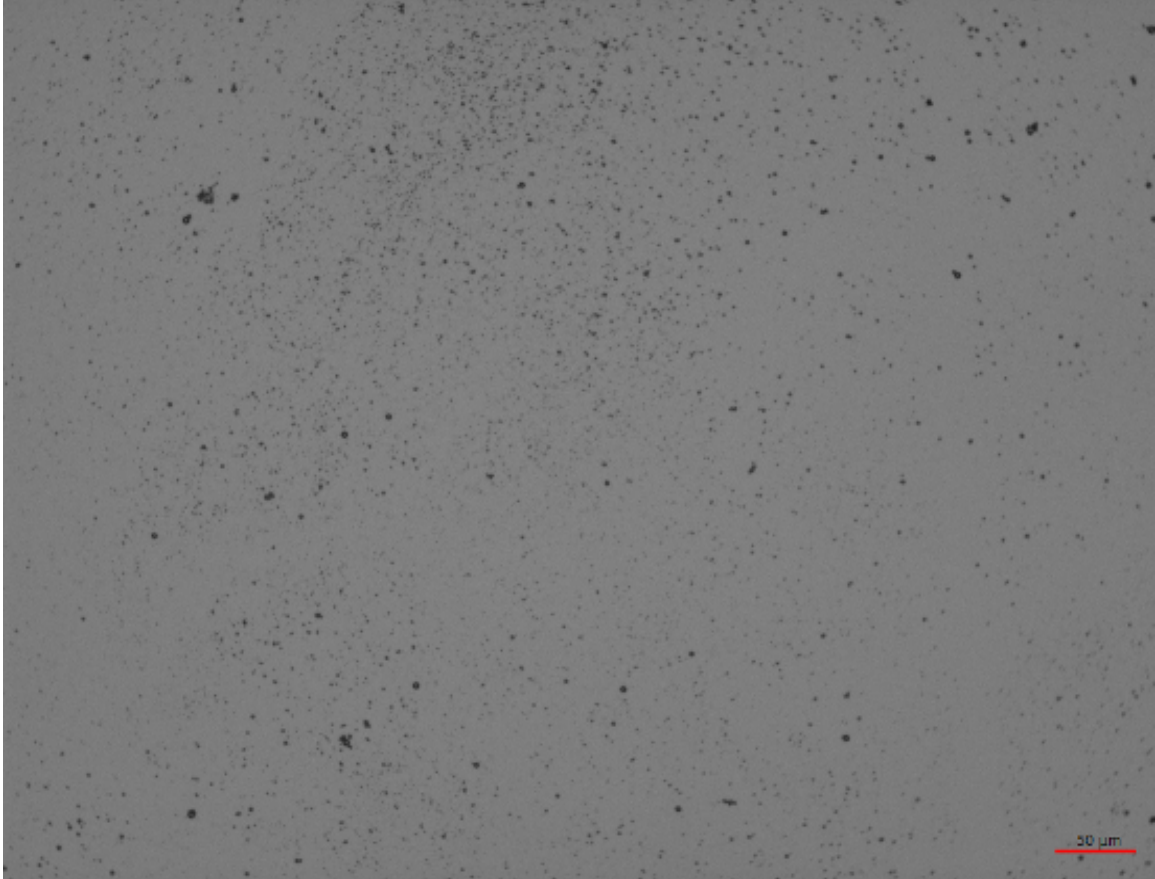


Figure 23: Representative brightfield microscopy image of cationic microbubbles, which can oscillate in response to ultrasound waves and enhance molecular delivery to nearby cells. Scale bar represents 50 μm .

V.2.5. Microbubble Attenuation Measurement

Acoustic attenuation measurements of microbubble solutions, which contained 100,000 T lymphocytes per mL in supplemented RPMI media, were conducted in a separate acoustic chamber to assess the effect of microbubble concentrations, ultrasound treatment pressure, and treatment time duration on microbubble destruction in the static and acoustofluidic configurations. A 3D-printed acoustic chamber was designed in SolidWorks and fabricated using an Ender-3 3D printer (Creality, Shenzhen, China) with a fused filament deposition of 1.75-mm polylactic acid (PLA) filament (McMaster-Carr). Two lead zirconate

titanate (PZT) transducers with a center frequency of 3.3 MHz and a diameter of 25 mm (StemInc, Davenport, FL, USA) were aligned opposite each other at a distance of 31 mm. The transducers were used as a source and receiver, respectively, to measure acoustic attenuation through each microbubble sample. The microbubble solution was added to 4.5-mL disposable polystyrene cuvettes (VWR, Radnor, PA, USA) with a 1-cm acoustic path length, which were placed in the acoustic chamber at the center of the ultrasound beam. Samples that were tested at different microbubble concentrations were diluted at a 1:4 ratio in 3 mL of PBS to prevent saturation of the acoustic attenuation signal. A waveform generator (DG822, Rigol, Suzhou, China) was used to generate a 3.3 MHz pulse with 500 cycle pulses at an interval of 10 ms. Received ultrasound signals were acquired using a digital oscilloscope (DS1202Z-E, Rigol) at a sampling rate of 10 MHz. All signals were transferred to a desktop computer for processing with MATLAB (Mathworks, Natick, MA, USA). The attenuation coefficient was calculated using previously described methods (Kopechek *et al.*, 2011). Attenuation coefficient in decibels per centimeter, $\alpha_{dB/cm}$, was calculated where S_r and S_s are the average power spectrum with and without ultrasound scatter, respectively, and x is the acoustic path distance, measured in cm between the acoustic source and acoustic receiver.

$$\alpha_{dB/cm} = \frac{10 \log_{10} \left(\frac{S_r}{S_s} \right)}{x}. \quad (3)$$

The peak magnitude in the frequency domain was determined at 3.3 MHz for each sample. Without ultrasound scatter references were acquired with Jurkat T solution containing no microbubbles diluted at a 1:4 ratio in 3 mL of PBS.

V.2.6. Statistical Analysis

Statistical analysis was performed using ANOVA with the statistical significance defined as $p < 0.05$ and n represents individual repeats for each experiment. Between group comparisons were applied by using post-hoc analysis with Tukey's test. Statistical analysis was performed using SPSS 26 (Armonk, NY, USA). Bars in figures represent means \pm standard error.

V.3. Results

V.3.1. Effect of Microbubble Concentration on Intracellular Calcein Delivery in Static Ultrasound System

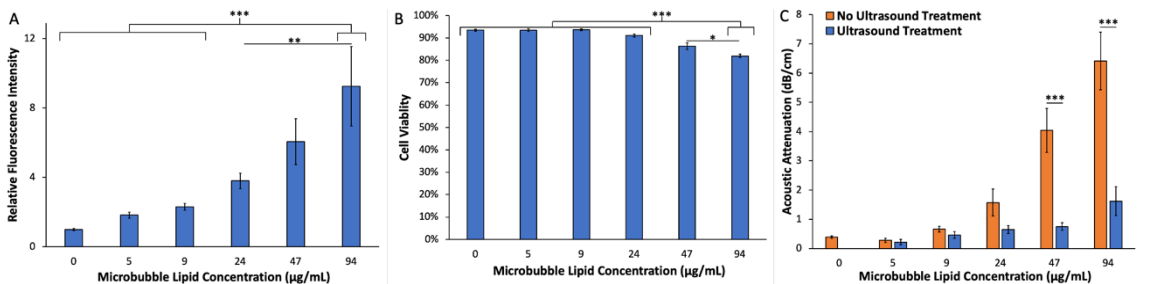


Figure 24: (A) Delivery efficacy of calcein (100 $\mu\text{g/mL}$) with varying microbubble concentrations using static ultrasound treatment (3.8 MPa, 30s). 94 $\mu\text{g/mL}$ microbubble concentration enhanced biomolecular delivery of calcein compared to 0-9 $\mu\text{g/mL}$ microbubble concentrations (ANOVA $p < 0.001$, $n = 7-8/\text{group}$) and 24 $\mu\text{g/mL}$ microbubble concentration ($p < 0.01$). (B) 94 $\mu\text{g/mL}$ microbubble concentration had reduced viability compared to 0-24 $\mu\text{g/mL}$ microbubble concentrations ($p < 0.001$) and 47 $\mu\text{g/mL}$ microbubble concentration ($p < 0.05$), respectively. Cell viability remained above 80% for all treatment groups. (C) Acoustic attenuation was significantly reduced for 47 and 94 $\mu\text{g/mL}$ microbubble concentrations when treated with ultrasound compared to no ultrasound treatment controls, indicating significant microbubble destruction occurred at these concentrations (ANOVA $p < 0.001$, $n = 6/\text{group}$).

Ultrasound-mediated delivery of calcein to Jurkat T lymphocytes at various microbubble concentrations were evaluated using flow cytometry measurements after ultrasound treatment at an output pressure of 3.8 MPa with an ultrasound

exposure time of 30 s. The ultrasound output pressure of 3.8 MPa was previously identified to be the minimum acoustic pressure required for complete microbubble destruction during acoustofluidic treatment (Centner *et al.*, 2021a). Cationic microbubble concentrations between 0-94 $\mu\text{g/mL}$ were tested, and the highest level of molecular delivery occurred after ultrasound treatment at a microbubble concentration of 94 $\mu\text{g/mL}$ (Figure 24A, ANOVA $p < 0.001$, $n = 7-8/\text{group}$). Post-hoc analysis indicated that intracellular fluorescence was significantly higher after ultrasound treatment at 94 $\mu\text{g/mL}$ microbubble concentration compared to 0 $\mu\text{g/mL}$, 5 $\mu\text{g/mL}$, 9 $\mu\text{g/mL}$, or 24 $\mu\text{g/mL}$, respectively ($p < 0.01$). No statistically significant difference in molecular delivery was detected between the 47 $\mu\text{g/mL}$ and 94 $\mu\text{g/mL}$ microbubble concentrations ($p > 0.05$). Measurements of cell membrane integrity using PI staining, as an indicator of cell viability, revealed a general decreasing trend at increasing microbubble concentrations (Figure 24B, ANOVA $p < 0.001$, $n = 7-8/\text{group}$). Cell viability was significantly lower after ultrasound treatment with 94 $\mu\text{g/mL}$ microbubble concentration compared to treatment with 0 $\mu\text{g/mL}$, 5 $\mu\text{g/mL}$, 9 $\mu\text{g/mL}$, 24 $\mu\text{g/mL}$, or 47 $\mu\text{g/mL}$, respectively ($p < 0.05$), although differences in cell viability between treatment conditions were relatively small and viability remained above 80% after treatment at all microbubble concentrations between 0-94 $\mu\text{g/mL}$. Acoustic attenuation of each sample was also measured to assess the effect of ultrasound treatment on microbubble destruction at each microbubble concentration. Compared to acoustic attenuation measurements in negative control samples without ultrasound treatment, no statistically significant differences in microbubble destruction were observed at

microbubble concentrations of 5 $\mu\text{g/mL}$, 9 $\mu\text{g/mL}$, and 24 $\mu\text{g/mL}$, respectively (Figure 24C, ANOVA $p>0.05$, $n=6/\text{group}$), possibly due to low sensitivity of the acoustic attenuation measurements at these microbubble concentrations. However, significant microbubble destruction was detected after ultrasound treatment at microbubble concentrations of 47 $\mu\text{g/mL}$ and 94 $\mu\text{g/mL}$, respectively ($p<0.001$). Intracellular fluorescence intensity levels were highly correlated with levels of microbubble destruction ($R^2 = 0.94$), which suggests that increased microbubble destruction is associated with enhanced intracellular molecular delivery during ultrasound treatment in a static system. Furthermore, cell viability was inversely correlated with microbubble destruction ($R^2 = 0.99$).

V.3.2. Effect of Microbubble Concentration on Intracellular Calcein Delivery in Acoustofluidic Device

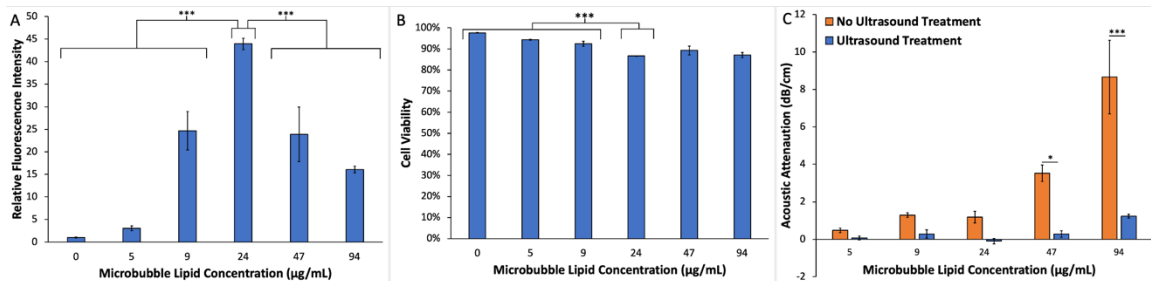


Figure 25: (A) Delivery efficacy of calcein (100 $\mu\text{g/mL}$) with varying microbubble concentrations using acoustofluidic treatment (3.8 MPa). 24 $\mu\text{g/mL}$ microbubble concentration enhanced molecular delivery of calcein compared to all other microbubble concentrations (ANOVA $p<0.001$, $n=5-6/\text{group}$). (B) 24 $\mu\text{g/mL}$ microbubble concentration had decreased viability compared to lower microbubble concentrations (0-9 $\mu\text{g/mL}$). However, cell viability remained above 85% for all treatment groups. (C) Acoustic attenuation was significantly reduced for 47 $\mu\text{g/mL}$ (ANOVA $p<0.05$, $n=6/\text{group}$) and 94 $\mu\text{g/mL}$ ($p<0.001$) microbubble concentrations when treated with ultrasound compared to no ultrasound treatment controls, indicating significant microbubble destruction occurred at these concentrations.

Intracellular delivery of calcein in Jurkat T lymphocytes was evaluated using flow cytometry after acoustofluidic treatment at various microbubble concentrations. Post-hoc analysis indicated that calcein delivery was significantly enhanced after acoustofluidic treatment with 24 $\mu\text{g}/\text{mL}$ microbubble concentration, compared to all other microbubble concentrations tested with the acoustofluidic system (Figure 25A, ANOVA $p < 0.001$, 5-6/group). Cell viability was slightly lower after acoustofluidic treatment at 24 $\mu\text{g}/\text{mL}$ microbubble concentration compared to the negative control group without acoustofluidic treatment or compared to acoustofluidic treatment at microbubble concentrations of 5 $\mu\text{g}/\text{mL}$ or 9 $\mu\text{g}/\text{mL}$, respectively (Figure 25B, ANOVA $p < 0.001$, $n = 5-6/\text{group}$), but cell viability remained above 85% after acoustofluidic treatment at all microbubble concentrations tested between 0-94 $\mu\text{g}/\text{mL}$. Acoustic attenuation was very low after acoustofluidic treatment with microbubble concentrations of 5 $\mu\text{g}/\text{mL}$, 9 $\mu\text{g}/\text{mL}$, and 24 $\mu\text{g}/\text{mL}$, although there were no statistically significant differences (Figure 25C, ANOVA $p > 0.05$, $n = 6/\text{group}$). Significant microbubble destruction was observed after acoustofluidic treatment at 47 $\mu\text{g}/\text{mL}$ and 94 $\mu\text{g}/\text{mL}$ microbubble concentrations, respectively, compared to measurements at microbubble concentrations of 47 $\mu\text{g}/\text{mL}$ and 94 $\mu\text{g}/\text{mL}$ without ultrasound treatment ($p < 0.05$ and $p < 0.001$, respectively). Microbubble destruction was poorly correlated with relative intracellular fluorescence levels ($R^2 = 0.00$), which suggest that increased microbubble destruction is not associated with enhanced molecular delivery based on microbubble concentration in the acoustofluidic system.

V.3.3. Effect of Ultrasound Output Pressure on Molecular Delivery in Static Ultrasound System

Molecular delivery was evaluated with flow cytometry after treatment with a static ultrasound system at various ultrasound pressures for 30 seconds with a microbubble concentration of 94 $\mu\text{g/mL}$. Ultrasound treatment significantly enhanced molecular delivery compared to the negative control group without ultrasound treatment (Figure 26A, ANOVA $p < 0.001$, $n = 9-10/\text{group}$). Post-hoc analysis indicated that there was a statistically significant increase in molecular delivery at a peak negative output pressure of 5.1 MPa compared to no ultrasound (0 MPa) and 2.5 MPa ultrasound pressure output ($p < 0.001$), but no statistically significant differences were detected between ultrasound output pressures of 3.8 MPa and 5.1 MPa ($p > 0.05$). Flow cytometry analysis of PI staining indicated a general trend of decreasing cell viability with increasing ultrasound output pressure. Post-hoc analysis indicated that cell viability after treatment with at an ultrasound output pressure of 5.1 MPa was significantly lower compared to treatment with ultrasound output pressures of 0 MPa (no ultrasound) or 2.5 MPa (Figure 26B, ANOVA $p < 0.001$, $n = 9-10/\text{group}$). Although cell viability was reduced with ultrasound treatment, in all treatment conditions over 65% of cells remained viable. Acoustic attenuation of each sample was measured to assess the effect of ultrasound output pressure on microbubble destruction during treatment in the static system. A significant decrease in acoustic attenuation was observed with ultrasound treatment compared no ultrasound treatment (Figure 26C, ANOVA

$p < 0.001$, $n = 6/\text{group}$). Post-hoc analysis indicated that there was a statistically significant difference in attenuation after treatment at ultrasound output pressures of 3.8 MPa and 5.1 MPa compared to no ultrasound treatment ($p < 0.001$), indicating that higher ultrasound pressures are required for significant levels of microbubble destruction during treatment for 30 seconds with a microbubble concentration of $94 \mu\text{g}/\text{mL}$. No statistically significant differences in microbubble destruction were observed between ultrasound output pressures of 3.8 MPa and 5.1 MPa ($p > 0.05$). Microbubble destruction was highly correlated with relative intracellular fluorescence levels ($R^2 = 0.91$), which suggests that increased microbubble destruction is associated with enhanced intracellular molecular delivery during ultrasound treatment in a static system.

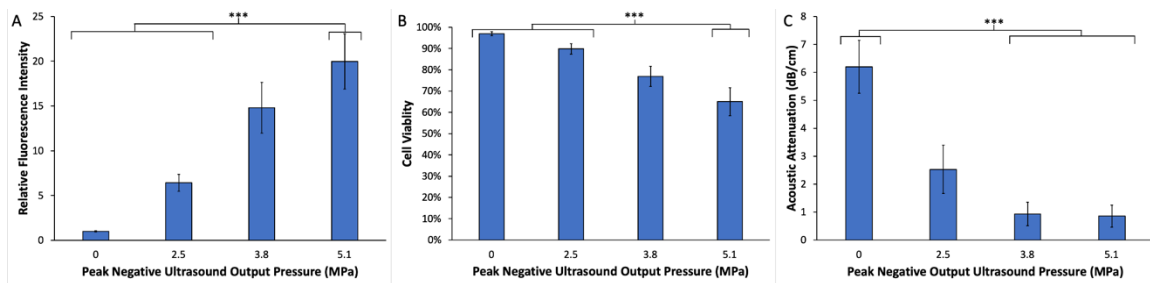


Figure 26: (A) Static ultrasound treatment (30s) with $94 \mu\text{g}/\text{mL}$ microbubble concentration and varying peak negative output pressure. 5.1 MPa peak negative pressure enhanced calcein ($100 \mu\text{g}/\text{mL}$) delivery compared to all other 0 MPa and 2.5 MPa, respectively (ANOVA $p < 0.001$, $n = 9-10/\text{group}$). (B) Cell viability remained above 65% in all samples. Cationic microbubble present with and without ultrasound treatment at different treatment pressure. (C) Acoustic attenuation was significantly reduced in samples treated with ultrasound pressures above 2.5 MPa (ANOVA $p < 0.001$, $n = 6/\text{group}$), indicating microbubble destruction at higher acoustic pressures.

V.3.4. Effect of Ultrasound Output Pressure on Molecular Delivery in Acoustofluidic System

Acoustofluidic-mediated molecular delivery was evaluated with flow cytometry after treatment at various peak negative ultrasound output pressures between 0-5.1 MPa. A significant increase in calcein delivery was detected after ultrasound treatment with the acoustofluidic device, compared to the negative control group without ultrasound treatment (Figure 27A, ANOVA $p < 0.001$, $n = 6-7/\text{group}$). Post-hoc analysis indicated that molecular delivery in the acoustofluidic system was significantly enhanced at ultrasound output pressures of 3.8 MPa and 5.1 MPa compared to 0 MPa (no ultrasound) and 2.5 MPa ($p < 0.001$). Post-hoc analysis also indicated that there was no statistically significant difference in molecular delivery between ultrasound output pressures of 3.8 MPa and 5.1 MPa ($p > 0.05$). Flow cytometry analysis of PI staining indicated that acoustofluidic treatment reduced cell viability compared to the negative control group without ultrasound (Figure 27B, ANOVA $p < 0.001$, $n = 6-7/\text{group}$). Treatment with higher ultrasound output pressures (3.8 MPa and 5.1 MPa) caused a statistically significant decrease in viability compared to no ultrasound treatment (0 MPa) and treatment at lower ultrasound output pressures (2.5 MPa, $p < 0.001$), respectively. However, cell viability remained above 75% viability after acoustofluidic treatment at all treatment conditions (peak negative ultrasound output pressure between 0-5.1 MPa). Acoustic attenuation of each sample was measured to assess the effect of acoustofluidic ultrasound pressures on microbubble destruction. No statistically significant differences in microbubble destruction were observed after treatment at

ultrasound output pressures of 0 MPa (no ultrasound) or 2.5 MPa (Figure 27C, ANOVA $p>0.05$, $n=4-6/\text{group}$), but there was a significant decrease in acoustic attenuation after acoustofluidic treatment at ultrasound output pressures of 3.8 MPa and 5.1 MPa, compared to the control group without ultrasound. Additionally, acoustic attenuation was higher after acoustofluidic treatment at an ultrasound output pressure of 2.5 MPa compared to treatment at ultrasound output pressures of 3.8 MPa ($p<0.05$) and 5.1 MPa ($p<0.01$), indicating higher levels of microbubble destruction at increased ultrasound pressures in the acoustofluidic device. Intracellular fluorescence levels and microbubble destruction were highly correlated ($R^2 = 0.99$), which suggest that increased microbubble destruction is associated with intracellular molecular delivery during acoustofluidic treatment.

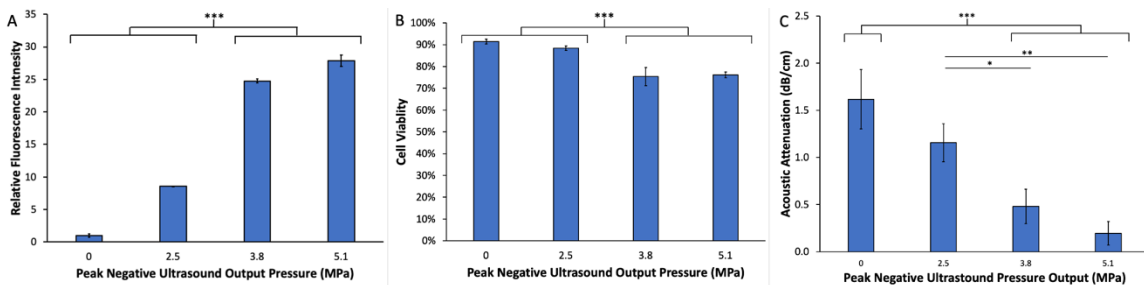


Figure 27: (A) Acoustofluidic device delivery efficacy of calcein (100 $\mu\text{g}/\text{mL}$) with 24 $\mu\text{g}/\text{mL}$ microbubble concentration and varying peak negative output pressures. 3.8 and 5.1 MPa conditions enhanced calcein delivery in Jurkat T lymphocytes compared to 0 MPa (no ultrasound treatment) and 2.5 MPa, respectively (ANOVA $p<0.001$, $n=6-7/\text{group}$). (B) Cell viability was reduced in 3.8 MPa and 5.1 MPa treatment conditions compared to 0 MPa and 2.5 MPa treatment conditions, respectively ($p<0.001$). Cell viability remained above 75% in all samples. (C) Acoustic attenuation was significantly reduced in samples treated with ultrasound pressures above 2.5 MPa compared to flow conditions without ultrasound treatment (ANOVA $p<0.001$, $n=4-6/\text{group}$). Additionally, 3.8 MPa ($p<0.05$) and 5.1 MPa ($p<0.01$) had decreased acoustic attenuation compared to 2.5 MPa, indicating microbubble destruction at higher acoustic pressures.

V.3.5. Effect of Ultrasound Treatment Time on Molecular Delivery in Static System

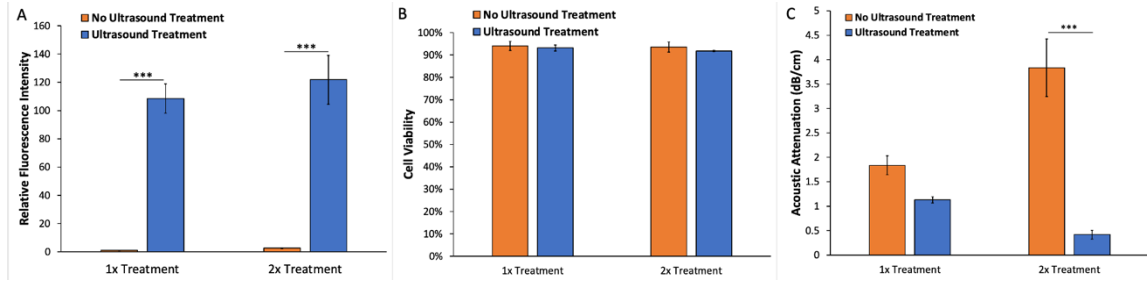


Figure 28: (A) Delivery efficacy of calcein (100 $\mu\text{g}/\text{mL}$) with varying treatment time for acoustofluidic treatment (3.8 MPa, 24 $\mu\text{g}/\text{mL}$ microbubble concentration). 1x acoustofluidic treatment and 2x acoustofluidic treatment enhanced biomolecular delivery of calcein compared to their no ultrasound treatment control, respectively (ANOVA $p < 0.001$, $n = 6/\text{group}$). (B) Cell viability remained above 85% for all treatment groups with no statistical significance detected between groups. (C) Acoustic attenuation was significantly reduced in samples with multiple acoustofluidic treatments compared to multiple flow only control where microbubbles were added prior to each treatment (ANOVA $p < 0.001$, $n = 6/\text{group}$).

The effect of various ultrasound treatment durations between 0-60 s was tested with flow cytometry after treatment in the static system at a microbubble concentration of 94 $\mu\text{g}/\text{mL}$. Ultrasound treatment increased molecular delivery compared to the negative control group without ultrasound treatment (0 s treatment duration; Figure 28A, ANOVA $p < 0.001$, $n = 7-9/\text{group}$). Post-hoc indicated that molecular delivery was significantly higher with a 45 s treatment duration compared to 15 s treatment duration ($p < 0.001$) or 30 s treatment duration ($p < 0.01$), but no statistical difference was detected between 45 s treatment duration and 60 s treatment duration ($p > 0.05$). Flow cytometry analysis of PI staining indicated a general trend that as treatment time increased there was a corresponding decrease in cell viability. Post-hoc analysis revealed a statistically significant

decrease in cell viability after ultrasound treatment compared to the negative control group without ultrasound treatment (Figure 28B, ANOVA $p < 0.01$, $n = 7-9$ /group), but there were no statistically significant differences in cell viability between ultrasound treatment groups, and cell viability remained 75% in all treatment conditions (ultrasound treatment durations between 0 – 60 s). Acoustic attenuation of each sample was measured to assess the effect of ultrasound treatment duration in a static system on intracellular molecular delivery. Post-hoc analysis indicated that acoustic attenuation was significantly decreased in samples with ultrasound treatment durations of 30 s or longer compared to the negative control group without ultrasound treatment (0 s, Figure 28C, ANOVA $p < 0.01$, $n = 6-12$ /group), indicating that microbubble destruction persists for more than 15 s during ultrasound treatment. However, no statistically significant differences in acoustic attenuation were detected between ultrasound treatment durations of 30 s, 45 s, and 60 s ($p > 0.05$). A significant correlation was still observed between microbubble destruction and molecular delivery with an $R^2 = 0.94$, suggesting that increased microbubble destruction is highly correlated with increased molecular delivery.

V.3.6. Effect of Ultrasound Duration on Molecular Delivery in Acoustofluidic System

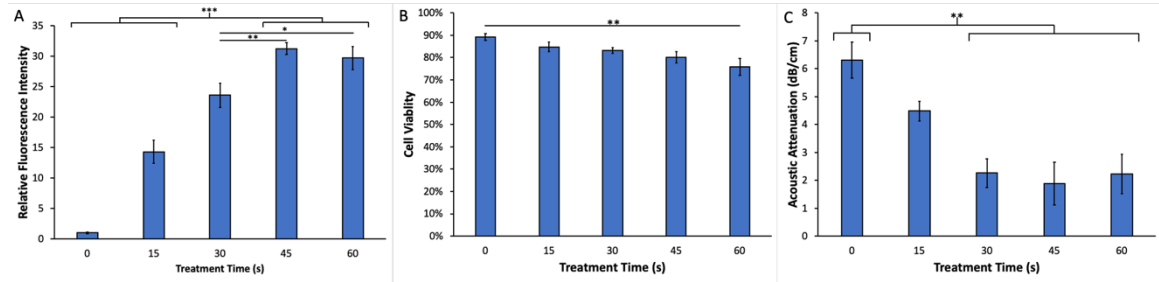


Figure 29: (A) Delivery efficacy of calcein (100 $\mu\text{g}/\text{mL}$) with varying treatment time for static ultrasound treatment (5.1 MPa, 94 $\mu\text{g}/\text{mL}$ microbubble concentration). 45 and 60 seconds of static ultrasound treatment time enhanced biomolecular delivery of calcein compared to no ultrasound treatment (0 seconds) and 15 seconds of static ultrasound treatment time (ANOVA $p < 0.001$, $n = 7-9/\text{group}$). Additionally, 45 second static ultrasound treatment time enhanced calcein delivery compared to 30 seconds of static ultrasound treatment time ($p < 0.01$). Similar results were observed between 45 seconds and 30 seconds of ultrasound treatment time ($p < 0.05$). (B) Cell viability was reduced with 60 seconds of treatment time compared to 0 second treatment time (no ultrasound; $p < 0.01$). Cell viability remained above 70% for all treatment groups. (C) Acoustic attenuation was significantly reduced in samples with 30 seconds or above of ultrasound treatment time compared to 0 seconds (ANOVA $p < 0.01$, $n = 6-12/\text{group}$).

The impact of ultrasound treatment duration on calcein delivery to Jurkat T lymphocytes was investigated with flow cytometry after treatment in the acoustofluidic system. Samples were circulated through the acoustofluidic device one time or two times (1x and 2x ultrasound durations, respectively, with a microbubble concentration of 24 $\mu\text{g}/\text{mL}$ added before each pass through the device) and ultrasound treatment (3.8 MPa ultrasound output pressure) or without ultrasound. Exposure time for the acoustofluidic group is approximately 2-3 seconds per exposure with a flow rate of 100 mL/hr. Molecular delivery was significantly higher after 1x and 2x ultrasound treatment compared to their

respective negative control groups without ultrasound treatment (Figure 29A, ANOVA $p < 0.001$, $n = 6/\text{group}$). Although the ultrasound treatment duration was double in the 2x treatment group, post-hoc analysis indicated that there was no statistically significant difference in calcein delivery between the two ultrasound treatment duration groups, as measured by flow cytometry ($p > 0.05$). Flow cytometry analysis of PI staining indicated that there were no significant differences in cell viability between ultrasound treatment groups and control groups without ultrasound treatment, and cell viability remained above 85% in each group (Figure 29B, ANOVA $p > 0.05$, $n = 6/\text{group}$).

The effect of ultrasound treatment on microbubble destruction was assessed after acoustofluidic treatment. No statistically significant difference in acoustic attenuation was detected between the 1x ultrasound treatment duration and no ultrasound treatment (Figure 29C, ANOVA $p > 0.05$, $n = 6/\text{group}$), but a significant difference in attenuation was measured between the 2x ultrasound treatment duration and no ultrasound treatment ($p < 0.001$).

V.3.7. Comparison of Refined Static and Acoustofluidic Conditions on Intracellular Molecular Delivery

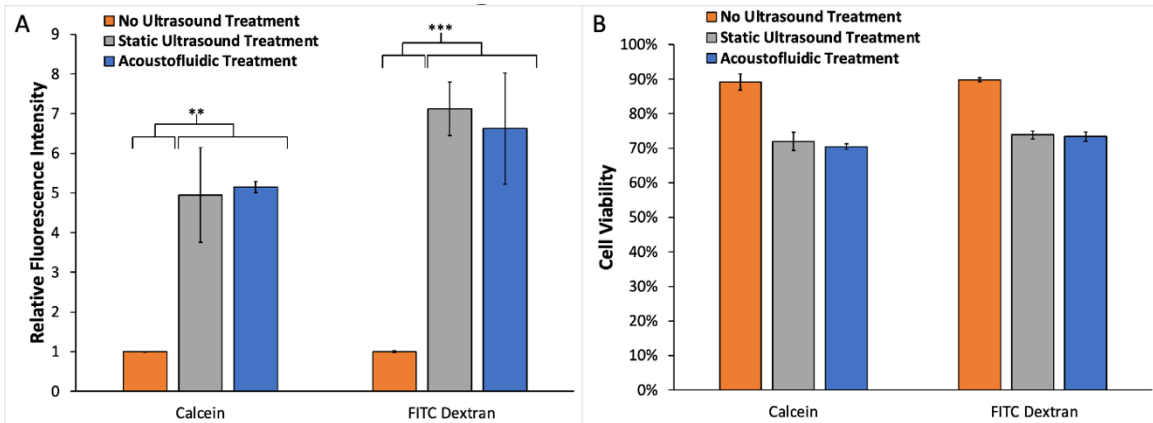


Figure 30: (A) Delivery efficacy using 0.6 $\mu\text{g}/\text{mL}$ (1 mM) of calcein (0.6 kDa) and 150 $\mu\text{g}/\text{mL}$ (1 mM) of 150 kDa FITC-Dextran were assessed with refined static treatment (5.1 MPa, 45 s, and 94 $\mu\text{g}/\text{mL}$ microbubble concentration) and acoustofluidic treatment (5.1 MPa, 24 $\mu\text{g}/\text{mL}$ microbubble concentration) parameters. Static treatment and acoustofluidic treatment enhanced biomolecular delivery of calcein (ANOVA $p < 0.01$, $n = 5-6/\text{group}$) and 150 kDa FITC-Dextran ($p < 0.001$) compared to negative control (no ultrasound treatment), respectively. (B) Static and acoustofluidic treatment had decreased cell viability compared to negative control ($p < 0.001$). No statistically significant differences in cell viability were detected between static and acoustofluidic treatment for calcein and 150 kDa FITC-Dextran treatment groups, respectively ($p > 0.05$).

The efficiency of intracellular molecular delivery in Jurkat T lymphocytes was measured after treatment in the static system and the acoustofluidic system at refined conditions for direct comparison between each configuration. Delivery of a small molecule (calcein; 0.6 kDa) and a large molecule (150 kDa FITC-Dextran) were both measured for comparison. Static ultrasound treatment and acoustofluidic treatment significantly enhanced molecular delivery of calcein (Figure 30A, ANOVA $p < 0.01$, $n = 5-6/\text{group}$) and 150 kDa FITC-Dextran ($p < 0.001$) compared to negative control groups without ultrasound treatment. There was not a statistically difference in intracellular delivery of calcein or 150 kDa FITC-Dextran

between static ultrasound treatment and acoustofluidic treatment ($p>0.05$), indicating that the acoustofluidic system achieved similar molecular delivery results to static ultrasound treatment. Flow cytometry analysis of PI staining indicated that there was a statistically significant decrease in cell viability after treatment with the static ultrasound system (Figure 30B, ANOVA $p<0.001$, $n=5-6$ /group) and acoustofluidic treatment ($p<0.001$) compared to negative control groups without ultrasound. However, no statistically significant differences in cell

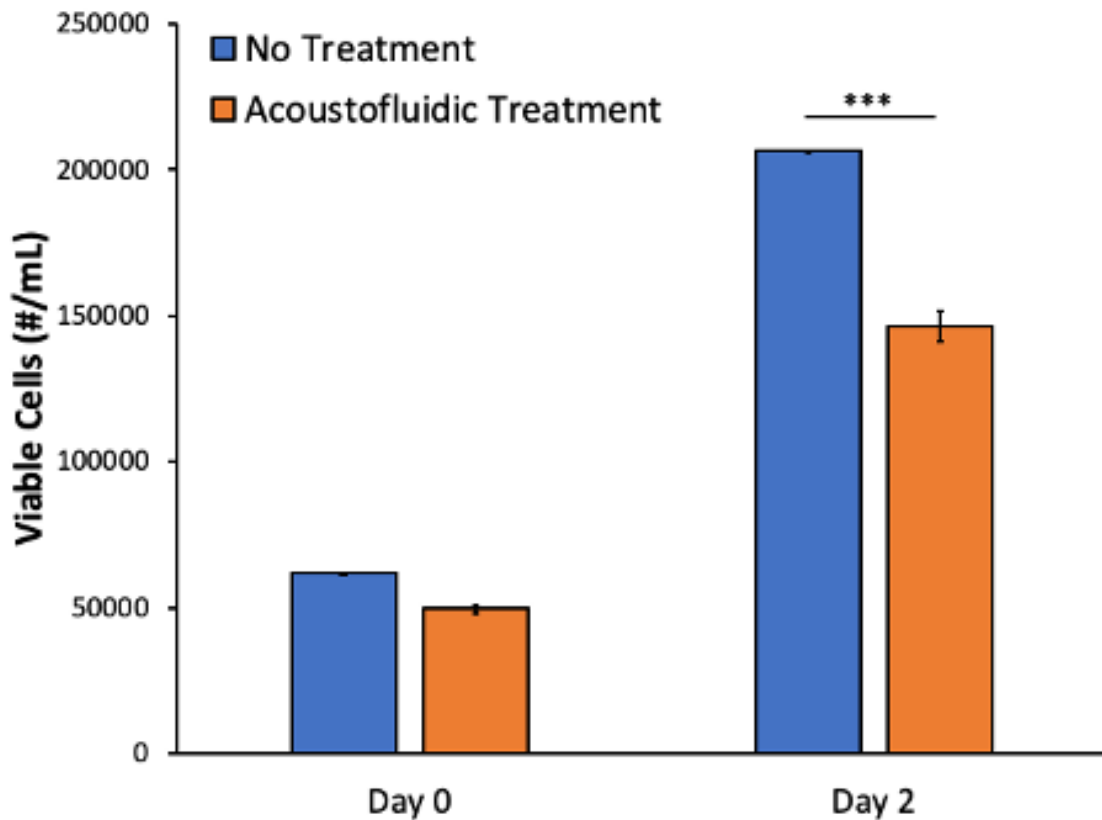


Figure 31: Cell viability and proliferation after acoustofluidic treatment, as measured with trypan blue assay. Immediately after treatment (day 0), the number of viable cells was not statistically different between acoustofluidic treatment and the flow only control group (ANOVA $p>0.05$, $n=5$ /group). At two days after treatment, the number of viable cells was higher in the flow only control group compared to the acoustofluidic treatment group ($p<0.001$), but cell proliferation was evident by higher numbers of viable cells in both groups compared to day 0 ($p<0.001$).

viability were detected between each ultrasound configuration ($p>0.05$) and cell viability remained above 70% after all treatment conditions tested.

Cell viability was also measured using trypan blue assay immediately after treatment (day 0) and two days after treatment to assess cell survival and proliferation over time after treatment. As shown in Figure 31, the number of viable cells was not statistically different between acoustofluidic treatment and the flow only control group immediately after treatment (ANOVA $p>0.05$, $n=5$ /group). At two days after treatment, the number of viable cells was higher in the flow only control group compared to the acoustofluidic treatment group ($p<0.001$), but cell proliferation was evident in both groups due to the higher numbers of viable cells compared to day 0 ($p<0.001$). These results indicate that a high number of cells remain viable and continue to proliferate after acoustofluidic treatment.

V.4. Discussion

Acoustofluidics is a rapidly developing field with a broad range of applications such as particle/cell manipulation and separation (Bruus *et al.*, 2011; Gedge and Hill, 2012b; Lenshof *et al.*, 2012; Wu *et al.*, 2017). More recently, acoustofluidic-mediated delivery has generated significant interest (Belling *et al.*, 2020a; Centner *et al.*, 2020; Centner *et al.*, 2021b; Salari *et al.*, 2021). However, acoustofluidic-mediated molecular delivery to cells has not been directly compared with static ultrasound systems. In this study, a 3D-printed concentric spiral acoustofluidic system was tested in comparison with a static ultrasound system using the same P4-1 ultrasound transducer array. The impact of various treatment conditions on intracellular molecular delivery was evaluated in each ultrasound

treatment system. Intracellular delivery of small molecules (0.6 kDa calcein) and large molecules (150 kDa FITC-dextran) were assessed in each system. Intracellular delivery of large molecules, such as clustered regularly interspaced short palindromic repeats (CRISPR) endonucleases and proteins, are of clinical significance since they have the capacity to modulate protein expression, induce genome editing, alter cell behavior, and inhibit or enhance interactions in desired cells, such as T lymphocytes, for immune therapies, gene correction, and cell/tissue engineering (Cho *et al.*, 2013; Ebina *et al.*, 2013; Barrangou and Doudna, 2016; Lee *et al.*, 2019). 150 kDa FITC-dextran is similar in molecular weight to CRISPR endonucleases, which are promising techniques for genomic modification with high specificity (Kocak *et al.*, 2019). Additionally, 150 kDa FITC-dextran has a larger molecular weight than most mammalian proteins. For example, hemoglobin, a proteinaceous macromolecule in red blood cells that carries oxygen to tissue, has a molecular weight of approximately 65 kDa (Billett, 1990). Thus, our findings provide important insights into molecular delivery of large molecules in acoustofluidic systems, relative to a traditionally utilized static configuration.

Previous acoustofluidics applications for molecular delivery have generally utilized polydimethylsiloxane (PDMS)-based photolithography techniques or a glass substrate to generate acoustofluidic devices (Belling *et al.*, 2020a; Centner *et al.*, 2020; Centner *et al.*, 2021b; Salari *et al.*, 2021). PDMS-based acoustofluidics devices offer distinct advantages, such as rapid device generation and the ability to produce very small channel dimensions. However, PDMS-based

acoustofluidic devices have important limitations since PDMS can have batch-to-batch variability in geometric dimensions, which can alter the ultrasound field in the acoustofluidic channel for each batch of devices (Hill *et al.*, 2002). This can have a significant impact on reproducibility for applications such as particle/cell sorting, enrichment, and molecular delivery (Hill *et al.*, 2002; Johansson *et al.*, 2009; Centner *et al.*, 2020; Centner *et al.*, 2021b). Glass substrate-based acoustofluidic devices allows certain molecules and cells to adhere to the channel walls (Belling *et al.*, 2020a; Salari *et al.*, 2021). T lymphocytes, however, are anchorage independent and tethering biomolecules to a capillary wall may severely reduce processing rate, which can limit availability of essential therapies. Processing rate is fundamentally important for T lymphocyte therapies, such as CAR T, which often require approximately 10^8 cells for each treatment (Neelapu *et al.*, 2017; Maude *et al.*, 2018; Schuster *et al.*, 2019). To address these limitations, a 3D-printed plastic-based concentric spiral acoustofluidic device allows consistent fabrication of acoustofluidic devices with consistent channel and device dimensions, which can increase reproducibility and consistency for acoustofluidic applications.

Unique to our acoustofluidic delivery technique is the utilization of microbubbles as a mediator of molecular delivery. Other studies have focused on other effects of ultrasound, such as acoustic radiation forces and microstreaming effects, where ultrasound is applied continuously to induce these effects (Belling *et al.*, 2020a; Salari *et al.*, 2021). Acoustic radiation force has been utilized to force cells to the distal portion of the channel where cells shear against the wall for

enhanced molecular delivery (Belling *et al.*, 2020a). With our acoustofluidic configuration, acoustic radiation force is not expected to force cells to pressure nodes and antinodes, as a short pulse (less than 1% duty cycle) was utilized in this study instead of continuous ultrasound. Additionally, thermal effects are not expected to play an important role in molecular delivery due to the low duty cycle (<1%) and short exposure time (~2-3 s) in our acoustofluidic device (Centner *et al.*, 2021a). However, acoustic radiation force may still potentially play a role in delivery as microbubbles can be forced radially toward cells even with short ultrasound pulse durations (Zhou *et al.*, 2012). Microbubble destruction resulting from cavitation has been shown to induce temporary pores in the plasma membrane for effective sonoporation (Zhou *et al.*, 2012; Hu *et al.*, 2013b). Additionally, microstreaming is induced by microbubble oscillation/cavitation and may contribute to molecular delivery (Marmottant and Hilgenfeldt, 2003; Collis *et al.*, 2010). Although the *in situ* acoustofluidic pressures within the channels have not been directly measured, it's feasible that microbubble oscillation/cavitation may be a predominant mechanism as our ultrasound output pressure is significantly above the stable/inertial cavitation threshold for lipid-coated microbubbles (Helfield *et al.*, 2016a). These effects could potentially facilitate molecular delivery via sonoporation, but further research is required to determine predominant mechanisms.

In this study, acoustic attenuation was measured to assess the correlation between microbubble destruction and molecular delivery. In the static configuration, reduced microbubble attenuation relative to the control group was

positively correlated with increased molecular delivery ($R^2= 0.91$). This is consistent with prior studies that observed reduced microbubble attenuation with increased ultrasound treatment time in a static configuration (Escoffre *et al.*, 2013). Interestingly, a similar trend was not observed with acoustofluidic treatment ($R^2=0.00$), indicating that there was no linear relationship between microbubble attenuation and molecular delivery. With the acoustofluidic device, a microbubble concentration of 24 $\mu\text{g/mL}$ enhanced molecular delivery to Jurkat T lymphocytes compared to all other microbubble concentrations tested with the acoustofluidic device. We previously reported a similar trend with acoustofluidic delivery in erythrocytes (Centner *et al.*, 2020). A possible explanation for this effect is that higher microbubble concentrations can induce “shadowing” effects due to increased scattering and attenuation of ultrasound waves through microbubble solutions, resulting in reduced ultrasound pressures in more distal locations. The residence time in the 1-mm concentric spiral acoustofluidic channel is significantly shorter ($\sim 2\text{-}3$ s) compared to the 45 s treatment duration in the static configuration. Thus, there is an optimal “therapeutic window” for microbubble concentration that will enhance molecular delivery to cells with the selected acoustofluidic parameters.

The effect of ultrasound output pressure on molecular delivery has been previously described using a static ultrasound setup (Bhutto *et al.*, 2018); however, few studies have utilized cationic microbubbles for molecular delivery to T lymphocytes, which express anionic glycoproteins and glycolipids on the plasma membrane surface (Springer, 1990). Cationic microbubbles may have increased

affinity to the plasma membrane due to charge-charge interactions, and it has been previously shown that cationic microbubble induce increased molecular delivery levels to T lymphocytes compared to neutral microbubbles when undergoing ultrasound treatment (Centner *et al.*, 2021a). Similar trends were observed with static treatment and acoustofluidic treatment, as both conditions had a general increase in molecular delivery at higher ultrasound output pressures (>3.8 MPa).

Ultrasound treatment duration was also investigated in the static treatment configuration and the acoustofluidic system. An increase in molecular delivery was observed with static treatment until 45 s, with no differences detected between 45 s and 60 s. Yet, static treatment had similar acoustic attenuation for ultrasound durations of 30-60 s. It is possible that the microbubble lipid shell may rupture within 30 s but cavitation activity may continue for a longer duration of time. Without an intact lipid shell, the perfluorocarbon gas molecules may rapidly dissolve into the liquid medium before acoustic attenuation measurements are acquired (Sarkar *et al.*, 2009). Unlike static treatment, acoustofluidic treatment did not have a statistically significant difference in molecular delivery when comparing acoustofluidic treatment with one pass and two passes through the device ($p>0.05$), suggesting that repeated exposure does not enhance molecular delivery. We previously determined that residence time within the acoustofluidic device can influence molecular delivery (Centner *et al.*, 2020), but the parameters in the earlier study were significantly different (slower flow rate, lower ultrasound pressure, different channel dimensions, and different cell type). In this study, it is possible that the amount of microbubble destruction that occurred during the first pass

caused maximum levels of molecular delivery, which was not further enhanced during the second pass through the acoustofluidic device.

Refined static treatment and refined acoustofluidic treatment enhanced molecular delivery for calcein ($p < 0.01$) and FITC-dextran ($p < 0.001$) compared to respective negative controls. No statistically significant differences were detected between static treatment and acoustofluidic treatment regardless of molecular size, indicating that similar levels of molecular delivery were achieved with each configuration. Although the level of molecular delivery was similar between each configuration, the acoustofluidic system offers distinct advantages compared to static treatment, especially for anchorage independent cells such as T lymphocytes. Static treatment is labor intensive, has limited throughput, and has increased risk of variability between batches, whereas the acoustofluidic system enables faster processing rate, less treatment time, and a lower microbubble concentration compared to static treatment while achieving similar levels of molecular delivery with small and large molecules. Future integration of a single-element transducer within a 3D-printed fluidic chamber with preprogrammed acoustic settings will enable non-specialized personnel to easily operate this device in a closed flow system to maintain a sterile environment. Increased cell concentration, increased flow rate, and parallelization are feasible options to further improve scalability for cell manufacturing applications. Our findings in this study represent an early step towards development of optimized methods for molecular delivery of exogenous macromolecules for potential T lymphocyte therapies, such as CAR-T.

V.5. Conclusion

This study indicates that microbubble concentration and ultrasound pressure are key factors in optimizing molecular delivery to T lymphocytes using static ultrasound systems or acoustofluidic systems. Additionally, ultrasound treatment duration was a significant factor in delivery efficiency using the static ultrasound system. Similar levels of molecular delivery were achieved for small and large molecules with refined parameters in each system, yet acoustofluidic treatment required only ~2-3 s treatment duration and 24 $\mu\text{g/mL}$ microbubble concentration for optimal delivery, whereas static ultrasound treatment required 45 s treatment duration and 94 $\mu\text{g/mL}$ microbubble concentration. These results indicate that acoustofluidic treatment is an effective approach for intracellular delivery of biomolecules and offers distinct advantages for cell manufacturing applications. Further development of this technology could potentially improve manufacturing processes for cell-based therapies such as CAR T, which may expand treatment availability and improve patient outcomes.

CHAPTER VI– BIOMODULATORY EFFECTS
OF MOLECULAR DELIVERY IN HUMAN T
CELLS USING A 3D-PRINTED
ACOUSTOFLUIDIC DEVICES

VI.1. Introduction

Cell-based therapies have the capacity to significantly improve patient outcomes for a variety of diseases that include cancer, autoimmune diseases, infectious diseases, and metabolic diseases (Deeks *et al.*, 2002; Brentjens *et al.*, 2007; Buzhor *et al.*, 2014; Schuster *et al.*, 2017; Annesley *et al.*, 2018a; Ying *et al.*, 2019). Chimeric antigen receptor (CAR)-T cells are genetically-engineered T cells that express receptors to target specific proteins, and CAR-T treatments have significantly improved patient outcomes in B-cell malignancies, such as leukemia or lymphoma (Annesley *et al.*, 2018a). In clinical trials, complete remission has been observed in up to 90% of B-cell acute lymphoblastic leukemia patients after treatment with CAR-T cells (Davila *et al.*, 2014; Turtle *et al.*, 2016; Gardner *et al.*, 2017). Although tremendous results have been observed with CAR-T for treatment of certain diseases (Choe *et al.*, 2021), challenges with current CAR-T manufacturing techniques, in particular the exogenous delivery of biomolecules into T cells, have prevented widespread adoption of this promising therapy (Stoiber *et al.*, 2019).

Viral vector technology is the primary approach being utilized for *ex vivo* modification of T cells. Viral vectors can efficiently deliver nucleic acids to T cells; however, the efficiency of viral delivery is highly variable between individual cells due to variations in intrinsic properties of certain cells. Additionally, viral vector delivery techniques can potentially have adverse effects such as insertional mutagenesis and undesired multiplicity of infection (Wahlers *et al.*, 2001a; Piscopo *et al.*, 2018). Non-viral transfection approaches have generally focused on passive

delivery methods in mammalian cells via physical techniques such as electroporation or shear stress-mediated membrane permeabilization (Sugar and Neumann, 1984a; Hashimoto and Takemoto, 2015a; DiTommaso *et al.*, 2018). Static electroporation techniques have generated significant interest by utilizing an applied voltage to induce transient perforation in the plasma membrane and transiently enhance intracellular uptake of biomolecules (Sugar and Neumann, 1984a). Standard methods for electroporation currently have several limitations, including challenges with scale-up for manufacturing processes, generally lower delivery efficiency compared to viral vectors, limited types of buffers that can be used during electroporation processing, and significant risk of epigenetic modifications (Nayerossadat *et al.*, 2012b; Falk *et al.*, 2017). Epigenetic modifications can induce a significant increase in cytokine release, which can cause severe immunomodulatory effects after treatment (Falk *et al.*, 2017). Recently, a microfluidic squeezing platform has been developed that induces transient perforations in the plasma membrane of cells passing through a very narrow constricted channel at a high velocity, which induces higher shear stress forces on the cell membranes and enhances molecular delivery (DiTommaso *et al.*, 2018). A fundamental limitation of this technology is the potential for aggregates of cells or other material to cause blockage of the narrow microfluidic channels which are required for efficient delivery, which can be a challenge for large-scale processing (Dressaire and Sauret, 2016).

Functionally loaded drug delivery vehicles could be another potential option for *ex vivo* modifications of cells. Drug delivery vehicles have generated significant

interest for therapeutic applications in humans by improving drug uptake in cells through mechanisms such as pH-sensitive release, temperature-sensitive release, and enhanced endocytosis activity (Oh and Park, 2014; Sun *et al.*, 2017b; Zhang *et al.*, 2021). These drug delivery vehicles have significant potential for therapeutic applications in humans, as they can improve uptake in target cells while diminishing uptake in non-specific cells. However, this is less critical in *ex vivo* modification as non-target cells can be separated through other techniques, such as centrifugation and magnetic-activated cell sorting (MACS). Thus, the capacity to improve delivery of molecular compounds to T cells more quickly, efficiently, and reliably, is a fundamental need for cell therapy manufacturing.

To address these limitations, ultrasound technology has been utilized to rapidly deliver biomolecules into cells using ultrasound contrast agents (*i.e.*, microbubbles), typically through a mechanism known as “sonoporation” (Bhutto *et al.*, 2018; Centner *et al.*, 2020). Sonoporation can occur when ultrasound-mediated microbubble cavitation induces transient perforation of cell membranes, which enables intracellular transport of macromolecules that may otherwise be impermeable due to properties such as size and charge. Cavitation-induced pores in the cell membrane typically reseal quickly via active repair mechanisms that are influenced by factors such as membrane pore size and extracellular solute concentration, but biomolecules can be rapidly delivered directly into the cytoplasm within seconds during sonoporation before the pores reseal (Zhou *et al.*, 2008; Hu *et al.*, 2013b). Microbubbles are currently FDA-approved for clinical applications involving cardiac imaging, and they are also in development for gene therapy and biomolecular

delivery applications, including antigenic protein delivery or transfection of immune cells such as Dendritic Cells and T cells (Dewitte *et al.*, 2014; Centner *et al.*, 2021b). Enhancing molecular delivery efficiency is a fundamental parameter for achieving more effective *ex vivo* modifications of cells, including transformation of immune cells for cell therapy applications. The coupling of ultrasound and microbubbles potentially offers a solution to address the molecular delivery limitations of other approaches. Custom ultrasound setups with static solutions are typically utilized for studies involving ultrasound-mediated molecular delivery to cells, using a single-element transducer or transducer array placed in a medium (such as water or cell culture media) with cells suspended or adhered in a static sample chamber (such as a well plate, petri dish, or test tube) (Bhutto *et al.*, 2018; Janis *et al.*, 2021). However, these static sample chambers for ultrasound delivery generally have limited throughput, which is a significant limitation for potential large-scale manufacturing of cell therapies.

Acoustofluidic technologies, which deliver ultrasound into fluidic channels, offer a potential solution to increase throughput of sonoporation-based molecular delivery processing. Previous studies have demonstrated that acoustofluidics can rapidly enhance intracellular delivery of small (\leq kDa) and large (\geq kDa) molecular compounds (Belling *et al.*, 2020a; Centner *et al.*, 2020). We have previously developed acoustofluidic systems that utilize exogenous microbubbles to enhance molecular delivery to multiple cell types, including cancer cells, erythrocytes, and T cells (Centner *et al.*, 2020; Centner *et al.*, 2021b; Janis *et al.*, 2021). This approach has the capacity to process cell solutions with continuous flow rates

above 100 mL/hr, which significantly increases throughput compared to static systems (Centner *et al.*, 2020; Janis *et al.*, 2021).

Although the concept of ultrasound-mediated molecular delivery is well established, the effect of biological factors on intracellular molecular delivery in an acoustofluidic device has yet to be characterized. The objective of this study was to determine the effect of biological and biochemical factors, including cell cycle phases, extracellular serum protein concentration, and extracellular calcium levels, that influence the efficiency of intracellular molecular delivery to human T cells in acoustofluidic channels. In this study, we initially assessed the effect of several key parameters on intracellular delivery efficiency of a fluorescent soluble compound (calcein) in human T cells. Additionally, a fluorescent macromolecule (150 kDa FITC-Dextran) was also utilized to study the effect of cell cycle phases on molecular delivery and to assess the effect of microbubble concentration on molecular delivery efficiency in a variety of human cell lines, demonstrating the potential utility of this approach as a platform technology. Furthermore, changes to actin and organelle structures in human T cells were assessed with confocal microscopy after acoustofluidic treatment. These results aim to provide new insights into key biological parameters that affect acoustofluidic-mediated molecular delivery in human T cells.

VI.2. Methods

VI.2.1. Molecular Delivery to Human T Lymphocytes

Jurkat T lymphocytes were cultured in RPMI-1640 medium (Cytiva Life Sciences, Marlborough, MA, USA) supplemented with 10% fetal bovine serum (FBS) and 1% penicillin/streptomycin at 37 °C and 5% CO₂ in a flat-bottom tissue culture flask. A549 cells, MDA-MB-231 cells, and HEK293 cells were cultured in DMEM medium (Cytiva Life Sciences) supplemented with 10% FBS and 1% penicillin/streptomycin at 37 °C and 5% CO₂ in a flat-bottom tissue culture flask. Cells were seeded at a concentration of 100,000 cells/mL. To assess the effect of cell plating density on molecular delivery efficiency, Jurkat T lymphocytes were also seeded at concentrations of 200,000 cells/mL and 300,000 cells/mL. Cells were harvested 2 days after initial seeding and were resuspended in complete RPMI-1640 (for Jurkat T cells) or complete DMEM (for other cell types) at a

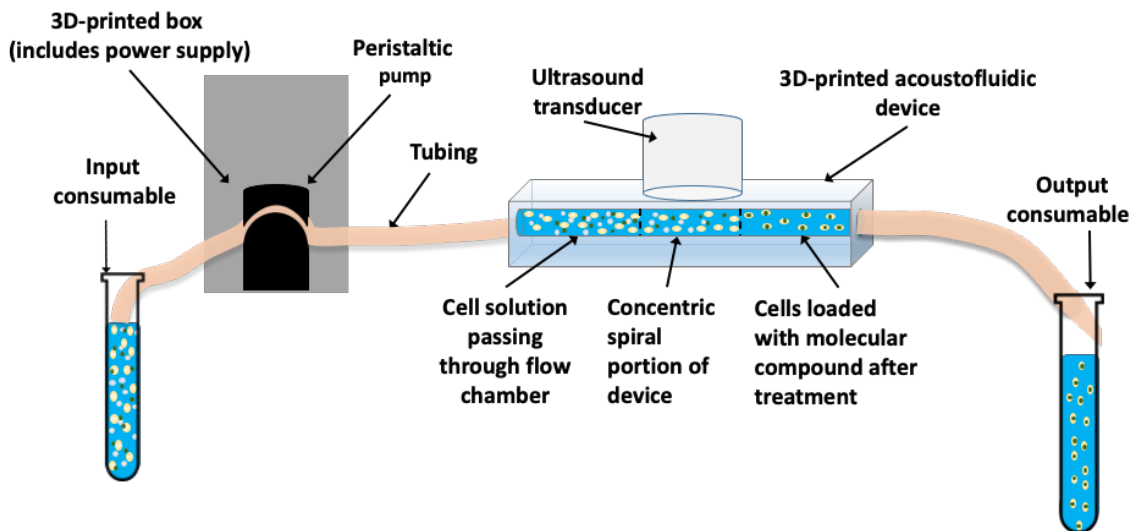


Figure 32: Schematic of acoustofluidic setup for intracellular molecular delivery to human cells. The acoustofluidic system utilizes an ultrasound transducer coupled with a 3D-printed flow chamber. A peristaltic pump is used to push solutions through the acoustofluidic channels and enhance intracellular molecular delivery (schematic is not to scale).

concentration of 100,000 cells/mL after centrifugation at 1500g for 5 minutes at 4 °C. Intracellular molecular delivery was assessed using 100 µg/mL calcein (Sigma-Aldrich, St. Louis, MO, USA) or 1.5 mg/mL 150 kDa-FITC Dextran (Sigma-Aldrich, St. Louis, MO, USA).

Acoustofluidic treatment was performed in a 1 mm x 1 mm 3D-printed flow chamber driven by a peristaltic pump, shown in figure 32. The flow chamber was designed in SolidWorks (Waltham, MA, USA) and fabricated in Accura 60 plastic using stereolithography 3D printing (Xometry, Gaithersburg, MD, USA). A concentric spiral channel design was utilized to increase residence time for cells within the ultrasound beam as they pass through the acoustofluidic channels (Centner *et al.*, 2021a). Input and output ports in the 3D-printed acoustofluidic device were threaded for stainless steel barbed tube fittings (10-32 threads, McMaster-Carr, Elmhurst, IL, USA) for connection to PVC tubing (1/16" ID, McMaster-Carr). Cells were pumped through the acoustofluidic device using a peristaltic pump at a flow rate of 1.5 mL/min (Boxer GmbH, Ottobeuren, Germany). An ATL P4-1 ultrasound transducer was placed directly on top of the plastic acoustofluidic device with a thin layer of ultrasound gel between surfaces to allow acoustic coupling, and B-mode pulses with a 2.5 MHz center frequency were generated by a Verasonics Vantage 64LE ultrasound imaging system. The free-field ultrasound pressure output was measured in a water tank using a 0.2 mm needle hydrophone (Precision Acoustics) at a distance of 40 mm from the P4-1 transducer.

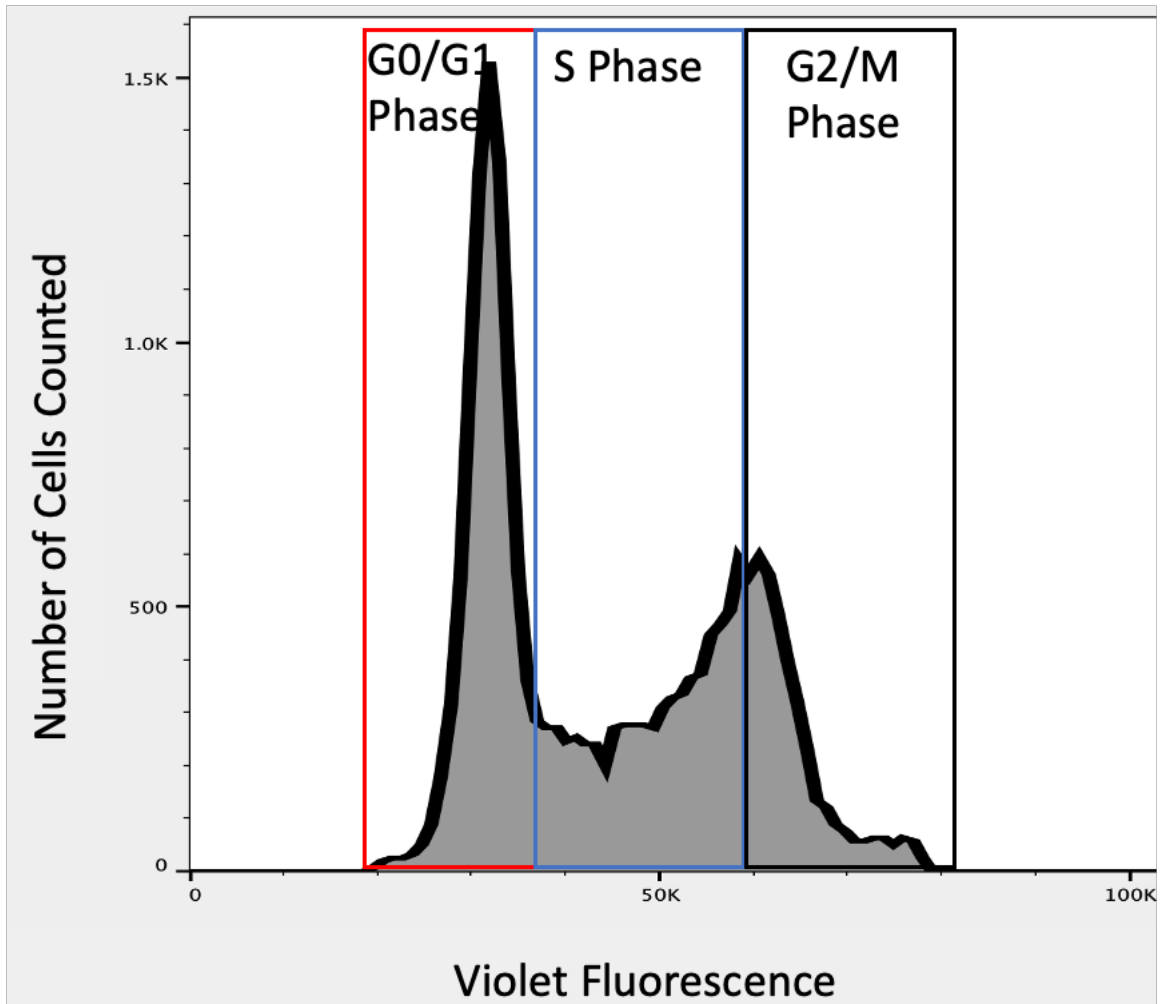


Figure 33: Representative flow cytometry histogram plot indicating the gating windows used to determine cell cycle phases of human Jurkat T cells with Vybrant DyeCycle staining. Values on the left portion (red), middle portion (blue), and right portion (black) of the x-axis represent G0/G1 Phase, S Phase, and G2/M Phase, respectively. The number of cells in each category are plotted on the y-axis.

Following acoustofluidic treatment, cells were centrifuged and washed three times with phosphate buffer solution (PBS) to remove extracellular fluorescent compounds. For analysis of cell cycle phases, cells were resuspended in complete RPMI instead of PBS after the final wash and incubated at 37 °C and 5% CO₂ for 30 minutes after adding Vybrant DyeCycle (Violet Stain; ThermoFisher Scientific, Waltham, MA, USA) at a final concentration of 5 μM. Flow cytometry (MACSquant, Miltenyi Biotec, Bergisch Gladbach, Germany) was utilized to assess intracellular

molecular delivery by measuring the mean fluorescence intensity of viable cells, as determined by absence of propidium iodide (PI) staining. A representative flow cytometry histogram plot is shown in figure 33 to illustrate the gating procedure for identifying cells in each phase of the cell cycle.

VI.2.2. Microbubble Synthesis

Microbubbles were synthesized as previously described to form perfluorobutane gas-filled microbubbles encapsulated by a cationic-charged phospholipid shell with a mean diameter of $2 \pm 1 \mu\text{m}$ (Kopeček *et al.*, 2019). Briefly, chloroform solutions of 1,2-distearoyl-sn-glycero-3-phosphocholine (DSPC, Avanti Lipids, Alabaster, AL, USA); 1,2-distearoyl-sn-glycero-3-ethylphosphocholine (DSEPC, Avanti Lipids); 1,2-distearoyl-sn-glycero-3-phosphoglycerol (DSPG, Avanti Lipids); and polyethylene glycol-40 stearate (Sigma-Aldrich, St. Louis, MO, USA) at a molar ratio of 100:43:1:4.5 were combined in a 20-mL glass vial and desiccated to remove chloroform. An aqueous micellar lipid solution was prepared by adding 1x PBS and sonicating (Qsonica, Newtown, CT, USA) to resuspend the dry lipid film. The resulting 10 mg/mL phospholipid solution was sealed in a 2-mL glass vial and the vial head space was filled with decafluorobutane gas (FlouroMed, Round Rock, TX, USA), followed by amalgamation for 45 s at 4350 cpm (DB-338, COXO, Foshan City, China) to form perfluorobutane gas-filled microbubbles. Cationic microbubble solution was added to cell solutions at concentrations of 2.5% v/v prior to acoustofluidic treatment,

except for microbubble concentration experiment (0-10% v/v) using different cell lines.

VI.2.3. Confocal Microscope Imaging

Prior to confocal microscopy, Jurkat T cells were plated at 5×10^5 cells/chamber in a 4-chambered, 35-mm CELLview cell culture dish (Greiner Bio-One, Kremsmünster, Austria) and incubated for 30 min at room temperature to allow cells to settle. Media was then removed, and cells were stained with 200 μ L of staining solution for 10 min at room temperature. CellMask Orange (ThermoFisher Scientific) was used to label F-actin filaments. A CytoPainter kit (Abcam, Cambridge, UK) was used to stain the ER and Golgi. Mitochondria were stained with 1 μ M of MitoView Blue and lysosomes were stained with 0.01X LysoView 405 (Biotium, Fremont, CA, USA). MitoView Blue and LysoView stains were brought to working concentration in the staining buffer provided by the CytoPainter kit. All dye stocks were made to their respective manufacturer's instructions and suggested working concentrations were used unless otherwise stated. After staining, cells were gently washed with 200 μ L of DPBS and subsequently imaged in 200 μ L of DPBS. All images were taken on a Nikon A1R confocal microscope (Nikon Instruments Inc., Melville, NY, USA).

VI.2.4. Statistical Analysis

Statistical analysis was performed using ANOVA with the statistical significance defined as $p < 0.05$. Between group comparisons were applied by using

post-hoc analysis with Tukey's test. Statistical analysis was performed using SPSS 28 (Armonk, NY, USA). Bars in figures represent means \pm standard error.

VI.3. Results

VI.3.1. Effect of Cell Plating Density on Molecular Delivery

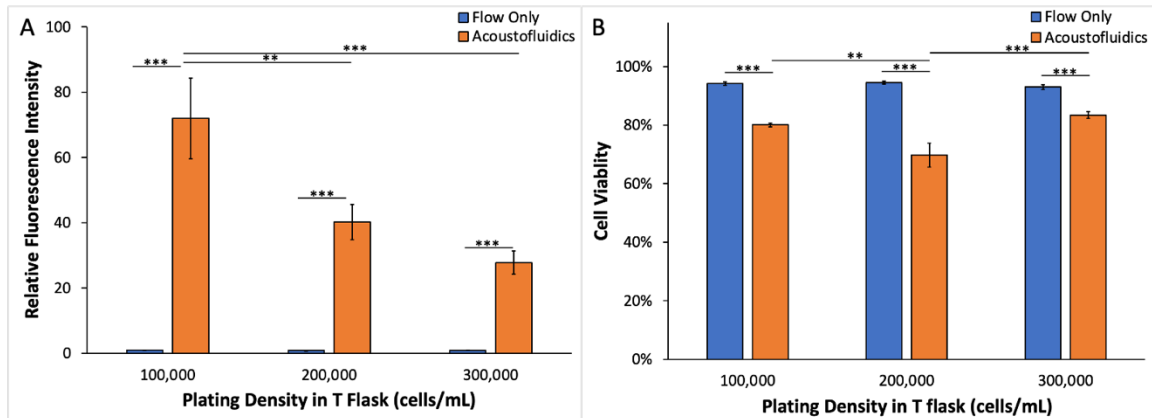


Figure 34: Effect of cell plating density on molecular delivery in Jurkat T cells. (A) Delivery efficiency of calcein (100 μ g/mL) in Jurkat T cells after acoustofluidic treatment with 2.5% v/v microbubbles dose and a peak rarefaction ultrasound pressure output of 5.1 MPa. Cells were resuspended at 100,000 cells/mL prior to acoustofluidic treatment after 2 days of culture with varying plating densities. Delivery efficiency was significantly enhanced after acoustofluidic treatment compared to corresponding flow only control groups (ANOVA $p < 0.001$, $n = 7-8$ /group). Molecular delivery was higher after acoustofluidic treatment in cells harvested from flasks with a plating density of 100,000 cells/mL compared to cells harvested from flasks with plating densities of 200,000 cells/mL ($p < 0.01$) and 300,000 cells/mL ($p < 0.001$). (B) Cell viability was reduced after acoustofluidic treatment compared to flow only conditions (ANOVA $p < 0.001$, $n = 7-8$ /group) but viability remained above 70% in all conditions. Viability was slightly lower after acoustofluidic treatment in cells harvested from flasks with plating densities of 200,000 cells/mL compared to plating densities of 100,000 cells/mL ($p < 0.01$) and 300,000 cells/mL ($p < 0.001$).

Acoustofluidic-mediated delivery of calcein to Jurkat T cells was evaluated after gating viable cells to determine the effect of initial plating density on molecular delivery after incubation for 2 days. Viable cells were counted using a trypan blue assay after harvesting cells from each flask, and all cell solutions were

resuspended at a concentration of 100,000 cells/mL. A microbubble concentration of 2.5% v/v was added to cell solutions for acoustofluidic treatment at a peak rarefaction ultrasound pressure output of 5.1 MPa. Fluorescence intensity was significantly increased for all acoustofluidic treatment groups regardless of initial plating density, relative to respective flow only control groups without ultrasound treatment (Figure 34A, ANOVA $p < 0.001$, $n = 7-8/\text{group}$). Additionally, fluorescence intensity was significantly higher in cells harvested from flasks with an initial plating density of 100,000 cells/mL, compared to cells harvested from flasks with plating densities of 200,000 cells/mL ($p < 0.01$) and 300,000 cells/mL ($p < 0.001$). Measurements of cell membrane integrity, using PI staining as an indicator of cell viability, indicated that acoustofluidic treatment decreased cell viability for all initial plating densities tested in this study, compared to each respective flow only control group (Figure 34B, ANOVA $p < 0.001$, $n = 7-8/\text{group}$). Additionally, cells harvested from flasks with an initial plating of 200,000 cells/mL had slightly lower viability after acoustofluidic treatment compared to plating densities of 100,000 cells/mL ($p < 0.01$) and 300,000 cells/mL ($p < 0.001$), but viability remained above 70% in all conditions. These results indicate that cell plating density can impact the efficiency of acoustofluidic-mediated molecular delivery in Jurkat T cells.

Modification of the actin cytoskeleton network was generally observed in cells after acoustofluidic treatment compared to cells in the flow only control groups (Figure 35). Small sites of F-actin accumulation occurred proximal to the cytoplasm (white arrows) in the acoustofluidic treatment group, whereas similar sites were not observed in the control groups without ultrasound treatment. Additionally,

filopodia formation was observed in the acoustofluidic treatment group, especially in cells harvested at lower plating density. Subsequently, increased numbers of F-actin filaments propagated to other parts of the actin cytoskeleton and appear to form dense actin patches in cells with acoustofluidic treatment.

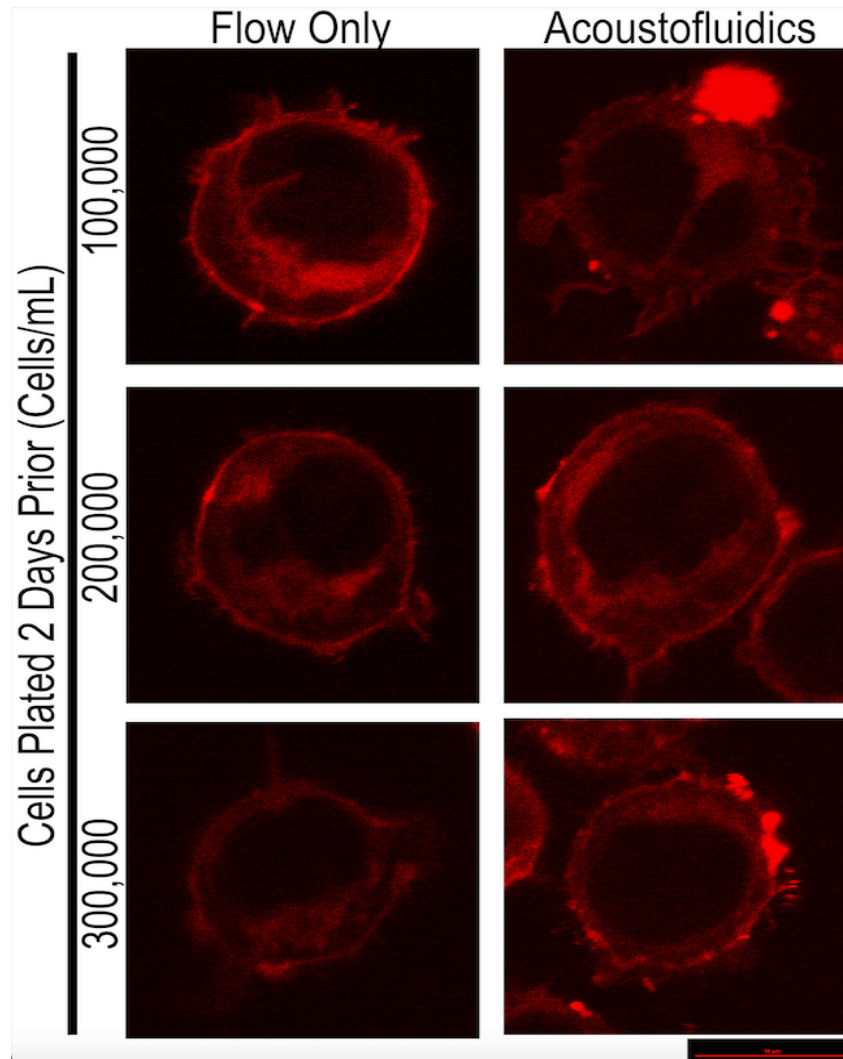


Figure 35: Confocal microscopy imaging of F-actin staining revealed differences in the cytoskeleton network between Jurkat T cells treated with flow only (control, left panels) and acoustofluidic treatment (right panels) for cells harvested from flasks seeded at different plating densities 2 days prior to treatment. Qualitative assessment indicates that polymeric F-actin increased in cells after acoustofluidic treatment compared to respective control samples. Additionally, confocal imaging indicates that increased polymerization occurred in cells harvested from flasks at low plating density (100,000 cells/mL) compared to medium plating density (200,000 cells/mL) and high plating density (300,000 cells/mL). Scale bar indicates 10 μm.

VI.3.2. Effect of Serum Concentration on Molecular Delivery

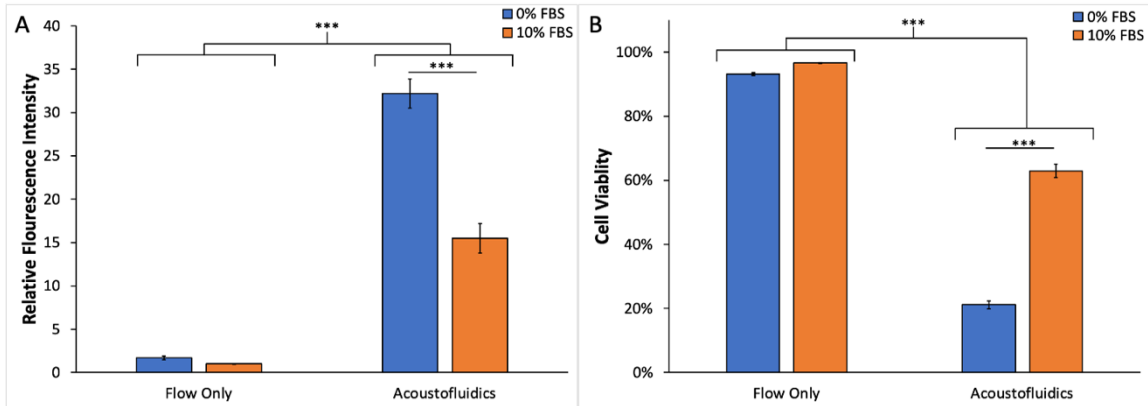


Figure 36: Effect of fetal bovine serum (FBS) concentrations on acoustofluidic-mediated molecular delivery in Jurkat T cells. (A) Delivery efficiency of calcein (100 $\mu\text{g}/\text{mL}$) with varying concentrations of fetal bovine serum (0% and 10%) and acoustofluidic treatment using a cationic microbubble concentration of 2.5% and a peak rarefaction ultrasound pressure output of 5.1 MPa. Acoustofluidic treatment without FBS (0%) and with 10% FBS in loading media increased molecular delivery compared to the respective flow only control groups (ANOVA $p < 0.001$, $n = 10-12/\text{group}$). Additionally, molecular delivery was significantly increased after acoustofluidic treatment with 0% FBS compared to 10% FBS ($p < 0.001$). (B) Cell viability was reduced after acoustofluidic treatment with 0% FBS and 10% FBS compared to respective flow only control groups (ANOVA $p < 0.001$, $n = 10-12/\text{group}$). Additionally, viability was further reduced after acoustofluidic treatment in cells without FBS compared to cells in 10% FBS ($p < 0.001$).

Acoustofluidic-mediated delivery of calcein to Jurkat T cells was evaluated with flow cytometry analysis in viable cells to determine the effect of fetal bovine serum concentration on molecular delivery efficiency. Viable cells were counted prior to experiments by using a trypan blue assay and cells were resuspended at 100,000 cells/mL in RPMI-1640 media without FBS (0% condition) or 10% FBS. Molecular delivery was significantly higher in cells with acoustofluidic treatment compared to the flow only control groups, regardless of FBS concentration (Figure 36A, ANOVA $p < 0.001$, $n = 10-12/\text{group}$). Tukey's test indicated that fluorescence intensity was significantly higher in cells after acoustofluidic treatment without FBS

relative to cells in 10% FBS ($p < 0.001$). Cell viability decreased after acoustofluidic treatment regardless of FBS concentration compared to respective flow only control groups (Figure 36B, ANOVA $p < 0.001$, $n = 10-12/\text{group}$). Viability was further reduced in cells after acoustofluidic treatment without FBS (less than 20% viability) compared to cells in 10% FBS ($p < 0.001$). These results indicate that serum concentrations can impact the efficiency of acoustofluidic-mediated molecular delivery in Jurkat T cells.

VI.3.3. Effect of Calcium Chelator on Molecular Delivery

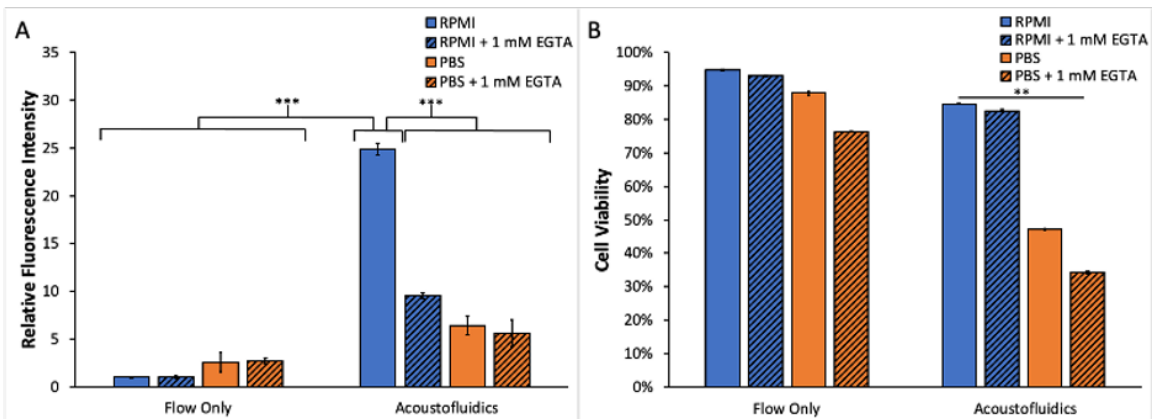


Figure 37: Effect of extracellular calcium on molecular delivery in Jurkat T cells. (A) Delivery efficiency of calcein (100 $\mu\text{g}/\text{mL}$) was measured with varying loading media (RPMI and 1x PBS) with and without calcium chelator (1 mM EGTA) and acoustofluidic treatment using a cationic microbubble concentration of 2.5% and a peak rarefaction ultrasound pressure output of 5.1 MPa. Acoustofluidic treatment with RPMI media significantly enhanced molecular delivery compared to flow only control groups or compared to acoustofluidic treatment in other media (ANOVA $p < 0.001$, $n = 6/\text{group}$). Acoustofluidic-mediated molecular delivery was significantly reduced for cells in RPMI + EGTA, indicating that addition of a calcium chelator influenced acoustofluidic delivery efficiency in Jurkat cells. (B) Cell viability was reduced after acoustofluidic treatment for all loading media compared to flow only control groups. Viability was further reduced for cells in PBS compared to cells in RPMI media for each treatment condition (ANOVA $p < 0.01$, $n = 6/\text{group}$).

Calcein delivery and cell viability were assessed for cells in complete FBS-supplemented RPMI or in PBS solutions with or without addition of a calcium chelator (1 mM EGTA). Molecular delivery was significantly higher for Jurkat T cells

in complete RPMI media compared to all flow only control groups and also cells with acoustofluidic treatment in PBS without calcium (Figure 37A, ANOVA $p < 0.001$, $n = 6/\text{group}$). Addition of a calcium chelator significantly reduced acoustofluidic-mediated molecular delivery efficiency for cells in complete RPMI media ($p < 0.001$). However, there was no statistically significant difference in molecular delivery for cells in PBS with or without calcium chelators. Cell viability was significantly reduced after acoustofluidic treatment for cells in PBS without calcium, compared to cells in complete RPMI media (Figure 37B, ANOVA $p < 0.01$, $n = 6/\text{group}$). Cell viability decreased slightly after addition of calcium chelators. These results indicate that extracellular calcium levels can impact the efficiency of acoustofluidic-mediated molecular delivery in Jurkat T cells.

VI.3.4. Effect of Cell Cycle Phases on Molecular Delivery

Acoustofluidic-mediated delivery of 150 kDa FITC-Dextran to Jurkat T cells was evaluated for cells at different cell cycle phases to assess whether cell cycle phase has an impact on molecular delivery efficiency. Viable cells were counted prior to experiments by using a trypan blue assay and cells were resuspended at 100,000 cells/mL in complete RPMI media with 10% FBS. Acoustofluidic treatment was conducted using a cationic microbubble concentration of 2.5% and a peak rarefaction ultrasound pressure output of 5.1 MPa. Molecular delivery was significantly higher after acoustofluidic treatment for cells in each phase of the cell cycle compared to their respective flow only control groups (Figure 38A, ANOVA $p < 0.001$, $n = 9/\text{group}$). Furthermore, molecular delivery was significant increased

after acoustofluidic treatment for cells in the S phase compared to cells in the G0/G1 phase ($p < 0.01$) or cells in the G2/M phase ($p < 0.001$). However, viability was lower after acoustofluidic treatment for cells in the G0/G1 phase compared to cells in the G2/M phase or the S phase after acoustofluidic treatment (Figure 38B, ANOVA $p < 0.001$, $n = 9/\text{group}$). Viability was slightly lower after acoustofluidic treatment for cells in the S phase compared to the respective flow only control group ($p < 0.05$), while no difference in cell viability was detected between acoustofluidic treatment and the flow only control group for cells in the G2/M phase. These results indicate that cell cycle phases can impact the efficiency of acoustofluidic-mediated molecular delivery in Jurkat T cells.

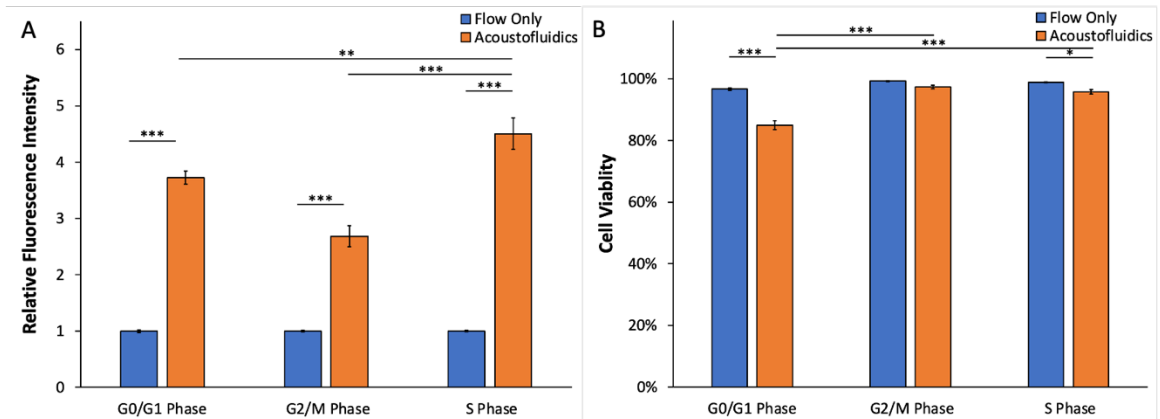


Figure 38: Effect of cell cycle phases on molecular delivery in Jurkat T cells. (A) Delivery efficiency of 150 kDa FITC-Dextran (1.5 mg/mL) was analyzed for cells in various cell cycle phases (G0/G1, G2/M, S) with acoustofluidic treatment using a cationic microbubble concentration of 2.5% and a peak rarefaction ultrasound pressure output of 5.1 MPa. Molecular delivery was significantly higher after acoustofluidic treatment for cells in all cell cycle phases compared to their respective flow only control groups (ANOVA $p < 0.001$, $n = 9/\text{group}$). Molecular delivery was further enhanced for cells in the S phase compared to cells in the G0/G1 phase ($p < 0.01$) or G2/M phase ($p < 0.001$). (B) Cell viability was reduced after acoustofluidic treatment for cells in the G0/G1 phase ($p < 0.001$) and S phase ($p < 0.05$) compared to their respective flow only control groups. Viability was lower for cells in the G0/G1 phase after acoustofluidic treatment compared to cells in the G2/M phase or S phase after acoustofluidic treatment ($p < 0.001$).

VI.3.5. Effect of Acoustofluidic Treatment on Cell Cycle Phase and Proliferation Rates

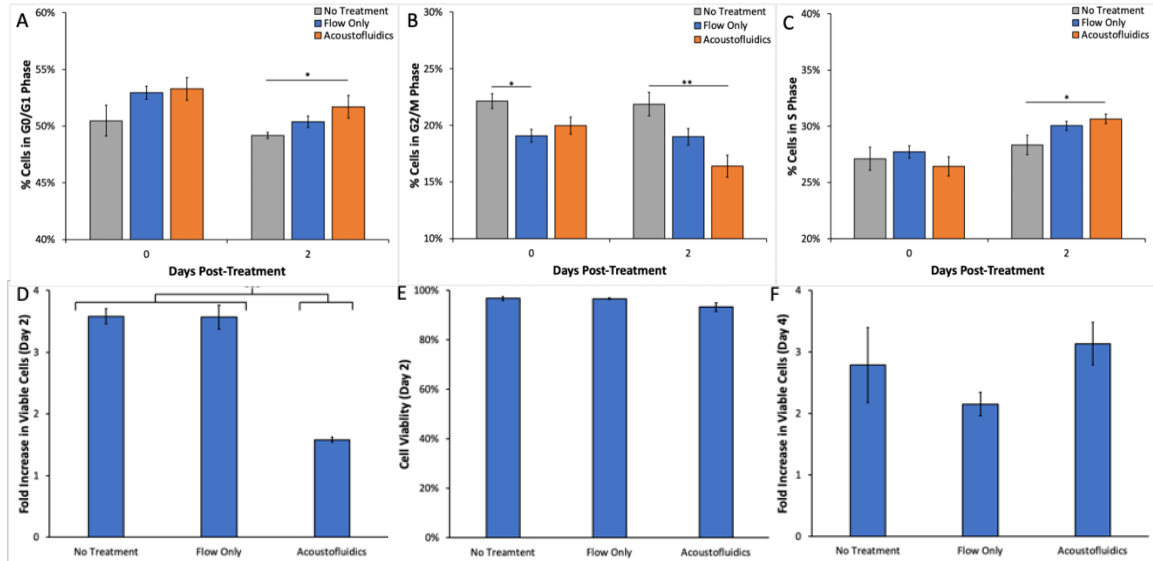


Figure 39: Effect of acoustofluidic treatment on cell cycle phases and proliferation rates. (A-C) The relative percentage of cells in each cell cycle phase was measured at 0 days and 2 days after acoustofluidic treatment compared to flow only control or no treatment groups. The percentage of cells in the G0/G1 phase and the S phase was significantly higher at 2 days after acoustofluidic treatment compared to their respective no treatment groups (ANOVA $p < 0.05$, $n = 6/\text{group}$), whereas the percentage of cells in the G2/M phase was significantly lower at 2 days after acoustofluidic treatment compared to the respective no treatment group. (D) The number of viable cells was significantly lower at 2 days after acoustofluidic treatment compared to no treatment and flow only control groups, as measured by trypan blue assay (ANOVA $p \leq 0.001$, $n = 4/\text{group}$). (E) High viability was observed for cells at 2 days after acoustofluidic treatment as measured by trypan blue assay, even though the overall number of cells was lower in the acoustofluidic treatment group compared to the control groups. (F) Cells were resuspended at a concentration of 100,000 cells/mL at 2 days after acoustofluidic treatment and cultured for an additional 2 days. After 4 days of culture post-treatment there was no statistically significant difference in the number of viable cells for the acoustofluidic treatment group compared to no treatment and flow only control groups, as measured by trypan blue assay (ANOVA $p > 0.05$, $n = 4/\text{group}$).

The impact of acoustofluidic treatment on cell cycle phases and proliferation of Jurkat T cells were evaluated using Vybrant DyeCycle staining and trypan blue assay, respectively (Fig. 39). The percentage of viable cells in the G2/M phase

was significantly lower at 2 days after acoustofluidic treatment compared to the respective no treatment control group (Figure 39B, ANOVA $p < 0.05$, $n = 6/\text{group}$). However, the percentage of viable cells in the G0/G1 phase and the S phase was significantly higher at 2 days after acoustofluidic treatment compared to their respective no treatment control groups (Figure 39A and 39C, $p < 0.05$). These results suggest that acoustofluidic treatment induces a shift in some cells toward the G0/G1 and S phases of the cell cycle and temporarily reduces mitosis. This trend is also observed in measurements of cell proliferation at 2 days after acoustofluidic treatment. Trypan blue measurements indicated that Jurkat T cells proliferated more slowly within 2 days after acoustofluidic treatment compared to no treatment and flow only control groups (Figure 39D, ANOVA $p \leq 0.001$, $n = 4/\text{group}$), but high viability was observed in all groups (Figure 39E). After 2 days of culture, cells from each group were resuspended at a concentration of 100,000/mL and cultured for 2 additional days. At 4 days of culture after acoustofluidic treatment (2 days after resuspending the cells), no statistically significant differences in proliferation were observed (Figure 39F, ANOVA $p > 0.05$, $n = 4/\text{group}$). Confocal microscopy images revealed significant differences in F-actin content in Jurkat T cells after acoustofluidic treatment, compared to cells in the flow only control group (Figure 40). However, at 2 days and 4 days after acoustofluidic treatment, differences in F-actin structure were minimal compared to cells in the flow only control group (Figure 40). These results suggest that acoustofluidic treatment has a transient impact on actin structure and proliferation

of Jurkat T cells, but they return to normal actin structure and proliferation rates within 4 days after treatment.

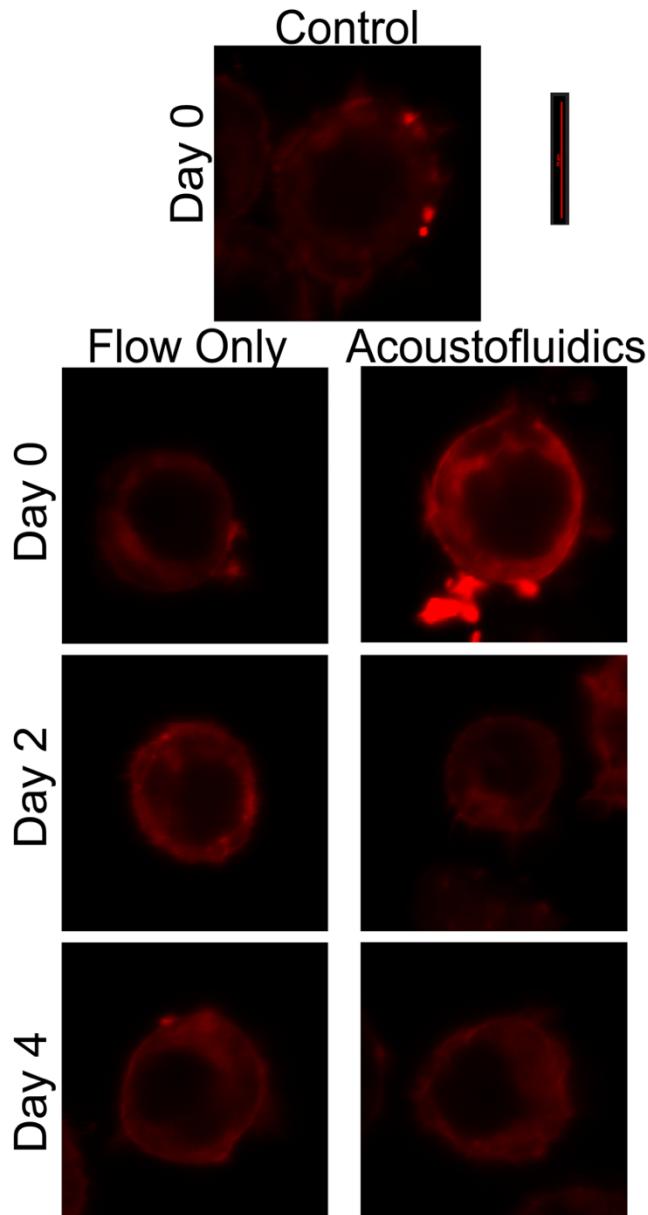


Figure 40: CellMask Orange was used to stain F-actin (indicated in red). Higher localized fluorescence indicated the presence of increased F-actin levels. A significant increase in F-actin levels was observed in Jurkat T cells after acoustofluidic treatment at day 0, compared to cells in the flow only control group. However, minimal differences in F-actin levels were observed at day 2 and day 4 after acoustofluidic treatment. Scale bar represents 10 μm .

VI.3.6. Effect of Acoustofluidic Treatment on Cellular Structures

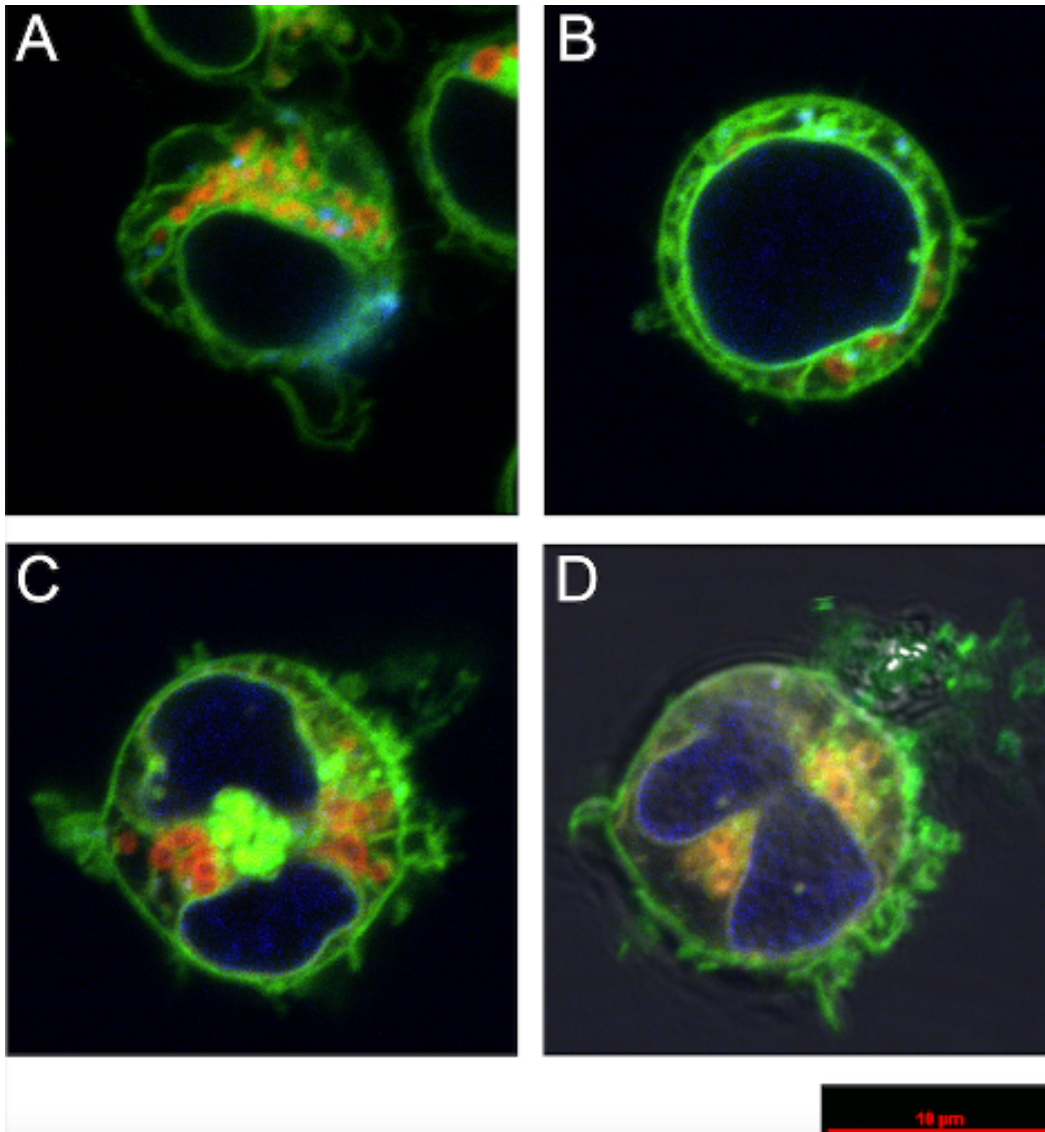


Figure 41: Effect of acoustofluidic treatment on cellular structures. Panel A represents cells in the flow only control group, whereas panels B-D represent cells after acoustofluidic treatment. Cells were stained with an ER (red), Golgi (green), and nuclear (dark blue) stain using the CytoPainter kit, while LysoView 405 was used to stain lysosomes (light blue). Panel A shows that minimal disruption to cellular structures occurred in the flow only control group. Panel B is an example of a cell that underwent acoustofluidic treatment but had minimal disruption to cell structures. Panels C and D represent a cell at different planes of view to illustrate structural changes that occurred after acoustofluidic treatment, including permeabilization of the nucleus. These images demonstrate that acoustofluidic treatment can cause significant disruption of cellular structures, including the nucleus, ER, Golgi, and lysosomes. Scale bar represents 10 μm .

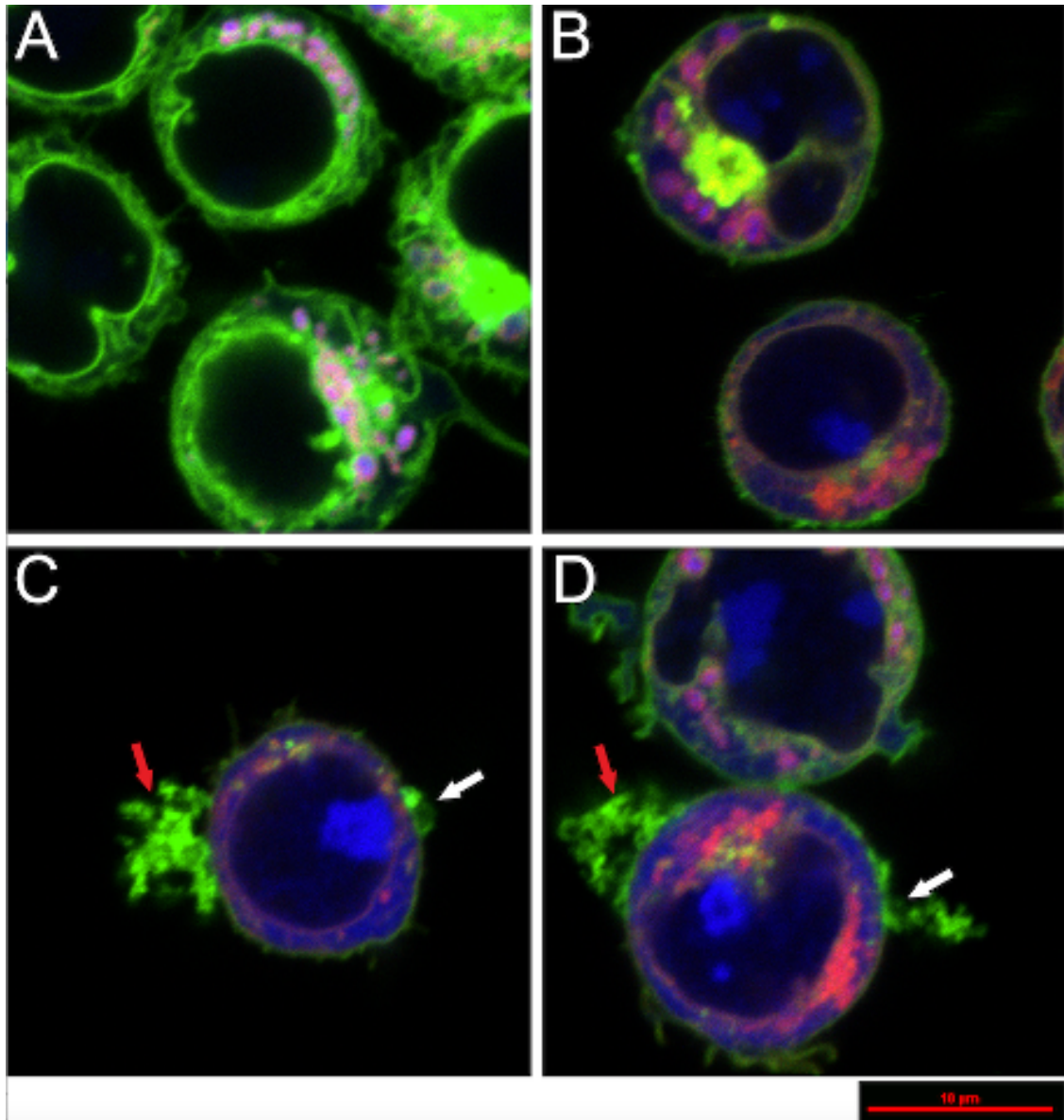


Figure 42: Effect of acoustofluidic treatment on cellular and nuclear structures. Panel A represents cells in the flow only control group, while panels B-D represent cells after acoustofluidic treatment. Cells were stained with an ER (red), Golgi (green), and nuclear (dark blue) stain using the CytoPainter kit, while MitoView Blue was used to stain mitochondria (light blue). Purple coloration is due to the very tight overlap of ER and mitochondria (red and light blue overlap). Panel B demonstrates cells with relatively minor disruption of the nucleus but major disruption of the ER, Golgi, and mitochondria. Panels C and D provide two examples of cells where the sonoporation wounds (white arrows and red arrows) are visible after acoustofluidic treatment. In panels B-D, blue fluorescence in the cytoplasm and as a node(s) in the nucleus is may be due to off-staining of the cationic mitochondrial dye, as it competes for anionic interaction partners with the cationic lipids and cationic ions that enter the cells during acoustofluidic treatment. Scale bar represents 10 μm .

Confocal microscopy images were acquired to assess the effect of acoustofluidic treatment on cellular structures and organelles. Representative cells from the flow only control group are shown in Figure 41A, where red represents ER, green represents Golgi, dark blue represents the nucleus, and light blue represents lysosomes. Figures 41B-D represent cells with acoustofluidic treatment using the same organelle staining methods. Figure 41B demonstrates a cell with minimal disruption of organelles after acoustofluidic treatment, whereas Figure 41C-D demonstrate significant disruption of organelles, including disruption of the nucleus (dark blue).

Confocal microscopy images were also acquired to assess the effect of acoustofluidic treatment on mitochondria and other cellular structures. Representative cells from the flow only control group as shown in Figure 42A, where green represents Golgi, light blue represents mitochondria, red represents ER, and purple represents overlap of mitochondria (light blue) and ER (red). The same dyes were also utilized to stain cells after acoustofluidic treatment (Figure 42B-D), but the blue mitochondria stain appeared to off-stain the cytoplasm and regions within the nucleus. This may be due to organelle disruption, which allows the cationic mitochondrial dye to bind to negatively charged components in other parts of the cell. Subsequently, the blue mitochondrial dye may be competing for anionic interaction partners with the cationic lipids and cationic ions that can enter the cell during acoustofluidic treatment. Furthermore, acoustofluidic treatment can induce transient sonoporation wounds (white arrows and red arrows), as shown in Figures 42C-D. These results demonstrate that acoustofluidic treatment can

induce transient changes in cellular structures, including the nucleus, which enables rapid uptake of therapeutic compounds into the cytoplasm or nucleus.

VI.3.7. Effect of Microbubble Concentration on Acoustofluidic Molecular Delivery in Different Cell Lines

To assess the efficiency of acoustofluidic-mediated molecular delivery in different cell lines, intracellular delivery of 150 kDa FITC-Dextran was assessed after acoustofluidic treatment in Jurkat T cells, MDA-MB-231 human breast carcinoma cells, human A549 lung carcinoma cells, and HEK293 cells at various microbubble concentrations. For Jurkat T cells, the highest amount of acoustofluidic-mediated intracellular delivery was observed at a microbubble concentration of 5% v/v compared to microbubble concentrations between 0% v/v - 1% v/v (Figure 43A, ANOVA $p < 0.01$, $n = 6/\text{group}$). and 10% v/v ($p < 0.05$). Viability was reduced after acoustofluidic treatment for all microbubble concentrations compared to the negative control condition without microbubbles (0% v/v, Figure 43B, ANOVA $p < 0.001$, $n = 6/\text{group}$). Additionally, cell viability was reduced after acoustofluidic treatment at microbubble concentrations of 2.5% v/v - 7.5% v/v compared to microbubble concentrations of 1% v/v and 10% v/v ($p < 0.001$).

Acoustofluidic-mediated intracellular delivery of 150 kDa FITC-Dextran to MDA-MB-231 cells was highest with a microbubble concentration of 5% v/v compared to lower microbubble concentrations or the negative control condition without microbubbles (0% v/v - 2.5% v/v; Figure 43C, ANOVA $p < 0.001$, $n = 6/\text{group}$) and compared to higher microbubble concentrations (7.5% v/v - 10% v/v;

$p < 0.001$). A slightly different trend was observed for cell viability, which indicated that cell viability was reduced after acoustofluidic treatment with microbubble concentrations of 2.5% v/v - 7.5% v/v compared to the negative control condition without microbubbles (0% v/v, Figure 43D, ANOVA $p < 0.001$, $n = 6/\text{group}$).

Intracellular delivery of 150 kDa FITC-Dextran was highest for A549 cells after acoustofluidic delivery with a microbubble concentration of 5% v/v compared to the negative control condition without microbubbles (0% v/v, Figure 43E, ANOVA $p < 0.001$, $n = 9/\text{group}$). Cell viability was reduced after acoustofluidic treatment with a microbubble concentration of 5% v/v compared to all other microbubble concentrations (Figure 43F, ANOVA $p < 0.001$, $n = 9/\text{group}$), but viability remaining above 80% for all groups.

For HEK293 cells, intracellular delivery of 150 kDa FITC-Dextran was significantly higher after acoustofluidic treatment with microbubble concentrations between 1% v/v - 10% v/v compared to the negative control condition without microbubbles (0% v/v, Figure 43G, ANOVA $p < 0.01$, $n = 3-6/\text{group}$). Additionally, acoustofluidic delivery was higher with a microbubble concentration of 5% v/v compared to 7.5% v/v ($p < 0.01$). Cell viability was reduced after acoustofluidic treatment with microbubble concentrations of 5% v/v - 10% v/v ($p < 0.001$, Figure 43H, ANOVA $p < 0.05$, $n = 3-6/\text{group}$) and 2.5% v/v ($p < 0.05$) compared to the negative control condition without microbubbles (0% v/v). Viability remained above 80% cell viability for all groups.

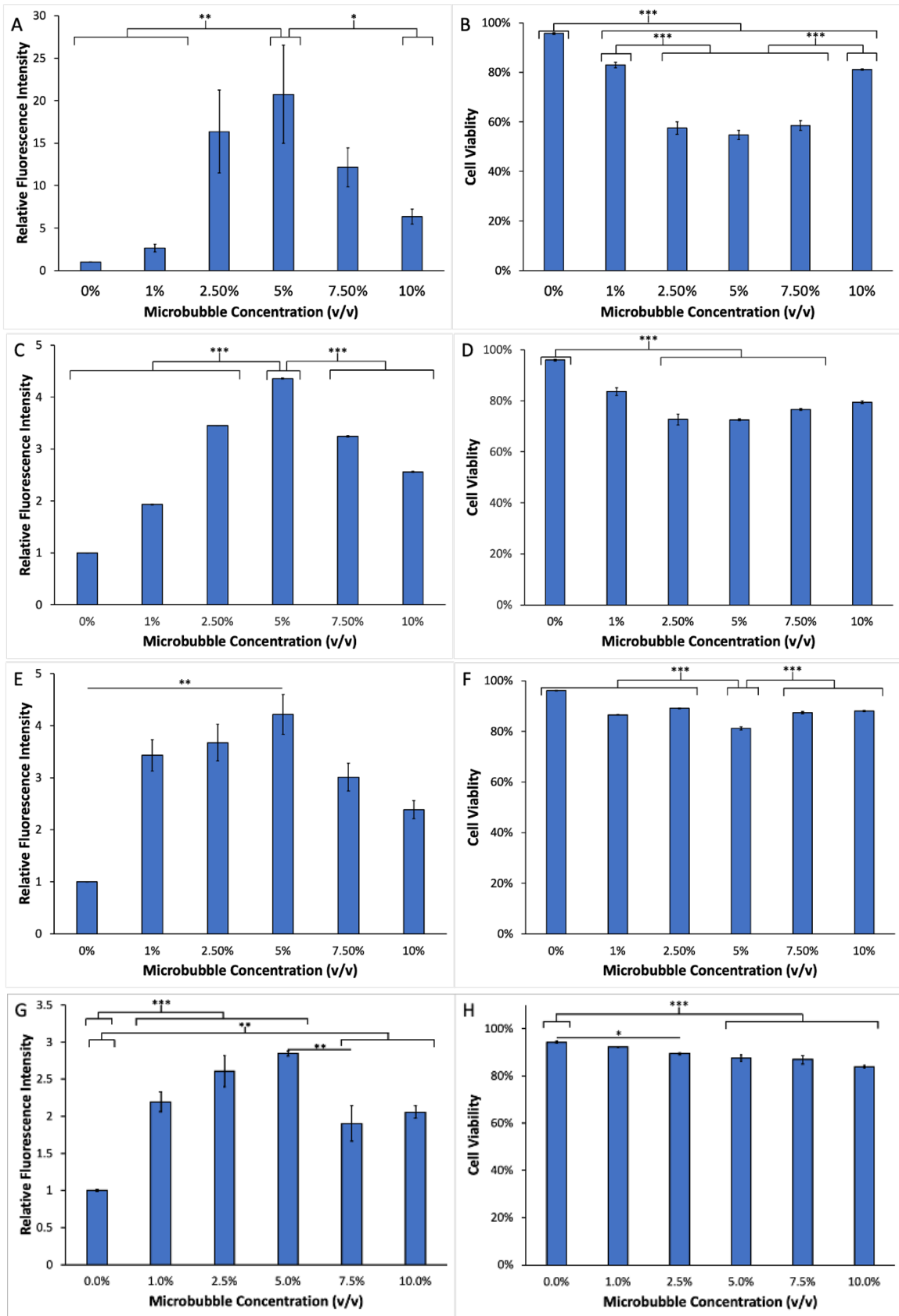


Figure 43: Comparison of acoustofluidic-mediated molecular delivery in different cell lines. (A) Delivery efficiency of 150 kDa FITC-Dextran (1 mM) to Jurkat T cells with varying microbubble concentration using acoustofluidic treatment (5.1 MPa). A microbubble concentration of 5% v/v significantly enhanced intracellular delivery of 150 kDa FITC-Dextran compared to microbubble concentrations of 0-1% v/v (ANOVA $p < 0.01$, $n = 6/\text{group}$) and compared to a microbubble concentration of 10% v/v ($p < 0.05$), respectively. (B) Cell viability was reduced after acoustofluidic treatment for all microbubble concentrations compared to the negative control condition without microbubbles (0% v/v; ANOVA $p < 0.001$, $n = 6/\text{group}$). Additionally, cell viability was reduced after acoustofluidic treatment at microbubble concentrations of 2.5%-7.5% v/v compared to microbubble concentrations of 1% v/v and 10% v/v ($p < 0.001$). (C) Delivery efficiency of 150 kDa FITC-Dextran (1 mM) to MDA-MB-231 human breast carcinoma cells with varying microbubble concentration using acoustofluidic treatment (5.1 MPa). A microbubble concentration of 5% v/v significantly enhanced intracellular delivery of 150 kDa FITC-Dextran compared to microbubble concentrations of 0-2.5% v/v or 7.5-10% v/v (ANOVA $p < 0.001$, $n = 6/\text{group}$). (D) Cell viability was reduced after acoustofluidic treatment at microbubble concentrations of 2.5%-7.5% v/v compared to the negative control condition without microbubbles (0% v/v, ANOVA $p < 0.001$, $n = 6/\text{group}$). (E) Delivery efficiency of 150 kDa FITC-Dextran (1 mM) to A549 human lung carcinoma cells with varying microbubble concentration using acoustofluidic treatment (5.1 MPa). A microbubble concentration of 5% v/v significantly enhanced intracellular delivery of 150 kDa FITC-Dextran compared to the negative control conditions without microbubbles (0% v/v, ANOVA $p < 0.001$, $n = 9/\text{group}$). (F) Cell viability was reduced after acoustofluidic treatment with a microbubble concentration of 5% v/v compared to microbubble concentrations of 0-2.5% v/v or 7.5%-10% v/v (ANOVA $p < 0.001$, $n = 9/\text{group}$), respectively. (G) Delivery efficiency of 150 kDa FITC-Dextran (1 mM) to HEK293 cells with varying microbubble concentration using acoustofluidic treatment (5.1 MPa). A microbubble concentration of 1-10% v/v significantly enhanced intracellular delivery of 150 kDa FITC-Dextran compared to the negative control condition without microbubbles (0% v/v, ANOVA $p < 0.01$, $n = 3-6/\text{group}$). Additionally, acoustofluidic treatment with a microbubble concentration of 5% v/v increased molecular delivery compared to 7.5% v/v ($p < 0.01$) (H) Cell viability was reduced after acoustofluidic treatment with a microbubble concentration of 5-10% v/v (ANOVA $p < 0.001$, $n = 3-6/\text{group}$) and 2.5% v/v ($p < 0.05$) compared to the negative control condition without microbubbles (0% v/v). Cell viability remained above 80% for all treatment conditions.

VI.4. Discussion

Acoustofluidic-mediated delivery of biomolecules to cells has the potential to become an important technology due to its capacity for rapid and efficient

delivery while potentially avoiding the limitations of viral vectors (Belling *et al.*, 2020a; Centner *et al.*, 2021b). The results of this study demonstrate for the first time that several key factors affect molecular delivery to human T cells with an acoustofluidic device, including the initial cell plating concentration, serum concentrations, extracellular Ca^{2+} levels in the media, and cell cycle phases. Additionally, biological characterization was further assessed using confocal microscopy to understand the impact of acoustofluidic treatment on changes in actin structure during cell membrane repair processes and on disruption of cellular organelles.

Initial plating density of human T cells was found to have a significant impact on molecular delivery and on cytoskeleton structure after treatment in the acoustofluidic device with exogenous microbubbles in the loading media. It was determined that lower initial cell plating density yielded improved molecular delivery with acoustofluidic treatment, but the exact reason is not fully understood. In addition, initial plating density may impact actin levels and also alter the relative percentage of cells in each phase of the cell cycle, which could both affect molecular delivery. This suggests that cell concentration may be a key factor for molecular delivery of biomolecules used in cell manufacturing applications, such as CAR-T. It appears that initial cell recovery dynamics (including actin polymerization) were sufficient to maintain viability for most cells after acoustofluidic treatment. Previous studies have indicated that modifications to the cytoskeleton occur where microbubble cavitation induces a transient pore in the plasma membrane (sonoporation) (Wang *et al.*, 2018; Yang *et al.*, 2020). Although

microbubble cavitation was not directly measured in this study, our prior studies demonstrated that acoustofluidic treatment in a 3D-printed device can cause significant microbubble destruction (Centner *et al.*, 2021a), which may be due to inertial cavitation activity. Acoustofluidic-driven microbubble cavitation near cell membranes can enable rapid delivery of exogenous biomolecules into cells. Unintended consequences of sonoporation include diffusion of additional compounds, such as ions and proteins, across the cell membrane and disruption of cellular homeostasis (McNeil and Kirchhausen, 2005), which may induce upregulation of exocytosis and endocytosis (Lentacker *et al.*, 2014). Actin polymerization has been suggested to have multiple functions, such as formation, invagination, and constriction of clathrin-coated vesicles, in addition to scission and departure of clathrin-coated vesicles (Yarar *et al.*, 2005; Kaksonen *et al.*, 2006; Aghamohammadzadeh and Ayscough, 2009; Ferguson *et al.*, 2009). Upregulation of clathrin-dependent endocytic vesicles have been observed after sonoporation, which could further enhance molecular delivery after acoustofluidic treatment (Fekri *et al.*, 2016). However, our previous work indicates that molecular delivery primarily occurs within 1 minute after acoustofluidic treatment (Centner *et al.*, 2021a), with a low level of additional molecular uptake continuing for at least 30 minutes after treatment.

The results indicate that cell cycle phases have an important impact on molecular delivery and cell viability after acoustofluidic treatment. Interestingly, molecular delivery and cell viability were not associated, suggesting that certain cell cycle phases may be optimal for molecular delivery and maintenance of cell

viability. Prior studies suggest that the typical deformation force required for perforation of the cell membrane may change based on the cell cycle, with S phase found to have the lowest Young's modulus in HeLa cells (Fan *et al.*, 2019). Given that there is an inverse relationship between the Young modulus of a biomaterial and the microjetting speed during cavitation, this may explain why molecular delivery was significantly higher in cells at the S phase compared to other cell cycle phases (Fong *et al.*, 2006). These intrinsic properties associated with cell cycle phases may be due to rearrangement of the cytoskeleton system throughout each phase of the cell cycle. Further studies are ultimately required to determine the effect of cell cycle phases on membrane pore formation and recovery rate. Additionally, cell cycle phases may also play a critical role in modulating molecular delivery to certain organelles, as certain components of the cell are modified and duplicated during each cell cycle phase. For example, during M phase the nuclear membrane is disrupted to enable cell division, which may allow direct intranuclear delivery of DNA for genome editing. The results of our study suggest that techniques to temporarily sync T cells to the S phase of the cell cycle may further enhance acoustofluidic-mediated molecular delivery.

Additionally, the effect of acoustofluidic treatment on cell proliferation, long-term viability (2+ days), and the percentage of cells in each cell cycle phase were assessed. At day 0, minimal differences were detected in the percentage of cells at each cell cycle phase for each treatment condition, with only a moderately significant difference found between no treatment and flow only control groups (without ultrasound) for cells in the G2/M phase. Interestingly, significant

differences in G0/G1 phase, S phase, and G2 phase were observed at 2 days after acoustofluidic treatment compared to the no treatment control group without ultrasound. Recently, a study investigated the effect of sonoporation on cell cycle phases in immortalized B cells and found that within 12 hr post-treatment there were significant changes in the relative number of cells in the G0/G1 phase and in the S phase, compared to control samples without sonoporation (Duan *et al.*, 2021).

Multiple factors could affect the relative percentage of cells in each cell cycle phase, such as apoptosis, necrosis, and reduced proliferation (Duan *et al.*, 2021). These factors could explain the lower number of viable cells that we observed at 2 days after acoustofluidic treatment compared to control groups without ultrasound treatment. Interestingly, no increase in the percentage of non-viable cells was detected at 2 days after acoustofluidic treatment compared control groups without ultrasound treatment. This suggests that the lower number of viable cells observed at 2 days after acoustofluidic treatment may be due to a reduction in proliferation rate rather than a loss of viability. However, this reduced proliferation rate appears to be transient, since there were no significant differences in the number of viable cells at 4 days after acoustofluidic treatment compared to control groups without ultrasound treatment, after cells were replated at a concentration of 100,000/mL at 2 days post-treatment. These results suggest that cells resume normal function and proliferation rates within 2 days after acoustofluidic treatment.

The impact of cell culture media supplements and metabolites (*i.e.*, extracellular fetal bovine serum and Ca^{2+} levels) on acoustofluidic-mediated molecular delivery and cell viability were also assessed. Serum contains vital components that include attachment-promoting proteins, hormones, vitamins, and growth factors which are essential for the cell growth and maintenance during culture for mammalian cells (Milo *et al.*, 1976; Marmottant and Hilgenfeldt, 2003; van der Valk *et al.*, 2010). In our study, we showed that using serum supplemented culture media during acoustofluidic treatment improved cell viability while reducing molecular delivery when treating with the acoustofluidic device. Multiple factors could explain this outcome: i.) serum proteins can modify metabolic processes which can alter cell viability and molecular delivery efficiency, ii.) anionic charged-surfaces on serum proteins may interact with cationic microbubbles via charge-charge interaction and subsequently reduce microbubble interaction with cells, iii.) serum proteins may compete with cationic microbubbles for binding sites on the plasma membrane of cells. Reduced-serum culture media was previously reported to reduce cell viability in immortal cell lines compared to serum-supplemented media (Rashid and Coombs, 2019). Interestingly, the study reported that serum proteins can also compete with transfection vehicles for cell surface receptors (Rashid and Coombs, 2019). This may be explained by the high number of reactive amino acid residues in serum proteins (*e.g.*, aspartic acid, glutamic acid) (Wu *et al.*, 2013). In fact, serum albumin proteins have been attached to microbubbles in some studies to stabilize the microbubble shell, although temporary disruption to the tertiary albumin structure by reduction of disulfide bonds is required for

enhanced binding to microbubbles (Du *et al.*, 2018). Given that conjugation of albumin proteins can affect microbubble interactions with cells, native albumin and other proteins in serum are also likely to interact with microbubbles and influence their interactions with the plasma membrane surface on cells. Negatively-charged amino acids on the exterior surface of proteins may have similar interactions with cationic microbubbles, which could reduce microbubble-cell interactions and limit plasma membrane damage during sonoporation.

Another key metabolite that can influence intracellular molecular delivery is Ca^{2+} , which is closely associated with regulation of many key biochemical functions of cells and has been shown to have an important role in cell membrane repair (Berridge *et al.*, 2003; Zhou *et al.*, 2008). In addition, extracellular Ca^{2+} (3 mM) has been shown to improve recovery of *Xenopus* oocytes after sonoporation by facilitating enhanced membrane repair compared to oocytes with lower levels of extracellular Ca^{2+} (Zhou *et al.*, 2008). In our study, we investigated the effect of a potent calcium chelator (EGTA) on molecular delivery and cell recovery when cells were suspended in RPMI culture media or PBS solutions. RPMI contains 0.42 mM Ca^{2+} in solution before FBS supplementation but Ca^{2+} is chelated in the presence of EGTA, which may reduce extracellular calcium being accessible intracellularly during sonoporation. Reduced amounts of extracellular calcium have been shown to cause decreased levels of contraction, exocytosis, endocytosis, membrane patching, and plugging after plasma membrane damage (Bement and Capco, 1991; Steinhardt *et al.*, 1994; Eddleman *et al.*, 1997; Terasaki *et al.*, 1997; Idone *et al.*, 2008; Moe *et al.*, 2015). In fact, extracellular Ca^{2+} influx has been

shown to improve F-actin patching of cell membranes. Without sufficient levels of intracellular Ca^{2+} , plasma membrane repair can be significantly inhibited, and the membrane can become very susceptible to irreversible damage. It's feasible that unbound EGTA can sequester intracellular Ca^{2+} , especially during sonoporation where plasma membrane and organelles are modified. This may explain the significant decrease in viability after acoustofluidic treatment for cells in PBS and 1mM EGTA solution. However, high cell viability was maintained after acoustofluidic treatment in FBS-supplemented RPMI solutions even with calcium chelators (1 mM EGTA). This finding may be due to EGTA binding to extracellular Ca^{2+} in FBS-supplemented RPMI solutions, such that very little unbound EGTA remains available to bind to intracellular Ca^{2+} . However, FBS-supplemented RPMI also contains many other ions and proteins which are absent from PBS, and these factors may also influence molecular delivery and cell viability. It's feasible that additional factors in FBS-supplemented RPMI solution may aid in repairing the plasma membrane and restoring cell homeostasis after sonoporation.

Another fundamental parameter that may influence molecular delivery is the temperature of the cell solution. In this study, the cell solution was stored on ice ($\sim 0^\circ\text{C}$) before and after treatment. Temperature may have important implications on lipid membrane properties as lower temperatures promote gel phase consistency where the cell membrane maintains a rigid layer, while higher temperatures promote membrane fluidity. In fact, a prior study investigated laser-induced transfection efficiency between 37°C – 45°C with different cell types and found that transfection efficiency at these temperatures may be cell type

dependent (Terakawa *et al.*, 2006). This outcome is likely caused by complex biological differences between cell types that may be influenced by different temperature responses (Terakawa *et al.*, 2006). Ultimately, further studies are required to understand thermal implications on molecular delivery in our acoustofluidic device.

The effect of exogenous microbubbles on acoustofluidic-mediated molecular delivery to human T cells and the impact of acoustofluidic treatment on organelle structures has not been previously characterized. Interestingly, we found that there is significant disruption of subcellular organelles with only 2-3 seconds of exposure time to ultrasound in the acoustofluidic channels. Importantly, we observed evidence that the nuclear membrane was disrupted, which may indicate that rapid, direct delivery of genomic material to the nucleus could be feasible with acoustofluidic treatment. Rapid delivery of genomic material to the nucleus is a challenge with current genomic delivery platforms, so acoustofluidic technology may offer advantages for rapid intranuclear delivery of DNA or other biomolecules. Additionally, we observed off-staining of the cationic blue dye in the nucleus after acoustofluidic treatment. It's possible that cationic lipids from microbubbles are being delivered into the nucleus. If so, genomic editing material, such as CRISPR-Cas9 components, could potentially be delivered directly into the nucleus during acoustofluidic treatment. Further studies are required to assess the efficacy of this platform for gene editing or other functional gene delivery applications.

The effect of microbubble concentration on intracellular delivery of molecular compounds after acoustofluidic treatment has been described

previously (Centner *et al.*, 2021a), but only with one cell line (Jurkat T cells). In this study, we also evaluated molecular delivery of a macromolecule (150 kDa) using the 3D-printed acoustofluidic device with multiple cell lines to assess whether differences in cell phenotype affect acoustofluidic-mediated molecular delivery and cell viability. For all cell lines tested in this study, a microbubble concentration of 5% v/v significantly enhanced intracellular delivery of 150 kDa FITC-Dextran compared to negative control groups without ultrasound treatment. However, at higher microbubble concentrations we observed reduced molecular delivery in each cell type. This trend may be explained by higher levels of multiple scattering within the acoustofluidic channels when high microbubble concentrations are present, which can reduce the ultrasound pressures to cells further away from the source transducer and lead to reduced levels of sonoporation. These results indicate that microbubble concentrations must be optimized for acoustofluidic-mediated molecular delivery, but the optimal parameters may be similar for multiple cell types.

Multiple biological parameters likely influence molecular delivery to cells. The activity of our cationic microbubble formulation is likely influenced by anionic charges expressed on the plasma membrane but may also be influenced by cell size. If plasma membrane surface charge is maintained, increased cell diameter should facilitate more microbubble-cell interactions and may enable higher levels of molecular delivery. For example, Jurkat T cells have a diameter of 10-16 μm , while naïve primary T cells have a diameter of 5-7 μm (Rosenbluth *et al.*, 2006; Tasnim *et al.*, 2018). If they have the similar membrane potentials, naïve primary

T cells should have less microbubble-cell interactions compared to Jurkat T cells and subsequently have reduced sonoporation effects on the cells. This may ultimately lead to lower levels of molecular delivery. For subcellular molecular delivery, it may be further complicated by organelle size and distance from the plasma membrane as microstreaming/microjetting effects from microbubble cavitation are reduced as distance increases. Thus, small distal organelle structures may be more challenging to modify by microbubble cavitation. Further studies are ultimately required to understand the impact of microbubble cavitation dynamics in our acoustofluidic device.

Prior acoustofluidic studies have extensively characterized the impact of physical parameters, such as ultrasound pressure amplitude, acoustofluidic channel geometry, and microbubble surface charge, on acoustofluidic-mediated molecular delivery (Centner *et al.*, 2021a). However, the impact of biological parameters such as cell cycle phase, cell plating density, and extracellular biological supplements on acoustofluidic-mediated molecular delivery was largely unknown. The results of this study demonstrate that key biological factors must be carefully regulated to achieve optimal delivery of biomolecules with acoustofluidic treatment, which may potentially lead to improved non-viral methods for manufacturing of cell therapies.

VI.5. Conclusions

This study provides new insights into biomodulatory effects of non-viral molecular delivery to human T cells using a novel 3D-printed plastic acoustofluidic

device requiring only 2-3 seconds of treatment time. These results demonstrate that changes in initial cell plating density have implications on the efficiency of acoustofluidic-mediated molecular delivery in human T cells. In addition, the results indicate that cell cycle phase can affect acoustofluidic molecular delivery to human T cells. This study also reveals that acoustofluidic treatment can induce changes to cellular organelle structures, which may enable delivery of biomolecules directly into the nucleus for gene editing or other applications. This study suggests that acoustofluidic technology holds promise for improved non-viral transfection and manufacturing of human T cell therapies.

CHAPTER VII – CONCLUSIONS AND FUTURE WORK

VII.1. Summary

The role of microbubbles in acoustofluidic delivery has not been previously studied. The central hypothesis of this dissertation is that an ***acoustofluidic platform and microbubbles enhance molecular delivery to human cells.***

Experiments in this dissertation were designed to address several relevant research questions:

1. *What are fundamental parameters that modulate molecular delivery efficiency?*

Fundamental properties that modulate molecular delivery efficiency in the PDMS-based acoustofluidic were determined and are described in Chapter III. Fundamental parameters that effect biomolecular delivery to erythrocytes were determined experimentally.

2. *Does microbubble destruction in the acoustofluidic channel correlate with molecular delivery to cells?*

The relationship between microbubble destruction and molecular delivery in 3D-printed acoustofluidic device were determined and are described in Chapter IV. Microbubble destruction and molecular delivery to human T cells were determined experimentally and the results were compared to assess their relationship.

3. *Does acoustofluidic treatment achieve similar molecular delivery levels as static ultrasound treatment?*

Molecular delivery levels to human T cells with acoustofluidic treatment and static ultrasound treatment were determined and are described in Chapter

V. With refined parameters, acoustofluidic treatment and static ultrasound treatment were experimentally determined with small molecules (≤ 1 kDa) and large molecules (≥ 10 kDa).

4. *What effects do acoustofluidic treatment and cell culture media formulations induce on molecular delivery and subcellular organelle structures?*

Acoustofluidic treatment in a 3D-printed acoustofluidic device and the effect of different cell culture media formulations were determined and are described in Chapter VI. Fundamental biological parameters that effect molecular delivery to T cells were determined experimentally.

VII.2. Results & Future Directions

The results of this dissertation imply that multiple parameters modulate biomolecular delivery to erythrocytes, such as flow rate, microbubble concentration, and ultrasound peak negative pressure generated with B-mode imaging. Additionally, increased microbubble destruction was observed with increasing ultrasound pressures when utilizing low ultrasound peak negative pressures (0.5-1.3 MPa). Having sufficient levels of microbubble cavitation is critical to enable intracellular delivery of impermeant compounds such as trehalose to erythrocytes. Acoustofluidic treatment showed the ability to increase recovery of freeze-dried erythrocytes compared to respective controls. This preliminary study laid the groundwork for subsequent experimental studies that further enhanced long-term storage of erythrocytes at ambient temperatures (Janis *et al.*, 2021).

Feasibility of the acoustofluidic platform was demonstrated using erythrocytes, but the PDMS-based acoustofluidic device had several limitations, including low processing rates, inconsistent device dimensions due to batch-to-batch variability, and frequency clogging or device damage during operation. Thus, a 3D-printed device was designed to enable consistent device dimensions and to increase device channel diameters for faster processing rates. Human T cells were utilized for these studies as acoustofluidic-mediated molecular delivery has the capacity to address current T-cell manufacturing limitations, which includes long processing times, inconsistent molecular delivery, and insertional mutagenesis. It was found that acoustofluidic channel geometry had important implications on molecular delivery, which may be influenced by fluidic properties, such as shear stress, and acoustic properties, such as ultrasound exposure time. Microbubble charge and microbubble dose were found to be critical parameters as they may influence microbubble-cell interaction and microbubble cavitation, respectively. Mechanisms of molecular delivery in acoustofluidic devices with exogenous microbubbles have not been previously described; however, it is feasible that multiple mechanisms may enhance molecular delivery, such as transient perforation and/or enhanced endocytosis. This study revealed that the fastest uptake of biomolecules with our acoustofluidic device was within minutes, indicating that formation of transient pores in cell membranes is likely the dominant mechanism of molecular delivery. Previous studies have shown that transient perforations can repair rapidly (Hu *et al.*, 2013b). Our acoustofluidic device also showed the ability to induce molecular delivery while maintaining high cell viability.

Although our acoustofluidic device has significant potential for a variety of applications, its ability to induce molecular delivery has not been directly compared to static ultrasound treatment methods. To properly assess this, acoustofluidic treatment and static ultrasound treatment parameters were refined based on ultrasound pressure, microbubble dose, and ultrasound exposure time. Refined parameters were directly compared using a small molecule (0.6 kDa calcein) and a large molecule (150 kDa-FITC Dextran). Acoustofluidic treatment and static ultrasound treatment achieved similar levels of molecular delivery for small and large molecules, even though acoustofluidic treatment was able to achieve this with a lower microbubble concentration and approximately 20x less exposure time (~2-3 s vs. 45 s) in human T cells.

Previous studies have shown that sonoporation can influence cell proliferation, cell viability, and cell cycle phases. These studies, however, were conducted in static ultrasound configurations with different acoustic parameters, microbubble properties, and different cell types. Furthermore, these studies did not characterize ultrasound effects on organelle structures and also did not assess the effects of biological and cell culture media formulation parameters on molecular delivery. Further characterization of acoustofluidic treatment on organelle structural modification, cell repair mechanisms, and cell proliferation is required for potential cell manufacturing applications. In our study, we found that acoustofluidic treatment can induce modification to the plasma membrane and nuclear membrane. Our acoustofluidic device can potentially induce rapid delivery of biomolecules to the nucleus for genome modification, if desired. This is a

significant advantage compared to current cell manufacturing technologies, which generally rely on viral vectors to induce delivery across the plasma membrane. Viral delivery then requires further time and molecular signaling to transport payloads into the nucleus. If cytosol delivery is only required, acoustofluidic parameters, such as ultrasound pressure, could be optimized to reduce nuclear delivery. Although perforations are formed in the plasma membrane, actin patches are rapidly formed to reverse perforation and help cells achieve homeostasis. Additionally, acoustofluidic treatment induces temporary disruptions in the cell cycle and briefly reduces proliferation, but it appears that normal cell proliferation resumes within 2 days after acoustofluidic treatment. This likely signifies that repair of organelle structures may be required after acoustofluidic treatment before entering subsequent cell division cycles. Future studies are ultimately required to understand the relationship between high molecular delivery levels and prolonged cell viability as initial studies only utilized PI staining as a proxy of cell viability within an hour of acoustofluidic treatment. This ultimately may not be representative of cell viability of high molecular delivery across a prolonged timeframe. Cells may be sorted based on molecular delivery levels to be assessed at longer timepoints. This will likely provide insights into reasons for reduced cell counts 48 hours post-treatment compared to respective controls. Additionally, cell cycle phase also influences molecular delivery and cell viability. Thus, syncing the cell cycle may potentially be utilized to further enhance molecular delivery and improve cell viability. Finally, cell plating density and cell culture media formulations were found to have important implications on molecular delivery and

cell viability. These results indicate that biological properties have a significant impact on acoustofluidic-mediated molecular delivery to human T cells along with cell viability.

Acoustofluidic treatment showed the capacity to modify both the plasma membrane and subcellular organelles, but implications on cellular signaling and functional activity have yet to be characterized. To understand the implications of acoustofluidic treatment, further studies are required to characterize changes in cellular signaling through techniques such as RNA sequencing and proteomics. Additionally, functional assays such as cytotoxicity assay, intracellular cytokine staining, and proliferation assay are required to ensure intended immunological function is achieved. These studies will provide critical information prior to conducting animal studies.

In summary, 3D-printed acoustofluidic devices represent a platform technology for cell manufacturing applications that can be used a variety of cell types and applications. The system allows users to modulate numerous parameters, including acoustofluidic and biological parameters, for their tailored applications. Further studies are ultimately required to assess the ability of acoustofluidic treatment to induce functional delivery compared to current cell manufacturing techniques. However, this dissertation was able to satisfy the central hypothesis and address underlying questions regarding acoustofluidic-mediated molecular delivery to human cells.

REFERENCES

- Aghamohammadzadeh, S., and Ayscough, K. R. (2009). "Differential requirements for actin during yeast and mammalian endocytosis," *Nat Cell Biol* **11**, 1039-1042.
- Annesley, C. E., Summers, C., Ceppi, F., and Gardner, R. A. (2018a). "The Evolution and Future of CAR T Cells for B-Cell Acute Lymphoblastic Leukemia," *Clin Pharmacol Ther* **103**, 591-598.
- Annesley, C. E., Summers, C., Ceppi, F., and Gardner, R. A. (2018b). "The Evolution and Future of CAR T Cells for B-Cell Acute Lymphoblastic Leukemia," *Clinical Pharmacology & Therapeutics* **103**, 591-598.
- Antfolk, M., Magnusson, C., Augustsson, P., Lilja, H., and Laurell, T. (2015). "Acoustofluidic, label-free separation and simultaneous concentration of rare tumor cells from white blood cells," *Anal Chem* **87**, 9322-9328.
- Arav, A., and Natan, D. (2012). "Freeze drying of red blood cells: the use of directional freezing and a new radio frequency lyophilization device," *Biopreserv Biobank* **10**, 386-394.
- Awasthi, R., Pacaud, L., Waldron, E., Tam, C. S., Jager, U., Borchmann, P., Jaglowski, S., Foley, S. R., van Besien, K., Wagner-Johnston, N. D., Kersten, M. J., Schuster, S. J., Salles, G., Maziarz, R. T., Anak, O., Del Corral, C., Chu, J., Gershgorin, I., Pruteanu-Malinici, I., Chakraborty, A., Mueller, K. T., and Waller, E. K. (2020). "Tisagenlecleucel cellular kinetics, dose, and immunogenicity in relation to clinical factors in relapsed/refractory DLBCL," *Blood Adv* **4**, 560-572.
- Barnkob, R., and Bruus, H. (2009). "Acoustofluidics: theory and simulation of radiation forces at ultrasound resonances in microfluidic devices," *Proc Mtgs Acoust* **6**, 020001.
- Barrangou, R., and Doudna, J. A. (2016). "Applications of CRISPR technologies in research and beyond," *Nat Biotechnol* **34**, 933-941.
- Belling, J. N., Heidenreich, L. K., Tian, Z., Mendoza, A. M., Chiou, T. T., Gong, Y., Chen, N. Y., Young, T. D., Wattanatorn, N., Park, J. H., Scarabelli, L., Chiang, N., Takahashi, J., Young, S. G., Stieg, A. Z., De Oliveira, S., Huang, T. J., Weiss, P. S., and Jonas, S. J. (2020a). "Acoustofluidic sonoporation for gene delivery to human hematopoietic stem and progenitor cells," *Proc Natl Acad Sci U S A* **117**, 10976-10982.
- Belling, J. N., Heidenreich, L. K., Tian, Z., Mendoza, A. M., Chiou, T. T., Gong, Y., Chen, N. Y., Young, T. D., Wattanatorn, N., Park, J. H., Scarabelli, L., Chiang, N., Takahashi, J., Young, S. G., Stieg, A. Z., De Oliveira, S., Huang, T. J., Weiss, P. S., and Jonas, S. J. (2020b). "Acoustofluidic sonoporation for gene delivery to human hematopoietic stem and progenitor cells," *Proceedings of the National Academy of Sciences* **117**, 10976-10982.
- Bement, W. M., and Capco, D. G. (1991). "Analysis of inducible contractile rings suggests a role for protein kinase C in embryonic cytokinesis and wound healing," *Cell Motil Cytoskeleton* **20**, 145-157.
- Berridge, M. J., Bootman, M. D., and Roderick, H. L. (2003). "Calcium signalling: dynamics, homeostasis and remodelling," *Nat Rev Mol Cell Biol* **4**, 517-529.

- Bhutto, D. F., Murphy, E. M., Priddy, M. C., Centner, C. C., Moore Iv, J. B., Bolli, R., and Kopechek, J. A. (2018). "Effect of Molecular Weight on Sonoporation-Mediated Uptake in Human Cells," *Ultrasound Med Biol* **44**, 2662-2672.
- Billett, H. H. (1990). "Hemoglobin and Hematocrit," in *Clinical Methods: The History, Physical, and Laboratory Examinations*, edited by rd, H. K. Walker, W. D. Hall, and J. W. Hurst (Boston).
- Bose, N., Zhang, X., Maiti, T. K., and Chakraborty, S. (2015). "The role of acoustofluidics in targeted drug delivery," *Biomicrofluidics* **9**, 052609.
- Brentjens, R. J., Riviere, I., Park, J. H., Davila, M. L., Wang, X., Stefanski, J., Taylor, C., Yeh, R., Bartido, S., Borquez-Ojeda, O., Olszewska, M., Bernal, Y., Pegram, H., Przybylowski, M., Hollyman, D., Usachenko, Y., Pirraglia, D., Hosey, J., Santos, E., Halton, E., Maslak, P., Scheinberg, D., Jurcic, J., Heaney, M., Heller, G., Frattini, M., and Sadelain, M. (2011). "Safety and persistence of adoptively transferred autologous CD19-targeted T cells in patients with relapsed or chemotherapy refractory B-cell leukemias," *Blood* **118**, 4817-4828.
- Brentjens, R. J., Santos, E., Nikhamin, Y., Yeh, R., Matsushita, M., La Perle, K., Quintas-Cardama, A., Larson, S. M., and Sadelain, M. (2007). "Genetically targeted T cells eradicate systemic acute lymphoblastic leukemia xenografts," *Clin Cancer Res* **13**, 5426-5435.
- Bruning, S. C., Rivens, I., Mouratidis, P., and Ter Haar, G. (2019). "Focused Ultrasound-Mediated Hyperthermia in Vitro: An Experimental Arrangement for Treating Cells under Tissue-Mimicking Conditions," *Ultrasound Med Biol* **45**, 3290-3297.
- Bruus, H. (2012). "Acoustofluidics 7: The acoustic radiation force on small particles," *Lab Chip* **12**, 1014-1021.
- Bruus, H., Dual, J., Hawkes, J., Hill, M., Laurell, T., Nilsson, J., Radel, S., Sadhal, S., and Wiklund, M. (2011). "Forthcoming Lab on a Chip tutorial series on acoustofluidics: acoustofluidics-exploiting ultrasonic standing wave forces and acoustic streaming in microfluidic systems for cell and particle manipulation," *Lab Chip* **11**, 3579-3580.
- Bunn, H. F., May, M. H., Kocholaty, W. F., and Shields, C. E. (1969). "Hemoglobin function in stored blood," *J Clin Invest* **48**, 311-321.
- Buzhor, E., Leshansky, L., Blumenthal, J., Barash, H., Warshawsky, D., Mazor, Y., and Shtrichman, R. (2014). "Cell-based therapy approaches: the hope for incurable diseases," *Regen Med* **9**, 649-672.
- Carugo, D., Ankrett, D. N., Glynne-Jones, P., Capretto, L., Boltryk, R. J., Zhang, X., Townsend, P. A., and Hill, M. (2011). "Contrast agent-free sonoporation: The use of an ultrasonic standing wave microfluidic system for the delivery of pharmaceutical agents," *Biomicrofluidics* **5**, 44108-4410815.
- Carugo, D., Aron, M., Sezgin, E., Bernardino de la Serna, J., Kuimova, M. K., Eggeling, C., and Stride, E. (2017). "Modulation of the molecular arrangement in artificial and biological membranes by phospholipid-shelled microbubbles," *Biomaterials* **113**, 105-117.

- Centner, C. S., Moore, J. T., Baxter, M. E., Long, Z. T., Miller, J. M., Kovatsenko, E. S., Xie, B., Menze, M. A., Berson, R. E., Bates, P. J., Yaddanapudi, K., and Kopechek, J. A. (2021a). "Acoustofluidic-mediated molecular delivery to human T cells with a three-dimensional-printed flow chamber," *J Acoust Soc Am* **150**, 4534.
- Centner, C. S., Murphy, E. M., Priddy, M. C., Moore, J. T., Janis, B. R., Menze, M. A., DeFilippis, A. P., and Kopechek, J. A. (2020). "Ultrasound-induced molecular delivery to erythrocytes using a microfluidic system," *Biomicrofluidics* **14**, 024114.
- Centner, C. S., Murphy, E. M., Stamp, B. F., Priddy, M. C., Moore, J. T., Bates, P. J., Menze, M. A., Yaddanapudi, K., and Kopechek, J. A. (2021b). "Assembly and Operation of an Acoustofluidic Device for Enhanced Delivery of Molecular Compounds to Cells," *J Vis Exp*.
- Chakraborty, N., Menze, M. A., Elmoazzen, H., Vu, H., Yarmush, M. L., Hand, S. C., and Toner, M. (2012). "Trehalose transporter from African chironomid larvae improves desiccation tolerance of Chinese hamster ovary cells," *Cryobiology* **64**, 91-96.
- Chen, C., Smye, S. W., Robinson, M. P., and Evans, J. A. (2006a). "Membrane electroporation theories: a review," *Med Biol Eng Comput* **44**, 5-14.
- Chen, C., Smye, S. W., Robinson, M. P., and Evans, J. A. (2006b). "Membrane electroporation theories: a review," *Medical & Biological Engineering & Computing* **44**, 5-14.
- Chen, J. Y., Scerbo, M., and Kramer, G. (2009). "A review of blood substitutes: examining the history, clinical trial results, and ethics of hemoglobin-based oxygen carriers," *Clinics (Sao Paulo)* **64**, 803-813.
- Chen, Y., Li, S., Gu, Y., Li, P., Ding, X., Wang, L., McCoy, J. P., Levine, S. J., and Huang, T. J. (2014). "Continuous enrichment of low-abundance cell samples using standing surface acoustic waves (SSAW)," *Lab Chip* **14**, 924-930.
- Chen, Y., Wu, M., Ren, L., Liu, J., Whitley, P. H., Wang, L., and Huang, T. J. (2016). "High-throughput acoustic separation of platelets from whole blood," *Lab Chip* **16**, 3466-3472.
- Chicaybam, L., Barcelos, C., Peixoto, B., Carneiro, M., Limia, C. G., Redondo, P., Lira, C., Paraguassu-Braga, F., Vasconcelos, Z. F., Barros, L., and Bonamino, M. H. (2016). "An Efficient Electroporation Protocol for the Genetic Modification of Mammalian Cells," *Front Bioeng Biotechnol* **4**, 99.
- Cho, S. W., Kim, S., Kim, J. M., and Kim, J. S. (2013). "Targeted genome engineering in human cells with the Cas9 RNA-guided endonuclease," *Nat Biotechnol* **31**, 230-232.
- Choe, J. H., Watchmaker, P. B., Simic, M. S., Gilbert, R. D., Li, A. W., Krasnow, N. A., Downey, K. M., Yu, W., Carrera, D. A., Celli, A., Cho, J., Briones, J. D., Duecker, J. M., Goretsky, Y. E., Dannenfelser, R., Cardarelli, L., Troyanskaya, O., Sidhu, S. S., Roybal, K. T., Okada, H., and Lim, W. A. (2021). "SynNotch-CAR T cells overcome challenges of specificity, heterogeneity, and persistence in treating glioblastoma," *Sci Transl Med* **13**.

- Collis, J., Manasseh, R., Liovic, P., Tho, P., Ooi, A., Petkovic-Duran, K., and Zhu, Y. (2010). "Cavitation microstreaming and stress fields created by microbubbles," *Ultrasonics* **50**, 273-279.
- Cosgrove, D. (2006). "Ultrasound contrast agents: an overview," *Eur J Radiol* **60**, 324-330.
- Crowe, J. H., Crowe, L. M., Carpenter, J. E., Petrelski, S., Hoekstra, F. A., Araujo, P. D., and Panek, A. D. (2011). "Anhydrobiosis: Cellular Adaptation to Extreme Dehydration," *Handbook of Physiology, Comparative Physiology*, 1445–1477.
- Crowe, J. H., Crowe, L. M., Wolkers, W. F., Oliver, A. E., Ma, X., Auh, J. H., Tang, M., Zhu, S., Norris, J., and Tablin, F. (2005). "Stabilization of dry Mammalian cells: lessons from nature," *Integr Comp Biol* **45**, 810-820.
- Dai, H., Zhang, W., Li, X., Han, Q., Guo, Y., Zhang, Y., Wang, Y., Wang, C., Shi, F., Zhang, Y., Chen, M., Feng, K., Wang, Q., Zhu, H., Fu, X., Li, S., and Han, W. (2015). "Tolerance and efficacy of autologous or donor-derived T cells expressing CD19 chimeric antigen receptors in adult B-ALL with extramedullary leukemia," *Oncoimmunology* **4**, e1027469.
- Datta, S., Coussios, C. C., McAdory, L. E., Tan, J., Porter, T., De Courten-Myers, G., and Holland, C. K. (2006). "Correlation of cavitation with ultrasound enhancement of thrombolysis," *Ultrasound Med Biol* **32**, 1257-1267.
- Davila, M. L., Riviere, I., Wang, X., Bartido, S., Park, J., Curran, K., Chung, S. S., Stefanski, J., Borquez-Ojeda, O., Olszewska, M., Qu, J., Wasielewska, T., He, Q., Fink, M., Shinglot, H., Youssif, M., Satter, M., Wang, Y., Hosey, J., Quintanilla, H., Halton, E., Bernal, Y., Bouhassira, D. C., Arcila, M. E., Gonen, M., Roboz, G. J., Maslak, P., Douer, D., Frattini, M. G., Giralt, S., Sadelain, M., and Brentjens, R. (2014). "Efficacy and toxicity management of 19-28z CAR T cell therapy in B cell acute lymphoblastic leukemia," *Sci Transl Med* **6**, 224ra225.
- Dayton, P., Klibanov, A., Brandenburger, G., and Ferrara, K. (1999a). "Acoustic radiation force in vivo: a mechanism to assist targeting of microbubbles," *Ultrasound Med Biol* **25**, 1195-1201.
- Dayton, P. A., Morgan, K. E., Klibanov, A. L., Brandenburger, G. H., and Ferrara, K. W. (1999b). "Optical and acoustical observations of the effects of ultrasound on contrast agents," *IEEE Trans Ultrason Ferroelectr Freq Control* **46**, 220-232.
- De Cock, I., Zagato, E., Braeckmans, K., Luan, Y., de Jong, N., De Smedt, S. C., and Lentacker, I. (2015). "Ultrasound and microbubble mediated drug delivery: acoustic pressure as determinant for uptake via membrane pores or endocytosis," *J Control Release* **197**, 20-28.
- De Temmerman, M. L., Dewitte, H., Vandenbroucke, R. E., Lucas, B., Libert, C., Demeester, J., De Smedt, S. C., Lentacker, I., and Rejman, J. (2011). "mRNA-Lipoplex loaded microbubble contrast agents for ultrasound-assisted transfection of dendritic cells," *Biomaterials* **32**, 9128-9135.
- Deeks, S. G., Wagner, B., Anton, P. A., Mitsuyasu, R. T., Scadden, D. T., Huang, C., Macken, C., Richman, D. D., Christopherson, C., June, C. H., Lazar, R., Broad, D. F., Jalali, S., and Hege, K. M. (2002). "A phase II randomized

- study of HIV-specific T-cell gene therapy in subjects with undetectable plasma viremia on combination antiretroviral therapy," *Mol Ther* **5**, 788-797.
- Delalande, A., Leduc, C., Midoux, P., Postema, M., and Pichon, C. (2015). "Efficient Gene Delivery by Sonoporation Is Associated with Microbubble Entry into Cells and the Clathrin-Dependent Endocytosis Pathway," *Ultrasound Med Biol* **41**, 1913-1926.
- Deng, J., Zhang, Y., Feng, J., and Wu, F. (2010). "Dendritic cells loaded with ultrasound-ablated tumour induce in vivo specific antitumour immune responses," *Ultrasound Med Biol* **36**, 441-448.
- Dewitte, H., Van Lint, S., Heirman, C., Thielemans, K., De Smedt, S. C., Breckpot, K., and Lentacker, I. (2014). "The potential of antigen and TriMix sonoporation using mRNA-loaded microbubbles for ultrasound-triggered cancer immunotherapy," *J Control Release* **194**, 28-36.
- DiTommaso, T., Cole, J. M., Cassereau, L., Bugge, J. A., Hanson, J. L. S., Bridgen, D. T., Stokes, B. D., Loughhead, S. M., Beutel, B. A., Gilbert, J. B., Nussbaum, K., Sorrentino, A., Toggweiler, J., Schmidt, T., Gyuelveszi, G., Bernstein, H., and Sharei, A. (2018). "Cell engineering with microfluidic squeezing preserves functionality of primary immune cells in vivo," *Proc Natl Acad Sci U S A* **115**, E10907-E10914.
- Doinikov, A. A., Haac, J. F., and Dayton, P. A. (2009). "Resonance frequencies of lipid-shelled microbubbles in the regime of nonlinear oscillations," *Ultrasonics* **49**, 263-268.
- Dressaire, E., and Sauret, A. (2016). "Clogging of microfluidic systems," *Soft Matter* **13**, 37-48.
- Du, J., Zhao, X., Li, B., Mou, Y., and Wang, Y. (2018). "DNA-loaded microbubbles with crosslinked bovine serum albumin shells for ultrasound-promoted gene delivery and transfection," *Colloids Surf B Biointerfaces* **161**, 279-287.
- Duan, X., Zhou, Q., Wan, J. M. F., and Yu, A. C. H. (2021). "Sonoporation generates downstream cellular impact after membrane resealing," *Sci Rep* **11**, 5161.
- Ebina, H., Misawa, N., Kanemura, Y., and Koyanagi, Y. (2013). "Harnessing the CRISPR/Cas9 system to disrupt latent HIV-1 provirus," *Sci Rep* **3**, 2510.
- Eddleman, C. S., Ballinger, M. L., Smyers, M. E., Godell, C. M., Fishman, H. M., and Bittner, G. D. (1997). "Repair of plasmalemmal lesions by vesicles," *Proc Natl Acad Sci U S A* **94**, 4745-4750.
- Eroglu, A., Russo, M. J., Bieganski, R., Fowler, A., Cheley, S., Bayley, H., and Toner, M. (2000). "Intracellular trehalose improves the survival of cryopreserved mammalian cells," *Nat Biotechnol* **18**, 163-167.
- Escoffre, J. M., Novell, A., Piron, J., Zeghimi, A., Doinikov, A., and Bouakaz, A. (2013). "Microbubble attenuation and destruction: are they involved in sonoporation efficiency?," *IEEE Trans Ultrason Ferroelectr Freq Control* **60**, 46-52.
- Falk, H., Forde, P. F., Bay, M. L., Mangalanathan, U. M., Hojman, P., Soden, D. M., and Gehl, J. (2017). "Calcium electroporation induces tumor eradication, long-lasting immunity and cytokine responses in the CT26 colon cancer mouse model," *Oncoimmunology* **6**, e1301332.

- Fan, P., Yang, D., Wu, J., Yang, Y., Guo, X., Tu, J., and Zhang, D. (2019). "Cell-cycle-dependences of membrane permeability and viability observed for HeLa cells undergoing multi-bubble-cell interactions," *Ultrason Sonochem* **53**, 178-186.
- Fan, Z., Chen, D., and Deng, C. X. (2013). "Improving ultrasound gene transfection efficiency by controlling ultrasound excitation of microbubbles," *J Control Release* **170**, 401-413.
- Fan, Z., Kumon, R. E., and Deng, C. X. (2014a). "Mechanisms of microbubble-facilitated sonoporation for drug and gene delivery," *Therapeutic Delivery* **5**, 467-486.
- Fan, Z., Kumon, R. E., and Deng, C. X. (2014b). "Mechanisms of microbubble-facilitated sonoporation for drug and gene delivery," *Ther Deliv* **5**, 467-486.
- Fan, Z., Liu, H., Mayer, M., and Deng, C. X. (2012). "Spatiotemporally controlled single cell sonoporation," *Proc Natl Acad Sci U S A* **109**, 16486-16491.
- Fekri, F., Delos Santos, R. C., Karshafian, R., and Antonescu, C. N. (2016). "Ultrasound Microbubble Treatment Enhances Clathrin-Mediated Endocytosis and Fluid-Phase Uptake through Distinct Mechanisms," *PLoS One* **11**, e0156754.
- Ferguson, S. M., Raimondi, A., Paradise, S., Shen, H., Mesaki, K., Ferguson, A., Destaing, O., Ko, G., Takasaki, J., Cremona, O., E, O. T., and De Camilli, P. (2009). "Coordinated actions of actin and BAR proteins upstream of dynamin at endocytic clathrin-coated pits," *Dev Cell* **17**, 811-822.
- Feril, L. B., Jr., Ogawa, R., Tachibana, K., and Kondo, T. (2006). "Optimized ultrasound-mediated gene transfection in cancer cells," *Cancer Sci* **97**, 1111-1114.
- Fitzpatrick, G. M., Cliff, R., and Tandon, N. (2013). "Thrombosomes: a platelet-derived hemostatic agent for control of noncompressible hemorrhage," *Transfusion* **53 Suppl 1**, 100S-106S.
- Fong, S. W., Klaseboer, E., Turangan, C. K., Khoo, B. C., and Hung, K. C. (2006). "Numerical analysis of a gas bubble near bio-materials in an ultrasound field," *Ultrasound Med Biol* **32**, 925-942.
- Forbes, M. M., Steinberg, R. L., and O'Brien, W. D., Jr. (2011). "Frequency-dependent evaluation of the role of definity in producing sonoporation of Chinese hamster ovary cells," *J Ultrasound Med* **30**, 61-69.
- Friend, J., and Yeo, L. Y. (2011). "Microscale acoustofluidics: Microfluidics driven via acoustics and ultrasonics," *Rev Mod Phys* **83**, 647.
- Gardlik, R., Palfy, R., Hodosy, J., Lukacs, J., Turna, J., and Celec, P. (2005). "Vectors and delivery systems in gene therapy," *Medical Science Monitor* **11**, RA110-121.
- Gardner, R. A., Finney, O., Annesley, C., Brakke, H., Summers, C., Leger, K., Bleakley, M., Brown, C., Mgebroff, S., Kelly-Spratt, K. S., Hoglund, V., Lindgren, C., Oron, A. P., Li, D., Riddell, S. R., Park, J. R., and Jensen, M. C. (2017). "Intent-to-treat leukemia remission by CD19 CAR T cells of defined formulation and dose in children and young adults," *Blood* **129**, 3322-3331.

- Gedge, M., and Hill, M. (2012a). "Acoustofluidics 17: theory and applications of surface acoustic wave devices for particle manipulation," *Lab on a Chip* **12**, 2998-3007.
- Gedge, M., and Hill, M. (2012b). "Acoustofluidics 17: theory and applications of surface acoustic wave devices for particle manipulation," *Lab Chip* **12**, 2998-3007.
- Gehl, J. (2003a). "Electroporation: theory and methods, perspectives for drug delivery, gene therapy and research," *Acta Physiologica Scandinavica* **177**, 437-447.
- Gehl, J. (2003b). "Electroporation: theory and methods, perspectives for drug delivery, gene therapy and research," *Acta Physiol Scand* **177**, 437-447.
- Geng, T., and Lu, C. (2013). "Microfluidic electroporation for cellular analysis and delivery," *Lab Chip* **13**, 3803-3821.
- Ghani, K., Wang, X., de Campos-Lima, P. O., Olszewska, M., Kamen, A., Riviere, I., and Caruso, M. (2009). "Efficient human hematopoietic cell transduction using RD114- and GALV-pseudotyped retroviral vectors produced in suspension and serum-free media," *Hum Gene Ther* **20**, 966-974.
- Gourevich, D., Volovick, A., Dogadkin, O., Wang, L., Mulvana, H., Medan, Y., Melzer, A., and Cochran, S. (2015). "In Vitro Investigation of the Individual Contributions of Ultrasound-Induced Stable and Inertial Cavitation in Targeted Drug Delivery," *Ultrasound Med Biol* **41**, 1853-1864.
- Greenwalt, T. J., Zehner Sostok, C., and Dumaswala, U. J. (1990). "Studies in red blood cell preservation. 2. Comparison of vesicle formation, morphology, and membrane lipids during storage in AS-1 and CPDA-1," *Vox Sang* **58**, 90-93.
- Grievink, H. W., Luisman, T., Kluft, C., Moerland, M., and Malone, K. E. (2016). "Comparison of Three Isolation Techniques for Human Peripheral Blood Mononuclear Cells: Cell Recovery and Viability, Population Composition, and Cell Functionality," *Biopreserv Biobank* **14**, 410-415.
- Grunebach, F., Muller, M. R., Nencioni, A., and Brossart, P. (2003). "Delivery of tumor-derived RNA for the induction of cytotoxic T-lymphocytes," *Gene Ther* **10**, 367-374.
- Guo, F., Mao, Z., Chen, Y., Xie, Z., Lata, J. P., Li, P., Ren, L., Liu, J., Yang, J., Dao, M., Suresh, S., and Huang, T. J. (2016). "Three-dimensional manipulation of single cells using surface acoustic waves," *Proc Natl Acad Sci U S A* **113**, 1522-1527.
- Haar, G. T., and Coussios, C. (2007). "High intensity focused ultrasound: physical principles and devices," *Int J Hyperthermia* **23**, 89-104.
- Hacein-Bey-Abina, S., Hauer, J., Lim, A., Picard, C., Wang, G. P., Berry, C. C., Martinache, C., Rieux-Laucat, F., Latour, S., Belohradsky, B. H., Leiva, L., Sorensen, R., Debre, M., Casanova, J. L., Blanche, S., Durandy, A., Bushman, F. D., Fischer, A., and Cavazzana-Calvo, M. (2010). "Efficacy of gene therapy for X-linked severe combined immunodeficiency," *N Engl J Med* **363**, 355-364.

- Halldorsson, S., Lucumi, E., Gomez-Sjoberg, R., and Fleming, R. M. T. (2015). "Advantages and challenges of microfluidic cell culture in polydimethylsiloxane devices," *Biosensors and Bioelectronics* **63**, 218-231.
- Hand, S. C., and Menze, M. A. (2015). "Molecular approaches for improving desiccation tolerance: insights from the brine shrimp *Artemia franciscana*," *Planta* **242**, 379-388.
- Haradin, A. R., Weed, R. I., and Reed, C. F. (1969). "Changes in physical properties of stored erythrocytes relationship to survival in vivo," *Transfusion* **9**, 229-237.
- Hashimoto, M., and Takemoto, T. (2015a). "Electroporation enables the efficient mRNA delivery into the mouse zygotes and facilitates CRISPR/Cas9-based genome editing," *Sci Rep* **5**, 11315.
- Hashimoto, M., and Takemoto, T. (2015b). "Electroporation enables the efficient mRNA delivery into the mouse zygotes and facilitates CRISPR/Cas9-based genome editing," *Scientific Reports* **5**, 11315.
- Hassan, M. A., Campbell, P., and Kondo, T. (2010). "The role of Ca(2+) in ultrasound-elicited bioeffects: progress, perspectives and prospects," *Drug Discov Today* **15**, 892-906.
- Hauser, J., Ellisman, M., Steinau, H. U., Stefan, E., Dudda, M., and Hauser, M. (2009). "Ultrasound enhanced endocytotic activity of human fibroblasts," *Ultrasound Med Biol* **35**, 2084-2092.
- He, C., Wang, J., Sun, S., Zhang, Y., and Li, S. (2019). "Immunomodulatory Effect after Irreversible Electroporation in Patients with Locally Advanced Pancreatic Cancer," *J Oncol* **2019**, 9346017.
- Helfield, B., Black, J. J., Qin, B., Pacella, J., Chen, X., and Villanueva, F. S. (2016a). "Fluid Viscosity Affects the Fragmentation and Inertial Cavitation Threshold of Lipid-Encapsulated Microbubbles," *Ultrasound Med Biol* **42**, 782-794.
- Helfield, B., Chen, X., Watkins, S. C., and Villanueva, F. S. (2016b). "Biophysical insight into mechanisms of sonoporation," *Proceedings of the National Academy of Sciences* **113**, 9983-9988.
- Helfield, B., Chen, X., Watkins, S. C., and Villanueva, F. S. (2016c). "Biophysical insight into mechanisms of sonoporation," *Proc Natl Acad Sci U S A* **113**, 9983-9988.
- Hengherr, S., Worland, M. R., Reuner, A., Brummer, F., and Schill, R. O. (2009). "High-temperature tolerance in anhydrobiotic tardigrades is limited by glass transition," *Physiol Biochem Zool* **82**, 749-755.
- Hernot, S., and Klivanov, A. L. (2008). "Microbubbles in ultrasound-triggered drug and gene delivery," *Adv Drug Deliv Rev* **60**, 1153-1166.
- Hill, M., Shen, Y., and Hawkes, J. J. (2002). "Modelling of layered resonators for ultrasonic separation," *Ultrasonics* **40**, 385-392.
- Hirsch, M. L., Wolf, S. J., and Samulski, R. J. (2016). "Delivering Transgenic DNA Exceeding the Carrying Capacity of AAV Vectors," *Methods Mol Biol* **1382**, 21-39.

- Hu, Y., Wan, J. M., and Yu, A. C. (2013a). "Membrane perforation and recovery dynamics in microbubble-mediated sonoporation," *Ultrasound in Medicine and Biology* **39**, 2393-2405.
- Hu, Y., Wan, J. M., and Yu, A. C. (2013b). "Membrane perforation and recovery dynamics in microbubble-mediated sonoporation," *Ultrasound Med Biol* **39**, 2393-2405.
- Idone, V., Tam, C., Goss, J. W., Toomre, D., Pypaert, M., and Andrews, N. W. (2008). "Repair of injured plasma membrane by rapid Ca²⁺-dependent endocytosis," *J Cell Biol* **180**, 905-914.
- Izadifar, Z., Babyn, P., and Chapman, D. (2017). "Mechanical and Biological Effects of Ultrasound: A Review of Present Knowledge," *Ultrasound Med Biol* **43**, 1085-1104.
- Izzo, P., Manicone, A., Spagnuolo, A., Lauta, V. M., Di Pasquale, A., and Di Monte, D. (1999). "Erythrocytes stored in CPD SAG-mannitol: evaluation of their deformability," *Clin Hemorheol Microcirc* **21**, 335-339.
- Jaatinen, T., and Laine, J. (2007). "Isolation of mononuclear cells from human cord blood by Ficoll-Paque density gradient," *Curr Protoc Stem Cell Biol* **Chapter 2**, Unit 2A 1.
- Janis, B. R., Priddy, M. C., Otto, M. R., Kopechek, J. A., and Menze, M. A. (2021). "Sonoporation enables high-throughput loading of trehalose into red blood cells," *Cryobiology* **98**, 73-79.
- Jinek, M., Chylinski, K., Fonfara, I., Hauer, M., Doudna, J. A., and Charpentier, E. (2012). "A programmable dual-RNA-guided DNA endonuclease in adaptive bacterial immunity," *Science* **337**, 816-821.
- Johansson, L., Nikolajeff, F., Johansson, S., and Thorslund, S. (2009). "On-chip fluorescence-activated cell sorting by an integrated miniaturized ultrasonic transducer," *Anal Chem* **81**, 5188-5196.
- Juffermans, L. J., Meijering, D. B., van Wamel, A., Henning, R. H., Kooiman, K., Emmer, M., de Jong, N., van Gilst, W. H., Musters, R., Paulus, W. J., van Rossum, A. C., Deelman, L. E., and Kamp, O. (2009). "Ultrasound and microbubble-targeted delivery of therapeutic compounds: ICIN Report Project 49: Drug and gene delivery through ultrasound and microbubbles," *Neth Heart J* **17**, 82-86.
- Kaksonen, M., Toret, C. P., and Drubin, D. G. (2006). "Harnessing actin dynamics for clathrin-mediated endocytosis," *Nat Rev Mol Cell Biol* **7**, 404-414.
- Kanias, T., and Acker, J. P. (2009). "Trehalose loading into red blood cells is accompanied with hemoglobin oxidation and membrane lipid peroxidation," *Cryobiology* **58**, 232-239.
- Kawai, T., and Akira, S. (2010). "The role of pattern-recognition receptors in innate immunity: update on Toll-like receptors," *Nat Immunol* **11**, 373-384.
- Kikawada, T., Saito, A., Kanamori, Y., Nakahara, Y., Iwata, K., Tanaka, D., Watanabe, M., and Okuda, T. (2007). "Trehalose transporter 1, a facilitated and high-capacity trehalose transporter, allows exogenous trehalose uptake into cells," *Proc Natl Acad Sci U S A* **104**, 11585-11590.
- Kim, K., and Lee, W. G. (2017). "Electroporation for nanomedicine: a review," *J Mater Chem B* **5**, 2726-2738.

- Kim, M., Bayly, P. V., and Meacham, J. M. (2021). "Motile cells as probes for characterizing acoustofluidic devices," *Lab Chip* **21**, 521-533.
- Klibanov, A. L. (2006). "Microbubble contrast agents: targeted ultrasound imaging and ultrasound-assisted drug-delivery applications," *Investigative Radiology* **41**, 354-362.
- Klibanov, A. L., Shevchenko, T. I., Raju, B. I., Seip, R., and Chin, C. T. (2010). "Ultrasound-triggered release of materials entrapped in microbubble-liposome constructs: a tool for targeted drug delivery," *Journal of Controlled Release* **148**, 13-17.
- Kocak, D. D., Josephs, E. A., Bhandarkar, V., Adkar, S. S., Kwon, J. B., and Gersbach, C. A. (2019). "Increasing the specificity of CRISPR systems with engineered RNA secondary structures," *Nat Biotechnol* **37**, 657-666.
- Kochenderfer, J. N., Dudley, M. E., Kassim, S. H., Somerville, R. P., Carpenter, R. O., Stetler-Stevenson, M., Yang, J. C., Phan, G. Q., Hughes, M. S., Sherry, R. M., Raffeld, M., Feldman, S., Lu, L., Li, Y. F., Ngo, L. T., Goy, A., Feldman, T., Spaner, D. E., Wang, M. L., Chen, C. C., Kranick, S. M., Nath, A., Nathan, D. A., Morton, K. E., Toomey, M. A., and Rosenberg, S. A. (2015). "Chemotherapy-refractory diffuse large B-cell lymphoma and indolent B-cell malignancies can be effectively treated with autologous T cells expressing an anti-CD19 chimeric antigen receptor," *J Clin Oncol* **33**, 540-549.
- Kochenderfer, J. N., Somerville, R. P. T., Lu, T., Shi, V., Bot, A., Rossi, J., Xue, A., Goff, S. L., Yang, J. C., Sherry, R. M., Klebanoff, C. A., Kammula, U. S., Sherman, M., Perez, A., Yuan, C. M., Feldman, T., Friedberg, J. W., Roschewski, M. J., Feldman, S. A., McIntyre, L., Toomey, M. A., and Rosenberg, S. A. (2017). "Lymphoma Remissions Caused by Anti-CD19 Chimeric Antigen Receptor T Cells Are Associated With High Serum Interleukin-15 Levels," *J Clin Oncol* **35**, 1803-1813.
- Kochenderfer, J. N., Wilson, W. H., Janik, J. E., Dudley, M. E., Stetler-Stevenson, M., Feldman, S. A., Maric, I., Raffeld, M., Nathan, D. A., Lanier, B. J., Morgan, R. A., and Rosenberg, S. A. (2010). "Eradication of B-lineage cells and regression of lymphoma in a patient treated with autologous T cells genetically engineered to recognize CD19," *Blood* **116**, 4099-4102.
- Kopechek, J. A., Carson, A. R., McTiernan, C. F., Chen, X., Hasjim, B., Lavery, L., Sen, M., Grandis, J. R., and Villanueva, F. S. (2015). "Ultrasound Targeted Microbubble Destruction-Mediated Delivery of a Transcription Factor Decoy Inhibits STAT3 Signaling and Tumor Growth," *Theranostics* **5**, 1378-1387.
- Kopechek, J. A., Carson, A. R., McTiernan, C. F., Chen, X., Klein, E. C., and Villanueva, F. S. (2016). "Cardiac Gene Expression Knockdown Using Small Inhibitory RNA-Loaded Microbubbles and Ultrasound," *PLoS One* **11**, e0159751.
- Kopechek, J. A., Haworth, K. J., Raymond, J. L., Douglas Mast, T., Perrin, S. R., Klegerman, M. E., Huang, S., Porter, T. M., McPherson, D. D., and Holland, C. K. (2011). "Acoustic characterization of echogenic liposomes: frequency-dependent attenuation and backscatter," *J Acoust Soc Am* **130**, 3472-3481.

- Kopechek, J. A., McTiernan, C. F., Chen, X., Zhu, J., Mburu, M., Feroze, R., Whitehurst, D. A., Lavery, L., Cyriac, J., and Villanueva, F. S. (2019). "Ultrasound and Microbubble-targeted Delivery of a microRNA Inhibitor to the Heart Suppresses Cardiac Hypertrophy and Preserves Cardiac Function," *Theranostics* **9**, 7088-7098.
- Kudo, N., Okada, K., and Yamamoto, K. (2009). "Sonoporation by single-shot pulsed ultrasound with microbubbles adjacent to cells," *Biophys J* **96**, 4866-4876.
- Kumon, R. E., Aehle, M., Sabens, D., Parikh, P., Han, Y. W., Kourennyi, D., and Deng, C. X. (2009). "Spatiotemporal effects of sonoporation measured by real-time calcium imaging," *Ultrasound Med Biol* **35**, 494-506.
- Kurashina, Y., Takemura, K., and Friend, J. (2017). "Cell agglomeration in the wells of a 24-well plate using acoustic streaming," *Lab Chip* **17**, 876-886.
- Lajoinie, G., De Cock, I., Coussios, C. C., Lentacker, I., Le Gac, S., Stride, E., and Versluis, M. (2016). "In vitro methods to study bubble-cell interactions: Fundamentals and therapeutic applications," *Biomicrofluidics* **10**, 011501.
- Lee, Y. W., Luther, D. C., Kretzmann, J. A., Burden, A., Jeon, T., Zhai, S., and Rotello, V. M. (2019). "Protein Delivery into the Cell Cytosol using Non-Viral Nanocarriers," *Theranostics* **9**, 3280-3292.
- Lenhof, A., Magnusson, C., and Laurell, T. (2012). "Acoustofluidics 8: applications of acoustophoresis in continuous flow microsystems," *Lab Chip* **12**, 1210-1223.
- Lentacker, I., De Cock, I., Deckers, R., De Smedt, S. C., and Moonen, C. T. (2014). "Understanding ultrasound induced sonoporation: definitions and underlying mechanisms," *Adv Drug Deliv Rev* **72**, 49-64.
- Li, H., Friend, J. R., and Yeo, L. Y. (2007). "Surface acoustic wave concentration of particle and bioparticle suspensions," *Biomed Microdevices* **9**, 647-656.
- Li, P., and Huang, T. J. (2019). "Applications of Acoustofluidics in Bioanalytical Chemistry," *Anal Chem* **91**, 757-767.
- Li, P., Mao, Z., Peng, Z., Zhou, L., Chen, Y., Huang, P. H., Truica, C. I., Drabick, J. J., El-Deiry, W. S., Dao, M., Suresh, S., and Huang, T. J. (2015). "Acoustic separation of circulating tumor cells," *Proc Natl Acad Sci U S A* **112**, 4970-4975.
- Lin, Y. C., Li, M., and Wu, C. C. (2004). "Simulation and experimental demonstration of the electric field assisted electroporation microchip for in vitro gene delivery enhancement," *Lab on a Chip* **4**, 104-108.
- Longsine-Parker, W., Wang, H., Koo, C., Kim, J., Kim, B., Jayaraman, A., and Han, A. (2013). "Microfluidic electro-sonoporation: a multi-modal cell poration methodology through simultaneous application of electric field and ultrasonic wave," *Lab Chip* **13**, 2144-2152.
- Majumder, J., Taratula, O., and Minko, T. (2019). "Nanocarrier-based systems for targeted and site specific therapeutic delivery," *Adv Drug Deliv Rev* **144**, 57-77.
- Mali, P., Aach, J., Stranges, P. B., Esvelt, K. M., Moosburner, M., Kosuri, S., Yang, L., and Church, G. M. (2013). "CAS9 transcriptional activators for target

- specificity screening and paired nickases for cooperative genome engineering," *Nat Biotechnol* **31**, 833-838.
- Marin, A., Muniruzzaman, M., and Rapoport, N. (2001). "Acoustic activation of drug delivery from polymeric micelles: effect of pulsed ultrasound," *J Control Release* **71**, 239-249.
- Marmottant, P., and Hilgenfeldt, S. (2003). "Controlled vesicle deformation and lysis by single oscillating bubbles," *Nature* **423**, 153-156.
- Maude, S. L., Laetsch, T. W., Buechner, J., Rives, S., Boyer, M., Bittencourt, H., Bader, P., Verneris, M. R., Stefanski, H. E., Myers, G. D., Qayed, M., De Moerloose, B., Hiramatsu, H., Schlis, K., Davis, K. L., Martin, P. L., Nemecek, E. R., Yanik, G. A., Peters, C., Baruchel, A., Boissel, N., Mechinaud, F., Balduzzi, A., Krueger, J., June, C. H., Levine, B. L., Wood, P., Taran, T., Leung, M., Mueller, K. T., Zhang, Y., Sen, K., Lebwohl, D., Pulsipher, M. A., and Grupp, S. A. (2018). "Tisagenlecleucel in Children and Young Adults with B-Cell Lymphoblastic Leukemia," *N Engl J Med* **378**, 439-448.
- McNeil, P. L., and Kirchhausen, T. (2005). "An emergency response team for membrane repair," *Nat Rev Mol Cell Biol* **6**, 499-505.
- Miller, D. L., Bao, S., and Morris, J. E. (1999). "Sonoporation of cultured cells in the rotating tube exposure system," *Ultrasound Med Biol* **25**, 143-149.
- Milo, G. E., Malarkey, W. B., Powell, J. E., Blakeslee, J. R., and Yohn, D. S. (1976). "Effects of steroid hormones in fetal bovine serum on plating and cloning of human cells in vitro," *In Vitro* **12**, 23-30.
- Moe, A. M., Golding, A. E., and Bement, W. M. (2015). "Cell healing: Calcium, repair and regeneration," *Semin Cell Dev Biol* **45**, 18-23.
- Moghimi, B., Muthugounder, S., Jambon, S., Tibbetts, R., Hung, L., Bassiri, H., Hogarty, M. D., Barrett, D. M., Shimada, H., and Asgharzadeh, S. (2021). "Preclinical assessment of the efficacy and specificity of GD2-B7H3 SynNotch CAR-T in metastatic neuroblastoma," *Nat Commun* **12**, 511.
- Morgan, R. A., Gray, D., Lomova, A., and Kohn, D. B. (2017). "Hematopoietic Stem Cell Gene Therapy: Progress and Lessons Learned," *Cell Stem Cell* **21**, 574-590.
- Mount, N. M., Ward, S. J., Kefalas, P., and Hyllner, J. (2015). "Cell-based therapy technology classifications and translational challenges," *Philos Trans R Soc Lond B Biol Sci* **370**, 20150017.
- Myrset, A. H., Fjerdingstad, H. B., Bendiksen, R., Arbo, B. E., Bjerke, R. M., Johansen, J. H., Kulseth, M. A., and Skurtveit, R. (2011). "Design and characterization of targeted ultrasound microbubbles for diagnostic use," *Ultrasound Med Biol* **37**, 136-150.
- Nayerossadat, N., Maedeh, T., and Ali, P. A. (2012a). "Viral and nonviral delivery systems for gene delivery," *Advanced Biomedical Research* **1**, 27.
- Nayerossadat, N., Maedeh, T., and Ali, P. A. (2012b). "Viral and nonviral delivery systems for gene delivery," *Adv Biomed Res* **1**, 27.
- Neelapu, S. S., Locke, F. L., Bartlett, N. L., Lekakis, L. J., Miklos, D. B., Jacobson, C. A., Braunschweig, I., Oluwole, O. O., Siddiqi, T., Lin, Y., Timmerman, J. M., Stiff, P. J., Friedberg, J. W., Flinn, I. W., Goy, A., Hill, B. T., Smith, M.

- R., Deol, A., Farooq, U., McSweeney, P., Munoz, J., Avivi, I., Castro, J. E., Westin, J. R., Chavez, J. C., Ghobadi, A., Komanduri, K. V., Levy, R., Jacobsen, E. D., Witzig, T. E., Reagan, P., Bot, A., Rossi, J., Navale, L., Jiang, Y., Aycock, J., Elias, M., Chang, D., Wieszorek, J., and Go, W. Y. (2017). "Axicabtagene Ciloleucel CAR T-Cell Therapy in Refractory Large B-Cell Lymphoma," *N Engl J Med* **377**, 2531-2544.
- Nightingale, S., Wanamaker, V., Silverman, B., McCurdy, P., McMurtry, L., Quarles, P., Sandler, S. G., Triulzi, D., Whitsett, C., Hillyer, C., McCarthy, L., Goldfinger, D., and Satcher, D. (2003). "Use of sentinel sites for daily monitoring of the US blood supply," *Transfusion* **43**, 364-372.
- Oh, N., and Park, J. H. (2014). "Endocytosis and exocytosis of nanoparticles in mammalian cells," *Int J Nanomedicine* **9 Suppl 1**, 51-63.
- Parmar, R., and Majumder, S. K. (2015). "Terminal rise velocity, size distribution and stability of microbubble suspension," *Asia-Pac. J. Chem. Eng.* **10**, 450-465.
- Patist, A., and Zoerb, H. (2005). "Preservation mechanisms of trehalose in food and biosystems," *Colloids Surf B Biointerfaces* **40**, 107-113.
- Paula, D. M., Valero-Lapchik, V. B., Paredes-Gamero, E. J., and Han, S. W. (2011). "Therapeutic ultrasound promotes plasmid DNA uptake by clathrin-mediated endocytosis," *J Gene Med* **13**, 392-401.
- Pereno, V., Aron, M., Vince, O., Mannaris, C., Seth, A., de Saint Victor, M., Lajoinie, G., Versluis, M., Coussios, C., Carugo, D., and Stride, E. (2018). "Layered acoustofluidic resonators for the simultaneous optical and acoustic characterisation of cavitation dynamics, microstreaming, and biological effects," *Biomicrofluidics* **12**, 034109.
- Petersson, F., Aberg, L., Sward-Nilsson, A. M., and Laurell, T. (2007). "Free flow acoustophoresis: microfluidic-based mode of particle and cell separation," *Anal Chem* **79**, 5117-5123.
- Pfuntner, A., Wier, L. M., and Stocks, C. (2006). "Most Frequent Procedures Performed in U.S. Hospitals, 2011: Statistical Brief #165," in *Healthcare Cost and Utilization Project (HCUP) Statistical Briefs* (Rockville (MD)).
- Piscopo, N. J., Mueller, K. P., Das, A., Hematti, P., Murphy, W. L., Palecek, S. P., Capitini, C. M., and Saha, K. (2018). "Bioengineering Solutions for Manufacturing Challenges in CAR T Cells," *Biotechnol J* **13**.
- Porter, D. L., Hwang, W. T., Frey, N. V., Lacey, S. F., Shaw, P. A., Loren, A. W., Bagg, A., Marcucci, K. T., Shen, A., Gonzalez, V., Ambrose, D., Grupp, S. A., Chew, A., Zheng, Z., Milone, M. C., Levine, B. L., Melenhorst, J. J., and June, C. H. (2015). "Chimeric antigen receptor T cells persist and induce sustained remissions in relapsed refractory chronic lymphocytic leukemia," *Sci Transl Med* **7**, 303ra139.
- Prel, A., Caval, V., Gayon, R., Ravassard, P., Duthoit, C., Payen, E., Maouche-Chretien, L., Creneguy, A., Nguyen, T. H., Martin, N., Piver, E., Sevrain, R., Lamouroux, L., Leboulch, P., Deschaseaux, F., Bouille, P., Sensebe, L., and Pages, J. C. (2015). "Highly efficient in vitro and in vivo delivery of functional RNAs using new versatile MS2-chimeric retrovirus-like particles," *Mol Ther Methods Clin Dev* **2**, 15039.

- Qi, J., Ding, C., Jiang, X., and Gao, Y. (2020). "Advances in Developing CAR T-Cell Therapy for HIV Cure," *Frontiers in Immunology* **11**, 361.
- Rahim, A., Taylor, S. L., Bush, N. L., ter Haar, G. R., Bamber, J. C., and Porter, C. D. (2006). "Physical parameters affecting ultrasound/microbubble-mediated gene delivery efficiency in vitro," *Ultrasound Med Biol* **32**, 1269-1279.
- Rashid, M. U., and Coombs, K. M. (2019). "Serum-reduced media impacts on cell viability and protein expression in human lung epithelial cells," *J Cell Physiol* **234**, 7718-7724.
- Rosenbluth, M. J., Lam, W. A., and Fletcher, D. A. (2006). "Force microscopy of nonadherent cells: a comparison of leukemia cell deformability," *Biophys J* **90**, 2994-3003.
- Rossi, A., Dupaty, L., Aillot, L., Zhang, L., Gallien, C., Hallek, M., Odenthal, M., Adriouch, S., Salvetti, A., and Buning, H. (2019). "Vector uncoating limits adeno-associated viral vector-mediated transduction of human dendritic cells and vector immunogenicity," *Sci Rep* **9**, 3631.
- Sahay, G., Querbes, W., Alabi, C., Eltoukhy, A., Sarkar, S., Zurenko, C., Karagiannis, E., Love, K., Chen, D., Zoncu, R., Buganim, Y., Schroeder, A., Langer, R., and Anderson, D. G. (2013). "Efficiency of siRNA delivery by lipid nanoparticles is limited by endocytic recycling," *Nat Biotechnol* **31**, 653-658.
- Salari, A., Appak-Baskoy, S., Coe, I. R., Abousawan, J., Antonescu, C. N., Tsai, S. S. H., and Kolios, M. C. (2021). "Dosage-controlled intracellular delivery mediated by acoustofluidics for lab on a chip applications," *Lab Chip* **21**, 1788-1797.
- Sarkar, K., Katiyar, A., and Jain, P. (2009). "Growth and dissolution of an encapsulated contrast microbubble: effects of encapsulation permeability," *Ultrasound Med Biol* **35**, 1385-1396.
- Satpathy, G. R., Torok, Z., Bali, R., Dwyre, D. M., Little, E., Walker, N. J., Tablin, F., Crowe, J. H., and Tsvetkova, N. M. (2004). "Loading red blood cells with trehalose: a step towards biostabilization," *Cryobiology* **49**, 123-136.
- Schuster, S. J., Bishop, M. R., Tam, C. S., Waller, E. K., Borchmann, P., McGuirk, J. P., Jager, U., Jaglowski, S., Andreadis, C., Westin, J. R., Fleury, I., Bachanova, V., Foley, S. R., Ho, P. J., Mielke, S., Magenau, J. M., Holte, H., Pantano, S., Pacaud, L. B., Awasthi, R., Chu, J., Anak, O., Salles, G., Maziarz, R. T., and Investigators, J. (2019). "Tisagenlecleucel in Adult Relapsed or Refractory Diffuse Large B-Cell Lymphoma," *N Engl J Med* **380**, 45-56.
- Schuster, S. J., Svoboda, J., Chong, E. A., Nasta, S. D., Mato, A. R., Anak, O., Brogdon, J. L., Pruteanu-Malinici, I., Bhoj, V., Landsburg, D., Wasik, M., Levine, B. L., Lacey, S. F., Melenhorst, J. J., Porter, D. L., and June, C. H. (2017). "Chimeric Antigen Receptor T Cells in Refractory B-Cell Lymphomas," *N Engl J Med* **377**, 2545-2554.
- Secomski, W., Bilmin, K., Kujawska, T., Nowicki, A., Grieb, P., and Lewin, P. A. (2017). "In vitro ultrasound experiments: Standing wave and multiple reflections influence on the outcome," *Ultrasonics* **77**, 203-213.

- Sennoga, C. A., Kanbar, E., Auboire, L., Dujardin, P. A., Fouan, D., Escoffre, J. M., and Bouakaz, A. (2017). "Microbubble-mediated ultrasound drug-delivery and therapeutic monitoring," *Expert Opin Drug Deliv* **14**, 1031-1043.
- Shah, S., Huang, X., and Cheng, L. (2014). "Concise review: stem cell-based approaches to red blood cell production for transfusion," *Stem Cells Transl Med* **3**, 346-355.
- Sharei, A., Trifonova, R., Jhunjhunwala, S., Hartoularos, G. C., Eyerman, A. T., Lytton-Jean, A., Angin, M., Sharma, S., Poceviciute, R., Mao, S., Heimann, M., Liu, S., Talkar, T., Khan, O. F., Addo, M., von Andrian, U. H., Anderson, D. G., Langer, R., Lieberman, J., and Jensen, K. F. (2015). "Ex vivo cytosolic delivery of functional macromolecules to immune cells," *PLoS One* **10**, e0118803.
- Sharei, A., Zoldan, J., Adamo, A., Sim, W. Y., Cho, N., Jackson, E., Mao, S., Schneider, S., Han, M. J., Lytton-Jean, A., Basto, P. A., Jhunjhunwala, S., Lee, J., Heller, D. A., Kang, J. W., Hartoularos, G. C., Kim, K. S., Anderson, D. G., Langer, R., and Jensen, K. F. (2013). "A vector-free microfluidic platform for intracellular delivery," *Proc Natl Acad Sci U S A* **110**, 2082-2087.
- Shi, J., Ahmed, D., Mao, X., Lin, S. C., Lawit, A., and Huang, T. J. (2009a). "Acoustic tweezers: patterning cells and microparticles using standing surface acoustic waves (SSAW)," *Lab on a Chip* **9**, 2890-2895.
- Shi, J., Huang, H., Stratton, Z., Huang, Y., and Huang, T. J. (2009b). "Continuous particle separation in a microfluidic channel via standing surface acoustic waves (SSAW)," *Lab on a Chip* **9**, 3354-3359.
- Shi, J., Huang, H., Stratton, Z., Huang, Y., and Huang, T. J. (2009c). "Continuous particle separation in a microfluidic channel via standing surface acoustic waves (SSAW)," *Lab Chip* **9**, 3354-3359.
- Shi, L., Wang, J. X., Stevens, L., Ness, P., and Shan, H. (2014). "Blood safety and availability: continuing challenges in China's blood banking system," *Transfusion* **54**, 471-482.
- Shields, C. W. t., Cruz, D. F., Ohiri, K. A., Yellen, B. B., and Lopez, G. P. (2016). "Fabrication and Operation of Acoustofluidic Devices Supporting Bulk Acoustic Standing Waves for Sheathless Focusing of Particles," *Journal of Visualized Experiments*.
- Shilton, R., Tan, M. K., Yeo, L. Y., and Friend, J. (2008). "Particle concentration and mixing in microdrops driven by focused surface acoustic waves," *Journal of Applied Physics* **104**, 014910.
- Shirakashi, R., Kostner, C. M., Muller, K. J., Kurschner, M., Zimmermann, U., and Sukhorukov, V. L. (2002). "Intracellular delivery of trehalose into mammalian cells by electroporation," *J Membr Biol* **189**, 45-54.
- Silverman, T. A., and Weiskopf, R. B. (2009). "Hemoglobin-based oxygen carriers: current status and future directions," *Transfusion* **49**, 2495-2515.
- Simon, T. L., McCullough, J., Snyder, E. L., Solheim, B. G., and Strauss, R. G. (2016). *Rossi's Principles of Transfusion Medicine* (John Wiley & Sons).

- Springer, T. A. (1990). "Adhesion receptors of the immune system," *Nature* **346**, 425-434.
- Steinhardt, R. A., Bi, G., and Alderton, J. M. (1994). "Cell membrane resealing by a vesicular mechanism similar to neurotransmitter release," *Science* **263**, 390-393.
- Stoiber, S., Cadilha, B. L., Benmebarek, M. R., Lesch, S., Endres, S., and Kobold, S. (2019). "Limitations in the Design of Chimeric Antigen Receptors for Cancer Therapy," *Cells* **8**.
- Stokes, G. G. (1851). "On the Effect of the Internal Friction of Fluids on the Motion of Pendulums," *Transactions of the Cambridge Philosophical Society* **9**, 8.
- Sugar, I. P., and Neumann, E. (1984a). "Stochastic model for electric field-induced membrane pores. Electroporation," *Biophys Chem* **19**, 211-225.
- Sugar, I. P., and Neumann, E. (1984b). "Stochastic model for electric field-induced membrane pores. Electroporation," *Biophysical Chemistry* **19**, 211-225.
- Sun, T., Zhang, Y., Power, C., Alexander, P. M., Sutton, J. T., Aryal, M., Vykhodtseva, N., Miller, E. L., and McDannold, N. J. (2017a). "Closed-loop control of targeted ultrasound drug delivery across the blood-brain/tumor barriers in a rat glioma model," *Proc Natl Acad Sci U S A* **114**, E10281-E10290.
- Sun, Y., Wang, Q., Chen, J., Liu, L., Ding, L., Shen, M., Li, J., Han, B., and Duan, Y. (2017b). "Temperature-Sensitive Gold Nanoparticle-Coated Pluronic-PLL Nanoparticles for Drug Delivery and Chemo-Photothermal Therapy," *Theranostics* **7**, 4424-4444.
- Szeto, G. L., Van Egeren, D., Worku, H., Sharei, A., Alejandro, B., Park, C., Frew, K., Brefo, M., Mao, S., Heimann, M., Langer, R., Jensen, K., and Irvine, D. J. (2015). "Microfluidic squeezing for intracellular antigen loading in polyclonal B-cells as cellular vaccines," *Sci Rep* **5**, 10276.
- Tasnim, H., Fricke, G. M., Byrum, J. R., Sotiris, J. O., Cannon, J. L., and Moses, M. E. (2018). "Quantitative Measurement of Naive T Cell Association With Dendritic Cells, FRCs, and Blood Vessels in Lymph Nodes," *Front Immunol* **9**, 1571.
- Terakawa, M., Sato, S., Ashida, H., Aizawa, K., Uenoyama, M., Masaki, Y., and Obara, M. (2006). "In vitro gene transfer to mammalian cells by the use of laser-induced stress waves: effects of stress wave parameters, ambient temperature, and cell type," *J Biomed Opt* **11**, 014026.
- Terasaki, M., Miyake, K., and McNeil, P. L. (1997). "Large plasma membrane disruptions are rapidly resealed by Ca²⁺-dependent vesicle-vesicle fusion events," *J Cell Biol* **139**, 63-74.
- Tlaxca, J. L., Anderson, C. R., Klibanov, A. L., Lowrey, B., Hossack, J. A., Alexander, J. S., Lawrence, M. B., and Rychak, J. J. (2010). "Analysis of in vitro transfection by sonoporation using cationic and neutral microbubbles," *Ultrasound Med Biol* **36**, 1907-1918.
- Tsujimoto, M., Imura, S., and Kanda, H. (2016). "Recovery and reproduction of an Antarctic tardigrade retrieved from a moss sample frozen for over 30 years," *Cryobiology* **72**, 78-81.

- Turtle, C. J., Hanafi, L. A., Berger, C., Gooley, T. A., Cherian, S., Hudecek, M., Sommermeyer, D., Melville, K., Pender, B., Budiarto, T. M., Robinson, E., Steevens, N. N., Chaney, C., Soma, L., Chen, X., Yeung, C., Wood, B., Li, D., Cao, J., Heimfeld, S., Jensen, M. C., Riddell, S. R., and Maloney, D. G. (2016). "CD19 CAR-T cells of defined CD4+:CD8+ composition in adult B cell ALL patients," *J Clin Invest* **126**, 2123-2138.
- Turtle, C. J., Hay, K. A., Hanafi, L. A., Li, D., Cherian, S., Chen, X., Wood, B., Lozanski, A., Byrd, J. C., Heimfeld, S., Riddell, S. R., and Maloney, D. G. (2017). "Durable Molecular Remissions in Chronic Lymphocytic Leukemia Treated With CD19-Specific Chimeric Antigen Receptor-Modified T Cells After Failure of Ibrutinib," *J Clin Oncol* **35**, 3010-3020.
- Uchida, T., Furukawa, M., Kikawada, T., Yamazaki, K., and Gohara, K. (2017). "Intracellular trehalose via transporter TRET1 as a method to cryoprotect CHO-K1 cells," *Cryobiology* **77**, 50-57.
- Ulmer, A. J., Scholz, W., Ernst, M., Brandt, E., and Flad, H. D. (1984). "Isolation and subfractionation of human peripheral blood mononuclear cells (PBMC) by density gradient centrifugation on Percoll," *Immunobiology* **166**, 238-250.
- van der Valk, J., Brunner, D., De Smet, K., Fex Svenningsen, A., Honegger, P., Knudsen, L. E., Lindl, T., Noraberg, J., Price, A., Scarino, M. L., and Gstraunthaler, G. (2010). "Optimization of chemically defined cell culture media--replacing fetal bovine serum in mammalian in vitro methods," *Toxicol In Vitro* **24**, 1053-1063.
- Versluis, M., Stride, E., Lajoinie, G., Dollet, B., and Segers, T. (2020). "Ultrasound Contrast Agent Modeling: A Review," *Ultrasound Med Biol* **46**, 2117-2144.
- Villanueva, F. S. (2010). "Myocardial perfusion imaging using ultrasound contrast agents: now or never?," *JACC Cardiovasc Imaging* **3**, 944-946.
- Vormittag, P., Gunn, R., Ghorashian, S., and Veraitch, F. S. (2018). "A guide to manufacturing CAR T cell therapies," *Curr Opin Biotechnol* **53**, 164-181.
- Wahlers, A., Schwieger, M., Li, Z., Meier-Tackmann, D., Lindemann, C., Eckert, H. G., von Laer, D., and Baum, C. (2001a). "Influence of multiplicity of infection and protein stability on retroviral vector-mediated gene expression in hematopoietic cells," *Gene Ther* **8**, 477-486.
- Wahlers, A., Schwieger, M., Li, Z., Meier-Tackmann, D., Lindemann, C., Eckert, H. G., von Laer, D., and Baum, C. (2001b). "Influence of multiplicity of infection and protein stability on retroviral vector-mediated gene expression in hematopoietic cells," *Gene Therapy* **8**, 477-486.
- Wang, F., Wang, H., Wang, J., Wang, H. Y., Rummel, P. L., Garimella, S. V., and Lu, C. (2008). "Microfluidic delivery of small molecules into mammalian cells based on hydrodynamic focusing," *Biotechnol Bioeng* **100**, 150-158.
- Wang, H. Y., and Lu, C. (2006). "High-throughput and real-time study of single cell electroporation using microfluidics: effects of medium osmolarity," *Biotechnol Bioeng* **95**, 1116-1125.
- Wang, M., Zhang, Y., Cai, C., Tu, J., Guo, X., and Zhang, D. (2018). "Sonoporation-induced cell membrane permeabilization and cytoskeleton disassembly at varied acoustic and microbubble-cell parameters," *Sci Rep* **8**, 3885.

- Wang, X., and Riviere, I. (2015). "Manufacture of tumor- and virus-specific T lymphocytes for adoptive cell therapies," *Cancer Gene Ther* **22**, 85-94.
- Wang, Z., Li, F., Rufo, J., Chen, C., Yang, S., Li, L., Zhang, J., Cheng, J., Kim, Y., Wu, M., Abemayor, E., Tu, M., Chia, D., Spruce, R., Batis, N., Mehanna, H., Wong, D. T. W., and Huang, T. J. (2020). "Acoustofluidic Salivary Exosome Isolation: A Liquid Biopsy Compatible Approach for Human Papillomavirus-Associated Oropharyngeal Cancer Detection," *J Mol Diagn* **22**, 50-59.
- Weaver, J. C. (1993). "Electroporation: a general phenomenon for manipulating cells and tissues," *Journal of Cellular Biochemistry* **51**, 426-435.
- Wu, J., and Nyborg, W. L. (2008). "Ultrasound, cavitation bubbles and their interaction with cells," *Adv Drug Deliv Rev* **60**, 1103-1116.
- Wu, M., Chen, K., Yang, S., Wang, Z., Huang, P. H., Mai, J., Li, Z. Y., and Huang, T. J. (2018). "High-throughput cell focusing and separation via acoustofluidic tweezers," *Lab Chip* **18**, 3003-3010.
- Wu, M., Ouyang, Y., Wang, Z., Zhang, R., Huang, P. H., Chen, C., Li, H., Li, P., Quinn, D., Dao, M., Suresh, S., Sadovsky, Y., and Huang, T. J. (2017). "Isolation of exosomes from whole blood by integrating acoustics and microfluidics," *Proc Natl Acad Sci U S A* **114**, 10584-10589.
- Wu, Y., Ihme, S., Feuring-Buske, M., Kuan, S. L., Eisele, K., Lamla, M., Wang, Y., Buske, C., and Weil, T. (2013). "A core-shell albumin copolymer nanotransporter for high capacity loading and two-step release of doxorubicin with enhanced anti-leukemia activity," *Adv Healthc Mater* **2**, 884-894.
- Yang, Y., Li, Q., Guo, X., Tu, J., and Zhang, D. (2020). "Mechanisms underlying sonoporation: Interaction between microbubbles and cells," *Ultrason Sonochem* **67**, 105096.
- Yang, Y., Wang, L., Bell, P., McMenamin, D., He, Z., White, J., Yu, H., Xu, C., Morizono, H., Musunuru, K., Batshaw, M. L., and Wilson, J. M. (2016). "A dual AAV system enables the Cas9-mediated correction of a metabolic liver disease in newborn mice," *Nat Biotechnol* **34**, 334-338.
- Yarar, D., Waterman-Storer, C. M., and Schmid, S. L. (2005). "A dynamic actin cytoskeleton functions at multiple stages of clathrin-mediated endocytosis," *Mol Biol Cell* **16**, 964-975.
- Yeo, L. Y., Chang, H. C., Chan, P. P., and Friend, J. R. (2011). "Microfluidic devices for bioapplications," *Small* **7**, 12-48.
- Ying, Z., Huang, X. F., Xiang, X., Liu, Y., Kang, X., Song, Y., Guo, X., Liu, H., Ding, N., Zhang, T., Duan, P., Lin, Y., Zheng, W., Wang, X., Lin, N., Tu, M., Xie, Y., Zhang, C., Liu, W., Deng, L., Gao, S., Ping, L., Wang, X., Zhou, N., Zhang, J., Wang, Y., Lin, S., Mamuti, M., Yu, X., Fang, L., Wang, S., Song, H., Wang, G., Jones, L., Zhu, J., and Chen, S. Y. (2019). "A safe and potent anti-CD19 CAR T cell therapy," *Nat Med* **25**, 947-953.
- Zhang, B., Shi, Y., Miyamoto, D., Nakazawa, K., and Miyake, T. (2019). "Nanostraw membrane stamping for direct delivery of molecules into adhesive cells," *Sci Rep* **9**, 6806.
- Zhang, C., Liu, J., Zhong, J. F., and Zhang, X. (2017a). "Engineering CAR-T cells," *Biomark Res* **5**, 22.

- Zhang, M., Oldenhof, H., Sydykov, B., Bigalk, J., Sieme, H., and Wolkers, W. F. (2017b). "Freeze-drying of mammalian cells using trehalose: preservation of DNA integrity," *Scientific Reports* **7**, 6198.
- Zhang, S., Fan, J., Xu, X., Chen, G., Zhu, F., and Yan, L. (2009). "An experimental study of the use of ultrasound to facilitate the loading of trehalose into platelets," *Cryobiology* **59**, 135-140.
- Zhang, Y. W., Tu, L. L., Tang, Z., Wang, Q., Zheng, G. L., and Yin, L. N. (2021). "pH-sensitive chitosan-deoxycholic acid/alginate nanoparticles for oral insulin delivery," *Pharm Dev Technol* **26**, 943-952.
- Zhao, S., Borden, M., Bloch, S. H., Kruse, D., Ferrara, K. W., and Dayton, P. A. (2004). "Radiation-force assisted targeting facilitates ultrasonic molecular imaging," *Mol Imaging* **3**, 135-148.
- Zhou, M., Gao, D., Yang, Z., Zhou, C., Tan, Y., Wang, W., and Jiang, Y. (2021). "Streaming-enhanced, chip-based biosensor with acoustically active, biomarker-functionalized micropillars: A case study of thrombin detection," *Talanta* **222**, 121480.
- Zhou, X., Yuan, J., Liu, J., and Liu, B. (2010). "Loading trehalose into red blood cells by electroporation and its application in freeze-drying," *Cryo Letters* **31**, 147-156.
- Zhou, Y., Shi, J., Cui, J., and Deng, C. X. (2008). "Effects of extracellular calcium on cell membrane resealing in sonoporation," *J Control Release* **126**, 34-43.
- Zhou, Y., Yang, K., Cui, J., Ye, J. Y., and Deng, C. X. (2012). "Controlled permeation of cell membrane by single bubble acoustic cavitation," *J Control Release* **157**, 103-111.

CURRICULUM VITAE

Connor Sterling Centner
connor.centner@louisville.edu
DOB: October 5th, 1994

EDUCATION AND TRAINING

- 2018 –2022 **PhD in Translational Bioengineering**, University of Louisville
Relevant Training and Courses: Biomedical Acoustics, Immunology, Cancer Biology, Clinical Practicum—Hematology/Oncology (James Brown Cancer Center)
Dissertation: Characterization of fundamental parameters that modulate acoustofluidic-mediated molecular delivery to cells
- 2017 –2018 **MEng in Bioengineering**, University of Louisville
Relevant Courses: Nanoscale Engineering, Tissue Engineering
Thesis: Tumor-targeted double emulsions for ultrasound-triggered delivery of molecular therapeutics
- 2013 – 2017 **BS in Bioengineering**, University of Louisville
Relevant Training: Clinical Engineering (Cincinnati Children’s Medical Center)

AWARDS & HONORS

- | | |
|-----------------|---|
| 10/2021 | NSF INTERN |
| 04/2021 | Doctoral Student Inventorship Award, Bioengineering Award |
| 07/2020-06/2021 | University of Louisville Fellowship |
| 04/2020 | Doctoral Student Exemplary Achievement Award, Bioengineering |
| 01/2020 | NSF INTERN |
| 09/2019 | Research!Louisville, 2 nd place in Doctoral Engineering Category |
| 08/2018-07/2019 | University of Louisville Fellowship |
| 04/2018 | Joseph Henry Award, Bioengineering |

PROFESSIONAL AFFILIATIONS

Member Acoustical Society of America (ASA)

ACADEMIC AND PROFESSIONAL EXPERIENCE

10/2021-03/2022 **Sexton Biotechnologies, A Biolife Solutions Company**
Research Scientist, Intern
Indianapolis, IN

01/2020-06/2020 **Sexton Biotechnologies, A Biolife Solutions Company**
Research Scientist, Intern
Indianapolis, IN

03/2018-07/2018 **United Parcel Services (UPS)**
Plant Engineering Supervisor
Louisville, KY

12/2016-04/2017 **Cincinnati Children's Medical Center**
Clinical Engineer, Intern
Cincinnati, OH

05/2016-08/2017 **Bridgestone**
Process and Research Engineer, Intern
Mesa, AZ

05/2016-08/2017 **Elite Biomedical Solutions**
Quality Engineer, Intern
Cincinnati, OH

PUBLICATIONS

Centner, C. S., Moore, J. T., Baxter, M. E., Long, Z. T., Miller, J. M., Kovatsenko, E. S., Xie, B., Berson, R. E., Bates, P. J., Yaddanapudi, K., Kopechek, J. A. (2021). Acoustofluidic-mediated molecular delivery to human T cells with a 3D-printed flow chamber. *The Journal of the Acoustical Society of America*.

Centner, C. S., Murphy, E. M., Stamp, B. F., Priddy, M. C., Moore, J. T., Bates, P. J., Menze, M. A., Yaddanapudi, K., & Kopechek, J. A. (2021). Assembly and operation of an acoustofluidic device for enhanced delivery of molecular compounds to cells. *Journal of Visualized Experiments*, (167). <https://doi.org/10.3791/62035>

Centner, C. S., Murphy, E. M., Priddy, M. C., Moore, J. T., Janis, B. R., Menze, M. A., DeFilippis, A. P., & Kopechek, J. A. (2020). Ultrasound-induced molecular

delivery to erythrocytes using a microfluidic system. *Biomicrofluidics*, 14(2), 024114. <https://doi.org/10.1063/1.5144617>

Murphy, E. M., **Centner, C. S.**, Bates, P. J., Malik, M. T., & Kopechek, J. A. (2020). Delivery of thymoquinone to cancer cells with AS1411-conjugated nanodroplets. *PLOS ONE*, 15(5). <https://doi.org/10.1371/journal.pone.0233466>

Centner, C. S., Murphy, E. M., Stivers, C. M., Burns, M. S., Priddy, M. C., Janis, B. R., Menze, M. A., & Kopechek, J. A. (2018). Development of a high-performance ultrasonic flow system for cell transformation. *2018 IEEE International Symposium on Signal Processing and Information Technology (ISSPIT)*. <https://doi.org/10.1109/isspit.2018.8705103>

Bhutto, D. F., Murphy, E. M., Priddy, M. C., **Centner, C. S.**, Moore IV, J. B., Bolli, R., & Kopechek, J. A. (2018). Effect of molecular weight on sonoporation-mediated uptake in human cells. *Ultrasound in Medicine & Biology*, 44(12), 2662–2672. <https://doi.org/10.1016/j.ultrasmedbio.2018.08.008>

CONFERENCES

- | | |
|---------|---|
| 11/2021 | Centner et al. Modulation of Acoustofluidic Parameters to Assess Effect on Molecular Loading in Human T Cells [Conference Presentation] 181 st Acoustical Society of America Meeting, Seattle, WA, United States |
| 10/2021 | Centner et al. Biomodulatory effect of acoustofluidic-induced molecular delivery to human T cells [Conference Poster] Research!Louisville 2021, Louisville, KY, United States |
| 12/2020 | Centner et al. Computational Modeling of Ultrasound Pressures in Acoustofluidic Channels for Enhanced Sonoporation [Conference Presentation] 179 th Acoustical Society of America Meeting, Remote |
| 10/2019 | Centner et al. Acoustofluidic Devices for Enhanced Intracellular molecular delivery [Conference Poster] Research!Louisville 2019, Louisville, KY, United States; BMES 2019, Philadelphia, PA, United States |
| 07/2019 | Centner et al. Effect of Acoustofluidic Flow on Intracellular Molecular Delivery [Conference Presentation] KY Nano+AM symposium, Louisville, KY, United States |
| 05/2019 | Centner et al. Standing Surface Acoustic Waves for Enhanced Intracellular Delivery of Molecular Compounds |

- [Conference Poster] 177th Acoustical Society of America Meeting, Louisville, KY, United States
- 05/2019 Centner et al. Standing Acoustic Waves in Microfluidic Channels for Enhanced Intracellular Delivery of Molecular Compounds [Conference Presentation] 177th Acoustical Society of America Meeting, Louisville, KY, United States
- 02/2019 Centner et al. Ultrasound-Driven Microfluidic Device for Enhanced Intracellular Delivery of Molecular Compounds [Conference Poster] 2019 Graduate Student Research Regional Conference, Louisville, KY, United States
- 12/2018 Centner et al. Development of High-Performance Ultrasonic Flow System for Cell Preservation [Preceding Article + Conference Presentation] 20th IEEE ISSPIT Symposium, Louisville, KY, United States
- 09/2017 Centner et al. Ultrasound-Target Delivery of Fluorescein to Cancer Cells Using Double Emulsions [Conference Poster] Research!Louisville 2017, Louisville, KY, United States

INVITED PRESENTATIONS

- 03/2021 Ultrasound Flow System for Improved Molecular Delivery. *University of Louisville: Bioengineering Department Seminar*
- 02/2022 Acoustofluidic-mediated molecular delivery for cell therapy applications. *University of Louisville: Bioengineering Department Seminar*